Mechanisms of deformation and energy dissipation in antler and arthropod cuticle with bio-inspired investigations

Paolino De Falco

Submitted in partial fulfillment of the requirements of the Degree of Doctor of Philosophy in Mechanical Engineering

School of Engineering and Materials Science

Queen Mary University of London

Supervisors:

Prof. Nicola Pugno

Dr. Himadri Gupta

Dr. Ettore Barbieri

September 2017

Declaration

I, Paolino De Falco, confirm that the research included within this thesis is my own work or that where it has been carried out in collaboration with, or supported by others, that this is duly acknowledged below and my contribution indicated. Previously published material is also acknowledged below.

I attest that I have exercised reasonable care to ensure that the work is original, and does not to the best of my knowledge break any UK law, infringe any third party's copyright or other Intellectual Property Right, or contain any confidential material.

I accept that the College has the right to use plagiarism detection software to check the electronic version of the thesis.

I confirm that this thesis has not been previously submitted for the award of a degree by this or any other university.

Signature:

Date: 29/09/2017

Abstract

Bio-composite hierarchical materials have attracted the interest of the academic community operating in the field of bio-inspired materials for their outstanding mechanical properties achieved via lightweight structural designs. Antler and mantis shrimp's cuticle are extreme examples of materials naturally optimised to resist impacts and bear dynamic loading. Firstly, a class of finite-element fibril models was developed to explain the origin of heterogeneous fibrillar deformation and hysteresis from the nanostructure of antler. Results were compared to synchrotron X-ray data and demonstrated that the key structural motif enabling a match to experimental data is an axially staggered arrangement of stiff mineralised collagen fibrils coupled with weak, damageable interfibrillar interfaces. Secondly, the cuticle of the crustacean Odontodactylus scyllarus, known as peacock mantis shrimp, was investigated. At the nanoscale it consists of mineralised chitin fibres and calcified protein matrix, which form plywood layers at the microscale. Lamination theory was used to calculate fibrillar deformation and reorientation and, in addition, an analytical formulation was used to decouple in-plane fibre reorientation from diffraction intensity changes induced by 3D lamellae tilting. This animal also attracted my attention for using its hammer-like appendages to attack and destroy the shells of prey with a sequence of two strikes. Inspired by this double impact strategy, I performed a set of parametric finite-element simulations of single, double and triple mechanical hits, to compute the damage energy of the target. My results reveal that the crustacean attack strategy has the most damaging effect among the double impact cases, and lead me to hypothesise, that optimal damaging

dynamics exists, depending on the sequence of consecutive impacts and on their time separation values. These new insights may provide useful indications for the design of bio-inspired materials for high load-bearing applications.

Acknowledgements

I would like to thank all the people who contributed to the work described in this thesis. First and foremost, I thank my three supervisors: Prof. Nicola Pugno, Dr. Himadri Gupta and Dr. Ettore Barbieri. They all guided me through my project and contributed to my publications. Each of them imparted invaluable knowledge and skills that will serve as base and inspiration for my future research. Prof. Pugno showed me how to develop simple concepts and make them interesting. It was very fascinating to look at the way he approaches new ideas and formulates intriguing questions. I really appreciate Dr. Gupta for his kindness and professionalism. Working with him even in the weekend was a pleasure and a useful training. He dedicated a lot of time to my projects and I will be always grateful to him for that. He will be an enormous source of inspiration for my future research and he will always represent the type of researcher I would like to become. Dr. Ettore Barbieri has been one my best friends in London. He guided me through all the difficulties. I have been very lucky to find such a nice person always supporting me and giving me nice advice. His door was always opened for me and every meeting an occasion to learn new concepts.

I would also like to thank Queen Mary University of London and the School of Engineering and Material Science for providing all the necessary to work in a comfortable and professional environment. My gratitude is also extended to Jonathon Hills and Saima Ahmed from the administration team. They were always available, kind and quick with solving issues. Furthermore, it was also of

extreme importance to work together with my colleagues: Andrew, Giovanni, Francesca, Federica, Yanhong and Jingyi. Their friendship was very helpful to overcome difficult moments.

A special thank goes to my girlfriend, Kristina, who always supported and helped me during hard and very busy periods.

Living far from my original home was very formative. It has been a life lesson and also the way to realise how deep and wonderful is the love which links me to my family. My parents and my sisters have been always supporting and encouraging me. Observing their joy for my successes made me very proud and glad. An infinite gratitude goes to them.

Publications

➤ De Falco, P., Barbieri, E., Pugno, N. M., & Gupta, H. S. (2017). *Staggered fibrils and damageable interfaces lead concurrently and independently to hysteretic energy absorption and inhomogeneous strain fields in cyclically loaded antler bone*. ACS Biomaterials Science & Engineering, 3(11), 2779-2787.

➤ Y. Zhang*, P. De Falco*, Y. Wang, E. Barbieri, O. Paris, N. J. Terrill, G. Falkenberg, N. M. Pugno and H. S. Gupta. (2017). *Towards in situ determination of 3D strain and reorientation in the interpenetrating nanofibre networks of cuticle*. *Nanoscale*, *9*(31), 11249-11260 (*These authors contributed equally to this work).

➤ L. Xi, P. De Falco, E. Barbieri, L. Bentley, C.T. Esapa, N.J. Terrill, S.D.M. Brown, R.D. Cox, N.M. Pugno, R.V. Thakker, G.R. Davis, H.S. Gupta. (2018). *Bone matrix development in steroid-induced osteoporosis is associated with a consistently reduced fibrillar stiffness linked to altered bone mineral quality. Acta Biomaterialia,* 76, 295-307*.*

➤ Ongaro, F., De Falco, P., Barbieri, E., Pugno, N. M. (2016). *Mechanics of filled cellular materials*. Mechanics of Materials, 97, 26-47.

Presentations by the candidate

- ➢ *MRI Christmas Symposium*. 9th December 2016, Queen Mary University of London.

- ➢ *The 12th World Congress on Computational Mechanics*. 24 – 29th July 2016, Seoul (Korea).

- ➢ *N8 HPC Network Event – Multiscale Computational Mechanics*. 30th October 2015, University of Sheffield (UK).

- ➢ *Industrial Liaison Forum*. 29th October 2015, Queen Mary University of London.

Table of contents

List of figures

15

16

parametrised variables are A) the fibril volume fraction, B) the Young's modulus

of mineral spherules and C) the Young's modulus of chitin.

Figure 5.9 - 3D tilting of in-plane fibres under tensile loading. (a)-(c) The

rings represent sections of the 3D spherical intensity distributions shown in

figure 5.2, for both (002) (inner ring) and (110) (outer ring). Rings are colour

coded for intensity levels. The different images in (a) – (c) represent different

orientations (via the tilt angles α, β), shown via the schematic of the Bouligand

layer (green fibres; colour online) inside the ring. Yellow axes and fibre

distribution represent the untilted ($\alpha = \beta = 0°$) reference state. (d)-(f)

Corresponding azimuthal intensity plots $I(\chi)$ for the 2D intensity sections, with

the horizontal reference line in each plot denoting the untilted configuration. (g)

Stress-strain curve for a representative cuticle sample, with symbols I-III

denoting from where the three azimuthal intensity curves in the following section

(h) are taken. (h) Azimuthal intensity plots from points I-III in (g), vertically

translated for representational clarity only. Solid lines denote fits to the

analytical model (**Equation 77**). (i) Tilt angles α (left abscissa) and β (right

abscissa) as a function of tissue strain, for the sample shown in (g), obtained by

fits to the analytical model. A decrease of the off-axis tilt angleα, indicating load-

induced alignment of the Bouligand layer toward the tensile axis, is observed.

Figure 5.10 - The mechanical response of out-plane fibre from L2 configuration.

(a) The intensity distributions on QS(110) sphere corresponding to in-plane and

out-of-plane fibres. (b) The intensity distributions on QS(002) sphere

corresponding to in-plane and out-of-plane fibres. (c) The intensity distributions

of (110) and (002) reflections on the intersection plane of the Ewald sphere and

deformation of the chitin nanofibres. (c) The deformation of the fibre plane composed of parallely arranged chitin fibres surrounded by protein and mineral matrix. (d) Schematic shows the in-plane rotation of mineralised chitin fibres due to external tensile load. (e) Schematic showing 3D fibre plane tilting due to external tensile load. (f) Scanning electron micrograph showing the plywood structure of In-plane chitin fibres is interrupted by the out-of-plane fibres running

List of tables

1 Motivation

During the last decades, material scientists and engineers tried to satisfy the increasing demand for tough, lightweight and impact resistant materials in aerospace, defence and, more in general, structural engineering by mimicking Nature. Bio-materials feature a set of types of behaviour such as multifunctionality, hierarchical organization, self-assembly and self-healing (Bosia, Abdalrahman et al. 2014) (Bosia, Abdalrahman et al. 2012) that justify the interest of researchers. Most biological materials, such as bone, arthropod cuticle (the exoskeleton of crustaceans) or tendons are complex composites that evolved into a range of hierarchical organizations whose design is of remarkable inspiration (Meyers, Chen et al. 2008). Their process of evolution lasted thousands of years and resulted in optimised materials made of basic building blocks such as proteins and brittle minerals that 'build' the final design thanks to a self-organization strategy during growth (Meyers, Chen et al. 2008). The mechanical properties of such bio-composites are often outstanding if compared to the weak basic constituents, due to a functional adaptation at all levels of hierarchy and length scales (Ji and Gao 2004, Fratzl and Weinkamer 2007). In fact, in these materials high toughness, strength and stiffness are often obtained thanks to a combination of structural designs and mechanisms of deformation occurring at each hierarchical level (Bouligand 1972, Launey, Buehler et al. 2010). These structural principles have spurred materials scientists to investigate biological systems and elucidate the principles behind these exceptional mechanical properties. In fact, a new area of research, known as bio-mimetic or bio-inspired materials science recently developed with the aim

of creating synthetic bio-inspired materials (Ji and Gao 2004, Meyers, Chen et al. 2008, Zimmermann, Gludovatz et al. 2013).

Although experimental and numerical methods have been employed focusing on these structural designs (Libonati, Gu et al. 2016), the high toughness and work to fracture of these bio-composites at the molecular, nano- and micro scales are not completely explored. For this reason, in this thesis I investigate the mechanical properties of two outstanding biological composites: the antler and the stomatopod cuticle which have shown a superior capability to resist dynamic and impact loads (**Figure 1.1**). My overall hypothesis in this thesis is that the structural organization and the mechanisms of deformation and energy dissipation are crucial for the impact resistance of these two bio-composites and, in this regard, the aim is to analyse and determine the structural factors enabling these mechanisms at different scales.
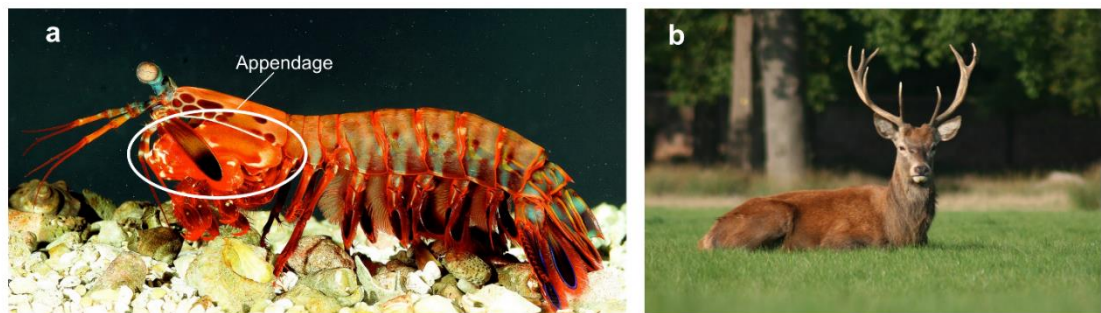
Figure 1.1 – Image of a) mantis shrimp (or stomatopod) and of b) deer's antler.

The mantis shrimp (stomatopod) is a ferocious predator of the Indian and Pacific oceans, whose smashing or spearing appendages and the telson (the rear part of the cuticle that the animal uses as a shield for defence), exhibit outstanding impact tolerance during preying (Patek and Caldwell 2005, Weaver,

Milliron et al. 2012) and during fights for defending the burrows (Taylor and Patek 2010). This animal uses its limbs to strike molluscs and it is able to destroy (without self-damaging) their shells which contain high toughness nacre material. Therefore, I could deduce that the cuticle outperforms the already high impact-resistance of the well-studied and analysed abalone nacre (Sun and Bhushan 2012). Hence, the stomatopod cuticle is an ideal biological model for the study of the factors determining the resistance of multiscale composites against dynamic loading.

Deer are ruminant mammals forming the family of Cervidae. Males of the most families of cervids use their antlers during the rutting season in the dominance battles for access to females (Clutton-Brock 1988). These fights usually are made of an initial clashing of the antlers, followed by a pushing match (Clutton-Brock, Albon et al. 1979). These very violent battles often result in severe injury and even death of one of the contender although antlers themselves display scarce signs of damage (Currey, Landete-Castillejos et al. 2009). This remarkable damage tolerance inspired scientists and justified the considerable effort and interest in analysing the structure of these hierarchical materials.

A key characteristic of the high energy absorption of antler that attracted my attention is the large hysteresis during cyclic loading whose origin was unknown. In situ synchrotron X-ray diffraction tests during tensile loading of antler showed heterogeneous fibrillar deformation and hysteresis (Gupta, Krauss et al. 2013). To explain the origin of these mechanisms from the nanostructure of antler, in **Chapter 4** I develop a class of finite element fibril

models whose predictions are compared to experimental data across a range of potential composite architectures.

Stomatopod cuticle is the second biological system that inspired this project and at the nanoscale consists of mineralised chitin fibres and calcified protein matrix forming (at the microscale) plywood structures (Bouligand 1972). In **Chapter 5** I investigated the anisotropic deformation patterns inside Bouligand lamellae, accompanied by load-induced fibre reorientation. In detail, the lamination theory was used to calculate in-plane fibre deformation and reorientation. This method, combined with synchrotron X-ray experimental data enabled the separation of deformation dynamics at multiple hierarchical levels, a critical consideration in the cooperative mechanics characteristic of biological and bio-inspired materials.

Biological systems also offer multiple examples of exceptional dynamic behaviour for predation that are a proof of an evolutionary adaption in the animal kingdom (Parker and Smith 1990). In fact, invertebrates such as ants and crustaceans underwent a process of evolution involving their hunting strategy but also the shape and the morphology of their appendages (Murphy and Patek 2012). As a result, these animals are able to attack their prey with extremely rapid strikes by using their appendages. For instance, the ant *Odontomachus bauri*, during predatory strikes is able to close its mandibles at speeds ranging from 36 to 64 m/s and accelerations on the order of 10^5 g. Similarly, the crustacean *Odontodactylus scyllarus*, known as peacock mantis shrimp, is a tremendous predator that uses its limbs to attack and hit the shells of preys with a 'two-strikes strategy' reaching speeds of the order of 20 m/s and

acceleration of 10^5 g. Specifically, the first strong strike of about 480 N triggers a cavitation bubble in the seawater which provokes a successive hit (about twice weaker than the first one and with a time delay of 0.5 ms) on the prey upon collapsing (Patek and Caldwell 2005). Inspired by this double impact strategy, in **Chapter 6** I present a set of parametric finite-element simulations of single, double and triple mechanical hits, using spherical projectiles and flat aluminium targets, to compute the damage energy of the target. Several sequences of impacts, different diameters (3, 4 and 6 mm) of the projectile and various time separation values between consecutive impacts (in the range 0.0 - 0.8 ms), were tested, by keeping the kinetic energy value of the projectile fixed, to check the effects of splitting this amount of energy over multiple hits.

Both analytical and numerical approaches have been used to develop these projects. In fact, when problems where relatively simple to solve I approached them with an analytical formulation (**Chapter 5**) based on specific hypotheses and equations that were solved using the software *Matlab*. In other cases the complexity of the calculations and of the analysed problems (**Chapters 4-6**) led us to perform simulations using the software *Abaqus* whose algorithms are based on the Finite Element Method (FEM), a numerical method that is usually employed for simulating complex engineering and mathematical problems (Zienkiewicz, Taylor et al. 1977).

A schematic summary of the objectives of this thesis is provided below.

Objectives:

- ➢ Investigate the mechanisms responsible for hysteresis and heterogeneity at the fibrillar level in antler.

- ➢ Find a formulation to compute fibre deformation and reorientation in arthropod cuticle.

- ➢ Investigate the dynamics of the mantis shrimp's attacks and find evidence of strategies for inflicting maximum amount of damage.

2 Hierarchical structure and mechanics in biological materials: arthropod cuticle and antler

The reasons behind the decision of investigating the mechanism of deformation and energy dissipation of the arthropod cuticle and bone are explained in **Chapter 1**. In this chapter I provide an overview of the hierarchical structure of these two bio-materials.

2.1 Arthropod cuticle

Arthropods are invertebrate animals having an exoskeleton, jointed appendages and segmented body (Neville 2012). They are classified in five orders (Manton 1977):

1. Crustaceans, such as lobsters, crabs, crayfishes and shrimps with coupled appendages

2. Trilobites, a group of marine animals that are nowadays extinct

3. Chelicerates, such as horseshoe crabs, spiders and scorpions with appendages placed in front or above their mouth

4. Myriapods, including millipedes and centipedes with several body segments and paired legs

5. Haxapods, which are mainly insects with the body divided into an anterior head and posterior abdomen.

These animals appeared on the Earth during the Cambrian period (about 500 millions of years ago) and naturally evolved in the species that nowadays we observe. The success of their evolution can be attributed to their ability to adapt and to their exoskeleton, a natural armour optimised to resist impacts and

protect the internal organs (García-Bellido and Collins 2004). Made of polysaccharide chitin, proteins and inorganic constituents (Cutler 1980, GREENAWAY 1985), the arthropod cuticle (exoskeleton) evolved into a multiscale structure at different length scale exhibiting impressive mechanical properties. The main constituent, chitin $(C_8H_{13}O_5N)_n$, is a long chain-polysaccharide and exists in different molecular forms. One of these forms is the α-chitin (Van de Velde and Kiekens 2004) that combined with a tough protein matrix, a stiff mineral phase and a variable level of water, confers to the nanostructure both toughness and stiffness (Roer and Dillaman 1984). The form α-chitin (**Figure 2.1**) is made of tightly antiparallel chains (a chain in one direction alternates with another in the opposite direction) arranged in a crystalline orthorhombic form. Other forms of chitin are: β-chitin that is less crystalline than the type α and is built in monoclinic unit cells with parallel chains and γ-chitin where two parallel chains alternate with one antiparallel chain (Ruiz-Herrera 1991).
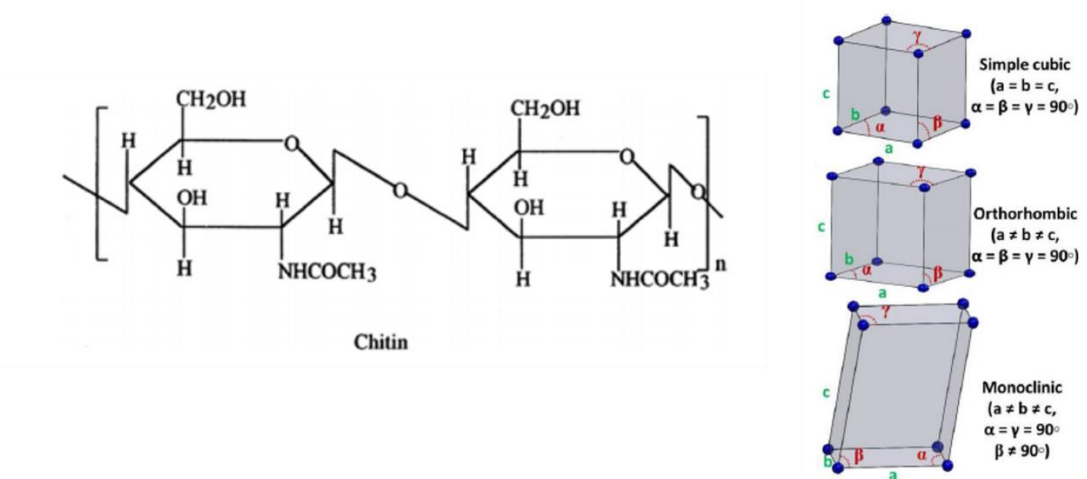
Figure 2.1 - Structure of chitin and example of cubic, orthorhombic and monoclinic unit crystals (Dutta 2015, Zhang 2016).

The Young's modulus of different types of cuticle ranges between 1 KPa and 50 MPa for soft cuticle (cuticle is soft is when containing equal weight fractions of chitin and protein, and from 40 to 75% water while it is stiff when containing from 15 to 30% weight fraction of chitin and only 12% of water (Vincent and Wegst 2004), can be in the order of MPa for the elastomeric cuticle of the larva, but it is able to reach up to 20 GPa in the dry cuticle of locusts' wings and tibiae (Vincent and Wegst 2004). This huge variability in the mechanical properties of cuticle is one of the reasons that has enhanced the interest of many materials scientists who are trying to explain how it is possible to obtain different mechanical properties using the same basic constituents with the final aim to replicate the biological behaviour (bio-mimetics is the science of imitating Nature) and create novel materials for engineering applications (Barthelat 2007, Fratzl and Weinkamer 2007).

The crustacean cuticle differs from other types of cuticle as it undergoes the process of calcification (Roer and Dillaman 1984, Nikolov, Petrov et al. 2010) that increases the stiffness up to 100 GPa without reducing the levels of structural toughness (typically cuticle toughness varies in the range 0.2 – 2 KJ/m^2) (Vincent and Wegst 2004, Luquet 2012) (**Figure 2.2**).
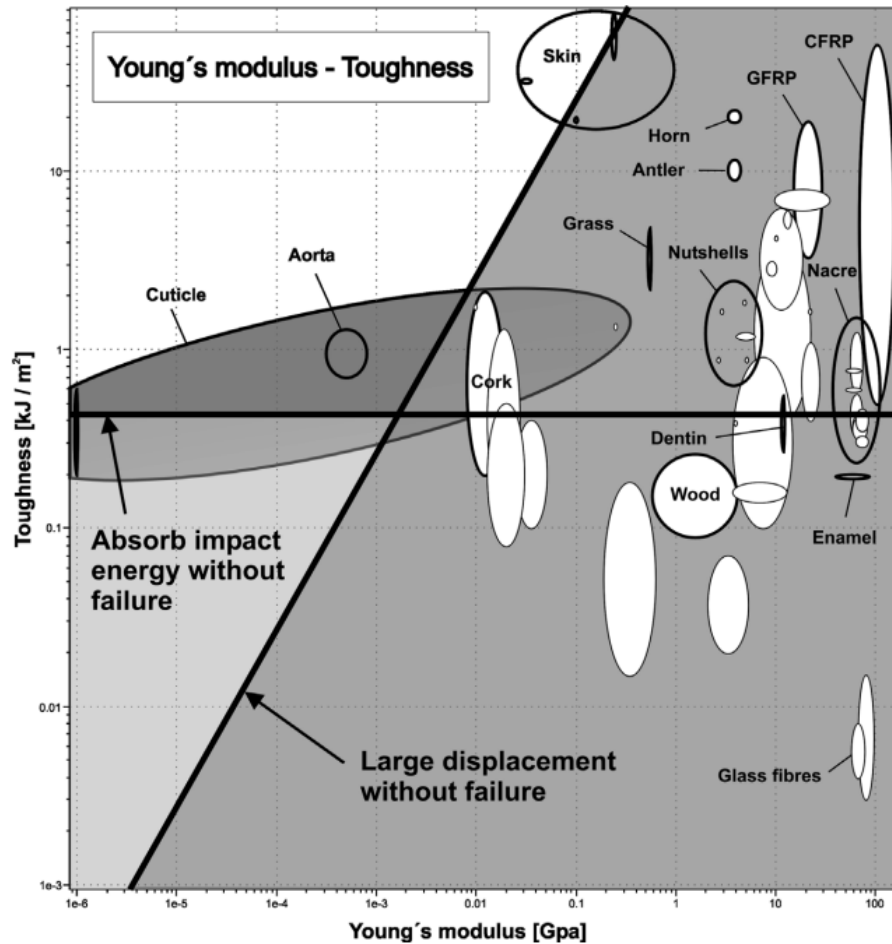
Figure 2.2 – Material chart plotting toughness versus Young's modulus for several natural materials (Vincent and Wegst 2004).

Crustaceans are a subphylum of arthropods which includes lobsters, shrimps, crabs and barnacles. These animals have a rigid exoskeleton, made of a layered cuticle (**Figure 2.3**) (membrane layer, endocuticle, exocuticle and epicuticle) with the function of protection against competitors and the environment, desiccation, and of support for muscle attachment. The overall mechanical properties of cuticle are outstanding compared with the basic constituents. In fact, while the strength of the mineral and protein phase reaches, respectively, values of 20 and 30 MPa, at macro-scale values up to 10 times higher are experimentally measured (Ji and Gao 2004).

The reasons of this impressive increase in the mechanical properties lie in the hierarchical structure of this material (**Figure 2.3**). In details, natural structural materials exhibit mechanical properties through complex hierarchical architectures and load-absorbing mechanisms occurring at each length level. This hierarchical design recurs in Nature in the forms of other hard tissues like wood, bone and shells (Fratzl and Weinkamer 2007). Understanding the composition of these structures and explaining the mechanisms determining, at each length scale, the mechanical properties of these bio-composites is one of the main challenges for researchers in the field of bio-mimetic and bio-inspired materials (Vincent and Wegst 2004).
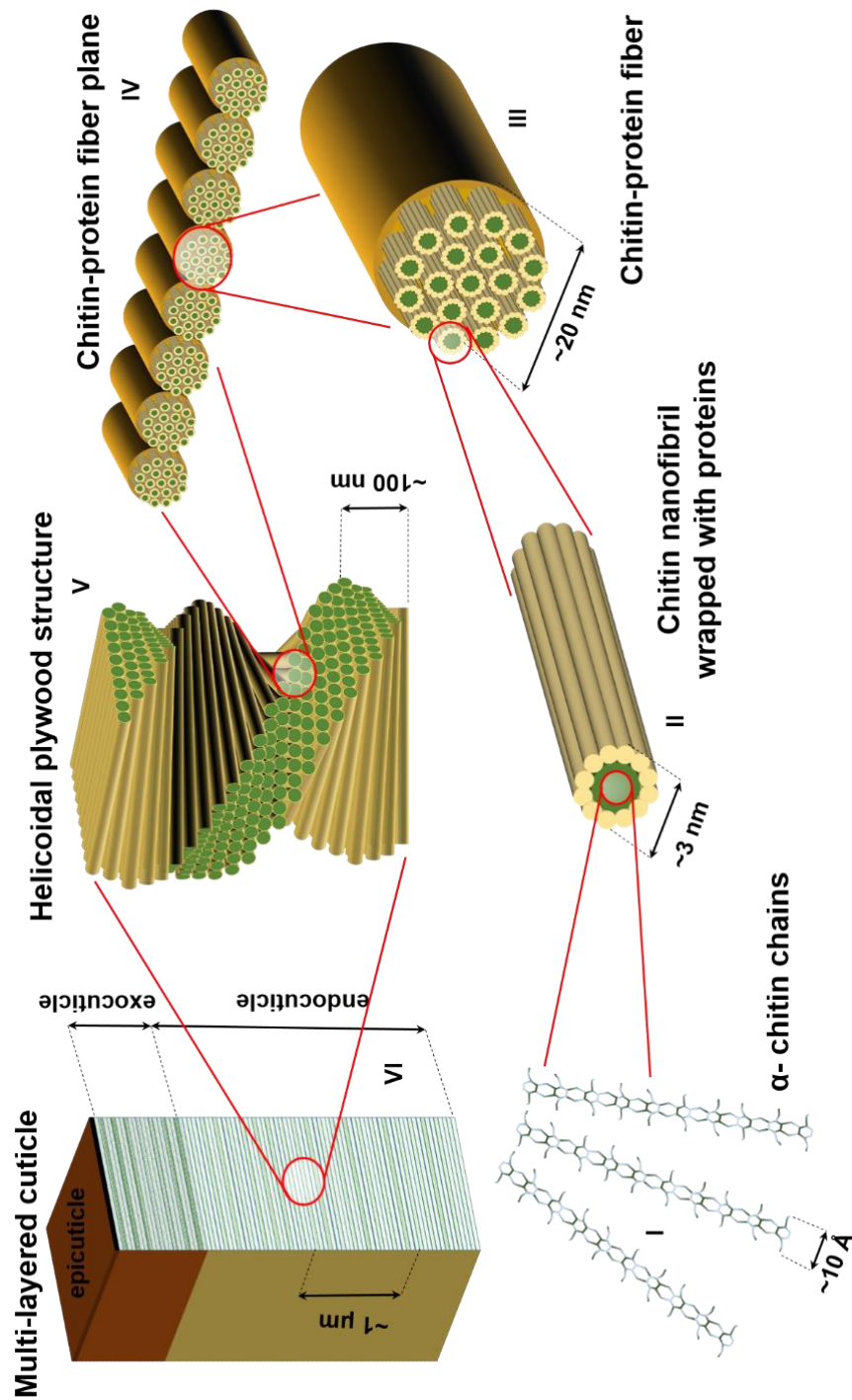
Figure 2.3 - Hierarchical structure in arthropod cuticle. *The first hierarchical level consists of the polysaccharide molecules forming the α-chitin chains (I). At a higher hierarchical level (II), these chains, embedded in proteins, build the chitin nanofibrils which are assembled within a protein matrix to create the fibres (III). These fibres are arranged in planes which are stacked following a helicoidal pattern (V). At the highest level of hierarchy, all the sub-levels are incorporate in the endo and exocuticle layers (VI).*

Characteristic of crustacean cuticle is the capability to achieve very high toughness and impact resistance (Dunlop and Fratzl 2010, Grunenfelder, Suksangpanya et al. 2014), which are properties needed as the cuticle is the functional barrier to the external environment experienced by such crustaceans. In addition, mineralised cuticle uses a smart honeycomb-like design to transport nutrients in the tissue: a network of pore canals (in the shape of ellipses with major and minor axes respectively of ≈400 nm and ≈200 nm) (**Figure 2.4V***) are organised perpendicularly to a set of fibres (I will call them out-of-plane fibres in **Chapter 5**) which transport the nutrients (Raabe, Al-Sawalmih et al. 2007). Finally, crustacean cuticle also renovates with moulting cycles achieved over weeks (Welinder 1975).

In the following paragraphs a description and analysis of the structure, material properties and the mechanisms arising at each hierarchical level in crustacean cuticle is provided.

2.1.1 Overview of the hierarchical structure in crustacean cuticle

Biological structures adapt, change function during growth, renew their material and build hierarchies (Meyers, Chen et al. 2008). The macroscopic behaviour of these materials depends on the interaction between structural properties at different scales (Buehler 2007). At the molecular level, in crustacean cuticle, acetylglucosamine molecules polymerise forming chains of chitin. At the higher hierarchical level, chitin molecules are assembled to form crystalline α-chitin nanofibrils with a diameter of the order 1 -10 nm (**Figure 2.3II**). Each nanofibril is then embedded in proteins, constituting a chitin-protein fibre (**Figure 2.3III**)

with a diameter of about 20 nm (Nikolov, Fabritius et al. 2011). Combined with a mineral-protein matrix, these nano-fibres are arranged into horizontal fibre planes (≈10 nm thick) forming a lamellar structure (≈10 µm thick). In details, these planes lay upon each other and gradually rotated along the axis normal to the surface of the planes forming the lamellar structure (**Figure 2.3IV**). These types of 'quasi-continuously' orientated structures are also known as plywood or Bouligand (Bouligand 1972, Meyers, Lin et al. 2006) structures, and are similarly found in other tissues like bone, but with different features. Specifically, the orientation of the lamellae in bone follows a 'discrete' distribution rather than a quasi-continuous one as in cuticle (Weiner and Wagner 1998). In the cuticle lamellae, the continuous arrangement of fibres is interrupted by a system of pore canals that allow the transport of minerals after moulting (the process of renewing the crustaceans' old exoskeleton with a new one). As result, the tissue takes the form of a honeycomb-like structure (**Figure 2.4V***), a term which was first used by D. Raabe and coworkers (Raabe, Al-Sawalmih et al. 2007).
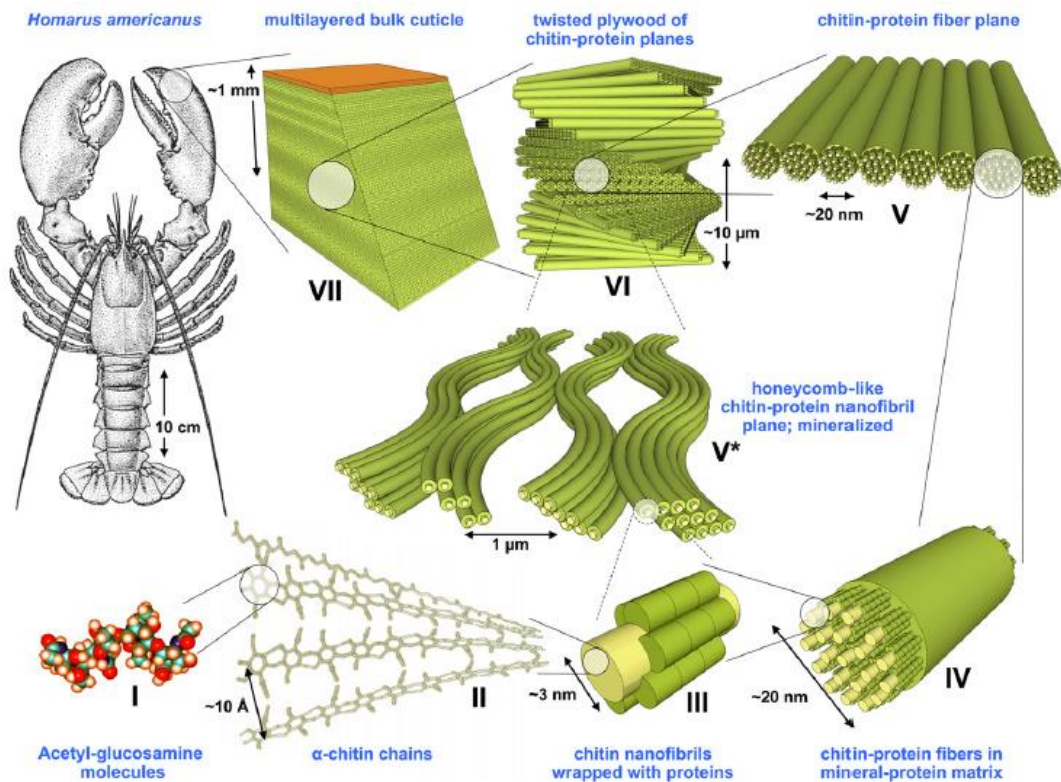
Figure 2.4 - Hierarchical structure of the arthropod cuticle. *The first hierarchical level consists of the acetyl-glucosamine molecules (I) forming α-chitin chains. (II) At a higher hierarchical level, these chains, embedded in proteins, build the chitin nanofibrils (III) which are assembled within a protein matrix to create the fibres. For the lobster Homarus americanus level IV is not present. In fact, the fibre planes are made of protein-wrapped nanofibrils which are arranged to form a pore canal system giving as result a honeycomb-like structure. Fibres are arranged in planes (V) which are stacked following a twisted pattern (VI). At the highest level of hierarchy, all the sub-levels are incorporate in the endo and exocuticle layers (VII) (Nikolov, Fabritius et al. 2011).*

Through the process of evolution, crustaceans developed specialised structural features for each single part or appendage of the exoskeleton, which have different functional requirements. For instance, in the mantis shrimp (**Figure 2.5**) while the abdominal part (tergite) is curved and quite regular, the tail, used by the animal for defence and known also as telson, features a more complex 3D wavy shape, probably optimised for impact resistance and hence for absorbing energy and resisting penetration of the impactor (Taylor and Patek

2010). The specialization of cuticle to different shapes and functions is related to a multitude of factors, including the level of mineralization, fibre orientation, and cross-linking of the tissues, and provides a rich functional range of structures of interest to researcher in the fields of bio-inspired materials and bio-mimetics. In general, however, the external layer of crustacean's cuticle (exocuticle) naturally evolved to resist against impacts and wear, hence these part is usually more calcified. The inner region, the endocuticle, instead, is made of less stable minerals, such as ACC (amorphous calcium carbonate) and amorphous calcium phosphate (ACP).
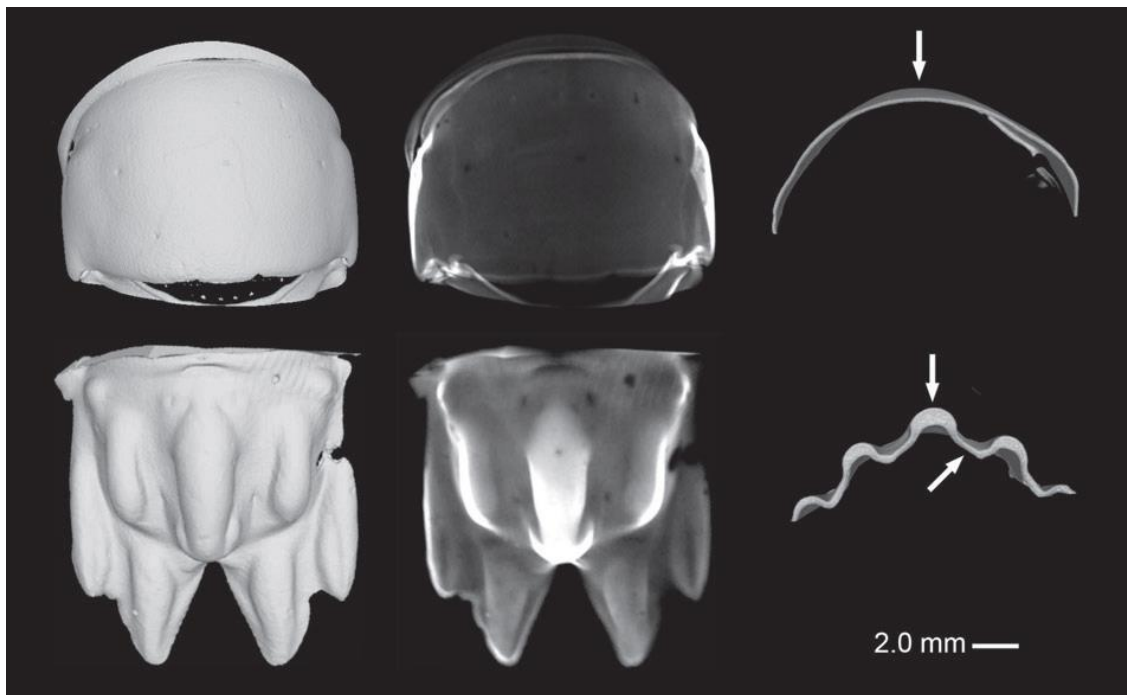
Figure 2.5 - Micro-CT images of the abdominal tergite (upper row) and the telson (lower row) parts of the cuticle of the mantis shrimp. In both the 2D section and 3D shape, the telson (lower part of figure) exhibits a more complex wavy geometry if compared to the tergite (upper part of figure) (Taylor and Patek 2010).

Further details about the material properties of the hierarchical crustaceans' cuticle will be provided in the following sections.

2.1.1.1 Molecular level

At the molecular level, cuticle consists of chitin, a relatively poorly characterised protein phase, and mineral (mostly but not exclusively calcium carbonate). The percentage of these three constituents varies between different species within a wide of each component: chitin 10 – 20%, protein 13 – 50%, and mineral 15 – 70% (Díaz-Rojas, Argüelles-Monal et al. 2006).

Chitin is one of the most common natural polymers on the Earth, and is a common constituent in the cell walls of fungi and arthropod exoskeletons. It is used for medical, industrial and commercial applications and is present in Nature as crystalline microfibrils that are a few nanometres thick. Specifically, chitin accelerates the skin healing process and can be used to produce 100% bio-degradable plastic but also to prepare food and cosmetic products for its antioxidant and antimicrobial properties (Fernandez and Ingber 2014, Hamed, Özogul et al. 2016). In addition, due to its abundance, the chitin based materials are also cheap which makes them competitive on the industrial markets.

Chitin molecules are linear polysaccharide of β-1,4-linked N- acetylglucosamine residues (**Figure 2.4**). They are very similar to cellulose. Specifically, the only difference with cellulose consists of a hydroxyl group that is substituted by an acetyl amine group in chitin (Younes and Rinaudo 2015). Different packing and arrangements of the molecular chains of the crystal cell determine the form of chitin: α, β and γ (as shown in **Figure 2.1**). Different experimental techniques exist to determine the molecular structure of chitin, such as X-ray diffraction, Infra-red (IR) spectroscopy and Carbon-13 nuclear magnetic resonance (13C-NMR) (Van de Velde and Kiekens 2004, Al-Sawalmih, Li et al. 2008, Younes

and Rinaudo 2015). X-ray diffraction can be used to understand the crystalline structure of chitin, and can potentially (when combined with a microfocus beam) resolve gradients in this structure across chitinous tissues (Yamaguchi, Itoh et al. 2003). The IR spectroscopy and 13C-nuclear magnetic resonance (NMR) methods resolve molecular groups and conformation, and are hence suited to observe the difference between polymorphic forms of chitin (Focher, Naggi et al. 1992).

A recurrent motif in bio-mineralised tissues is the presence at the nanoscale of two phases, organic and inorganic (Fratzl and Weinkamer 2007), forming a composite material with increased mechanical properties if compared to the initial phases (Ji and Gao 2004). Both protein and mineral (organic and inorganic, respectively) phases occur in cuticle. Calcium carbonate ($CaCO_3$) represents the primary mineral phase in the matrix of crustacean cuticle and in general of aquatic organisms such as the abalone nacre (Lin, Chen et al. 2008). Other forms of mineral in crustacean cuticle are calcium phosphate ($Ca_3O_8P_2$), calcium sulphate ($CaSO_4$) hydroxyapatite ($Ca_{10}(PO_4)6(OH)_2$) and fluoroapatite ($Ca_5(PO_4)_3F$) (Vincent and Wegst 2004, Nikolov, Fabritius et al. 2011). The amount, crystallinity, nanostructure and the spatial arrangement of these bio-minerals influence the material properties of cuticle and is also adapted to the natural function of cuticle. Specifically, it is known that stiffness of the macro-structure increases with increasing mineralization (as the mineral reinforces the ductile organic phase), but defining and developing constitutive models to elucidate the structural function of minerals is a hard task. In fact, to the best of my knowledge, it is only for the much more widely studied hard tissue of bone that a first multiscale approach using a combination of models, mechanical

measurements and imaging techniques like micro computed tomography is available (Wagner, Lindsey et al. 2011). Functional and species variation exists: when cuticle has a function of armour against intensive predatory attacks, like crabs, the tissue is stiff and highly mineralised, while for animals using fast movements to prey and escape from enemy (lobsters and shrimps, for example) the tissue evolved into a lighter and less mineralised cuticle (Boßelmann, Romano et al. 2007).

2.1.1.2 Chitin nanofibrils and fibres

The molecular chains, embedded in proteins, are self-assembled into chitin nanofibrils which are clustered together, and, in turn, assembled within a matrix (made of proteins and minerals) to create chitin fibres (with a diameter ranging between 20 and 100 nm). Two sets of chitin fibres have been identified within the crustacean cuticle. Most of them (in-plane fibres) appear aligned to the cuticle surface of arthropods while the second set (out-of-plane fibres) extends through the pore canals perpendicularly to the cuticle surface of crustaceans (**Figure 2.6**) (Fabritius, Sachs et al. 2009).
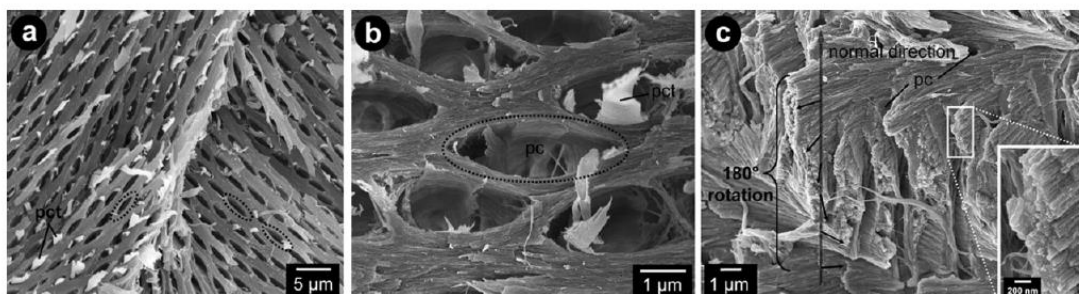
Figure 2.6 - Microstructure of the lobster cuticle. a) Twisted plywood structure and pore canal system made of flexible fibres. b) High magnification image shows the pore canals and the out-of-plane fibres. c) Rotating planes of parallel fibres in the twisted plywood structure (Fabritius, Sachs et al. 2009).

The out-of-plane fibres transport the material for the moulting stage of cuticle (Fabritius, Sachs et al. 2009). Although measurements of the 'transverse' stiffness (transverse is the direction of the out of plane fibres) are available in literature for the lobster Homarus americanus (Fabritius, Sachs et al. 2009), it may be of interest to understand which are the specific role and function that these fibres fulfil with regard to the mechanical properties of the material. The crystalline units in chitin are aligned to the topological texture of chitin fibres (the c-axis of chitin cell is aligned to the longitudinal axis of fibre). This aspect is of fundamental importance for researchers as it allows the estimation of the fibre direction from the experimental measurements (e.g. with X-ray diffraction techniques) of the orientation of crystals (Raabe, Al-Sawalmih et al. 2007).

2.1.1.3 Lamellar structure

Chitin-protein fibres are arranged in single parallel planes (with a thickness of 20-100 nm) which are stacked upon each other forming a gradually twisted rotated structure (**Figure 2.3V**). This particular lamellar arrangement leads to high stiffness in all the directions in-plane (transversely isotropic), which has implications for the impact resistance and toughness of the structure. In fact, through experimental and numerical analyses inspired by arthropod cuticle, it has been demonstrated that the helicoidal structure reduces the damage propagation through the thickness of the whole structure during impact events and increases the structural toughness and residual strength (Grunenfelder, Suksangpanya et al. 2014). In general, in biological fibre composites, when a crack starts propagating a fracture pattern arises following the path of least resistance, which means generally propagating through the softer matrix rather

than severing the high tensile strength fibres. For this reason, in a helicoidal arrangement of mineralised chitin fibres, cracks continuously deviate from the original path during their propagation, resulting in a large increase of the surface area in the crack propagation direction and in an amplification of the total energy dissipated during impacts, as proved for engineering composites (Grunenfelder, Suksangpanya et al. 2014). It is noted that the analogy may not be exact for cuticle, as the stiffness of the mineralised matrix has been estimated (from modelling) to not be that different from cuticle fibrils (Nikolov, Petrov et al. 2010). Another important phenomenon occurring in Bouligand-type structures is the reorientation of lamellae in response to the applied loads, but while intuitively clear on physical grounds, such a phenomenon has been far less studied compared to crack propagation in bio-composites. A recent study investigated the mechanical behaviour of an armoured fish (*arapaima gigas*) scale (Yang, Sherman et al. 2014) which shows an irregular Bouligand structure with angles between consecutive lamellae of: 86.7°, -34.5°, -69.2°, and 66.9°. The authors found that a set of these lamellae reorient towards the tensile axis and deform in tension while another set of them compresses and reorients toward the opposite direction (Yang, Sherman et al. 2014). I note here that an analytical model to investigate lamellar reorientation and deformation is a part of the current thesis, and will be provided in **Chapter 5.**

2.1.1.4 Mesoscale structure

With the term mesoscale the tissue hierarchical level is indicated. The entire cuticle is made of three layers: endocuticle, exocuticle, and an outer thinner layer, the epicuticle (**Figure 2.3VI**). The external layer, the epicuticle, is ≈1 - 5

µm thick and serves as a mineralised barrier to the outside world (Kuballa, Merritt et al. 2007). It is made of minerals (spherulitic calcite) and a lipid-protein matrix (Roer and Dillaman 1984). The exo- and endocuticle exhibit significant structural and morphological differences. In the exocuticle layer (≈200 - 300 µm thick) there are helicoidally distributed sheets and the chitin–protein fibres are well visible (Nikolov, Petrov et al. 2010). The exocuticle is usually calcified, with an irregular distribution of minerals (specifically calcium carbonate, calcium phosphate, fluoropatite and calcium sulphate (Amini, Tadayon et al. 2015)), constituting about one-third of the entire cuticle. Here, three different sites for mineral deposition exist: within pore canals, between fibres and within fibrils. The endocuticle is the main and thickest layer (≈250 µm – 2.5 mm thick) of the whole tissue (50% of the entire cuticle). It consists of layered lamellae which are aligned in planes parallel to the surface of exoskeleton. Within the endocuticle the mineral content decreases (mostly amorphous calcium carbonate) and the size of the pore canals increases (Sachs, Fabritius et al. 2006) as well as the pitch of rotation of lamellar planes (from ≈10 µm in the exocuticle to ≈30 µm in the endocuticle). In addition, the chitin–protein fibres are less disseminated as compared to the exocuticle (Nikolov, Petrov et al. 2010). The membrane layer, under the endocuticle, instead is non-calcified (Nagasawa 2012) and it is made only of chitin and proteins. I remark that the thickness and structure of cuticle in the dactyl (ending part of the appendage that the *Odontodactylus scyllarus* employs as a hammer to attack and destroy the shells of prey(Weaver, Milliron et al. 2012)) is different (**Figure 2.7**). Specifically, three regions can be distinguished: the impact region (≈50 - 70 µm thick), the periodic region (≈2 mm thick), and the lateral striated region (≈0.5 mm thick). In the impact region there is a particular form of Bouligand structure where the in- and out of plane fibres

are compressed taking a sinusoidal shape (**Figure 2.7F**). This waviness gradually decreases in the periodic region ending with a 'smooth' lamination (traditional helicoidal Bouligand structure) (Kisailus and Zavattieri 2015). In the striated regions, instead, unidirectional fibres extend along the circumference of the dactyl (Kisailus and Zavattieri 2015). Also the mineral content changes in the dactyl region: most of minerals in the impact region are in the form of crystalline hydroxyapatite while the periodic and striated regions are made of amorphous calcium phosphate and calcium carbonate.
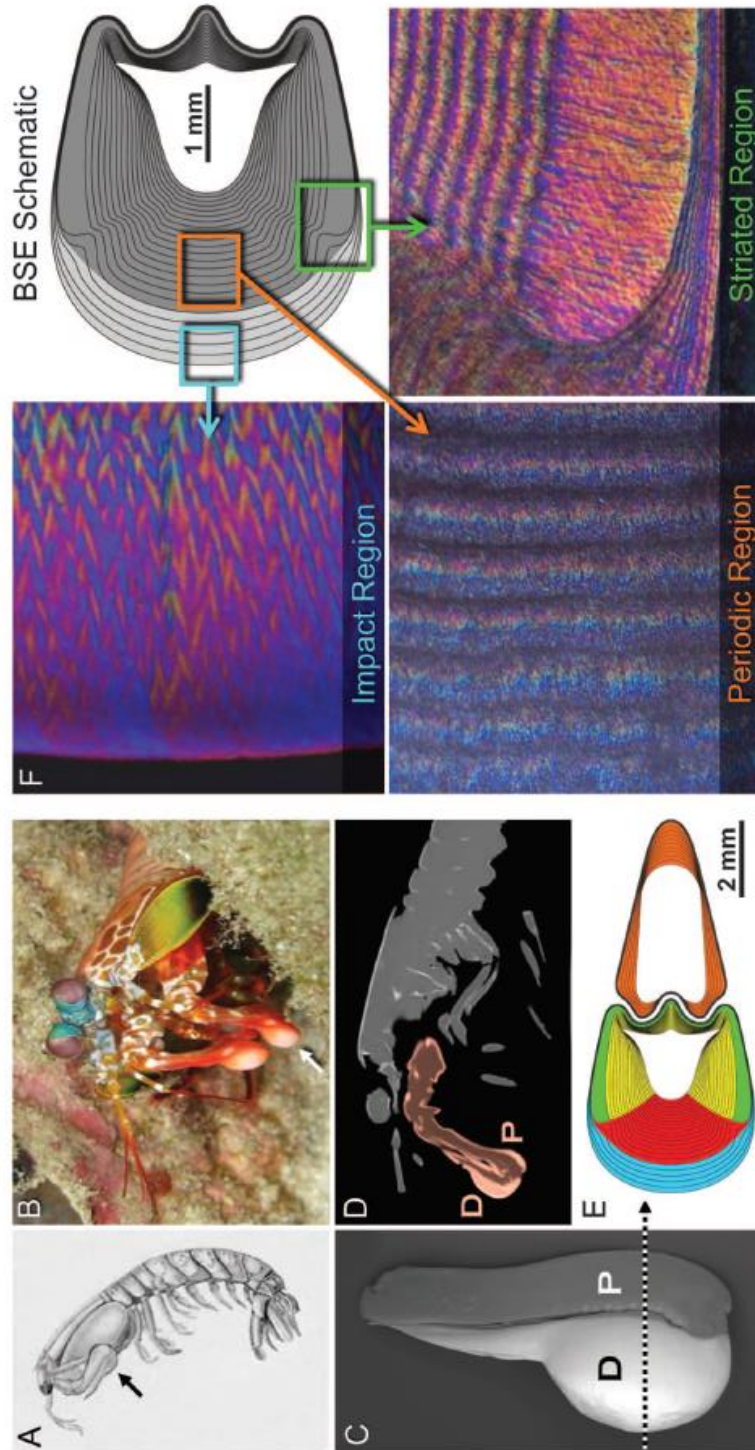
***Figure 2.7 - Structure of the stomatopod dactyl club.** A) – B) Mantis shrimp body. The arrow indicates the dactyl club. C) Scanning electron micrograph of the club's external surface and (D) a micro-computed tomographic longitudinal section of the animal (D indicates the dactyl and P the propodus). E) Cross-sectional schematic of the club showing three distinct structural regions: (i) The impact zone (blue), (ii) the periodic zone (red and yellow) and (iii) the striated zone. The periodic region of the propodus is shown in orange. F) Optical micrographs showing the three detected zones (Weaver, Milliron et al. 2012).*

2.1.2 Mechanics of cuticle

Crustaceans have a hard exoskeleton which provides a framework for muscle attachment and protects their soft body from enemies and various kinds of diseases (Nagasawa 2012). This sophisticated level of protection may be achieved thanks to different mechanisms of deformation and energy dissipation at each hierarchical level. For this reason, it is necessary to consider all the structure-property relations at all length scales to comprehend the macroscopic mechanical properties of cuticle.

2.1.2.1 Nanoscale mechanics

The knowledge of cuticular mechanical properties at the nanoscale is provided by modelling and molecular dynamic simulations methods, whilst still little is known from the experimental point of view (Nikolov, Petrov et al. 2010). At the molecular level, the elastic modulus of the crystalline region in the direction parallel to the chain axis is a parameter of interest. This value depends on the molecular system of bonds in the crystalline structure. X-ray diffraction is an experimental technique mainly used to measure the Young's modulus of chitin along the main chain axis. Because chitin nanofibres within cuticle usually have a complex 3D structure with different strains and stresses in different orientations, the few measures I have located in the scientific literature were made on particular cuticles exhibiting simple parallel chitin fibril orientation. Specifically, a first value of the Young's modulus of chitin was estimated from X-ray diffraction tests by Nishino and co-workers (Nishino, Matsui et al. 1999) in 1999 reporting a value of 41 GPa. Later, Ogawa and co-workers (Ogawa, Kimura et al. 2010) measured a higher value (59.3 GPa) from a X-ray diffraction

test on a crab tendon with parallel chitin fibrils (which have been treated to remove the protein content). A specific issue concerning these experiments at the molecular length scale is the level of reliability of the measured moduli previously reported. In fact, these values were either acquired from biological tissue, with no certainty of the purity of chitin fibrils and of the structural integrity of the molecules, or tested in situ but imposing the restriction of a single fibre orientation inside the tissues. Ideally, one would prefer to measure the molecular stresses and strains in the complex three-dimensional design of cuticle-based tissues in the same place where the deformation or fracture is occurring, without isolating the chitin fibrils from other components at the molecular level, or structural elements at higher hierarchical levels.

The mechanical properties of cuticle are also determined by the organic phase (proteins). Specifically, proteins are fundamental for their role of binding with the crystalline region in nanofibrils and with chitin fibrils in fibres. Modelling and experimental approaches have estimated the elastic modulus and Poisson's ratio of proteins in nanofibrils within the fibres in lobster cuticle (see **Section 3.1**) as 56 MPa and 0.28, whereas (at one scale above) the elastic modulus and Poisson's ratio of the protein within the mineral protein matrix which surrounds the chitin fibres are considered to be 570 MPa and 0.28 (Nikolov, Fabritius et al. 2015). However, these estimates arise from comparing a limited set of macroscopic mechanical data with the outcome from developed multiscale models through homogenization methods (Nikolov, Fabritius et al. 2011, Nikolov, Fabritius et al. 2015), and are consequently not as reliable as direct measurements. Several experimental and modelling methods have been developed to characterise the material at each length scale (Nikolov, Petrov et

al. 2010, Amini, Masic et al. 2014) (Raabe, Al-Sawalmih et al. 2007). A detailed analysis of the main mechanical properties of typical arthropod tissue from the nano to the macroscale will be provided in the following sections.

2.1.2.2 Microscopic mechanics

Of particular interest is the cuticle of the dactyl club, the end part of the mantis shrimp's appendages, which displays a set of characteristics to resist failure during repetitive high-energy loading events. At the microscopic level, nanoindentation tests (local ~micron-scale measures of elastic and plastic properties (Amini, Tadayon et al. 2015), combined with post-indentation high-magnification field-emission scanning electron microscopy (FESEM) observations, were used to induce local surface deformation and to measure gradients and anisotropy in the hardness and the elastic properties of arthropod dactyl cuticles (Amini, Tadayon et al. 2015). Specifically, a high resolution multi-sectional modulus and hardness maps of the inner (periodic region) and outer (impact region) layers of the dactyl clubs combined with a measure of the elastic modulus and hardness from the load-displacement curves were obtained[64] (results are shown in **Figure 2.8**).
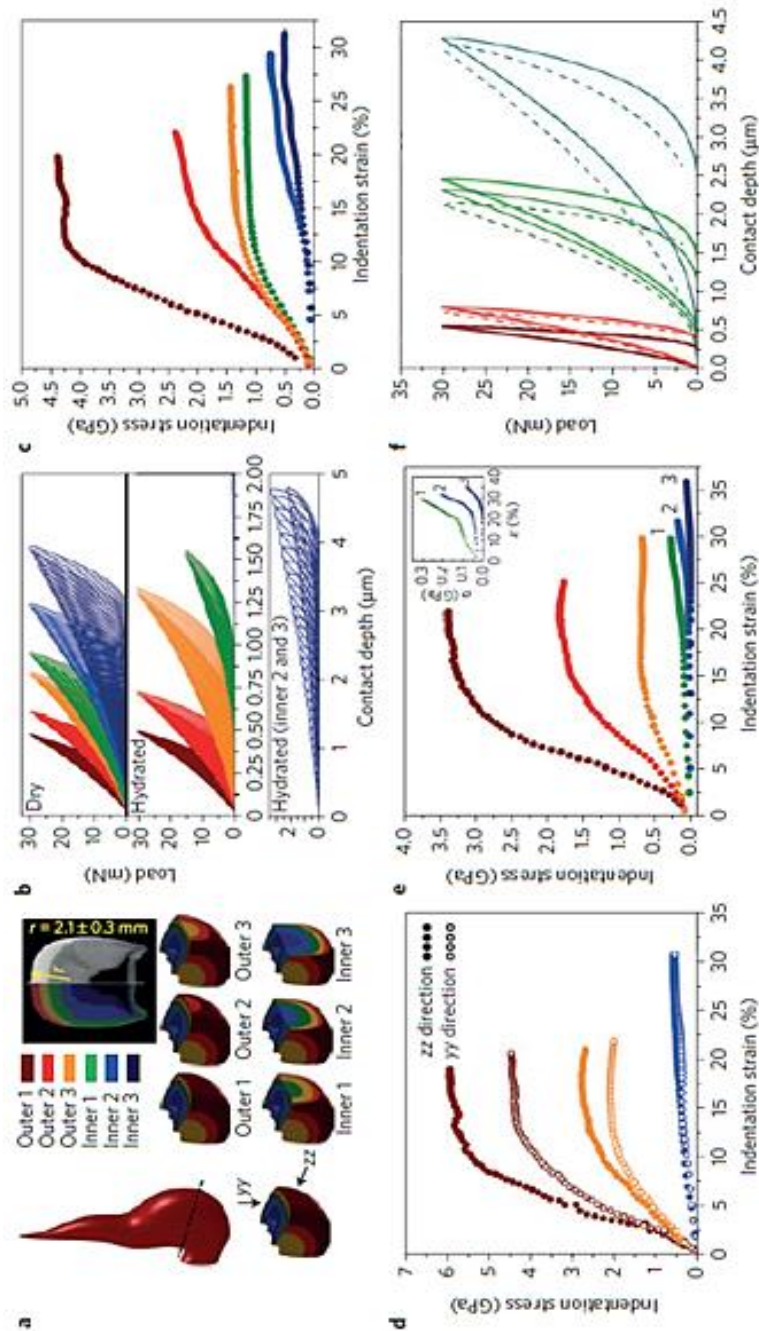
Figure 2.8 – Results from nanoindentation tests on the dactyl club of the mantis shrimp. *a) The analysed regions of the cross-section of the club are indicated using different colours. b) Partial loading–unloading curves collected from indentation tests in dry and hydrated conditions. The water content in hydrated conditions is 4–5wt % in the outer layers and 10wt % in the inner layers. c) Indentation stress-strain curves in dry conditions obtained from the partial loading–unloading curves shown in figure b. d) Indentation stress–strain curves, in dry conditions in the yy and zz directions. e) Indentation stress–strain curves in hydrated conditions showing the strain-hardening behaviour of the inner layers. f) Loading–unloading curves in hydrated conditions, illustrating the influence of loading rate, measured at 0.6mN/s (thick line), 6mN/s (thin lines), and 300mN/s (dashed lines) (Amini, Tadayon et al. 2015).*

In the outer layers the indentation response was anisotropic (**Figure 2.8d**) with a gradual reduction in yield stress moving from the outer layers towards the inner layers. The elastic modulus and the yield stress (5.0 ± 0.1 GPa) were higher in the zz direction rather than in the yy direction (3.5 ± 0.1 GPa) (yy and zz directions are shown in **Figure 2.8a**). The level of hydration affected the mechanical properties of the cuticle. Under hydrated conditions, the different behaviour of inner and outer layers becomes more evident (**Figure 2.8c-e**). The effect of the viscoelastic organic phase was verified through indentation measurements at different loading rates (**Figure 2.8f**). In the outer regions no rate effect was found and in the following inner layer the influence of loading rate was negligible. Instead, in the other inner regions, a small loading rate effect was observed due to the larger content of viscoelastic chitin (relative to the less viscoelastic mineral).

Figure 2.9 illustrates the mechanisms of deformation and energy dissipation arising in the outer and inner regions after indentation tests. Specifically, localised interfacial sliding and gradual rotation of fluorapatite crystals were detected as responsible of energy dissipation in the outer regions (**Figure 2.9c**). Amini and co-workers (Amini, Tadayon et al. 2015) found that the macroscopic size of dactyl club is below the critical size that marks the switch from plastic to brittle behaviour in Hertzian tests that are used to measure the load for the onset of damage for a specific indenter radius (Rhee, Kim et al. 2001). In addition, strain hardening was observed, as a result of microchannel densification in the inner regions. The amount of energy dissipated by plastic yielding (in percentage of the total contact energy) was 20-25% in the outer

layer, 30-35% in the next outer layer and reached up to 50% in the inner layers, indicating that through the mechanism of microchannel densification these inner layers could absorb higher relative amounts of energy (Amini, Tadayon et al. 2015). In addition, shear-induced cracks and crack fibril bridging were observed in the FESEM (Field Emission Scanning Electron Microscope) images (**Figure 2.9d**) and act as toughening mechanisms.
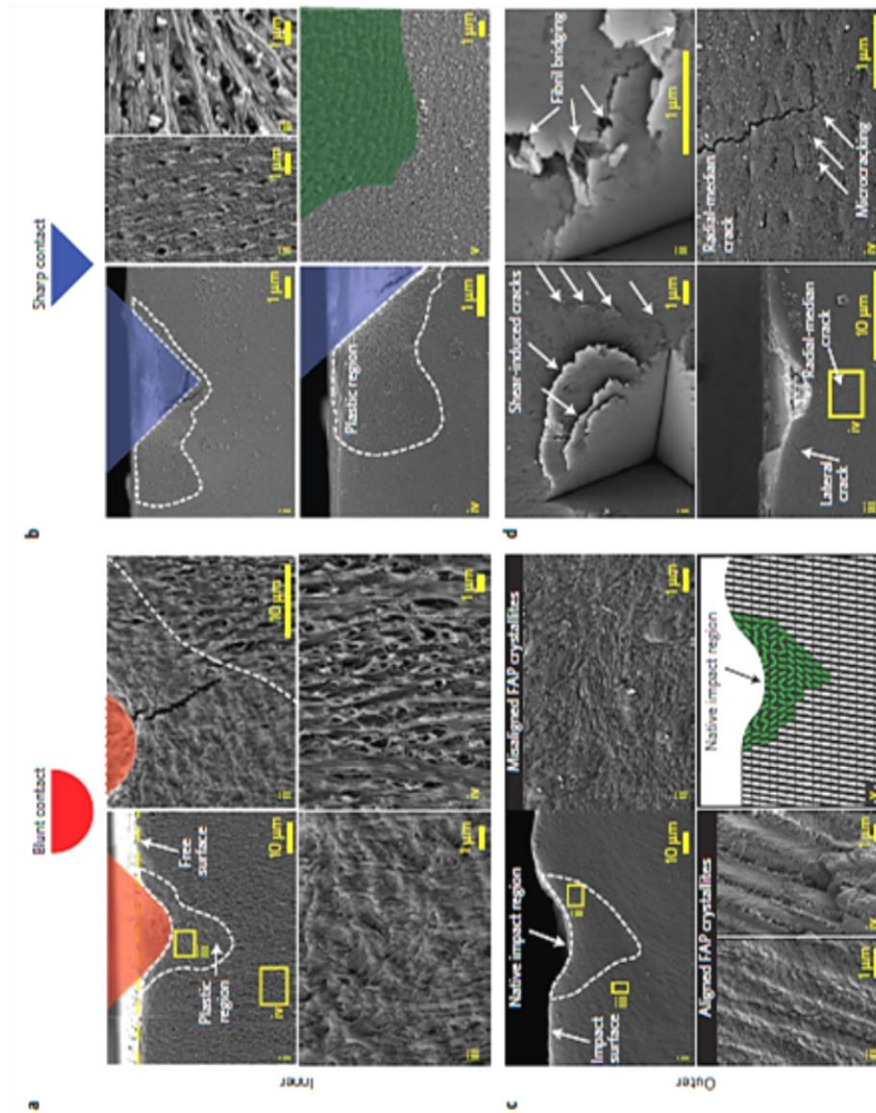
Figure 2.9 - Deformation and damage mechanisms of the dactyl clubs observed by post-indentation FESEM. *a) Blunt contact; i plastic and elastic regions in the inner layers; ii higher - magnification figure showing the boundaries between the two regions; iii and iv microchannel densification regions under contact, representing closed channels in the plastic region and open channels in the elastic region. b) Sharp contact, inner layers: i low-magnification micrograph displaying the transition between the elastic and plastic regions; ii and iii microchannels before indentation loads; iv - v elastic-plastic transition, with green area in v representing the densified structure. c) Blunt contact in the outer layers; i low-magnification micrograph including both the plastic and the elastic regions; ii highly misalignment of fluorapatite crystals; iii high magnification of the elastic region; iv fracture surface of the impact region; v schematic figure showing the misalignment of crystals near the impacted region. d) Sharp indenter acting on the outer layers: i shear-induced lateral cracks; ii fibril bridging between the two sides of a lateral crack; iii nucleated cracks; iv formation of microcracks surrounding the main crack (Amini, Tadayon et al. 2015).*

All these described mechanisms are beneficial for the toughness of the dactyl cuticle. Similar results were obtained from indentation tests combined with microcomputed tomographic analyses on the mantis shrimp's dactyl club (Weaver, Milliron et al. 2012). Specifically, the elastic modulus varies from 70 GPa in the impact region to 35 GPa in the periodic region and drops to 10 GPa in the striated zone. This modulus mismatch across the whole dactyl serves as a deflector to prevent catastrophic crack propagation, as shown from previous theoretical analysis of fracture toughness in layered materials with different elastic moduli (Fratzl, Gupta et al. 2007) and contributes to the dactyl's impact resistance.

Nanoindentation tests (Sachs, Fabritius et al. 2006) on the cuticle of the lobster of the *Homarus Americanus,* instead, show that, in the direction normal to the surface of the exocuticle and endocuticle, the Young's modulus ranges respectively between 9.5 - 10.1 GPa and between 5.4 - 6.6 GPa, while in the transverse direction between 8.6 – 9.4 GPa for the exocuticle (**Figure 2.10**).
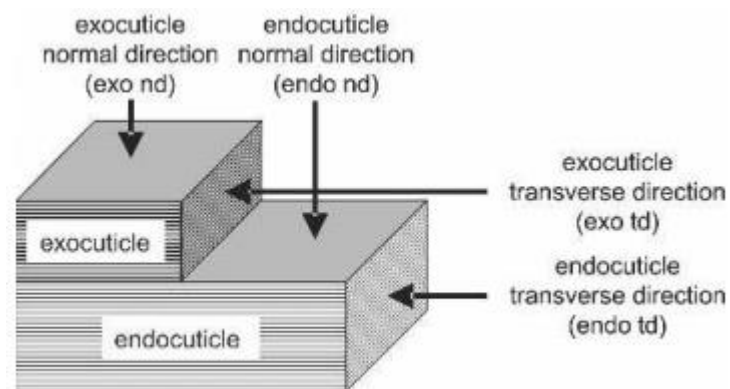
Figure 2.10 - Schematic figure showing the directions used for the indentation tests (Sachs, Fabritius et al. 2006).

2.1.2.3 Macroscopic mechanical properties of arthropod cuticle

An important role in determining the mechanical properties of cuticle is played by the presence of water. In fact, when the content of water increases, the cuticle becomes softer and the stiffness decreases correspondingly. Soft cuticle usually contains equal weight fractions of chitin and protein, and 40 – 75% of water whereas harder cuticles contain 15 – 30% weight fraction of chitin and only 12% of water. As an example, stiffness can vary from 1 KPa in the highly hydrated membrane of the locust, via about 1 MPa for the resilin, to 60 MPa in the abdominal cuticle of Rhodnius (an insect of the subfamily of Triatominae) and finally to 20 GPa in the cuticle of the locust appendage (Vincent and Wegst 2004).

Tensile and compression tests, in dry and wet states, have been performed to investigate the macroscopic mechanical properties of the lobster *Homarus americanus* cuticle (Fabritius, Sachs et al. 2009). **Figures 2.11a-b**, demonstrate that the mechanical behaviour of the lobster cuticle were substantially affected by the hydration state. In fact, the presence of water can break the hydrogen bonds between proteins themselves and between protein and chitin (Nissan 1976). Specifically, in the dry state, the lobster cuticle exhibits a brittle behaviour with a linear elastic curve that reaches the value of strain to fracture of 0.7%, while the wet cuticle shows plastic deformation with a yielding strain of 0.5% and a strain to fracture of 1.8% (**Figure 2.11a**). The Young's modulus of the dry samples is included in the range of 5.8 - 7.0 GPa, whereas it is only 4.8 GPa in case of wet samples.
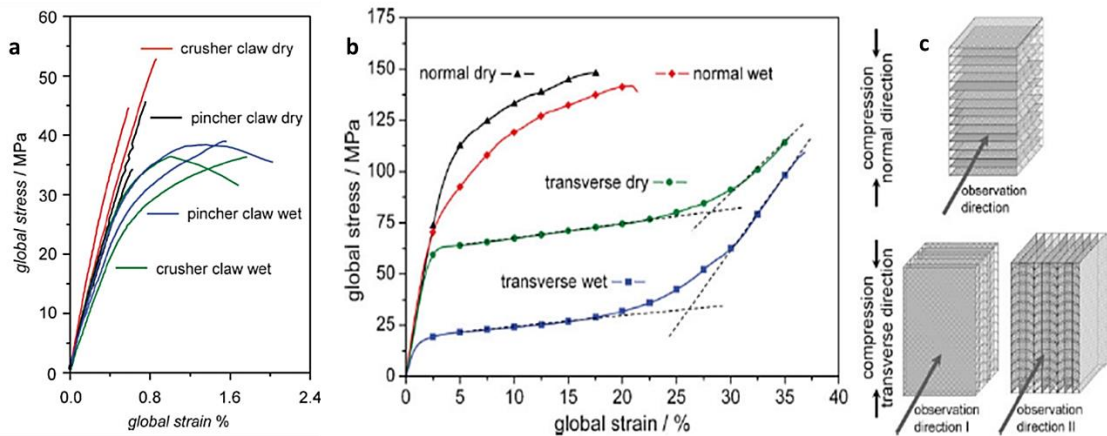
Figure 2.11 - Results from tensile and compression tests on the mineralised endocuticle of the lobster Homarus americanus. a) Global stress-strain behaviour under tension of the endocuticle, of both pincher and crusher claw in dry and wet conditions. b) Compression tests of the endocuticle, in normal and transverse directions (in figure c are represented these directions), both in dry and wet conditions (Fabritius, Sachs et al. 2009).

Figure 2.11b shows results for compression tests in normal and transverse direction (Fabritius, Sachs et al. 2009). As shown in **Figure 2.11c**, for the compression tests in transverse direction of the cuticle, the two possible observation directions are: parallel to the surface (observation direction I) and perpendicular to the surface of the cuticle (along the cross section: observation direction II). In normal direction the endocuticle exhibits a linear elastic pattern, and a subsequent strain to yield of 2.4% in dry and 1.8% in wet conditions. On the other hand, the samples tested in transverse direction show an extended plateau region after a relatively small elastic region, and at the end a strain hardening. This plateau arises as areas of high strain which expand across the fibres determining the collapse of the pore canal system. In addition, once the yield is reached, the fibres tend to gather (densification process) rather than separate resulting in the observed strain hardening (**Figure 2.11b**) (Fabritius, Sachs et al. 2009). In addition, the strains to fracture values in normal direction

are much lower than the corresponding values in the transverse direction. Specifically, respectively for dry and wet state, in normal direction are: 18.7-19.4% and in wet conditions are: 42.3-35.6% (Fabritius, Sachs et al. 2009). These results were explained by the authors by considering that the system of pore canals considerably affects the mechanical responses of cuticle under compression. When the cuticle is loaded in transverse direction, the pore canals are compressed and broaden in transverse direction (**Figure 2.12a**) while in the normal direction (which corresponds to the long axis of the pore canals) the extension along the axis of the pore canal is negligible. This behaviour can be seen as effect of the honeycomb-like structure that these canals form. In addition, a significant difference was observed in the failure of the samples. While the samples tested under compression in the normal direction failed by cleavage, the samples tested in transverse direction showed a distinct fracture plane, oriented perpendicular to the cuticle surface and 45° to the compression direction (**Figure 2.12b**) (Fabritius, Sachs et al. 2009). This is an effect of the progressive failure of the structure occurring along the long axes of the pore canals, from one pore canal to the next located on different planes.
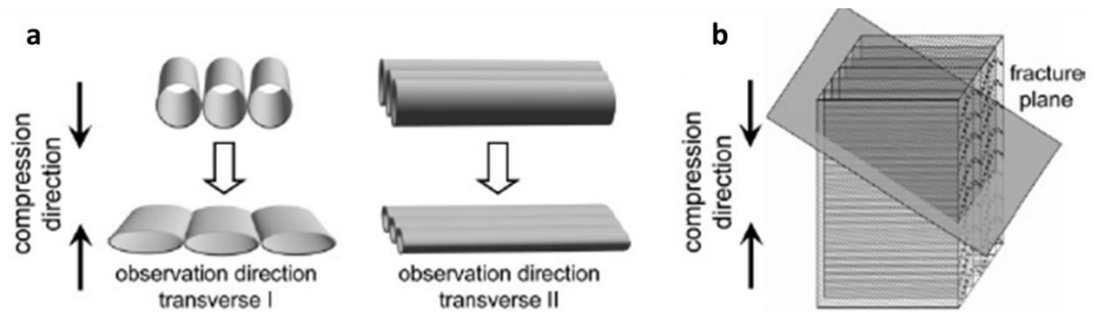
Figure 2.12 - Deformation state of pore canals compressed in the transverse direction. *a) In the transverse I direction lateral broadening caused by collapsing pore canals is visible. During the observation of the cuticle's cross section along the transverse II direction, this broadening also occurs, but is not visible because the pore canals are parallel to the observation direction. b) The orientation (45°) of the fracture plane in samples tested in transverse direction (Fabritius, Sachs et al. 2009).*

The yield strain is higher in the normal than in the transverse direction and increases passing from wet to dry condition. Scanning Electron Microscopy images also show that in layers where the fibres are perpendicular to the loading direction the pore canals collapse and microcracks arise. In layers where fibres are oriented longitudinal to the compression load, fibres buckle forming irregular cavities (**Figure 2.13**) (Fabritius, Sachs et al. 2009).
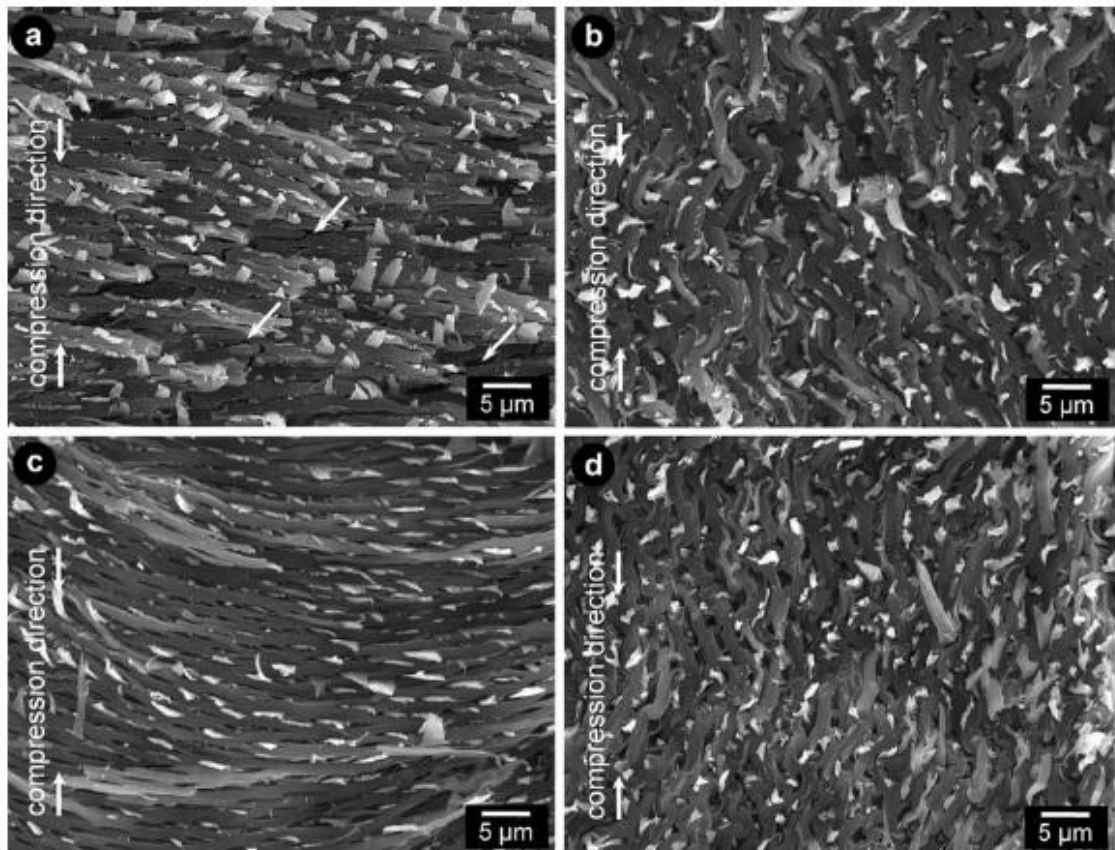
Figure 2.13 - Scanning electron microscopy images for compressed samples in (a-b) dry and (c-d) wet state. Micro-cracks appear only in the dry case and are indicated by white arrows (Fabritius, Sachs et al. 2009).

2.2 Bone and antler

Bone of present-day mammals and birds is a multifunctional organ that provides support for the body and protection for internal organs, contributes to motion, stores minerals and maintains pH level in blood (Currey 2002). In addition, bone can adapt to loads and environment by regulating its size and it is able to heal its microcracks or fractures (Novitskaya, Chen et al. 2011). Here, a continuous process of remodelling occurs via specialised cells known as osteoclasts that remove material and others know as osteoblasts that replace the old tissue with the new one (Martin and Burr 1989). Bone is produced inside the body and contains water (Currey 2002) which plays an important role in its mechanical

behaviour (**see Section 2.2.2**). I will compare and contrast a "typical" bone mechanical properties and structure (like bovine femoral bone) versus an unusual type of bone (antler) in what follows.

From the material perspective, bone is a composite made mainly of collagen mineralised with calcium phosphate or hydroxyapatite and contains living cells and blood vessels. In some unusual types of bone like antler these cells are all dead by the time animals start using it. In terms of the main factor to regulate the mechanical properties in bone, they are mainly affected by the amount of mineral in the tissue: the more is the mineral the stiffer (and at the same time more brittle) bone becomes (Currey 1999). Antler has some of the lowest relative mineral content, as it contains 30 – 35 wt% of protein substance which is considerably higher than the correspondent amount in typical bone (20 – 30 wt%) and 55 – 60 wt% of mineral phase which is lower than the amount that is found in typical bone (60 – 70 wt%) (Currey 1999). Furthermore, antler (particularly elk antler) has the highest strain to failure (about 12%) of the entire bone family which is six time higher than the correspondent value for human cortical bone (Launey, Buehler et al. 2010). It is also one of the toughest materials in nature among the living organisms. Its high fracture toughness is attributed to the relatively low mineral volume fraction (which leads to a lower stiffness) compared with human bone (**Figure 2.14**) (Launey, Buehler et al. 2010). In addition, its relative low yield strength (**Figure 2.14**) in the longitudinal direction allows the formation of plastic regions near the cracks. This mechanism reduces the overall stresses level and enhances inelastic deformations contributing to the material toughness (Launey, Buehler et al. 2010).
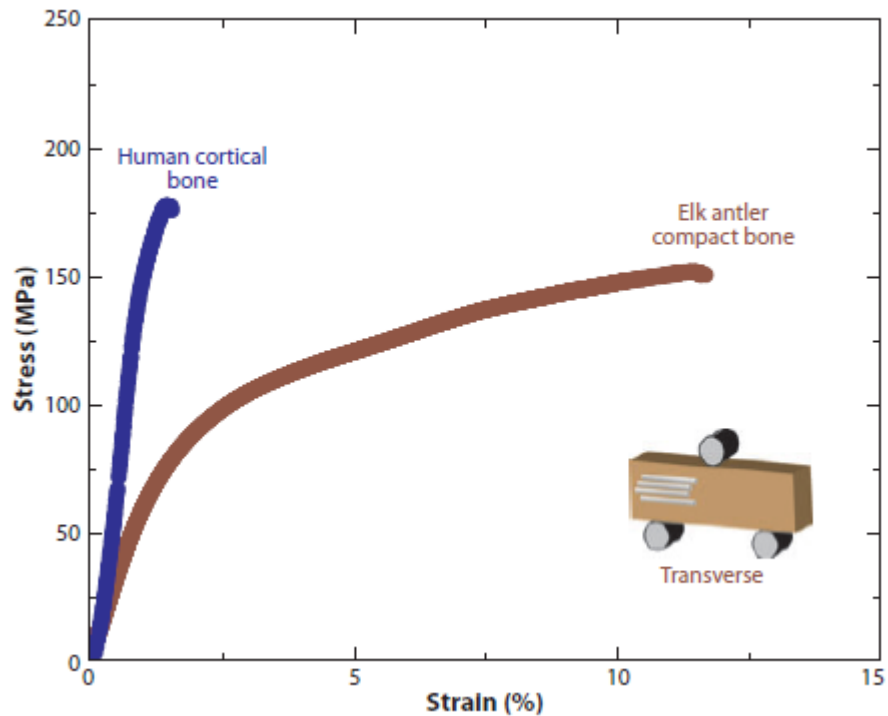
Figure 2.14 – Stress strain curve from a three-point bending tests for human bone and antler in the transverse (perpendicular to fibres) direction (Launey, Buehler et al. 2010).

In order to understand the mechanical properties of bone (and its variants, such as antler) it is fundamental to analyse the structural relationship between the components and the mechanisms of deformation and energy dissipation at the different level of the hierarchical organization (analogous to my discussion of cuticle before). In fact, it has been shown that at each hierarchical level its mechanical properties vary. For instance, the Young's modulus of large human cortical specimens under tensile testing is in the range of 14 - 20 GPa (Reilly, Burstein et al. 1974) while micro-bending tests report a corresponding value of 5.4 GPa (single osteon) (Choi, Kuhn et al. 1990). In the following sections a detailed description of the different hierarchical levels in antler and a summary of the existing knowledge of the properties of the structural elements at each scale length are provided.

Bone and antler feature similar hierarchical structures and mechanisms of deformation and energy dissipation. In the following sections I will describe the two biological systems. Since most of the following description can be applied to both bone and antler and since most of the literature refers to bone, I will use the word 'bone' to generally describe the structure and the mechanisms of bone and antler. However, I will specify the differences when it is necessary.

2.2.1 Hierarchical structure of bone

Bone, as shown in **Figure 2.15**, at the nanometre scale length is a composite of stiff inorganic hydroxyapatite platelets interleaved with a softer organic matrix, made principally of type I tropocollagen proteins (Weiner and Wagner 1998). This sub-structure, together with an intrafibrillar phase of non-collagenous proteins and mineral, forms mineralised fibrils (roughly 100 nm in diameter and 5-10 µm or more in length) (Launey, Buehler et al. 2010) which are arranged into aggregate structures at larger length scales, such as fibril arrays and lamellae (Meyers, Chen et al. 2008). At the micro-level there are Haversian systems, osteons and single trabeculae while the macrostructure is made of cancellous and cortical bone (Rho, Kuhn-Spearing et al. 1998).
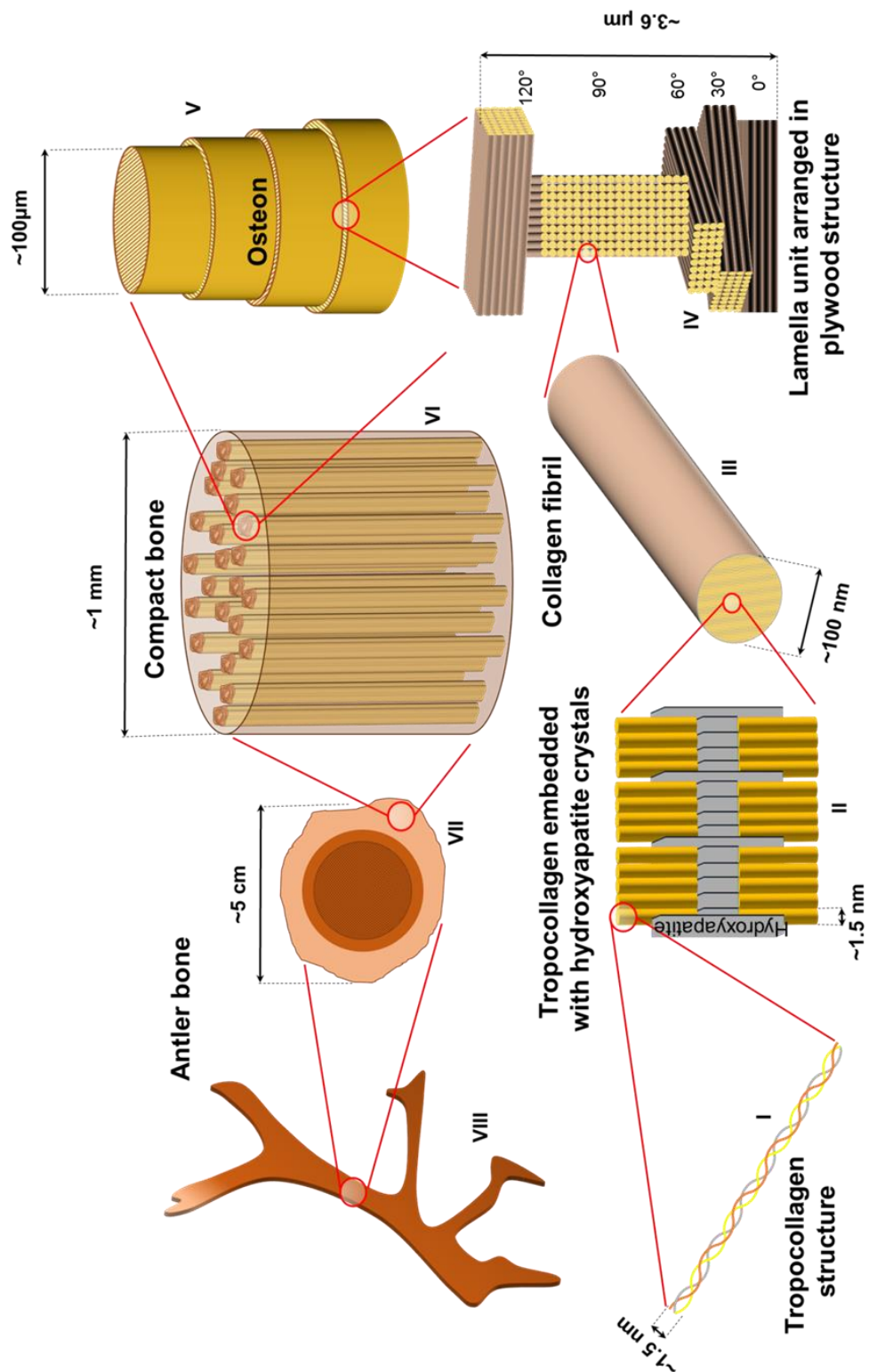
Figure 2.15 - Hierarchical structure in bone. *The collagen fibrils (II) are made of tropocollagen molecule (I) and hydroxyapatite mineral.   At the following hierarchical level, these fibrils are wrapped in a protein-based matrix (III) forming a plywood structure: the lamella unit (IV). This group is repeated in the osteon (V) which is part of the compact bone (VI) and therefore of the bone structure (VII-VIII).*

2.2.1.1 Molecular level

The nanostructure of bone is composed of crystals of a mineral phase, collagen and non-collagenous organic protein. Minerals are made of poorly crystalline form of hydroxyapatite (carbonated apatite or dahllite) which are in the form of platelets (with length and width typically ranging from 30 to 200 nm and thickness ranging from 3 to 10 nm, measured by atomic force microscopy) (Hassenkam, Fantner et al. 2004). In terms of their localization and growth within the nanostructure, there is an evidence from electron microscopy and other methods that these platelets occur within the discrete spaces between the collagen fibrils, limiting the growth of the mineral crystals, and forcing the crystals to be discrete and discontinuous (Rho, Kuhn-Spearing et al. 1998). The mineral crystals show a specific crystalline orientation with their c axis (longitudinal crystallographic axis) that is roughly parallel to the long axes of the collagen fibrils (Kuhn-Spearing, Rey et al. 1996).

Bone is subjected to a mineralization process. It is believed that crystals initially form within the gap region of the collagen fibrils, later grow in the overlap region, and finally extend to the extrafibrillar space (Siperko and Landis 2001) (**Figure 2.16**). There are no studies able to quantify with certainty the amount of mineral content that is inside and outside the collagen fibrils (Sasaki, Tagami et al. 2002), which is a matter of current debate. However a recent study (Alexander, Daulton et al. 2012), based on scanning transmission electron microscopy experiments, shows that less or equal to 42% of apatite mineral is included in the gap spaces while less or equal to 28% of it is located in the intermolecular spaces between adjacent collagen molecules. As a result, 30% or more of mineral must lay in the region external to fibrils.
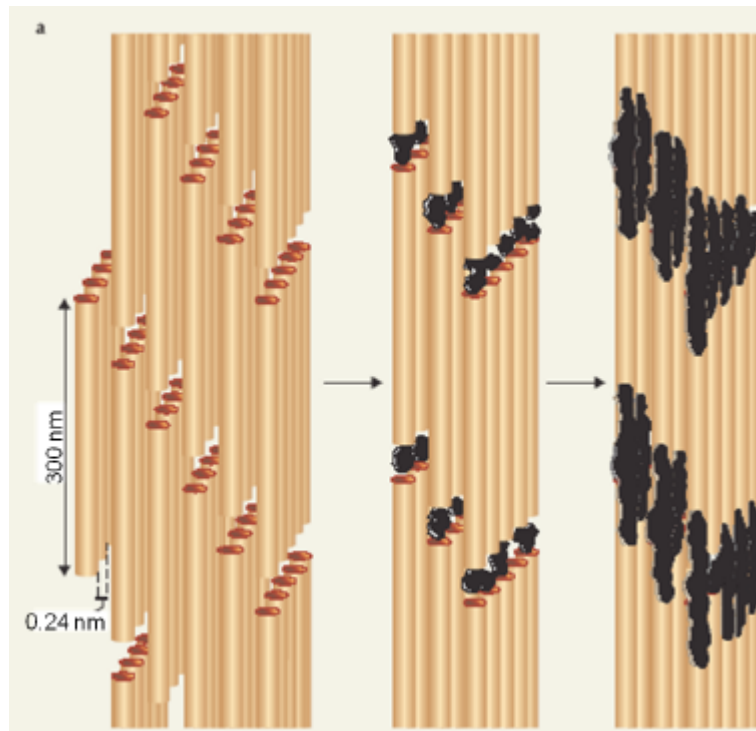
Figure 2.16 - Mineralization process in bone. *Nucleation of minerals in the gap region between the tropocollagen molecules and on the external sides (Ritchie, Buehler et al. 2009).*

The main organic component of the matrix is type I collagen. Collagen proteins are 85-90% of the total amount of proteins in bone (the rest are called non-collagenous proteins). In collagen, the protein molecule (tropocollagen) aggregate to form fibrils and are made of three polypeptides of the same length with 67 nm periodicity and 40 nm gaps or holes between the ends of the molecules (Rho, Kuhn-Spearing et al. 1998). The tropocollagen molecules are cylindrically shaped, with a diameter of approximately 1.5 nm and length of 300 nm (Weiner and Wagner 1998). They are parallel to each other and staggered by one-fourth of their length (Rho, Kuhn-Spearing et al. 1998).

The mechanical behaviour and composition of the extrafibrillar matrix is still a matter of research. It seems that the extrafibrillar matrix is composed of non-collagenous proteins such as osteopontin, proteoglycans and decorin (Launey,

Buehler et al. 2010). These proteins hold together the mineralised fibrils (Fantner, Hassenkam et al. 2005) and may play a role to regulate the size, orientation and process of crystals deposition (Rho, Kuhn-Spearing et al. 1998). Further studies are necessary to clarify their contribution to the mechanical properties of anter.

2.2.1.2 Microstructure

Above the molecular level bone can be distinguished into two forms: woven and lamellar bone. In these tissues, set of fibrils are packed together to form fibres which are arranged in different configurations depending on the specific region of bone (Weiner and Wagner 1998). Woven bone is characterised by an irregular distribution of collagen fibres and is highly mineralised and quite porous. Lamellar bone instead is more precisely arranged and less mineralised than woven bone. Lamellar structure is present in bones that are load-carrying and impact resisting (Weiner, Traub et al. 1999). Here, the fibres are arranged in planes called lamellae which are usually wrapped in concentric layers around a canal known as osteon or Haversian system. These fibres lie within the lamellar plane and tend to be all oriented in one direction although there is evidence of lamellae following a less homogenous angular distribution (Ascenzi, Bonucci et al. 1978). Weiner and co-workers (Weiner, Traub et al. 1999) found that lamellar bone is made of a series of lamellar units (which are about 3 to 5 μm thick), each of which is made of 5 sub-layers with fibrils orientated at 0°, 30°, 60°, 90° and 120° (the last layer is small in rat bone and large in baboon and human bones), where 0° represents the direction perpendicular to the bone long axis.

2.2.1.3 Macrostructure

At the macro-structural level two types of bone are identified: cortical (or compact) and cancellous (or trabecular). Cancellous bone is found in the internal part of many bones and it is spongy with struts or rods like elements, known as trabeculae, of 100-300 μm in diameter and marrow-filled cavities (Rho, Kuhn-Spearing et al. 1998). Compact bone is solid and includes osteons (they measure 0.2 mm in diameter), canaliculi and blood vessels (Haversian and Volkmann's channels) with an external layer known as periosteum (Currey 2002) (**Figure 2.17**).
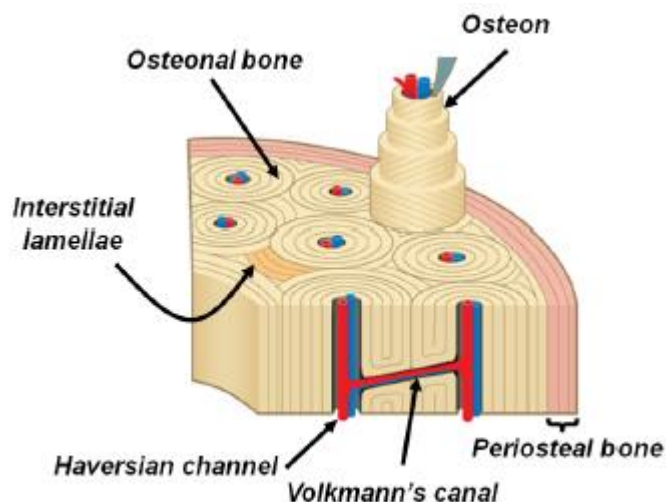
Figure 2.17 - Cross section of compact bone (Novitskaya, Chen et al. 2011).

2.2.2 Mechanics of bone

Bone is a hierarchically organised material and its mechanical properties depend on: type, scale of observation, amount of mineralization, degree of

hydration, porosity, orientation, strain rate and age (Novitskaya, Chen et al. 2011).

Water is one of the main components of bone (15-25 % of the total volume) and it drastically affects the mechanical properties of bone. It is present in the gaps within the fibrils, between the triple-helical molecules, between the collagen fibrils and between the fibres (Katz and Li 1973). Bone usually shows lower stiffness and strength but higher strain to failure and toughness in the hydrated state than in the dry state (Novitskaya, Chen et al. 2011). For instance, the Young's modulus in the dry state can be up to 20% higher in cortical bone and up to 40% higher in trabecular bone when compared with the hydrated state (Currey 2002). Less mineralised bone, such as bone, include a higher amount of water in comparison with higher mineralise bone. In this case part of water is located within and around the fibrillar gaps in place of mineral (Novitskaya, Chen et al. 2011).

Porosity can be considered as the proportion of the total volume where bone tissue is missing. Usually pores are filled by the marrow but in birds it is possible to find gas (Currey 2002). Porosity reduces the structural weight and increases the energy absorption (McKittrick, Chen et al. 2010). In fact, porous bone features higher fracture toughness but lower strength than normal bone (McKittrick, Chen et al. 2010). The effect of increasing porosity is similar to the one of increasing the degree of hydration with the substantial difference that porosity lessens while water increases the structural weight (McKittrick, Chen et al. 2010). The main effect of porosity on mechanical properties of bone is the reduction of the elastic modulus. There are several models expressing the

relation between the Young's modulus and the density. For instance, a model (Bonfield and Clark 1973) shows that the Young's modulus E of a porous cortical bone is related to Young's modulus E_0 of a bone tissue containing no porosity by the **Equation 1,** where p is the density. From this equation it is possible to state that for a compact bone containing 5% porosity the elastic modulus decreases of 10%.

$$E = E_0 \left(1 - 1.9p + 0.9p^2 \right) \tag{1}$$

Similarly, a model accounting for the relationship between the Young's modulus and the density in trabecular bone is expressed by **Equation 2**, where E^* and ρ^* are the Young's modulus and density of a porous bone while E and ρ are the respective values for solid bone (Novitskaya, Chen et al. 2011).

$$\frac{E^*}{E} = \left(\frac{\rho^*}{\rho} \right)^2 \tag{2}$$

The level of mineralization affects significantly the mechanical response of bone. **Figure 2.18** clearly shows for different type of bio-composites that as the mineral fraction increases the bending strength also increases while the toughness, on the contrary, decreases.
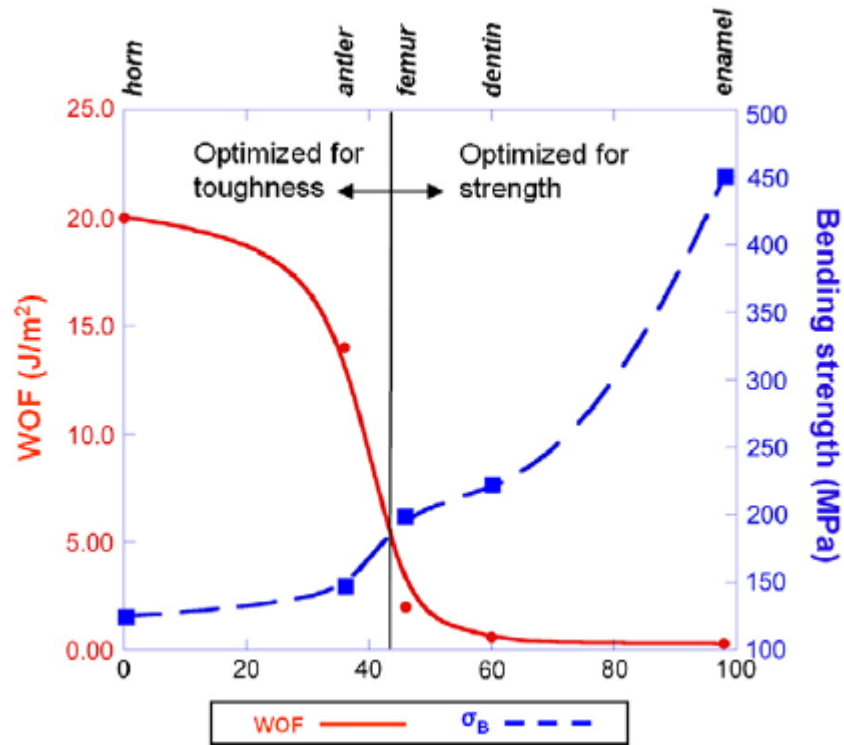
Figure 2.18 - Effect of degree of mineralization on the work of fracture (WOF) and bending strength for different bio-polymers (McKittrick, Chen et al. 2010).

The intersection of the two curves in **Figure 2.18** represents the optimum configuration which occurs at the value corresponding to typical mammal bone (45% of mineral content), indicating that bone is optimised for both toughness and strength (McKittrick, Chen et al. 2010). These results can be explained considering the brittle nature of mineral content (hydroxyapatite) which increases the stiffness but confers brittleness to the whole bio-composite. Also the Young's modulus of these materials is affected by the level of mineralization. For instance, compact bone, compact bovine femur, human dentin and human enamel, respectively with a volume fraction of 57%, 67%, 70% and 98%, have an elastic modulus of 7.8 GPa, 13.5 GPa, 17.6 GPa and 80 GPa (McKittrick, Chen et al. 2010), showing a positive correlation.

The mechanical properties of bone are also influenced by the orientation of its constituents which results in anisotropy. For instance, the elastic modulus and strength in compact human bone are higher in the longitudinal direction (aligned to longitudinal axis of bone) rather than in the transversal one (Novitskaya, Chen et al. 2011). Specifically, the longitudinal Young's modulus of human compact bone ranges from 16 to 23 GPa while the transversal one between 6 and 13 GPa. It has been demonstrated that the mechanical properties of biological plywood structures significantly depend on the orientation of fibres within the lamellar structure. While it has not been extensively applied to bone (with the exception of the study made by Pidaparti and co-workers (Pidaparti, Chandran et al. 1996), lamination theory of synthetic composites may be a valid analytic tool to take into account the anisotropy due to different lamellar orientations and to measure the mechanical properties of the plywood structure in bone.

Bone is a viscoelastic material and its mechanical response is strain-rate sensitive. The mechanical response of bone under dynamic loads is of enormous interest as most of the catastrophic events causing fracture of bone occur at high strain rate. In **Figure 2.19** different compressive stress strain curves at various strain rates are shown.
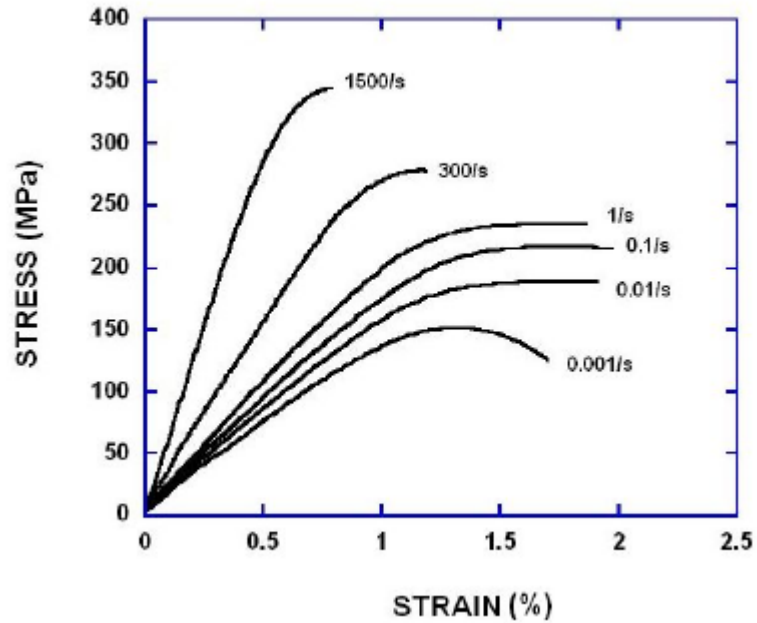
Figure 2.19 - Stress strain curves for human cortical bone under compressive load and different strain rate (Novitskaya, Chen et al. 2011).

These curves clearly show that as the strain rate increases the strain to failure decreases while the Young's modulus and the strength increase. Similar behaviour is confirmed in another study on equine bone (Kulin, Jiang et al. 2011).

It has been shown that the level of mineralization in human bone increases until a certain age and then decreases (**Figure 2.20**).
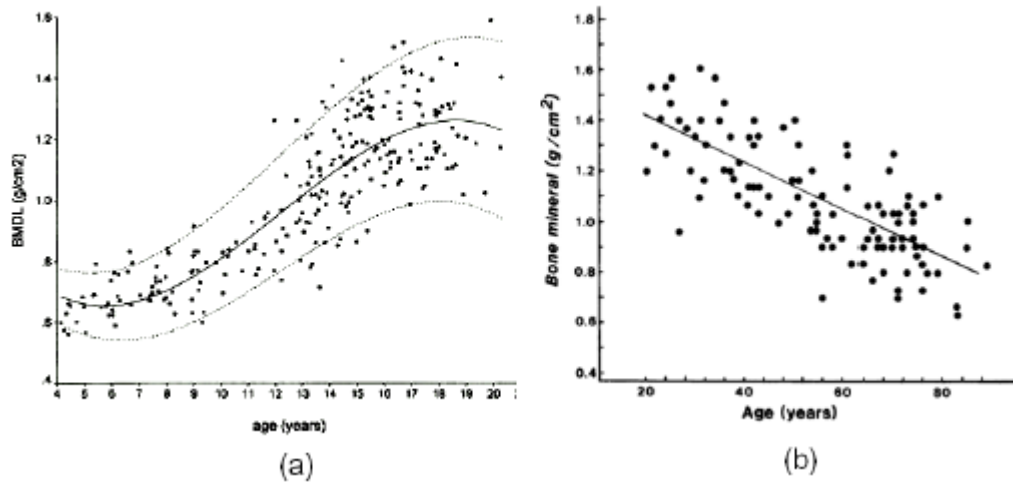
Figure 2.20 - Bone mineral density (BMD) in lumbar spine as function of age for (a) young women and (b) old women (Novitskaya, Chen et al. 2011).

This decrease in mineralization is especially due to osteoporotic diseases which afflict people of middle and older age. Specifically, osteoporosis reduces the bone mass density provoking the disruption of the trabecular structure with the formation of large voids reducing the stiffness and promoting fracture phenomena (Lubarda, Novitskaya et al. 2012). Also static toughness and impact strength in human cortical bone reduces with age. Other effects like collagen degradation (Danielsen, Mosekilde et al. 1994) and increasing density of un-remodelled cracks (Currey, Brear et al. 1996) influence negatively the mechanical properties in bone.

2.2.2.1 Nano-mechanics

A complete review (Gautieri, Vesentini et al. 2011) of the nano-mechanics of collagen micro fibril reported the Young's modulus values for single collagen molecule and for collagen fibrils in wet and dry state (**Table 2.1**). These values are derived from the average of other values obtained with experimental and

numerical technique, such as X-ray diffraction, AFM tests, atomistic modelling and simulations, etc.

Hierarchical level	Young's modulus [GPa] (Grunenfelder, Suksangpanya et al.)
Collagen molecule	4.8±2.0
Collagen fibril, wet	0.6±0.2
Collagen fibril, dry	3.26

Table 2.1 – Comparison of the Young's modulus of collagen molecule and collagen fibrils in dry and wet state (Gautieri, Vesentini et al. 2011).

An estimation of the elastic modulus of the mineral content in bone was offered by Gupta and co-workers (Gupta, Schratter et al. 2005). They used a combination of experimental data and modelling to predict this parameter and attributed to it a value of ≈100 GPa. The volume fraction was calculated from the calcium concentration measured in quantitative Backscattered Electron images. A reasonable value of the mineral volume fraction in antler (Currey 2002) is ≈ 0.3 (the lowest among all the types of bone). Instead, typical values for human and bovine bone are ≈ 0.36, while the highest value was found for the whale's bulla (≈ 0.56) (Currey 2002).

2.2.2.2 Micro-mechanics

At the microscale the predominant element contributing to the mechanical properties of compact bone is the individual osteon (**Figure 2.17**), whose mechanical properties in isolation have been widely analysed by Ascenzi and co-workers (Ascenzi and Bonucci 1967, Ascenzi and Bonucci 1968, Ascenzi, Baschieri et al. 1990, Ascenzi, Baschieri et al. 1994). They found, under tensile tests, that for single osteon where lamellae are mostly oriented along the

longitudinal direction of bone the elastic modulus is 12 GPa and the strength is 120 MPa, while for osteons with a inhomogeneous angular distribution of lamellae the elastic modulus is 5.5 GPa and the strength is 102 MPa (Ascenzi and Bonucci 1967). In compression, the respective values for the elastic moduli halve while for the strength they remain constant (Ascenzi and Bonucci 1968). Similarly, the two types (with regular and irregular lamellar distribution) of osteons present bending stiffness of 2 and 3 GPa and bending strength values of 390 MPa and 350 MPa (Ascenzi, Baschieri et al. 1990). Instead, in torsion the shear moduli are respectively 20 and 15 GPa and strength values 200 and 160 MPa (Ascenzi, Baschieri et al. 1994).

Experimental tensile tests on human individual trabeculae (with an approximate diameter of 0.18 mm and length of 2.3 mm) and micro-specimens of human cortical bone (approximately 0.3 x 0.3 x 2.2 mm) show that the mean elastic modulus for the compact bone is 18.6±3.5 GPa while for the trabecular bone is 10.4±3.5 GPa (Rho, Ashman et al. 1993). Previous studies (Runkle and Pugh 1975, Townsend, Rose et al. 1975) reported approximate measurements of the loads required to bend a single trabecula and showed that the Young's modulus in compression ranges between 9 and 14 GPa.

2.2.2.3 Macro-mechanics

Some of the first comparisons of the mechanical properties of different bone tissues were provided by Currey (Currey 1979). He performed three-point bending tests and compared three types of bone: the antler of a deer (*Cervus elaphus*), the femur of a cow (*Bos taurus*) and the tympanic bulla of a whale

(*Balenoptera physalus*). The aim was to measure the work of fracture (that is a measure of the necessary amount of work for a crack to propagate) and the stiffness of these three types of bone (results in **Table 2.2**) (Currey 1979).

	Antler	Femur	Bulla
Work of fracture [J m^{-2}]	6186	1710	200
Bending strength [MPa]	179.4	246.7	33
Modulus of elasticity [GPa]	7.4	13.5	31.3
Mineral content [wt%]	59.3	66.7	86.4
Density [10^3 Kg m^{-3}]	1.86	2.06	2.47

Table 2.2 – Mechanical properties of antler, femur and bulla.

The level of mineralization can be immediately related to the work of fracture. In fact, for the bulla, where the degree of mineralization is the highest (among the three type of bones here considered), the fracture was brittle while for antler, which shows the lowest mineral content, the fracture was ductile (Currey 1979). The highest bending strength instead was measured for the femur which has an intermediate level of mineral content. These results for bending strength are overall in agreement with the trend shown in **Figure 2.18** although the numerical values do not completely match. Indeed, **Figure 2.18** shows a value of roughly 150 MPa for the bending strength of the antler and of roughly 200 MPa for the bending strength of the femur.

Table 2.3 shows the material properties of compact and cancellous antler compared with the respective quantities for the whole antler. Results show that

compact antler is more mineralised than cancellous antler (Chen, Stokes et al. 2009).

Property	Compact antler	Cancellous antler	Total antler
Density [g cm^{-3}]	1.72±0.04	0.50±0.05	1.35±0.10
Mineral content [wt%]	56.9±1.0	43.4±0.4	50.1±0.5
Mineral volume fraction	0.36	0.25	0.3

Table 2.3 – Mineral and density of compact and cancellous antler (Chen, Stokes et al. 2009).

A comparison of the mechanical behaviour of bovine femur, together with dry and hydrated elk antler is provided in **Table 2.4**. Overall, results show that bovine femur is more mineralised, stiffer and stronger than elk antler which, instead, features a higher fracture toughness (Chen, Stokes et al. 2009).

Property	Elk antler (dry)	Elk antler (rehydrated)	Bovine femur
Density [g cm^{-3}]	1.72		2.06
Mineral content [wt%]	56.9		67
Elastic modulus [GPa]			
Bending (longitudinal)	7.60±0.25	6.98±0.26	26.1
Bending (transverse)	3.76±0.68	3.26±0.35	
Bending strength [MPa]			
Longitudinal	197.3±24		238
Transverse	66.7±10.7		
Compressive strength [MPa]			
Longitudinal	125.6±11.3		272
Transverse	44.5±17.1		146
Tensile strength [MPa]			
Longitudinal	115.4±16.6		144
Transverse	20.3±6.0		46
Fracture toughness [MPa m$^{1/2}$]	7.9±2.2	10.3±3.3	2-5

Table 2.4 – Mechanical properties of compact bone in elk antlers and bovine femora (Chen, Stokes et al. 2009).

2.2.3 Fracture toughness in bone: mechanisms of deformation and energy dissipation in bone

The mechanical response of bone is controlled by its material properties and by a series of mechanisms of deformation and energy dissipation occurring at each single length scale. Recent advances in experimental (such as X-ray microscopy, synchrotron X-ray diffraction, Raman spectroscopy) and modelling (such as multiscale models and simulations) techniques permitted the observation and estimation of these mechanisms at each hierarchical level. Fracture in bone results from the mutual competition between intrinsic damage mechanisms occurring ahead the crack tip and promoting the evolution of cracks and extrinsic shielding mechanisms behind the tip which increase the resistance to crack initiation and growth (Launey, Buehler et al. 2010) (**Figure 2.21**).
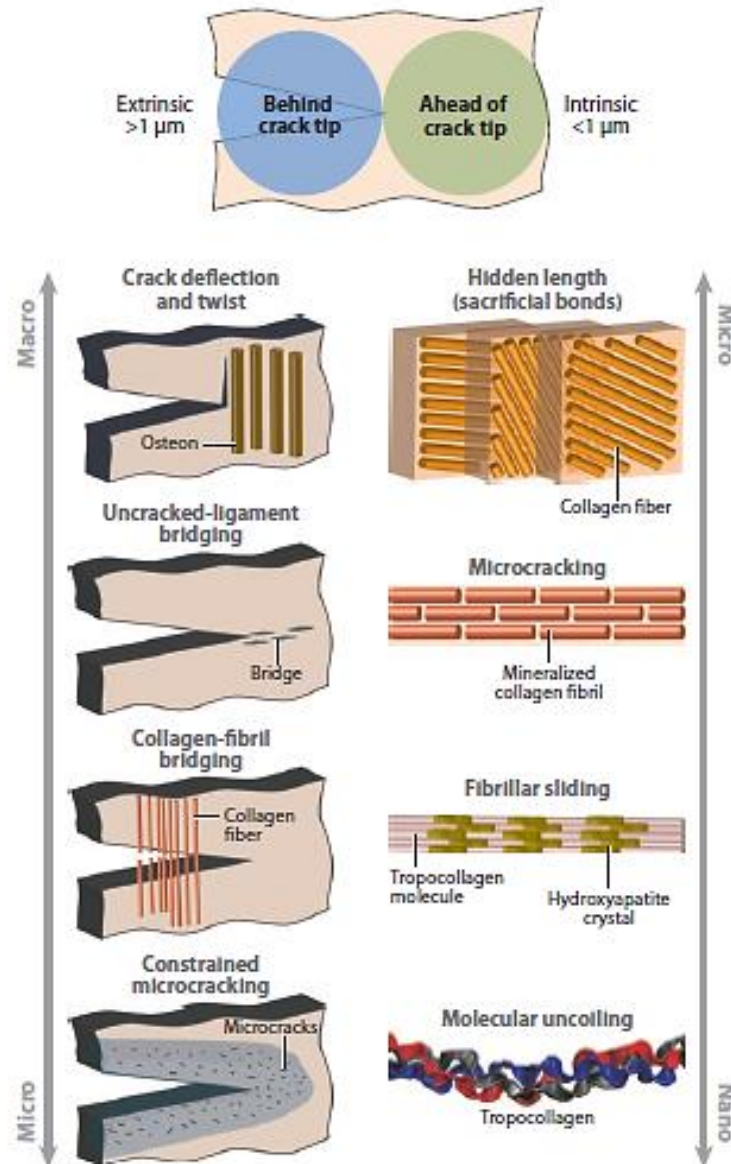
*Figure 2.21 - Mechanisms of deformation and energy dissipation in bone (Launey, Buehler et al. 2010). At each hierarchical level different mechanisms occur: molecular uncoiling and intermolecular sliding at the lowest level, microcracking and fibrillar sliding at the level of fibril arrays, breaking of sacrificial bonds and crack bridging at an higher level and crack deflection and crack bridging at the highest level (10-100 μm) (Launey, Buehler et al. 2010). Both collagen fibrils and mineral content are arranged in staggered configuration (elements at a certain layer/row are misaligned with respect to elements laying on adjacent layers, as shown in details in **Figure 4.1**).*

2.2.3.1 Intrinsic mechanisms

At the lowest hierarchical level the principal mechanisms of deformation are molecular stretching and uncoiling. These mechanisms provoke the breakage of H (hydrogen)-bond that is a reversible process. Indeed, due to short distance between the three polypeptide chains forming the tropocollagen molecule, H-bonds continuously break and reform leading to energy dissipation (Gautieri, Buehler et al. 2009).

The breakage of H-bonds is also associated to the sliding between tropocollagen proteins and hydroxyapatite minerals. In fact, due to the staggered configuration and to the material properties of the system, a mechanism of slippage between organic and inorganic components occurs involving the breakage of H-bonds. This slippage mechanism leads to energy dissipation once yielding begins and in addition to the formation of zone with lower material density (hence, less H-bonds) resulting in nanoscale voids (Buehler 2007). Buehler (Buehler 2007) compared mineralised and pure collagen fibrils (**Figure 2.22**) and found that mineralised fibrils show higher stiffness, strength and energy dissipation under deformation if compared with pure collagen fibrils. Specifically, the elastic modulus, yield strain and strength are 6.2 GPa, 6.7% and 0.6 GPa for mineralised collagen fibrils, while are, respectively, 4.6 GPa, 5% and 0.3 GPa for pure collagen fibrils (Launey, Buehler et al. 2010).

A similar sliding mechanism occurs at a higher hierarchical level between fibrils (also arranged in staggered configuration as shown in **Figure 2.21**). In fact, when collagen fibres are stretched the load is resolved into tensile deformation

of fibrils and shearing of extrafibrillar matrix (made of non-collagenous proteins) (Launey, Buehler et al. 2010). Here, sufficient energy is necessary to break sacrificial bonds that hold the fibrils together increasing the total energy to fracture the material and therefore the toughness (Fantner, Hassenkam et al. 2005). These bonds can reform allowing the material to partially reacquire the original strength once the load is removed. Gupta and co-workers (Gupta, Krauss et al. 2013) found that this intrafibrillar sliding is responsible for permanent plastic strain at the fibrillar level leading to high toughness in antler. In this context, in this thesis I investigate two new mechanisms at the fibrillar length scale of energy dissipation, known as heterogeneity and hysteresis, in **Chapter 4**.
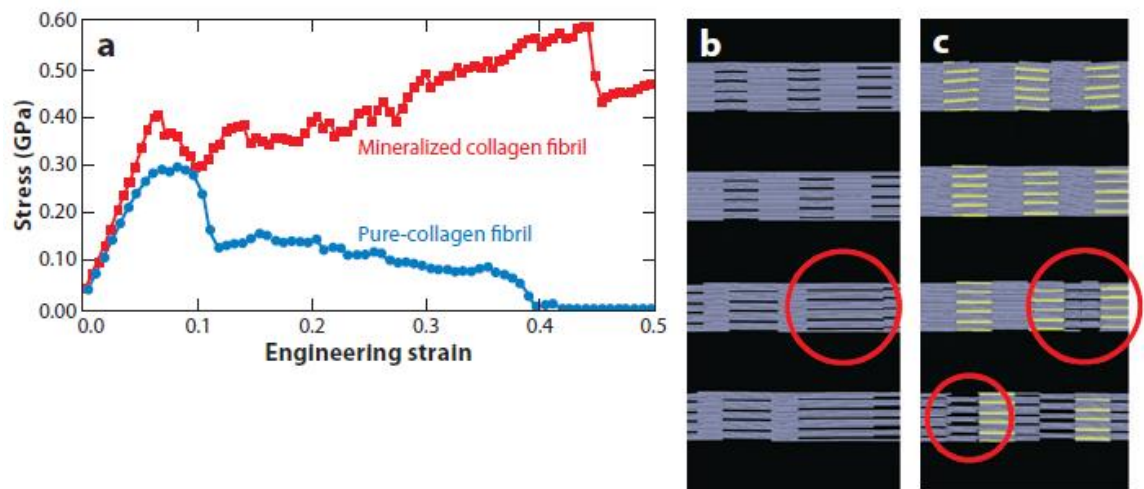
Figure 2.22 - Results from molecular dynamic simulations for (b) pure and (c) mineralised collagen fibrils. The differences in the two curves of (a) can be attributed to the slippage mechanism at the interface between mineral and tropocollagen molecules (Buehler 2007).

At the microscale, an important phenomenon of energy dissipation is known as microcracking characterised by the formation of numerous and short cracks (with a length of about 500 μm and width of about 100 μm (Mohsin, O'Brien et

al. 2006) caused by the fracture of hydroxyapatite crystals or delamination at interface between crystals and adjacent fibres (Launey, Buehler et al. 2010). This mechanism not only is an intrinsic mechanism (following the definition in **Section 2.2.3**) but is also one of the main extrinsic mechanisms, as explained in detail in **Section 2.2.3.2**.

2.2.3.2 Extrinsic mechanisms

Microcracks usually develop around a macro-crack forming plastic zones that reduces the stress levels nearby the crack. As a consequence, they form a sort of shield against crack propagation and protect the integrity of the entire structure. This phenomenon is known as constrained microcracking and contributes to the fracture toughness of bone by 0.05 MPa m$^{1/2}$ (Ritchie, Buehler et al. 2009). Microcracking is a fundamental phenomenon for the development of intrinsic mechanisms such as crack-bridging or crack-deflection. Crack bridging is verified in presence of intact regions between a primary growing crack and another initiated ahead. These zones are able to bear a substantial amount of load otherwise used to promote the crack propagation (Ritchie, Buehler et al. 2009). Crack deflection is characterised by directional variations of the propagating cracks dissipating a considerable amount of energy (Ritchie, Buehler et al. 2009).

In human cortical bone cement lines at the boundary of osteons are usually oriented along the longitudinal direction of bone which is also the direction where cracks preferably propagate. The relative direction between microcracks and main macro-cracks has a fundamental function in the toughening

mechanisms. In fact, cracks deflection and twisting arise when microcracks are mostly perpendicular to the main crack (this is observed along the transverse direction and contributes to the total fracture toughness of 3-20 MPa m$^{1/2}$ (Ritchie, Buehler et al. 2009)) while the mechanism of crack bridging (which adds a contribution of 1-2 MPa m$^{1/2}$ (Ritchie, Buehler et al. 2009) to the total fracture toughness) becomes predominant when microcracks are, instead, mostly parallel to the direction of the main crack (this occurs along the longitudinal direction) (**Figure 2.21**). These phenomena make bone tougher along the transverse direction than along the longitudinal one. For these reasons bone is more resistant to breakage rather than to splitting (Launey, Buehler et al. 2010).

It has been observed that collagen fibrils often bridge the gap due to a developing crack and provide additional resistance to crack propagation. This other mechanism is called collagen-fibril bridging and contributes to fracture toughness by typically 0.1 MPa m$^{1/2}$ (Ritchie, Buehler et al. 2009).

3 Multiscale models of arthropod cuticle and bone

Bio-composites such as cuticle and bone, possess outstanding mechanical properties while the behaviour of their basic constituents is quite modest (Meyers, Chen et al. 2008). These remarkable performances are achieved through their hierarchical organization and specific design at each length scale (Tai, Dao et al. 2007). Therefore, to understand the mechanical behaviour of the arthropod cuticle and bone, it is fundamental to consider the structure–property relations at all length scales. Another interesting aspect of natural materials is their ability to build multiple structures within the same system starting from the same basic constituents. For instance, the cuticle that at the macroscale consists of three layers (endo, exo and epicuticle) shows different behaviour at the internal and external layers. Specifically, the exocuticle is characterised by higher mineral content, smaller canal pores and lower pitch of rotation of the lamellar arrangement compared to the endocuticle (Sachs, Fabritius et al. 2006). The reasons of these specific designs and differences are still unknown and only detailed analyses could unveil them. Due to the limitation of the current experimental techniques for material characterisation (particularly at the nanoscale) and the complexity of the hierarchical structure of cuticle, the knowledge available on the structural and mechanical properties at different hierarchical levels of cuticle is still poor. For example, the mechanical properties and structures of the protein content are not completely clear.

An established approach to define the structure-property relationship in biological materials is based on computational analyses combined with

experimental data. Specifically, the process usually involves firstly, AFM (atomic-force microscopy) observations to create a map of the tissues and observe them, secondly, nanoindentation tests to determine the hardness of the contact and the Young's modulus (Oliver and Pharr 2004) of the test specimen and finally, Finite Element simulations to observe stress distribution or other specific parameters of interest. This method was used to investigate bone (Tai, Dao et al. 2007), nacre (Bruet, Qi et al. 2005) and fish scale (Bruet, Song et al. 2008), and does not explicitly consider the molecular scale analysing exclusively the higher hierarchical levels. Instead, atomistic molecular dynamic is a tool extensively applied to collagen-based materials to explore the mechanisms of energy deformation and dissipation at the atomistic and molecular levels (Buehler, Keten et al. 2008, Buehler and Yung 2009). Other methods to characterise the material properties of bio-composites at the nanoscale and mesoscale and their structural behaviour are based on the combination of experimental techniques (for instance mechanical tests coupled with synchrotron X-ray experiments) and analytical formulations or finite element simulations. An example of this type of approach is developed in **Chapter 5**. A more advanced and complete tool to analyse the structural properties and identify the key features in bio-materials is computational multiscale modelling including all the hierarchical levels. Usually, this method is aimed at obtaining the properties via a step-by-step homogenization process starting from the lowest scale and then passing the gained information to the upper levels of hierarchy (Nikolov, Fabritius et al. 2011).

3.1 Modelling of crustacean cuticle

An excellent example of the implementation of a complete multiscale modelling on crustacean cuticle comes from the studies of Nikolov and co-workers (Nikolov, Petrov et al. 2010, Nikolov, Fabritius et al. 2011) who developed a general method (that can be applied also to other bio-composites) and focused on the lobster Homarus Americanus, one of oldest natural examples of structural and armoured biological system that underwent a process of evolution since the Early Cambrian period (about 500 million years ago). This hierarchical model is based on ab-initio calculations at the nanoscale and specific techniques to find the homogenised properties of a heterogeneous representative volume element (RVE). To overcome the difficulties for isolating and testing single α-chitin nanofibrils, they used molecular dynamics (MD) simulations combined with DFT (density functional theory) to find the stiffness tensor of a single α-chitin crystal. At this level, they found that α-chitin is much stiffer in the chain direction c compared to the transverse directions due to the strong covalent bonds which are predominant along the c axis (while the H-bonds, responsible for cohesion along the transverse directions, are weaker). At higher levels, homogenization methods combined with experimental tests were employed to calculate the elastic behaviour of the system (Nikolov, Fabritius et al. 2011). A schematic summary of the experimental and numerical techniques employed at different length scale to calculate the Young's moduli is shown in **Figure 3.1** (Nikolov, Petrov et al. 2010).
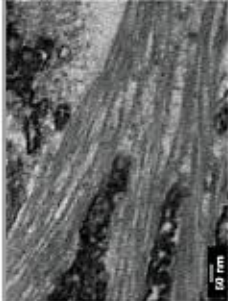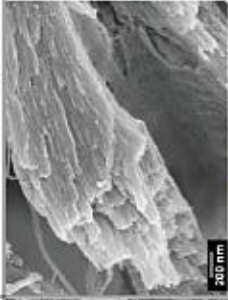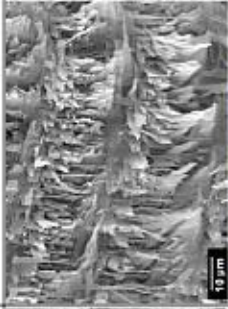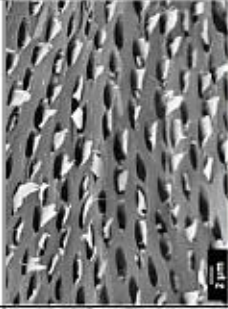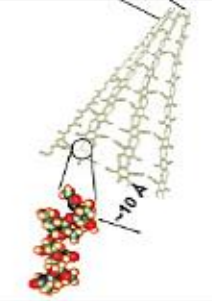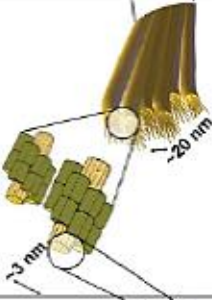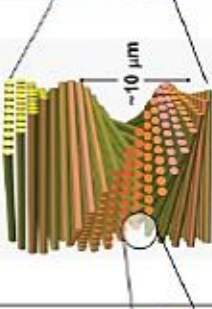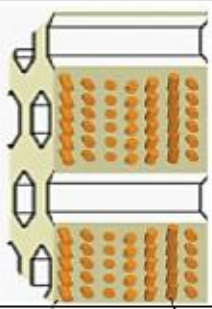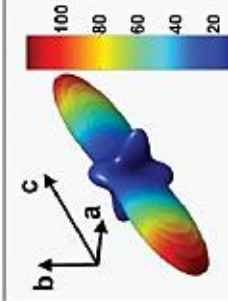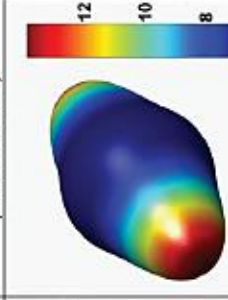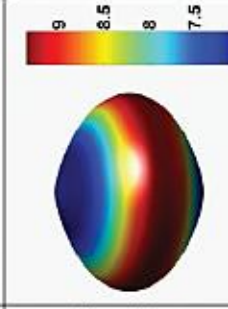
Scale	0.1 nm – 10 nm	10 nm – 100 nm	100 nm – 10 μm	10 μm – 1 mm
Hierarchical structure unit	α-chitin (H-bonded anti-parallel N-acetyl-glucosamine molecular chains)	Mineralized chitin-protein nanofibrils in a planar array	Twisted plywood stack of mineralized chitin-protein planes without pore canals	Twisted plywood stack of mineralized chitin-protein planes with pore canals
Experimental method	Transmission electron microscope	Field emission scanning electron microscope	Field emission scanning electron microscope	Field emission scanning electron microscope
Microstructure				
Schematic				
Simulation method	Ab initio; density functional theory	Mori-Tanaka scheme (chitin-protein fiber); Torquato 3-point scheme (mineral-protein matrix)	Dilute approximation, tensor rotation	Torquato 3-point homogenization
Elastic behavior, 3D maps of Young's modulus [GPa] a,b-axes: basal directions of the chitin unit cell c-axis: longitudinal (chain) axis of the chitin molecule				

Figure 3.1 - Elastic properties of the cuticle structure. The hierarchical structures, together with the experimental and numerical methods applied to the cuticle, are listed (Nikolov, Petrov et al. 2010).

Their results, valid only in elastic regime (small deformation), demonstrate that

the mechanical properties of cuticle mostly depend on the material properties of

the constituents at the higher hierarchical levels. Specifically, they introduced a sensitivity parameter to verify the effect of variations of design parameters such as volume fraction and material properties of the constituents and they found that the in-plane (along the fibres direction) cuticle modulus mostly depends on the overall content of mineral and volume fraction of chitin fibres. In addition, they verified that the anisotropy ratio (in-plane elastic modulus/out-of plane elastic modulus) decreases as the hierarchical level increases passing from 4.25 at the molecular level to 1.25 at the macro-scale (plywood structure with pore canals) (Nikolov, Petrov et al. 2010).

The exoskeleton of the mantis shrimp impressed scientists particularly for the damage tolerance of its dactyl clubs. In fact, one of the most impressive behaviour of this animal is not only the ability to smash tough snail shells with powerful strikes but also the capability of its dactyl clubs (that are used to hit the preys) to resist violent impacts. Yaraghi et al. (Yaraghi, Guarín-Zapata et al. 2016) investigated the structure of the dactyl club in the impact region (the outer layer of cuticle, see also **Figure 2.8**) and found the presence of a fibrous herringbone-like pattern terminating with a layer of nanoparticles of 65 nm in diameter. They performed finite element simulations and created 3D printed samples comparing the sinusoidal herringbone pattern found in the clubs with the helicoidal pattern typical of other parts of the cuticle such as the abdominal zone (**Figure 3.2**). Their results showed that the herringbone structure is able to absorb up to 3.43 times higher impact energy than the helicoidal structure and that the transversal Young's modulus of the herringbone-like system increases as the ratio between the amplitude and wavelength of the sinusoidal pattern increases (Yaraghi, Guarín-Zapata et al. 2016).
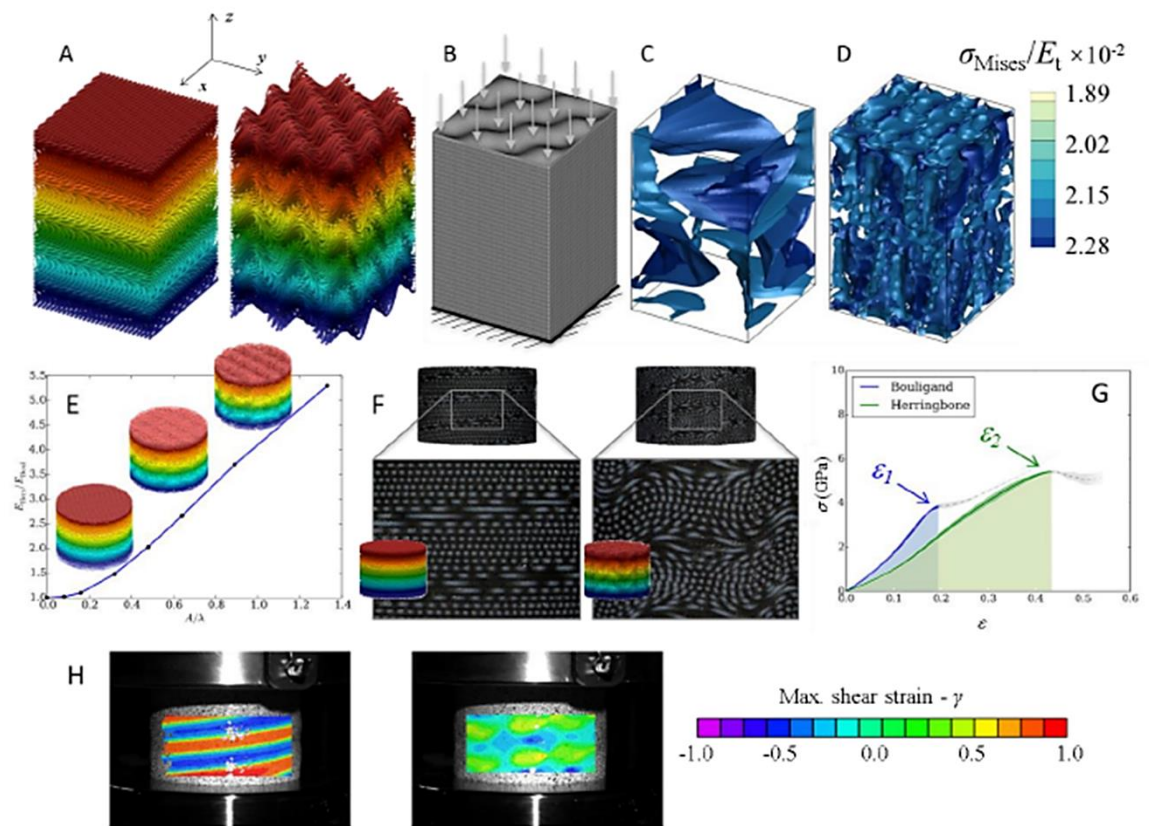
Figure 3.2 - Finite Element analysis and mechanical compression tests of 3D printed samples reproducing the helicoidal and herringbone patterns. (A) Geometry of the helicoidal and herringbone structures. Colours are representative of the position along the z-axis. (B) Mesh used for the analyses. (C-D) Surfaces of constant normalised von Mises stress ($\sigma_{Mises}/E_{transversal}$) for the values 1.89×10^{-2}, 1.95×10^{-2}, and 2.28×10^{-2}. (E) Relative Young's modulus for herringbone pattern with respect to the helicoidal case. The horizontal axis shows the aspect ratio between the amplitude and wavelength of the sinusoidal herringbone pattern. (F) 3D printed samples reproducing the helicoidal and herringbone shapes. (G) Results from compression tests for the 3D printed samples. (H) Comparison for the helicoidal 3D printed sample and the herringbone one at a deformation of 0.1 (Yaraghi, Guarín-Zapata et al. 2016).

In addition, their results showed that nanoparticles play an important role in the energy absorption mechanisms of cuticle preventing stress concentration and therefore crack propagation in the impact region (Yaraghi, Guarín-Zapata et al. 2016).

The helicoidal structure of cuticle inspired a recent study (Grunenfelder, Suksangpanya et al. 2014) by Grunenfelder and co-workers, where they applied the helicoidal design of cuticle to a carbon fiber-epoxy composite. Impact tests and finite element simulations were performed to investigate the impact resistance of the structure. Multiple layups with different rotation angles between consecutive plies were tested: unidirectional ([0]$_s$), quasi isotropic ([0/±45/90]$_{6s}$), 'small angle' ([0/7.8/…/180]$_s$), 'medium angle' ([0/16.3/…/180]$_{2s}$), 'large angle' ([0/25.7/…/180]$_{3s}$). Results demonstrate that a smaller rotation angle results in a reduction of impact damage and in an increase of residual strength (Grunenfelder, Suksangpanya et al. 2014).

3.2 Modelling of bone

A substantial number of modelling studies investigating the mechanisms of deformation and energy dissipation of different scales in bone is available. Analytical and computational approaches were widely used to explore the mechanics of bone and understand the reasons of its remarkable strength and toughness.

Fratzl and Weinkamer (Jäger and Fratzl 2000, Fratzl and Weinkamer 2007) developed a shear lag analytical model to calculate the effective Young's modulus of staggered arrangement of hydroxyapatite platelets embedded in a collagen matrix forming the collagen fibrils (**Figure 3.3**). Their model considered the effect of the aspect ratio of platelets and the staggered arrangement, part of the load is carried by the matrix through shear stresses. The Young's modulus of the composite is expressed by **Equation 3** where the coefficient k is shown in

Equation 4. A typical value of k for collagen tissues is ≈ 5.4 (Fratzl and Weinkamer 2007).

$$E^c = (1-\varphi)E^m + \varphi E^p / k \qquad (3)$$

$$k = 1 + \frac{4}{\rho^2} \frac{1-\varphi}{\varphi} \frac{E^p}{G^m} \qquad (4)$$

All the terms appearing in **Equations 3 and 4** are listed in **Table 3.1** (subscripts c, p and m indicate respectively composite, platelets and matrix).

Symbol	Meaning
E	Young's modulus
φ	Mineral volume fraction (platelets)
ρ	Platelets aspect ratio (L/D)
G	Shear modulus

Table 3.1 – Symbols used in Equations 3 and 4.
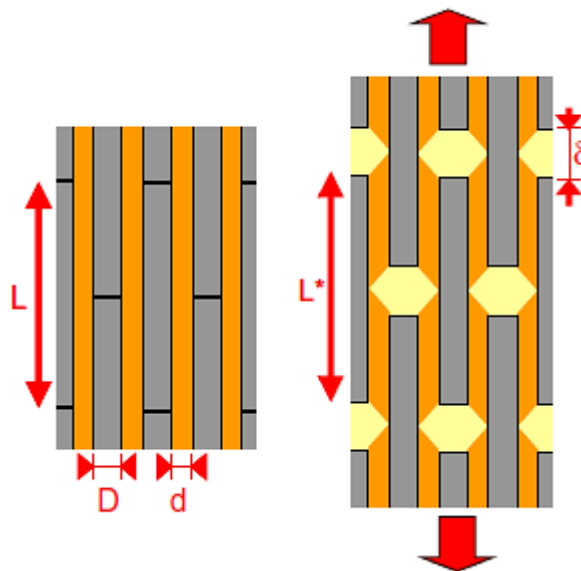
Figure 3.3 - Sketch of the two-dimensional staggered system made of stiff platelets (length L, thickness D, lateral spacing d, L deformed length, δ increase of space between particles) and glued together by a matrix (Fratzl and Weinkamer 2007).*

As a result, mechanical properties of collagen fibrils depend on the ability of mineral platelets to bear large tensile stress and of proteins component to carry shear stresses without failure. Therefore, the fracture toughness of the composite depends on the tensile strength of mineral platelets. Inspired by the model previously described (Fratzl and Weinkamer 2007), Gao and co-workers focused on the optimization of the strength of mineral platelets (Gao, Ji et al. 2003). They considered as ideal a defect-free mineral platelet and studied a realistic platelet containing material discontinuities (flaws) trapped within the mineral crystals. These flaws are equivalent to soft protein inclusions or embedded microcracks. Using concepts from fracture mechanics, they estimated a critical length for the thickness of minerals below which the fracture strength of a cracked platelet is identical to that of an ideal platelet. This length is of the order of magnitude of nanometer ($\approx$ 30 nm) below which the material is insensitive to crack-like flaws. Ranging the mineral platelets thickness between 3 and 10 nm, the strength of minerals is not affected by flaws. This finding leads to state that the nanometer size of mineral crystals in bio-composites provides the optimum fracture strength and maximum tolerance to material imperfections (Gao, Ji et al. 2003). Using a similar approach, they also estimated an optimum mineral aspect ratio that results to be $\approx$10 (Gao, Ji et al. 2003). Another mechanical model (Bar-On and Wagner 2011) for bio-composites including mineral platelets arranged in staggered configuration within a soft matrix was developed to predict the mechanical behavior of staggered composite(Cox 1952). This approach was also extended to a two scale analysis to calculate the effective elastic moduli of composite with staggered fibres including the effects of ply orientation at the larger scale (Bar-On and Wagner 2012). Results showed that for high fibre content the optimal micro-buckling strength is

obtained when staggering is included at the lowest scale in layers oriented at 45° within plywood composites with lamination sequence [0,±45,90]. This multiscale model could be potentially used to study the mechanical response of collagen fibre where both collagen fibrils (at the fibre length scale) and mineral platelets (at the lower length scale) are arranged in a staggered configuration. Specifically, it could be used to explain the reasons behind the hierarchical degradation that Gupta and co-workers (Gupta, Seto et al. 2006) measured with synchrotron X-ray diffraction method at different scale lengths in bone. In details, they found that, under tensile load, at the tissue, fibrillar, and mineral platelets levels, the strains decrease in a ratio of 12:5:2 (**Figure 3.4**).
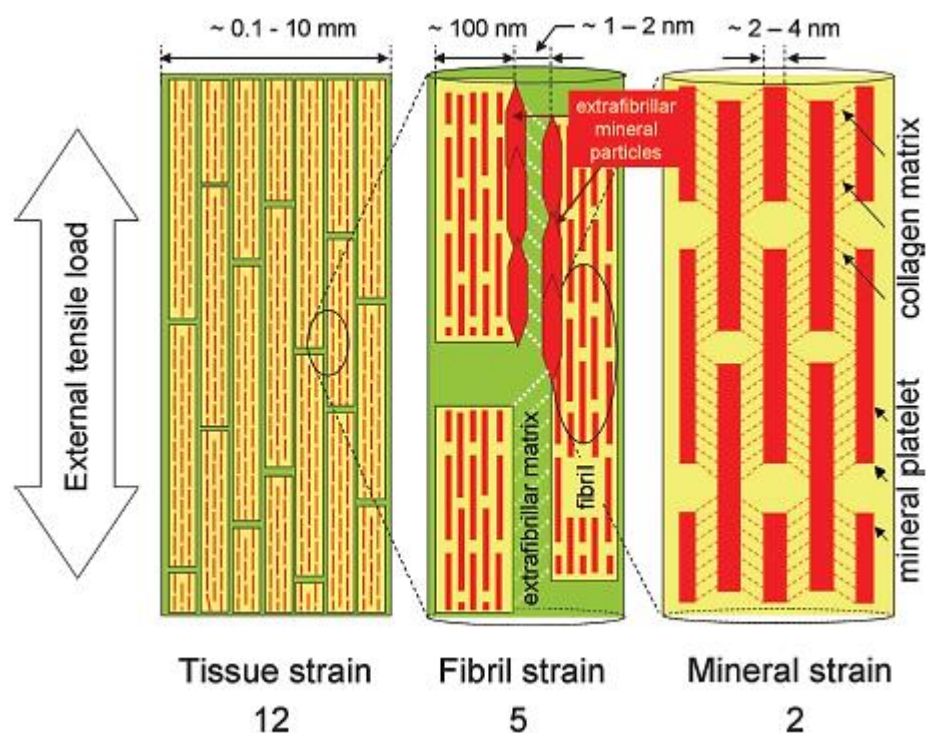
Figure 3.4 - Schematic model showing bone deformation under external tensile load at three different hierarchical levels (Gupta, Seto et al. 2006).

The fracture mechanics of staggered arrangements of fibers was instead studied by Barthelat and co-workers (Rabiei, Bekah et al. 2010). The authors developed an analytical method to predict the failure modes of the RVE

(representative volume element) which depend on geometrical factors and on the applied normal and shear stresses. Three different failure modes were identified: columnar, stair and shearing (Rabiei, Bekah et al. 2010). Specifically, columnar systems with platelets arranged in columns ad with well-defined core and overlap regions, mainly follow a columnar failure mode whereas, random arrangement, with undefined core and overlap regions, follow a stair mode. A third failure mode can occur if the applied shear reaches the shear strength of the interface (Rabiei, Bekah et al. 2010) (**Figure 3.5**).
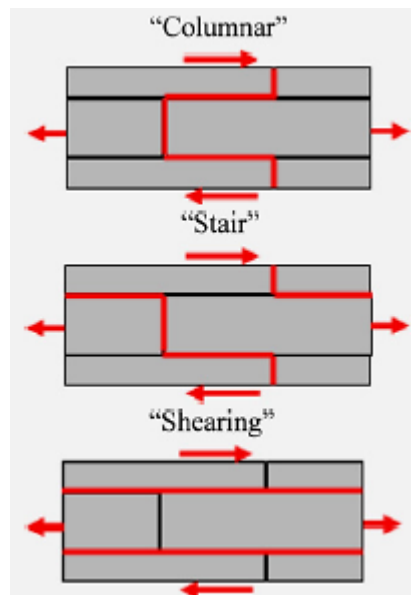
Figure 3.5 - Possible RVE failure modes for staggered arrangements (Rabiei, Bekah et al. 2010).

The analytical models of bone mainly focused on the elastic and fracture properties at the nano and micro-scales. However, most of these models idealise bone as a two dimensional system without considering the actual three dimensional configuration of fibrils and fibers (Sabet, Najafi et al. 2016). In addition, including non-linear material properties and modelling accurately sliding or debonding mechanisms are hard tasks. To overcome these

challenges computational methods such as finite elements or molecular dynamics simulations are used.

Finite element method was mostly used to analyse the mechanics of two-dimensional collagen fibrils (Sabet, Najafi et al. 2016). A cohesive FE model (Siegmund, Allen et al. 2008) was used to investigate the role of enzymatic and non-enzymatic cross links. The enzymatic process results in trivalent collagen cross-links located at the collagen overlap position while non-enzymatic collagen crosslinking occurs via spontaneous condensation of amino acids with no specific spatial arrangement (randomly placed) (Siegmund, Allen et al. 2008). Results showed that non-enzymatic cross links increase the stiffness and decrease the toughness of bone while enzymatic cross link slightly affect the mechanical properties of bone. Finite element method (Luo, Nakade et al. 2011) was also used to study the effect of mineral–collagen interfacial interaction on the damage progression in bone by considering three types of interfaces: strong, intermediate and weak. Strong interfaces represent ionic interactions, intermediate interfaces represent hydrogen bonds while the weak ones reproduce the van der Waals interaction forces. In this work, the damage is considered as partial or total failure of the cohesive finite elements between mineral platelets and collagen proteins. Results indicated that strong interfaces lead to the formation of linear cracks in bone, whereas weak interfaces provoke diffuse damage. In addition, intermediate interfaces govern the transition from linear microcrack to diffuse damage (Luo, Nakade et al. 2011). Mischinski and Ural (Mischinski and Ural 2011) employed finite element simulations to elucidate the mechanisms affecting crack penetration into osteons and crack deflection at the cement lines. The authors analysed a 2D model of a single

osteon surrounded by cement lines and interstitial bone (**Figure 3.6**). Cohesive finite elements, whose properties were based on previous experimental measurements, were used to model both the cement lines around the osteons and crack paths. Results revealed that the strength of cement lines plays an important role in crack deflection. Specifically, low cement line strength facilitated crack deflection into cement lines with no effect of the fracture toughness of the cement lines. However, the combination of low cement line fracture toughness and high strength did not assure crack deflection. They also found that longer cracks required lower strength and fracture toughness of cement lines to be deflected. In addition, the change of the elastic modulus of the osteon did not affect significantly the crack pattern while the change of the cohesive law influenced the crack trajectory (Mischinski and Ural 2011).
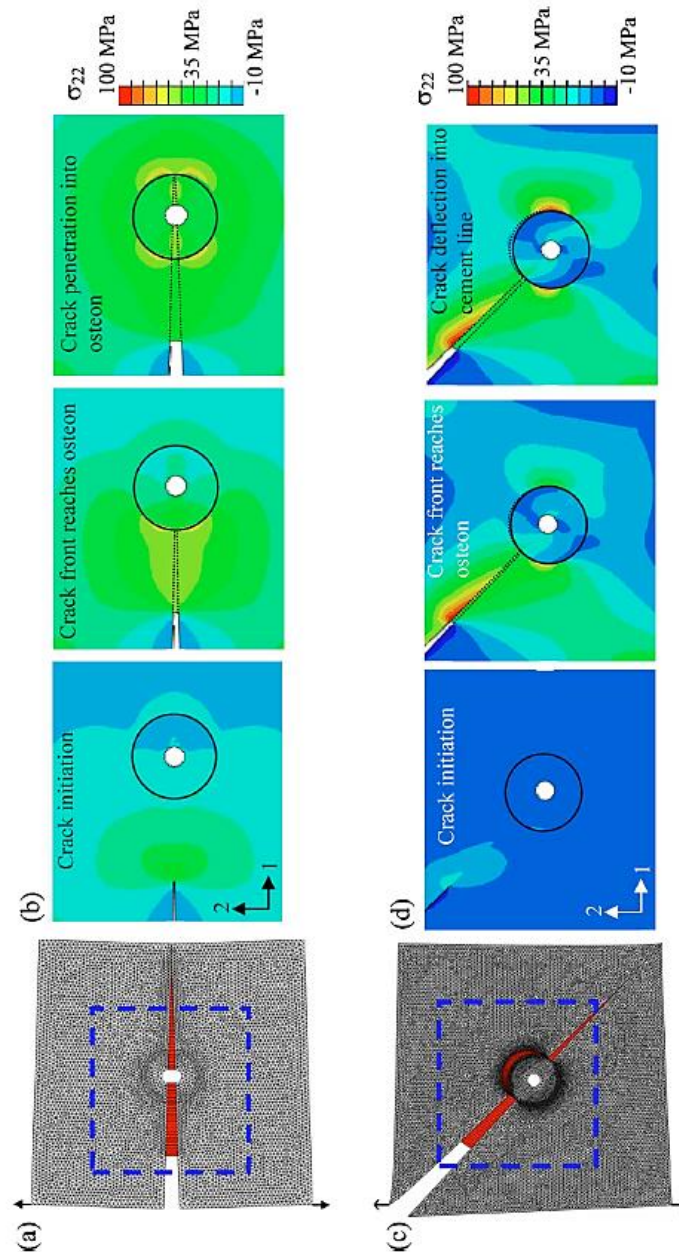
Figure 3.6 – Comparison between the crack patterns of 0° and 45° cracks propagating towards the osteon. *(a) Finite element sample showing crack propagation through an osteon for 0° crack. (b) Stress contours showing the different stages of crack propagation for 0° crack. (c) Finite element sample showing crack deflection into the cement line for 45° crack. (d) Stress contours showing the different stages of crack propagation for 45° crack that is deflected by the cement line. The initial cracks are modelled as completely open surfaces and the crack pattern (Mischinski and Ural 2011).*

A similar analysis (Abdel-Wahab, Maligno et al. 2012), focused on the effect of

cement lines on the fracture mechanics of bovine cortical bone, was conducted

108

using X-FEM (extended finite element method), an extension of the classical finite element method based on a set of enrichment functions used to define the domain in presence of cracks or discontinuities (Ghorashi, Valizadeh et al. 2012). In details, the study investigated the effect of microstructural constituents such as cement lines on the fracture mechanics of bone using a X-FEM-based cohesive segment to simulate crack initiation and propagation through the system. Three different models were analysed: homogeneous (model A), three-phase (model B, without cement lines) and four-phase composite (model C, with cement lines) (**Figure 3.7**).
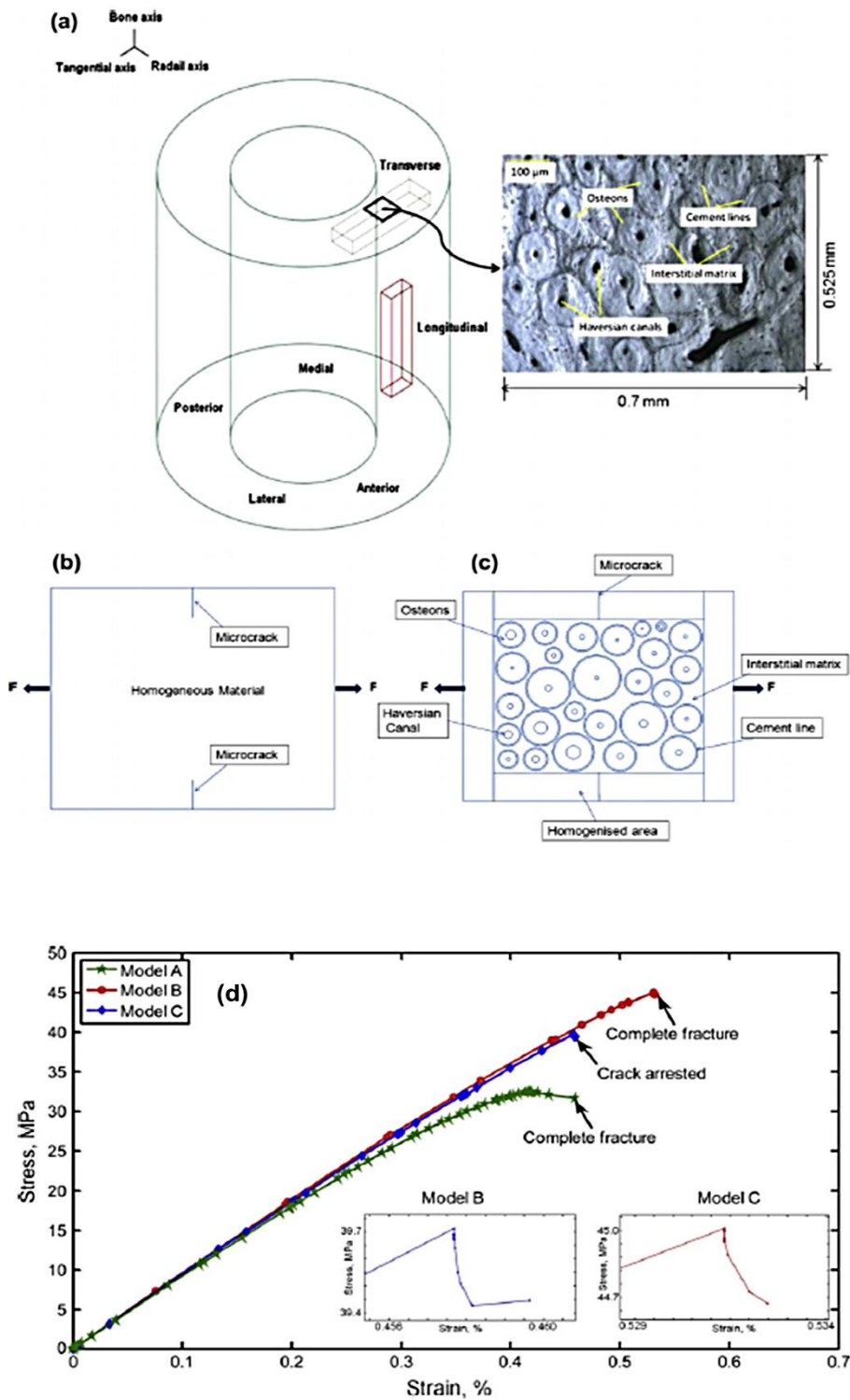
Figure 3.7 – (a) Micrograph of transverse cross-section of osteonal bovine bone, (b) schematic illustration of homogeneous model, and (c) schematic illustration of micro-structural model. (d) Stress strain curves for the three models (Abdel-Wahab, Maligno et al. 2012).

Results revealed a softening pattern in the stress strain curve for the homogeneous model A once cracks started propagating, while the introduction of a heterogeneous material in models B and C eliminated this softening behaviour. In addition, the presence of cement lines (model C) entailed higher levels of stress and for cracks propagation, while the presence of osteons affects the trajectories of crack propagation. Furthermore, the homogeneous model featured the lowest final fracture stress and strain; model B had the highest values, while in model C the cement lines arrested the crack propagation.

At the smallest hierarchical levels, experimental measures are often very challenging. For this reason, several molecular dynamics simulations at the atomistic level were performed to study the deformation and failure mechanisms of collagen molecule and collagen-mineral systems. Buehler and co-workers (Buehler 2008) examined the effect of cross-links density in collagen fibrils. Results revealed that higher cross-link densities caused larger yield strains and stresses as well as higher fracture stresses. In addition, the increase of cross-link density led to brittle deformation behaviour. Another study (Libonati, Nair et al. 2013) focused on the effect of geometry on strength, fracture toughness, stress distribution and crack propagation in mineral crystals with an edge crack. Results showed that crystal size is responsible for changes in the failure mode and stress distribution. Specifically, a decrease of crystal size causes a change from a brittle-like failure mode in bigger samples to a more diffuse failure mode in the smaller ones combined with a change from a heterogeneous stress field to homogeneous stress field. In addition, such decrease provokes a general improvement of strength, strain at failure and toughness, approaching the

values of the ideal crystal without flaws. The findings of this study reveal that below a critical size of ≈ 4.15 nm, mineral crystals become flaw-tolerant, as already stated by Gao and co-workers (Gao, Ji et al. 2003).

There are few studies in literature focused on multiscale modelling of bone but none of them included all the hierarchical scales (Sabet, Najafi et al. 2016). A two-dimensional multiscale analysis was proposed to predict the strength and deformation mechanisms in lamellar bone (Hamed and Jasiuk 2013). Firstly, finite element simulations were performed to analyse mineralised collagen fibrils including the effect of soft collagen proteins and stiff and brittle minerals. The obtained strength and elastic properties were then employed to analyse a single lamella made of mineralised fibrils glued together by non-collagen proteins. Finally, lamellar bone was modelled by forming plywood of single laminae with different orientation and studying the effect of these lamination sequences on bone strength and longitudinal and transversal elastic moduli (Hamed and Jasiuk 2013). At the nanoscale, sliding between collagen proteins and sliding at the interface between collagen and hydroxyapatite platelets were identified as responsible for the non-linear stress strain behaviour of collagen fibrils. At the higher level, results showed that the strength of a single lamella depends mostly on the strength of mineralised collagen fibrils which depends itself on the interaction between proteins and minerals. Specifically, a weak interaction between these two components better reproduces a typical stress strain curve of bone at that scale (**Figure 3.8c**). At the microscale, five systems with different lamination sequences were analysed: [0, 0, 0, 0, 0, 0, 0], [0, 90, 0, 90, 0, 90, 0], [0, 30, 60, 90, 120, 150, 180], [0, 15, 30, 45, 60, 75, 90], [0, 30, 60, 90, 120]. Results showed that for the last pattern, which reproduces the real

lamellar structure as found by Weiner and co-workers (Weiner, Traub et al. 1999), the strength of bone at microscale is 108.8 MPa confirming previous experimental data on bovine bone (Hamed and Jasiuk 2013).
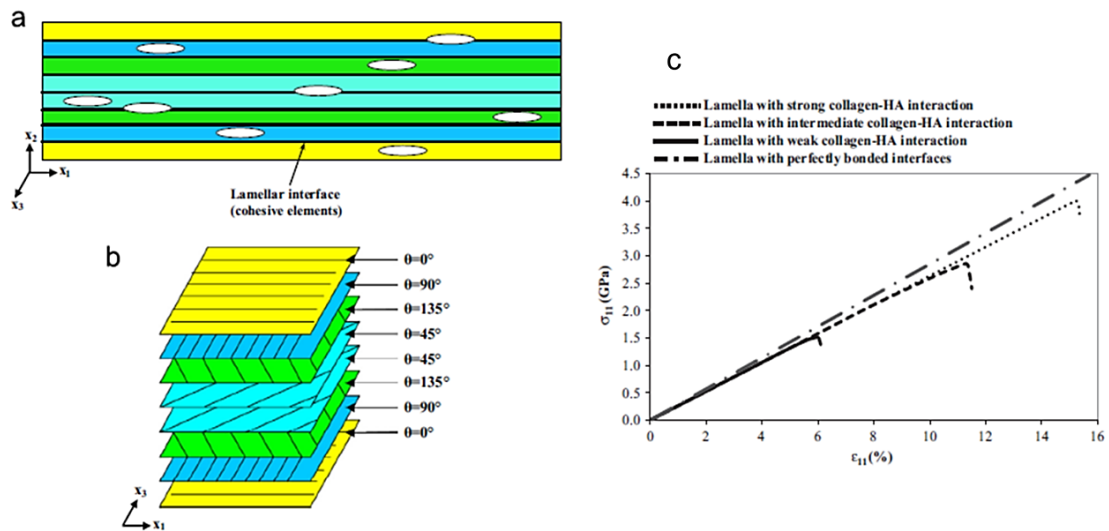
Figure 3.8 – Lamellar structure and stress–strain curve of a single lamella in the longitudinal (x1) direction for three types of collagen–HA interactions: strong, intermediate and weak (Hamed and Jasiuk 2013).

Most of the multiscale models for bone consider each scale separately transferring the information from the lower to the higher hierarchical level (Sabet, Najafi et al. 2016). Thus, there is the need to create models able to approach multiple scales simultaneously (concurrent multiscale modelling) and to consider the system as a continuum. This 'discrete approach' causes a series of limits which lead to questions about the determination of the number of hierarchical scales, and also about the size and the existence of a representative volume element (RVE). In addition, further studies would be opportune to fully comprehend effects of scale discretization (Sabet, Najafi et al. 2016).

4 Mechanisms of hysteresis and heterogeneous deformation in antler

In this Chapter I will use a terminology that is defined below:

- Yielding is the phenomenon corresponding to the situation when considerable elongation of a specimen under tensile test occurs with no noticeable increase in the tensile force (Gere and Goodno 2001). Yielding typically occurs after the proportional limit (point on the stress-strain curve at which the proportionality between stress and strain stops existing).

- Yield stress is the magnitude of stress required to cause yielding in the structure. It is also called yield strength, where the word 'strength' indicates the capacity of a structure to resist loads (Gere and Goodno 2001).

- Fracture strength is the critical value of stress at which fracture occurs. This is usually determined by performing a tensile test on a specimen as last point on the measured stress-strain curve (Gere and Goodno 2001).

- Fatigue resistance or strength is the highest stress that a material can withstand for a given number of cycles without breaking (Yukitaka and Masahiro 1983).

- Energy stored is the area under the curve 'load-displacement' of a material that follows the Hooke's law (this curve is a straight line) (Gere and Goodno 2001).

- Elastic strain energy is the energy recovered during the process of unloading. Inelastic strain energy is the energy dissipated in the process

of permanently deforming the system upon unloading (Gere and Goodno 2001).

- Work of fracture is the area under the load-displacement curve computed in correspondence of the displacement of complete fracture (Zehnder 2012).

- Fracture toughness is measured by the critical stress intensity factor K_c and critical strain energy release rate G_c and defines the resistance of materials against crack propagation (this definition presumes the presence of a crack with a certain size) (Vasiliev and Morozov 2013).

- Hysteresis is a lag in response exhibited by a system when reacting to changes in the external applied forces. In simpler terms once the system experiences a force and undergoes changes (loading), it returns back to its initial configuration (unloading) following a different path resulting in hysteretic loops on the stress strain curve. In my simulations, time is a 'pseudo' variable (Planchard 2017) that specifies the load level at different solution steps. Indeed, only the cyclic loading was defined in terms of 'pseudo' time but the solver did not consider the time dependent terms of the equation of motion (Chaichian, Merches et al. 2012). The area within each loop on the stress-strain curve indicates the amount of energy dissipated per unit of volume.

- Fibrillar heterogeneity in this chapter refers to the different (heterogeneous) fibril strain types of behavior, which are inferred from changes in SAXD diffraction patterns like peak broadening (Krauss, Fratzl et al. 2009).

4.1 Introduction

Natural structural materials exhibit mechanical properties through complex hierarchical architectures and load-absorbing mechanisms. These architectures evolved naturally from basic building blocks thanks to a 'self-organization' strategy during growth (Meyers, Chen et al. 2008). In fact, biological structures adapt, change function during growth, renew their material and build hierarchies (Fratzl and Weinkamer 2007). The macroscopic behaviour of these materials depends on the interaction between structural properties at different scales (Buehler 2007). Bio-composites, such as bone, shells and nacre, represent an excellent example of how the design at lower hierarchical scales confers higher mechanical properties than the single constituents (Ji and Gao 2004). Although the stiffness of these bio-composites is comparable to that of the basic constituent at the nanoscale, their fracture toughness results hugely increased. For instance, in bone and shell, the fracture toughness of the mineral constituents is $<<$ 1MPa*m$^{1/2}$ while the toughness of their macrostructure varies, respectively, in a range of 2 - 7 MPa*m$^{1/2}$ and 3 - 7 MPa*m$^{1/2}$.

Antler, as shown in **Figure 2.15**, at the nanometre scale length is a composite of stiff inorganic hydroxyapatite platelets interleaved with a softer organic matrix, made principally of type I tropocollagen proteins (Weiner and Wagner 1998). This sub-structure, together with an intrafibrillar phase of noncollageneous proteins and mineral, forms mineralised fibrils that are arranged into aggregate structures at higher levels and larger length scales, such as fibril arrays and lamellae (Meyers, Chen et al. 2008). The structural aspects of this architecture served as inspiration for bio-inspired materials that replicate the nanometre scale fibril-matrix (Pugno 2006, Bonderer, Studart et al.

116

2008, Bosia, Buehler et al. 2010, Bosia, Abdalrahman et al. 2012, Bosia, Abdalrahman et al. 2014) and intrafibrillar (Wang, Azaïs et al. 2012) structure, or at micrometre scales (Dimas, Bratzel et al. 2013) (Compton and Lewis 2014). Nonetheless, the mechanical interactions between the constituent units and the higher length scales remain a matter of active research. In particular, previous studies focused on how the hierarchical architecture brings functionally desirable properties such as high fracture toughness (Koester, Ager et al. 2008), energy absorption and fatigue resistance (Fleck and Eifler 2003).

At the range of 1 – 100 µm, accepted and validated toughness mechanisms are crack deflection and bridging (Nalla, Kinney et al. 2003), and constrained microcracking (Vashishth, Behiri et al. 1997). The nanoscale structure is believed to be of fundamental importance for bone toughness. However, it is both challenging to investigate experimentally (Hang and Barber 2011) as well as to explain the reasons of its mechanical properties at this scale with a model. Works to date mainly focused on either deformation beyond the yield point under uniaxial or localised loading (Tai, Dao et al. 2007, Hang and Barber 2011, Gupta, Krauss et al. 2013) or on post-hoc interpretation of electron microscopic images of loaded and fractured bone (Fantner, Hassenkam et al. 2005, Poundarik, Diab et al. 2012). These experimental studies led to hypothesise different toughness mechanisms (Launey, Buehler et al. 2010). Examples include intrafibrillar plasticity (Gupta, Krauss et al. 2013), sacrificial bonds within noncollageneous proteins (Fantner, Hassenkam et al. 2005), friction between collagen and mineral (Tai, Ulm et al. 2006), fibrillar sliding of mineralised collagen fibrils (Buehler 2007), interfibrillar sliding of collagen fiber arrays (Gupta, Wagermaier et al. 2005) and microcracking (Zioupos and Currey 1994).

At these small length scales relatively less clear evidence exists on the response to cyclic loading, although recent experimental work has begun to shed light on this question. For example, Schwiedrzik et al. (Schwiedrzik, Raghavan et al. 2014) focused on compression and cyclic micro-pillar tests on lamellar bone and measured axial and transverse apparent moduli and compressive strengths.

Antler is physiologically subjected to external periodic loading that can lead to fatigue failure, and high rate impact that instead can lead to fracture. It is then of considerable interest to understand how the nanostructure behaves under these loading conditions. Unfortunately, experimental information on the structural changes at the fibrillar and interfibrillar level in these loading modes is relatively scarce. Concurrently, the link between the types of fibrillar architecture and the developed cyclic inelastic response is also not very clear. In this regard, a recurrent generic motif in the architecture of hard biological composites is a staggered arrangement of fibrils (**Figure 4.1b**) (Barthelat and Rabiei 2011). This particular arrangement plays a key role in energy dissipation through sliding (Buehler and Yung 2009, Bar-On and Wagner 2011) and in enhancing the structural elastic properties (Bar-On and Wagner 2013, Xia, Ruiz et al. 2016). Gupta et al. (Gupta, Krauss et al. 2013) identified elastoplastic behaviour for the individual mineralised fibril under the assumption of staggered configuration of mineral platelets and collagen molecules inside the fibril.

The role of such a staggered configuration in cyclic loading and energy absorption is unexplored at the nanoscale. Recent *in situ* synchrotron SAXD/WAXD mechanical loading/unloading tests on antler (Gupta, Krauss et

al. 2013) show hysteresis in stress-strain curves at both the macroscopic and the fibrillar level. These results also highlight the presence of two groups of fibrils: plastically deforming fibrils, which exhibit larger deformation (which will be denoted type A in what follows), and elastically deforming fibrils (denoted type B), whose deformation remains at or under the strain at the material yield point. It is clear that these structural mechanisms may be related, and that the fibrillar hysteresis is an important component of the high work to fracture of antler, but its structural origins are far less understood. *In situ* experimental probes of the type described above need to be combined with ultrastructural modelling at the scale of 1-100 nm, in order to develop a deeper understanding of the relevant mechanisms.

In this chapter, I present a set of finite element simulations of the mineralised fibrils in antler under cyclic loading whose results, when matched to experiment, give an understanding of the causes of the fibrillar hysteresis. I will show that the combination of a damageable interface and staggered fibrillar arrangement turns out to be capable of explaining the experimentally observed hysteretic loops in loading/unloading curves. In addition, a clear explanation of the biphasic fibrillar deformation mechanisms, in terms of the dependence on interfacial strength and architecture, is here reported. These results provide new insights of toughening mechanisms at the nanoscale in antler.

4.2 Methods

4.2.1 Experimental method

The preparation description of antler specimens and the *in situ* mechanical tests with synchrotron small angle X-ray diffraction (SAXD) are described in detail in a previous paper (Gupta, Krauss et al. 2013), and summarized here briefly. The samples were taken from the antler cortical shell of a red deer (*Cervus elaphus*) near the antler-pedicle junction and tested with SAXD measurements, combined with cyclic loading. While the details are available in a previous paper (Krauss, Fratzl et al. 2009), they will be summarized here for completeness. **Figure 4.1a** shows a highly simplified schematic for tensile cyclic tests on hydrated antler specimens combined with time-resolved synchrotron SAXD measurements, where a synchrotron X-ray beam impinges on the specimen, leading to a sequence of SAXD patterns acquired as the sample is deformed.

As the details are presented in Gupta et al. (Gupta, Krauss et al. 2013), I note that a biphasic fibrillar deformation was experimentally observed, and will serve as part of the comparison of the presented model to experiment.

4.2.2 Numerical method and implementation of the model

Parametric finite elements simulations were performed to test a seven-layer staggered fibrillar system using *Abaqus* (Abaqus 6.14-1, Dassault Systemes). The two-dimensional model is made of 2800 CPS4R finite elements (CPS4R corresponds to 4-node, reduced integration with hourglass control). The plates, measuring 10 µm × 0.2 µm, represent the fibrils (with 200 nm or 0.2 µm radius (Fratzl and Weinkamer 2007) in antler and are connected through cohesive laws, which are shown in detail in **Figure 4.1b** (Xu and Needleman 1994).

Interfaces link both the lateral sides of fibrils ('mode I interface') and their bottom-up sides ('mode II interfaces') (see **Figure 4.2c** for interfaces definition). The model (**Figure 4.1b**) assumes initially linear elastic behaviour (**Equation 5**) followed by the initiation and evolution of damage. In **Equation 5**, the traction vector consists, as my models are two-dimensional, of two components t_n and t_s, which are, respectively, the normal and shear tractions, and δ_n and δ_s which represent the relative displacements between the nodes on the adjacent surfaces of two different fibrils. The simplest traction-separation law was used, where normal (K_{nn}) and tangential (K_{ss}) stiffness are not coupled (K_{ns} and K_{sn} are null in **Equation 5**).

$$t = \begin{bmatrix} t_n \\ t_s \end{bmatrix} = \begin{bmatrix} K_{nn} & 0 \\ 0 & K_{ss} \end{bmatrix} \begin{bmatrix} \delta_n \\ \delta_s \end{bmatrix} \tag{5}$$

As peak traction values for the mode I and mode II undamageable interfaces, I used generic values such as $t_n^0 = t_s^0 = 80$ MPa. These values are never achieved among the finite elements adjacent to the interfaces and do not affect the results. For mode II damageable interfaces the values $t_n^0 = 80$ MPa and $t_s^0 = 0.8$ MPa were adopted; t_n^0 is an arbitrary high value, never reached upon the structure, while t_s^0 is the shear stress occurring when at least one point in the structure reaches yielding. I followed the hypothesis (Gupta, Krauss et al. 2013) that heterogeneity, due to progressive mode II interface damage, starts occurring in correspondence of the yielding point. I imposed this condition by choosing as shear traction peak value, the maximum shear stress, recorded in a generic point of structure, which occurs when at least one finite element reaches the yielding stress prescribed by the material model used for the

simulations ($\sigma_y \approx 46$ MPa, which is the yield point observed experimentally for antler in Gupta et al. (Gupta, Krauss et al. 2013). The damage initiation values t_n^0 and t_s^0 were chosen such that mode I interfaces are never damageable, while the mode II interfaces could be either damageable or not. Therefore, I adopted a maximum stress criterion for the onset of damage (**Equation 6**) where damage initiates when the maximum ratio between the traction values at the interface ($<t_n>$, t_s) and the peak values (t_n^0 and t_s^0) reaches the value of one. The symbols <> represent the Macaulay brackets that are used to mean that a compressive traction does not initiate the damage.

$$max\left\{\frac{t_n}{t_n^0}, \frac{t_s}{t_s^0}\right\} = 1 \qquad (6)$$

The values $K_{nn} = K_{ss} = 100$ MPa were used as stiffness coefficients for both mode I and mode II interfaces. The choice of K_{nn} for the mode II interface and K_{ss} for the mode I interface has no effect on the results. The response of the system was then expected to be mainly affected by K_{nn} for the mode I interface and by K_{ss} for the mode II one. I performed parametric simulations, keeping all the parameters fixed except for K_{nn} for the mode I interface and K_{ss} for the mode II interface. I varied these values between 100 and 300 MPa/µm, with a step of 100 MPa/µm (in total 9 simulations), and I found that when $K_{nn} = K_{ss} =$ 100 MPa/µm the numerical maximum tissue strain matches the correspondent experimental value closely. I chose these coefficients such that both the numerical and the experimental systems achieve the same level of maximum tissue strain. I expressed the coefficients K_{nn} and K_{ss} as K in **Figure 4.1b**, as the figure is representative of a generic mode of fracture. The choice of K_{nn} for

the mode I interface and K_{ss} for the mode II interface is fundamental for the obtained results; in fact it affects not only the deformation of the system but also the hysteretic width of loops in stress-strain curves.

As displacements at failure of the interfaces, the arbitrary high values 10 µm and 3 µm were adopted, respectively for the undamageable interfaces and for the damageable interface. These levels of displacement values are never achieved by the finite elements in these simulations, over the course of the stress and strain range seen experimentally, and are hence selected to make sure that the damage occurs only in terms of stiffness degradation and never of complete failure. Specifically, I assumed that the stresses are always transferred through the interfaces. For damageable interfaces, once the damage initiates, the stiffness follows the degradation law: $K' = (1 - d) K$, where $d \in [0, 1]$ is the damageable variable. The total dissipated energy dissipated (per unit of area) through the process of damage of the interface is the area under the traction-separation curve (represented as G_c in **Figure 4.1b**). In **Table 4.1** the values adopted for the cohesive simulations are schematically summarised.
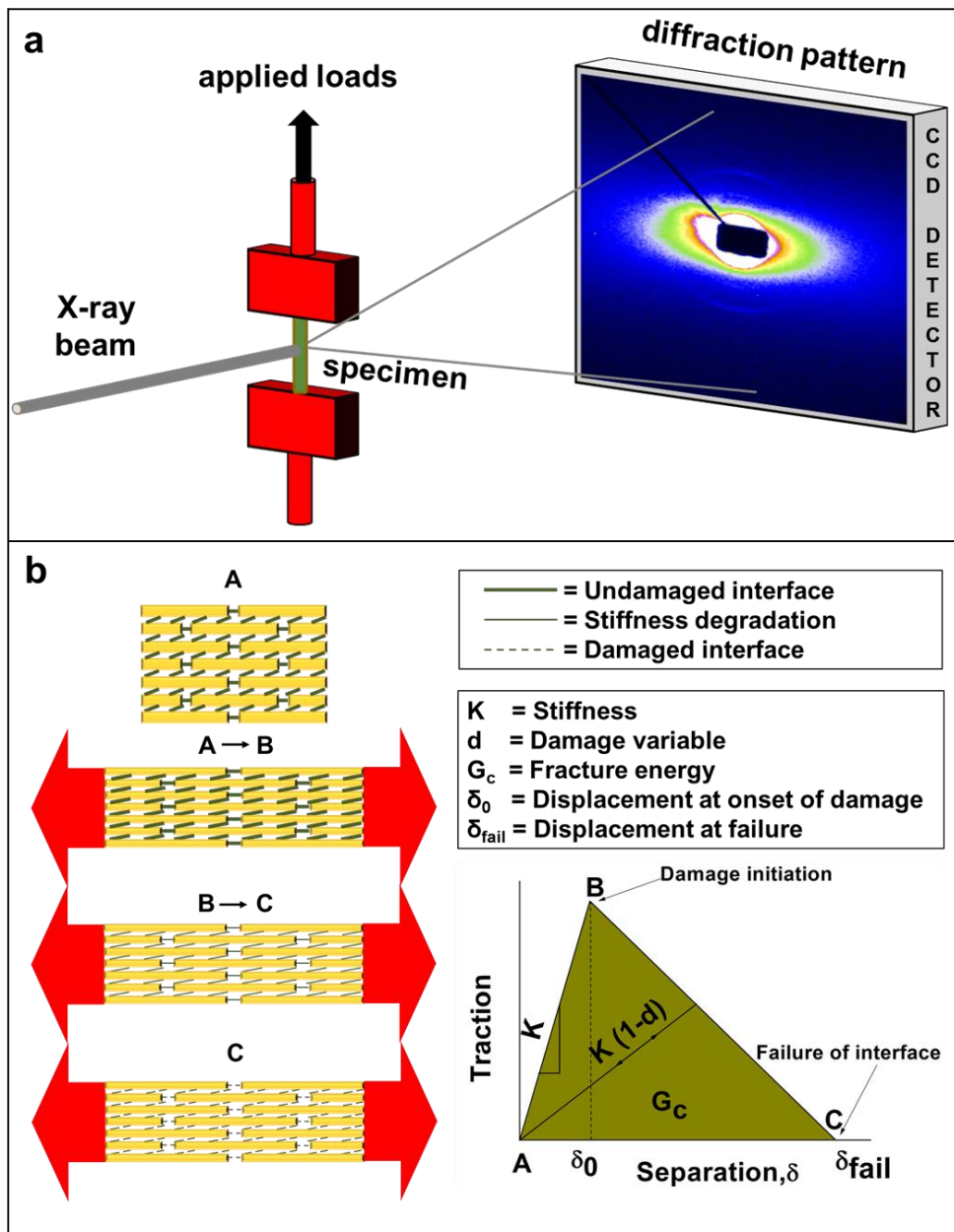
Figure 4.1 - Experimental and numerical methods. *(a) Experimental setup used for experiments at the synchrotron. Mechanical tester design for tensile testing. (b) Staggered fibril structure at the scale of 0.1 - 10 µm with cohesive surface behaviors at the interface. The interfibrillar interface is modeled with a cohesive-traction separation law. A-B: linear stiffness; B: onset of damage; B-C: damage evolution curve characterised by the stiffness degradation coefficient (1-d) K; C: failure of interface.*

	Mode I interface	Mode II undamageable interface	Mode II damageable interface
Elastic constant for fracture mode I: K_{nn} [MPa/μm]	**100**	100	100
Elastic constant for fracture mode II: K_{ss} [MPa/μm]	100	**100**	100
Peak traction for fracture mode I: t_n^0 [MPa]	**80**	80	100
Peak traction for fracture mode II: t_s^0 [MPa]	80	80	**0.8**
Separation value δ [μm]	10	10	**3**

Table 4.1 - Input values for cohesive models used in the FE analyses. Bold fonts indicate the parameters that critically affect the simulations.

The material properties adopted for the fibrils follow a previous model (**Figure 4.2a**) (Gupta, Krauss et al. 2013), with the Young's modulus of 15.8 GPa and the yielding of 46 MPa (**Figure 4.2b**). In other words, the elastoplastic behaviour of a single fibril, and its yield point and stiffness, are taken as a given, and arise from previous experimental work (Wess and Cairns 2005, Gupta, Krauss et al. 2013). Tensile and cyclic static simulations were performed to study respectively the biphasic fibrillar deformation and hysteretic loops in stress-strain curves. The applied loads reproduce the values used for experiments by Gupta et al. (Gupta, Krauss et al. 2013). Uniaxial traction, along the direction 1 (see **Figure 4.2c**), was applied to the top end of the finite element models and fixed support to the bottom end, while right and left sides

were kept unconstrained. In detail, a traction value of 60 MPa was imposed for the static tests and a sequence of different traction values for the cyclic tests (43 – 0 - 50 – 0 – 56 – 0 – 60 – 0 – 43 MPa). The uniaxial tissue strain was computed as ratio of the displacement of the loaded edge and the initial length, not by averaging the strain field. This is because the average of the strains over the structure does not account for the deformation of the cohesive interfaces. In fact, since cohesive interfaces are essentially springs, small gaps appear between the fibrils (visible, for example, in **Figure 4.4c**). These gaps are not cracks, but only representative of relative displacements between fibrils. **Figure 4.3** shows the mesh convergence test that was used to validate the adopted mesh.
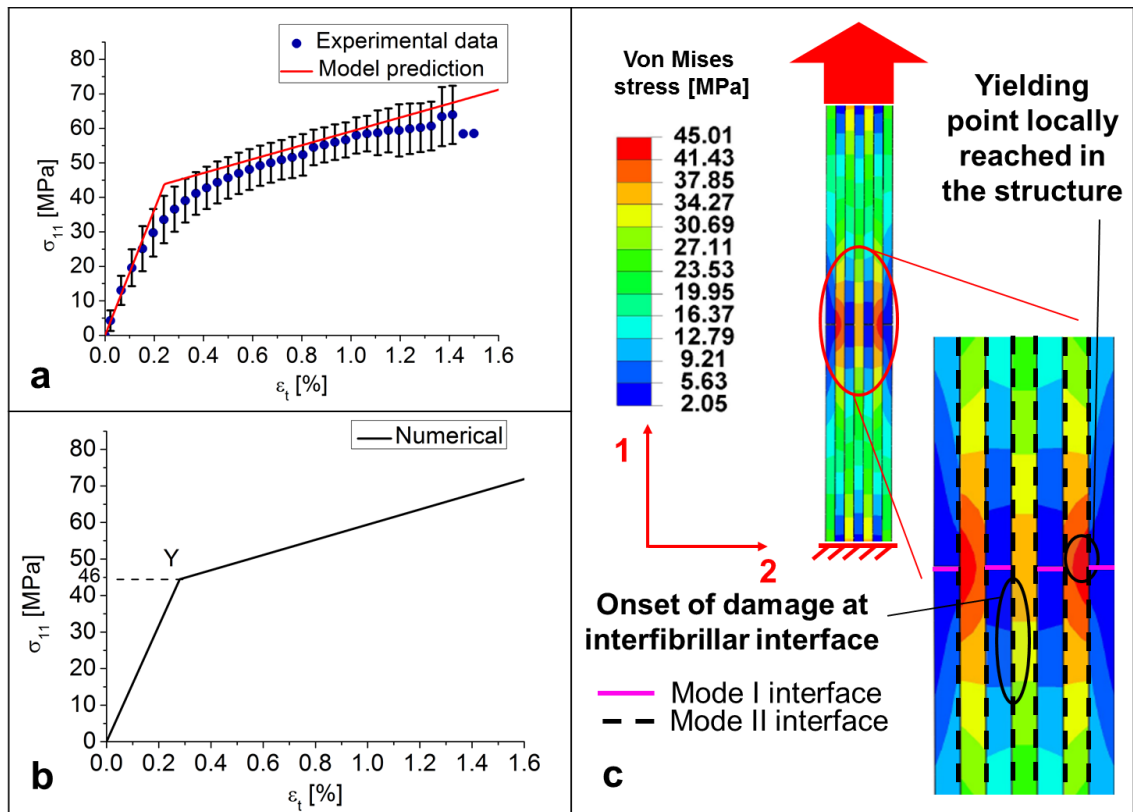
Figure 4.2 - Experimental and numerical fibril stress-strain curves. *(a) Experimental stress-strain curve for antler versus model prediction. Data are averaged from 10 uniaxial stretch-to-failure tests and bars are standard deviations. (b) Material properties input for simulations. (c) Cohesive interface characterization. The interface surrounding the central fibril starts damaging when at least one finite element of the whole structure reaches yielding at 46 MPa (maximum stress criterion).*
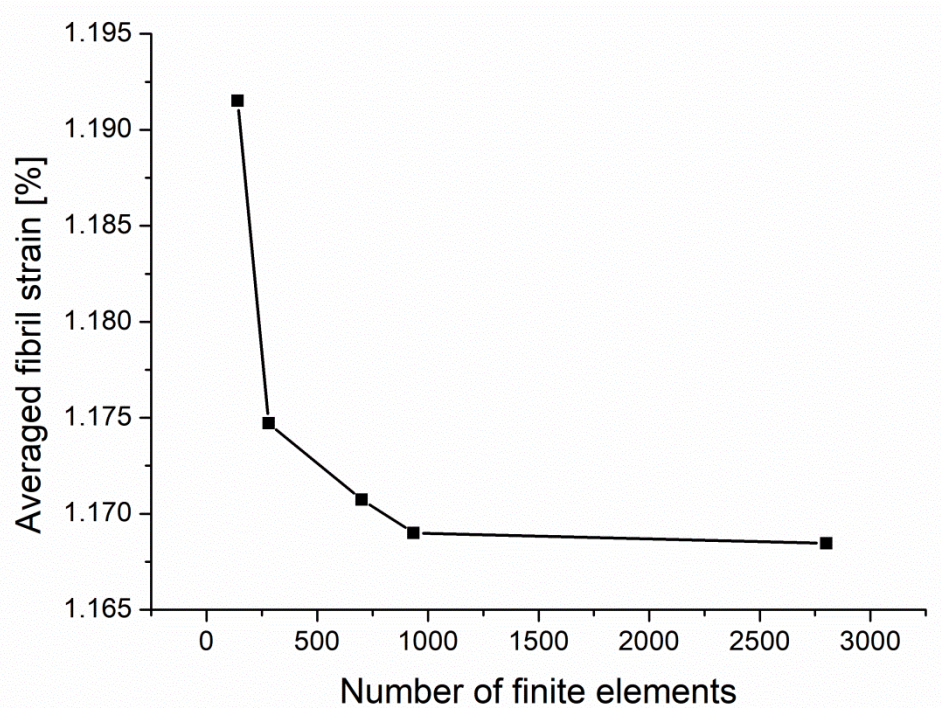
Figure 4.3 - Mesh convergence test for the model that includes damageable interfaces. *The averaged fibril strain was considered for the test. The last value of number of finite elements was used for the simulations (approximately 2800 elements).*

4.3 Results

4.3.1 Biphasic fibrillar deformations

As stated earlier, a main experimental finding in Gupta et al.(Gupta, Krauss et al. 2013) was a biphasic fibrillar deformation. My aim was to understand the role of cohesive interfibrillar surface interfaces in staggered mineralised fibril models, in enabling this behaviour. In this regard the multi-panel **Figure 4.4** shows an overview comparing strain distributions between experimental data and numerical simulations. These will be explored in detail below.

128
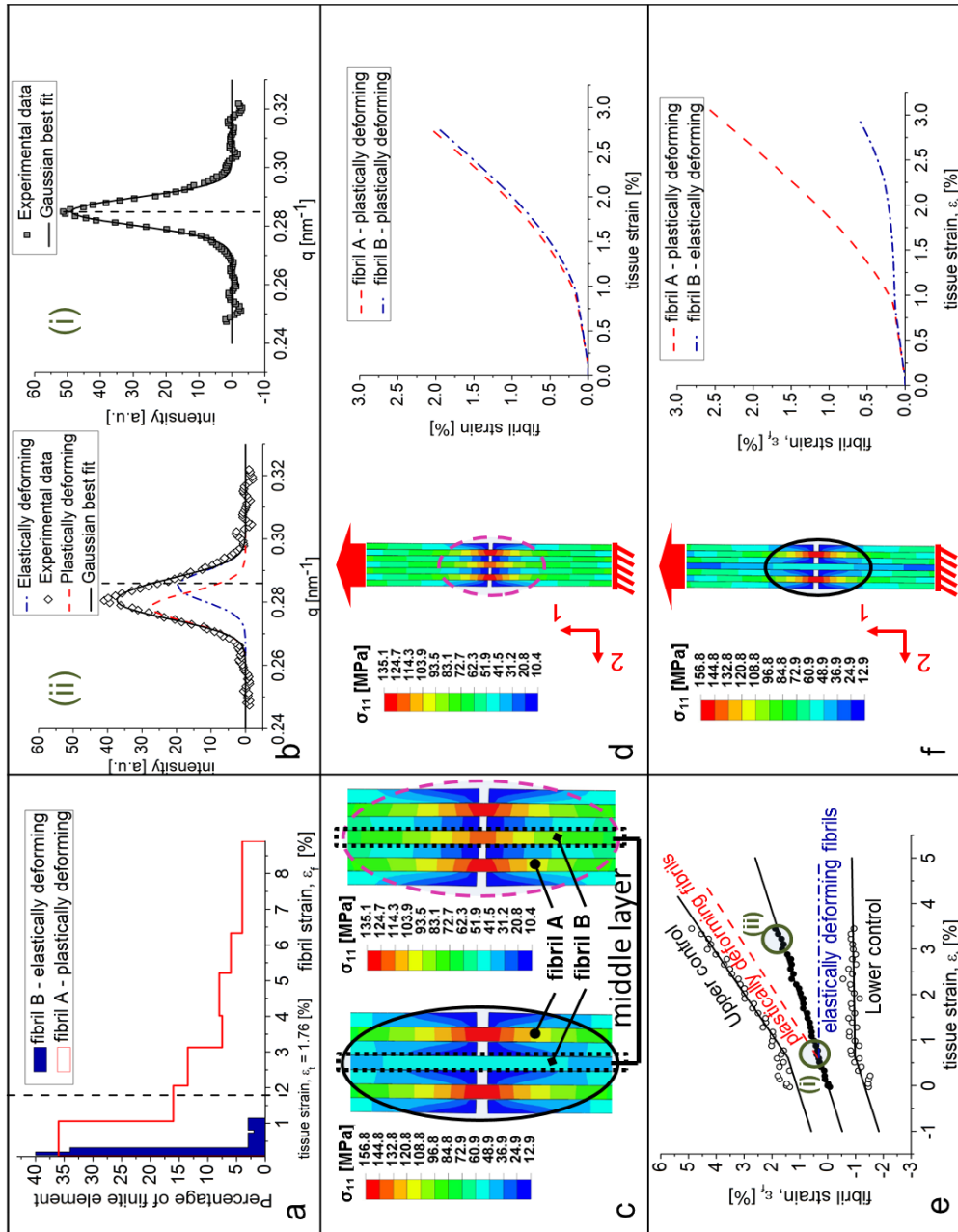
Figure 4.4 - Experimental and numerical fibrillar deformation mechanisms:
(a) Strain distribution for elastically and plastically deforming fibrils for a tissue strain value of 1.76 %. (b) SAXD intensity plots. (i) Tissue strain at the yield value of 0.6 % (highlighted by a circle and the letter (i) in figure c). (ii) Tissue strain at the value of 3.2 % (highlighted by a circle and the letter (ii) in figure c). (c) Stress distributions with and without damageable interfaces. Zoom from figures d and f. (d) Fibril behaviors in presence of undamageable interfaces between fibrils. Fibril b, at the center of the middle layer, deforms plastically. (e) Variation of mean fibril strain (filled circles) and upper and lower control lines plotted against tissue strain. The middle solid line is the linear regression against tissue strain. (f) Fibril behaviors in presence of damageable interface only between the middle layer and the adjacent two layers. Fibril b, at the center of the middle layer, deforms elastically.

129

For the tensile simulations I firstly adopted a non-damageable law for both the mode I and the mode II interfaces, shown previously in **Figure 4.2c**. The results of applied uniaxial traction on the fibrils are shown in **Figure 4.4d**, with relative magnification in **Figure 4.4c**, with both fibrils A and B plastically deforming, as expected. The maximum longitudinal stress (σ_{11}), reached in central region of the fibrils, is 135 MPa in fibril A and 119 MPa in fibril B, while the averaged stresses are respectively 65 MPa and 63 MPa, beyond the yield point.

Secondly, I found that the introduction of damageable mode II interface around the middle layer produces a differentiation of the fibril behavior. The damage of the interface around the middle layer partially 'isolates' fibril B, which is then not able to fully contribute to the load absorption. While fibril A remains elastoplastic in its deformation behaviour, the deformation of fibril B never exceeds the elastic range (**Figures 4.4c-f**). In fact, although the maximum longitudinal stress (σ_{11}), locally measured in a restricted region of fibril B, is 58 MPa (beyond the yield point), its homogenised stress is below the yield point (39 MPa). The corresponding values for fibril A are 157 MPa and 73 MPa respectively. Considering a particular level of macroscopic tissue strain beyond the yield point, such as $\varepsilon_t = 1.76$ % (**Figure 4.4a**), I find that most of the load (86 %) is carried by fibril A whose finite elements are able to stretch up to eight times more than the finite elements in fibril B. For this tissue strain value, the largest deformation in fibril A is $\varepsilon_f = 8.9$ % whilst in fibril B is $\varepsilon_f = 1.2$ %. In addition, the average deformation of fibril A is 0.9 % while for the fibril B the equivalent strain is 0.2 % (below the yield point).

In **Figure 4.4f**, curves show that numerical results are in good agreement with the experimental results shown in **Figure 4.4e,** where a comparison between experimental results and model predictions, developed by Gupta et al. (Gupta, Krauss et al. 2013), is presented. In particular, the figure includes the upper and lower control lines ($\varepsilon_{f,\pm 25\%}$), the best fit linear regression against tissue strain (middle solid line), and the model predictions for both the elastically deforming fibril (blue dash-dotted line) and the plastically deforming fibrils (red dashed line). In **Figures 4.4f-e**, the elastic and plastic patterns are clearly observable, as also demonstrated by the experimental results in **Figure 4.4b**, where the SAXD intensity plot (**Figure 4.4b(i)**) shows that all the fibrils are elastic at the yielding point (tissue strain = 0.6 %), while for a tissue strain of 3.2 % (**Figure 4.4b(ii)**) the coexistence of plastic and elastic fibrils occurs, with 58% of fibrils at ε_f = 2.95 % (plastic strain) whilst the remainder fraction at ε_f = 0.53% (elastic strain).

4.3.2 The role of mode II interfaces in cyclic loading
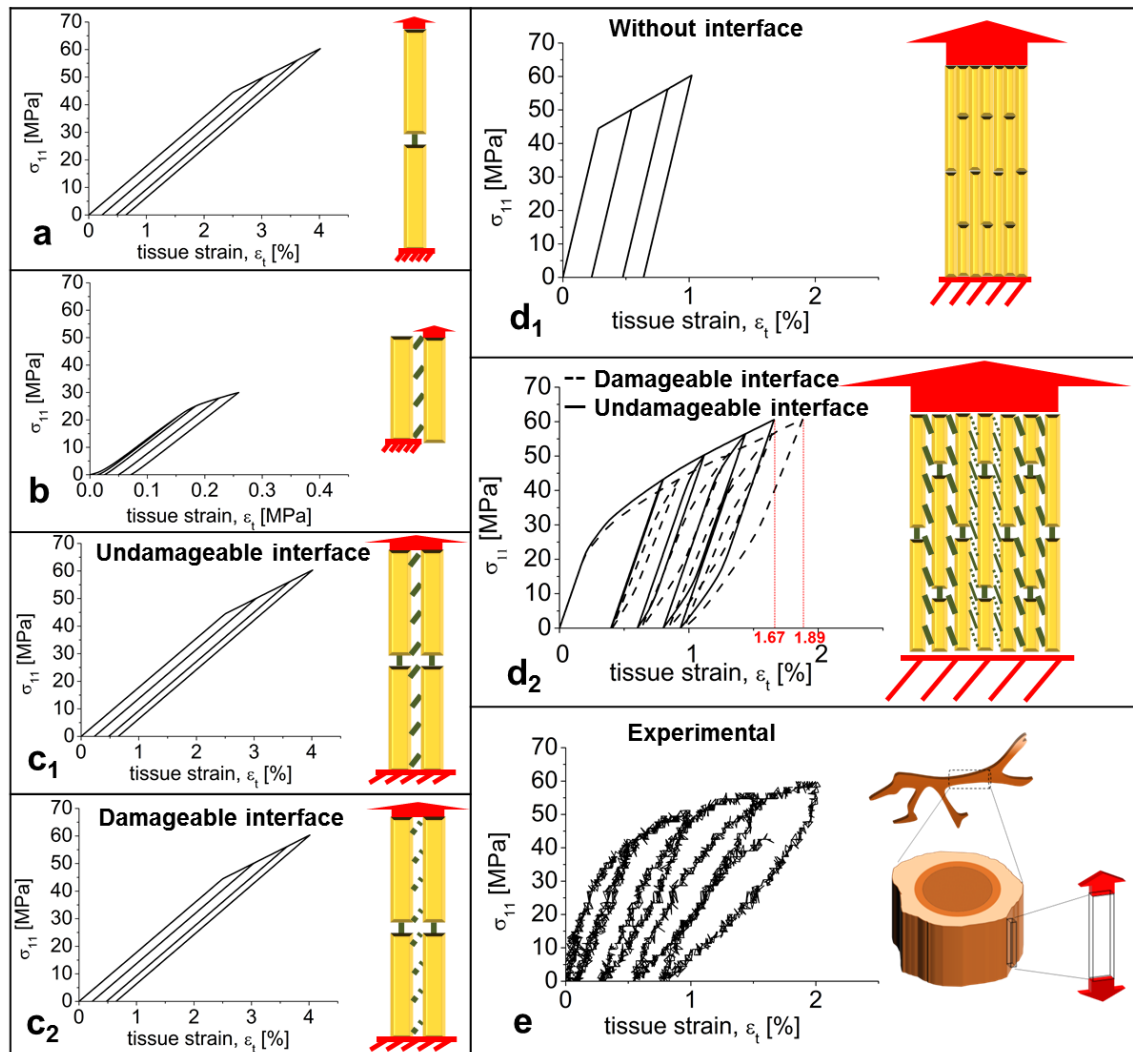
Figure 4.5 - Cyclic loading in different fibrillar geometries: Comparisons between numerical (figures a, b, c₁, c₂, d₁, d₂) and experimental results (Figure e). *(a) Two fibrils model with 'mode I' non damageable interface. (b) Two fibrils model with 'mode II' non damageable interface. (c₁) Four fibrils model with 'mode I' and 'mode II' non damageable interfaces, in aligned configuration. (c₂) Four fibrils model with 'mode I' non damageable interface and 'mode II' damageable interface, in aligned configuration. (d₁) Seven layers model without interfaces, in staggered configuration. (d₂) Comparison between two seven layers models in staggered configuration: damageable mode II interfaces at the middle layer versus undamageable ones. (e) Experimental results for cyclic loading on antler.*

A second main finding in Gupta et al. (Gupta, Krauss et al. 2013) was the existence of hysteresis at the fibrillar level. The elasto-plastic behaviors of a set

of different models under cyclic loading were simulated to discover the combined effects of fibril lateral arrangement and architecture, coupled with the interface types described in the previous subsection. I found that the experimentally observed hysteresis in the cyclic loading curves occurs when staggered fibril arrangement is coupled with mode I and mode II cohesive surface interfaces. In fact, the presence of only mode I or mode II interfaces for, respectively, a system of two aligned or two-column fibrils is clearly not responsible for hysteresis (**Figures 4.5a-b**). These effects do not arise from the limited number of fibrils considered: an increase in number of fibrils from two to four, in a condition of non-overlap, results in no hysteresis with both damageable and undamageable mode II interfaces (**Figure 4.5c1-c2**). As fibrils do not transmit load through shearing in the configurations shown in **Figures 4.5c1-c2**, no difference between damageable and undamageable mode II interface is observed. From this set of simulations, it was observed that only the concurrence of staggered fibril arrangement and cohesive surface interface (not necessary damageable) leads to hysteresis in loading/unloading stress strain curves (**Figure 4.5d2**). It can be seen from **Figure 4.5d1** that staggered but perfectly bonded fibrils (no cohesive interface) do not exhibit hysteresis and loading/unloading patterns perfectly overlap. The introduction of damageable mode II interfaces makes the structure more deformable. Indeed, as fibrils, in staggered configuration, transmit loading through shearing, damageable and then weaker mode II interfaces allow the whole structure to deform up to 1.89 %, while in a condition of non-damageable interfaces the tissue strain reaches the value of 1.67 % (**Figure 4.5d2**) at the same stress level of 60 MPa.

Numerical results for the cyclic loading curves are in very good agreement with experimental data (comparisons in **Figures 4.5d2**-**e**). Maximum tissue strains, in both cases, are about 1.9 % and furthermore, the structural yielding points occur at tissue strain ≈ 0.22 % and axial stress ≈ 25 MPa, earlier than the corresponding prediction in the material law (Gupta, Krauss et al. 2013) used for simulations.

This study shows how combination of finite elements simulations at fibrillar level, combined with experimentally derived information on ultrastructural plasticity of the fibril, enables the development of a model for the mechanical behaviour of antler under cyclic loading conditions which can explain both the energy dissipation (via hysteresis) as well as the concurrent heterogeneous pattern at the nanoscale. In addition, as shown in **Figure 4.6**, my parametric simulations allow me to conclude that the combination of:

a. staggered fibrillar configuration and damageable mode II interface leads to hysteresis and fibrillar heterogeneity;

b. staggered fibrillar configuration and undamageable mode II interface leads to hysteresis and fibrillar homogeneity;

c. aligned fibrillar configuration and perfectly bonded boundary conditions (without cohesive behaviors) at the interfaces leads to no hysteresis and fibrillar homogeneity.
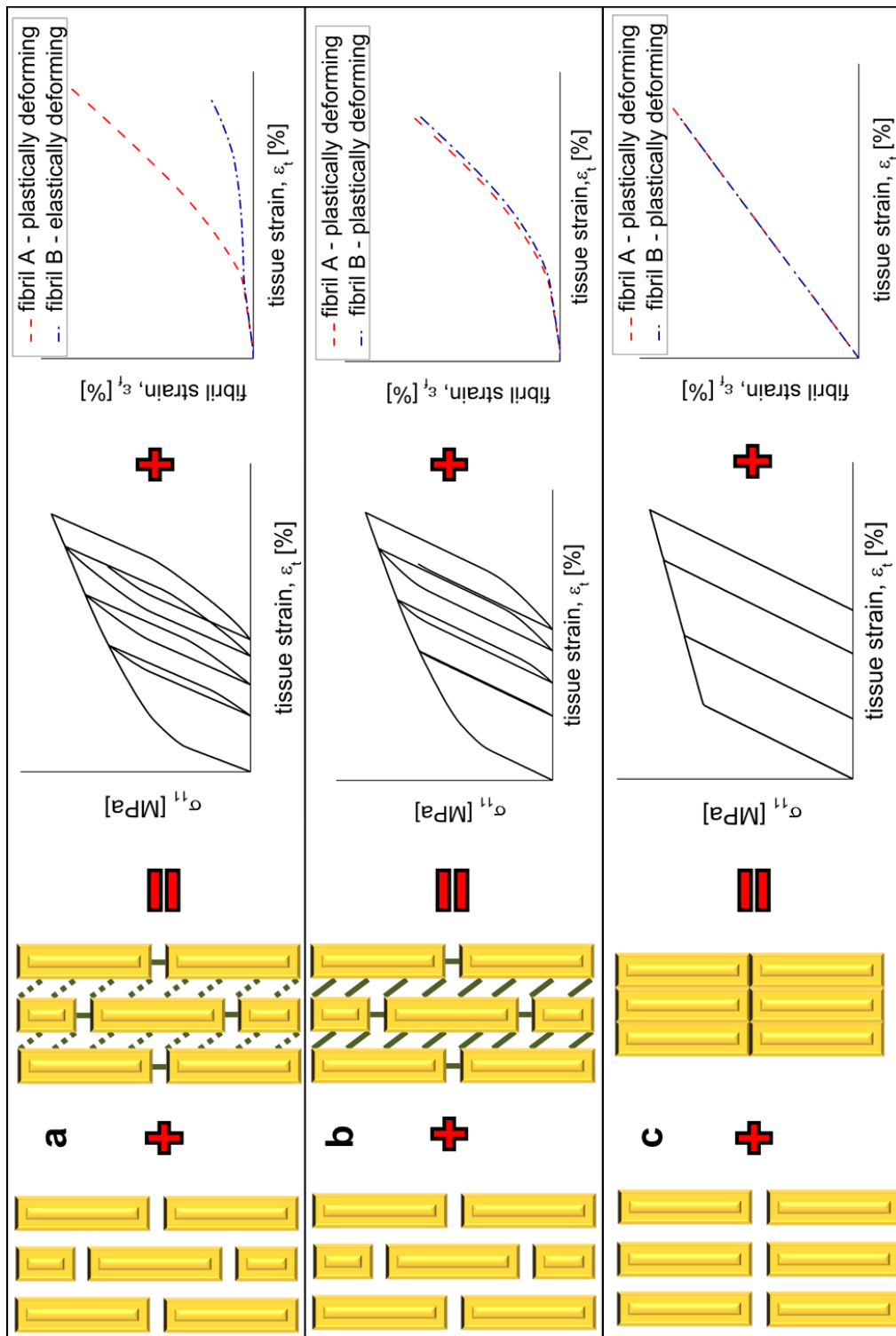
Figure 4.6 - Summary of main results. *(a) Staggered fibrillar configuration and damageable mode II interface are responsible for hysteretic stress strain curve and heterogeneous fibrillar deformation. (b) The inclusion of staggered configuration and undamageable interface leads to hysteresis and homogeneous fibril deformation. (c) Aligned fibrillar configuration and no interface lead to no hysteresis and homogeneous fibril deformation.*

In addition, the effect of different levels of overlap between staggered fibrils and different cohesive laws was investigated in the following sections.

4.3.3 Parametric studies of fibrillar overlaps and cohesive laws

A set of parametric simulations was performed to verify the influence of overlap between fibrils in staggered configuration and the effect of different cohesive laws for the damageable interfaces. Simulations prove that in both cases, with and without damageable interfaces, the staggered structure becomes more deformable (**Figures 4.7a-b**) as the overlap between fibrils at adjacent layers reduces from half to $1/8^{th}$ of the basic fibril length (see **Figure 4.7f** for the representation of overlap levels). It is also interesting to notice that the hysteretic loop widths decreases as the overlap decreases (**Figures 4.7c-d**). Furthermore, simulations show the relative insensibility of the results to the specific damage cohesive evolution laws. In fact, linear and exponential damage evolution laws with different displacement at failure values were tested and only slight differences (less than 5%) in the fibrillar behaviour were found (**Figure 4.7e**).
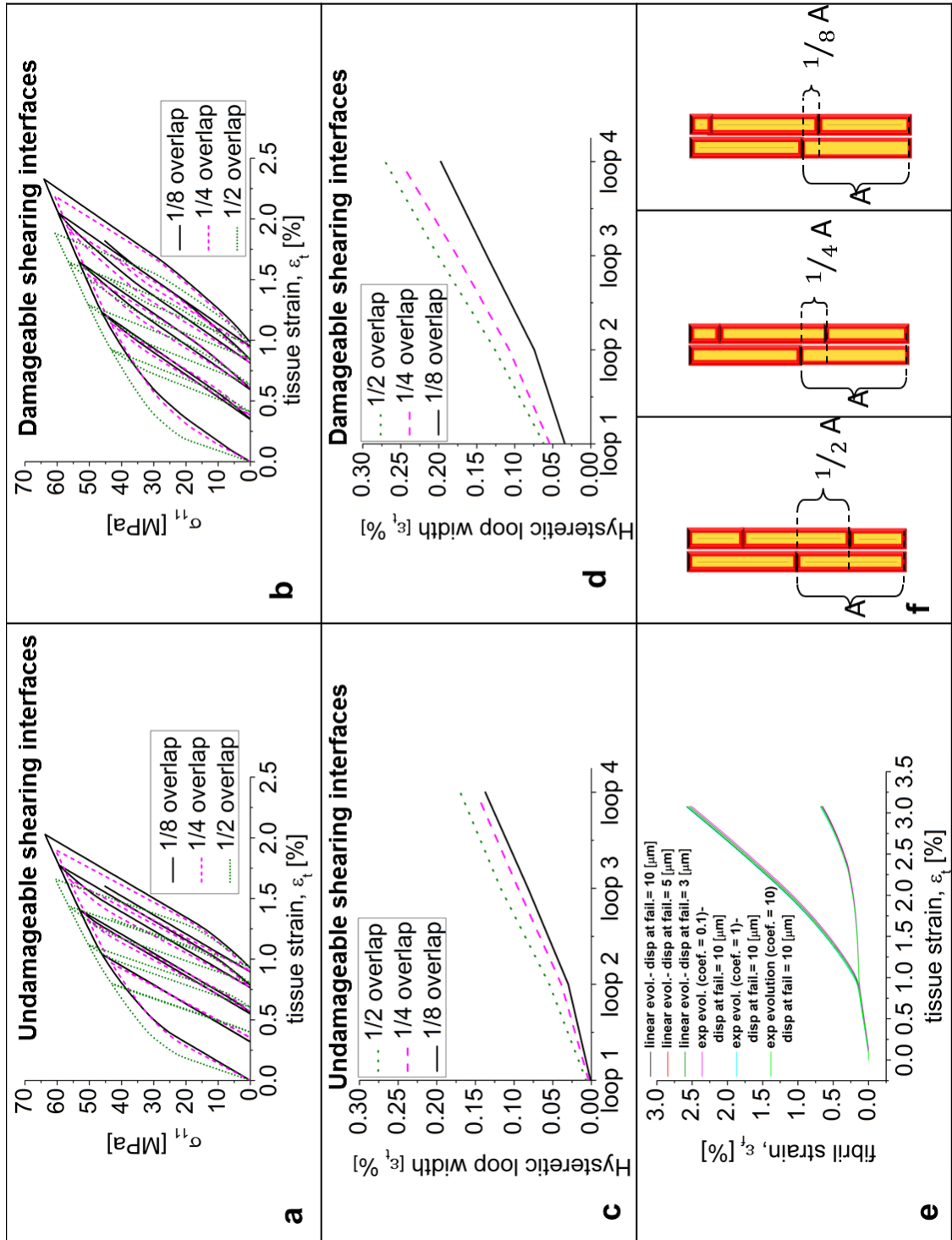
Figure 4.7 - Parametric simulations. *(a, b) Cyclic simulations for (a) undamageable interfaces and (b) damageable interfaces (only between the middle layer and the two adjacent ones) for different levels of overlap between fibrils at adjacent layers. (c, d) Increase in hysteretic loop width. (e) Results for different damage evolution laws describing the damageable interfaces. (f) Levels of overlap considered for simulations.*

4.3.4 Effects of interfaces on fibrillar stress distribution

The introduction of damageable interfaces is responsible for heterogeneity and stress redistribution within the staggered structure. In fact, simulations demonstrated that when fibrils at the middle layer (fibrils B) are embedded in damageable shearing interfaces, their capability of carrying loads reduces drastically compared with the predictions of the model where the interfaces are undamageable (60% less, in terms of maximum positive stress achievable) (**Figures 4.8a-b**). It is also observable that at the end of each unloading step, in the damageable-interfaces configuration (**Figure 4.8a**), fibril A undergoes compression (labelled by semi-transparent circle) while fibril B remains in tension. Instead, when the shearing interfaces are undamageable (**Figure 4.8b**), both types of fibrils result unloaded at the end of each unloading steps (at seconds 2, 4, 6 and 8).
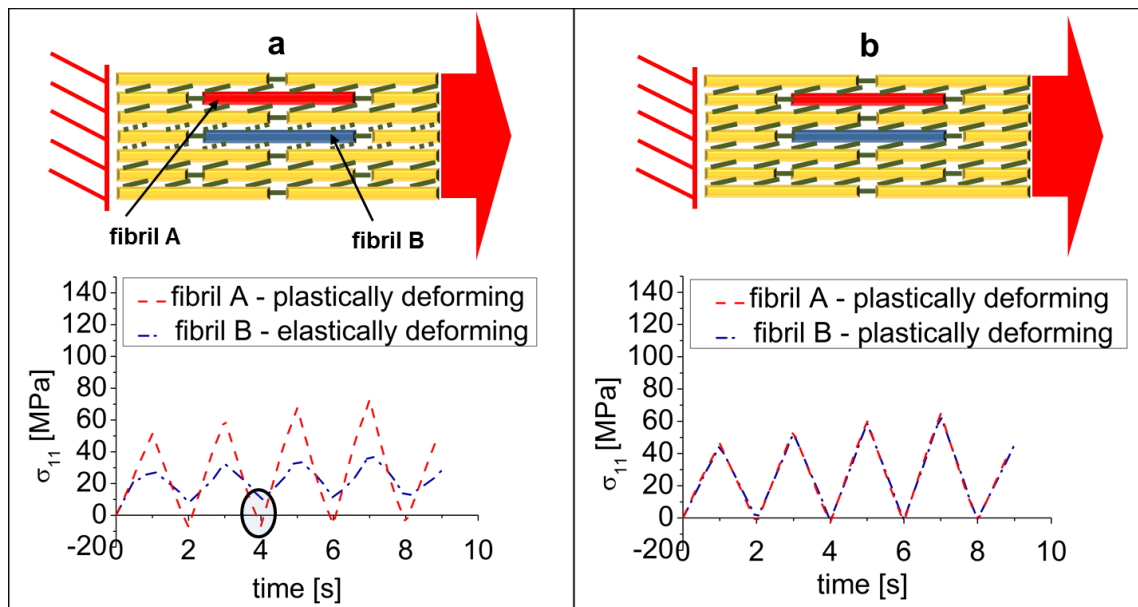
Figure 4.8 - Numerical stress variation in time for fibril A and B, when the interfaces surrounding the middle layer are (a) damageable or (b) undamageable.

4.4 Discussion and conclusion

Elastic deformation in bone at the nanoscale has been extensively studied (Jäger and Fratzl 2000, Ji and Gao 2004, Nikolov and Raabe 2008, Hamed, Lee et al. 2010, Bar-On and Wagner 2013) via multiscale fibre composite models that often treat bone material as a two-scale hierarchical composite; mineralised fibrils are arranged in a staggered manner, and fibrils themselves consist of mineral platelets staggered in a collagen matrix phase. Such models are usually validated by comparing the tissue-level modulus predictions to experimentally determined stiffness, though in an ideal scenario predictions of deformation and stress at multiple levels would be calculated and compared to experiment.

In the area of structural models for inelastic and damage accumulation in bone and antler, there are no modeling attempts for the structural response of the nanoscale material under cyclic loading. To fill this gap, here I proposed a model based on surface cohesive behavior. The main assumptions are to neglect the material properties of the interfibrillar matrix and to consider the fibrils linked by cohesive surfaces whose damage process occurs in terms of stiffness degradation. Previously, cohesive behaviour was used for studying the damage mechanisms of bone at different scales (Ural 2009, Mischinski and Ural 2011, Hamed and Jasiuk 2013, Lai and Yan 2017, Lin, Samuel et al. 2017). This approach, on the contrary, is based on cohesive stiffness representative of interfaces with negligible small thicknesses. The main difference between the two approaches is that in surface-based laws the damage evolution describes the degradation of the cohesive stiffness whereas in the continuum-based approach (Ural 2009, Mischinski and Ural 2011, Hamed and Jasiuk 2013, Lai

and Yan 2017, Lin, Samuel et al. 2017) the damage concerns the degradation of the material stiffness. The continuum model, called also cohesive zone model, can be used to analyse both interface and bulk fracture. For example, Hamed and Jasiuk (Hamed and Jasiuk 2013) created a multiscale model for studying the mechanisms of damage in bone and used the cohesive zone for modelling the fracture of the interface between collagen and hydroxyapatite platelets but also the fracture inside the fibrillar components. They found that the mesh size of cohesive elements had a significant effect on the strength of the mineralised fibrils. A recent study (Lai and Yan 2017) investigated the evolution of damage in staggered array of mineralised collagen fibrils (MCF) embedded in extrafibrillar protein matrix modelled by continuum cohesive finite elements. The authors found that the failure mechanisms of the extrafibrillar matrix play a dominant role on the energy dissipation capacity of the system. Lin et al. (Lin, Samuel et al. 2017) recently provided evidence as to the importance of the extrafibrillar matrix, considered as composite of hydroxyapatite crystals embedded in an interface modelled by cohesive finite elements, in the pre-yield deformation and failure mode of bone. They found that a tough interface provokes ductile deformation of matrix, as in the case of wet bone, whereas a brittle interface causes brittle deformation, as in dry bone.

Hysteresis, at higher scales in bone, has been found in experiments, but relatively few bone-specific models exist. Ascenzi et al. (Ascenzi, Benvenuti et al. 1985) tested single osteons and found hysteresis loops under tension. They discovered that the collagen orientation is the main factor to determine the features of hysteresis loops. In both, the presented experimental results and in other references such as Ascenzi et al. (Ascenzi, Benvenuti et al. 1985), the

width of hysteretic loops tends to increase as the applied stress increases. In terms of modelling of the hysteresis loop width, the work of Evans and co-workers, who carried out modelling and numerical analysis of ceramic matrix composite deformation (Vagaggini, Domergue et al. 1995), is relevant, although their model is applied to a different class of materials. They derived expressions for which the maximum hysteresis loop width depends on the Young's modulus of both, the fibrils and the matrix, the fibril radius and the fibril volume fraction, but also on the stress conditions, such as the maximum stress reached in the system. At lower scales an analytical model explained the inelastic response of bone (Mercer, He et al. 2006), indicating stress/strain hysteresis in loading/unloading tests. In their model, the authors found the shear yielding of the interface between collagen fibrils and mineral platelets to be the cause of irreversible slip and then of hysteresis. Hysteresis, in the presented staggered fibrillar models, is due to the presence of cohesive surface interfaces and in detail, to zones of stress concentration. In fact, I found that, once stretched or released (null surface traction applied to the structure) finite elements of the horizontally adjacent fibrils (fibrils on the same layer) are under-loaded, while finite elements of the underlying fibrils are over-loaded (**Figure 4.4c**). This mechanism of stress concentration combined with the plastic material properties result in hysteretic behavior of the system.

The simulations I showed in this chapter were run with a quasi-static approach. This means that the inertial forces were not considered for the calculations of the equilibrium conditions (equilibrium between external and internal forces). Indeed, no value of material density was defined as input for the simulations. Therefore, the cyclic loading conditions were achieved by imposing a

succession of steps (with the loading advancing in time), each of them starting from the final stress/strain conditions achieved by the previous step. This approach allowed to reduce drastically the computational time (less and simpler equations to solve) and to focus on the static behavior of the analysed staggered systems rather than on their dynamic one. However, it is known (Doghri 2013), (Gere and Goodno 2001) that inertia plays a dominant role in high-speed events, such as impacts or high strain-rate loads (Hight and Brandeau 1983). Therefore, in the future it would be interesting to further develop my model by keeping the same geometries and verifying the effect on the mechanical properties and on hysteretic loops of inertial forces (especially in the zones where gaps between fibrils arise).

The second finding regards heterogeneous fibrillar deformation caused by partially damageable interfaces. Heterogeneity in the behaviors of mineralised tissue was detected as a mechanism contributing to energy dissipation (Fantner, Hassenkam et al. 2005, Tai, Dao et al. 2007). Mechanical properties of individual mineralised collagen have been only recently analyzed thanks to the development of innovative experimental techniques. While the fibrillar structure of collagenous tissues was explored extensively during the last decades (for a review see (Wess and Cairns 2005)), only more recently have their mechanical properties been determined experimentally (Shen, Dodge et al. 2008, Hang and Barber 2011). Heterogeneity in fibrillar deformation were found in antler cortical tissue by Krauss et al. (Krauss, Fratzl et al. 2009) by using a time-resolved synchrotron small angle X-ray diffraction technique, coupled with tensile testing. They found that heterogeneity in fibrillar deformations starts after the macroscopic yielding. Hang and Barber (Hang and Barber 2011) performed

tensile testing on individual fibrils from antler using atomic force microscopy and scanning electron microscopy. They found heterogeneous deformations in fibrils showing either yield or strain hardening. The structural mechanism for interfacial failure between fibrils may involve the breakage of sacrificial bonds in the noncollageneous proteins found in the interfibrillar matrix (Fantner, Hassenkam et al. 2005). These weak calcium mediated bonds within and between proteins such as osteopontin or osteonectin have been proposed to play a significant role in bone toughness (Gupta, Fratzl et al. 2007, Thurner, Chen et al. 2010) Recently, Poundarik et al. (Poundarik, Diab et al. 2012) proposed a mechanism of clusters of extrafibrillar mineral held together by non-collagenous protein glue. Under deformation, this model generates an inhomogeneous strain and stress pattern at the fibrillar level. While I found, instead, that damageable mode II interfaces are responsible for heterogeneous strain fields, the structural origin of such damage may involve mechanisms as proposed by Poundarik et al. (Poundarik, Diab et al. 2012) . In detail, fibrils surrounded by damageable interfaces behave elastically while other fibrils reach higher stress values after yielding. At lower scales, Buehler (Buehler 2007) found the existence of a range of adhesive energy values between molecule ($0.01 - 1$ J/m^2) which optimises the toughening mechanisms. Following this concept of optimization, a possible application of my model may be a parametric approach to evaluate the types of mechanical behaviors of interfaces which lead to optimised toughness. It must be remarked that in the presented models, I consider damage only as stiffness degradation of cohesive surfaces and not as failure and that I use a 2D model. In terms of multiscale modelling of toughness, the current model will allow one to homogenise the properties at the fibrillar scale and these homogenised properties could be

inserted into a larger-scale 3D model for the study of crack propagation and damage in real antler.

In conclusion, by constructing a finite element model for the inelastic cyclic loading response of mineralised collagen fibrils in antler, I show that the hysteresis observed is due to interfibrillar staggering leading to inhomogeneous stress fields along the fibril and localised intrafibrillar plasticity, while the inhomogeneous deformation arises from the weak interfaces between fibrils, potentially mediated by sacrificial bonds in the noncollageneous proteins between fibrils.

5 Towards in situ determination of 3D strain and reorientation in the interpenetrating nanofibre networks of cuticle

The experimental sections and the experimental results that I describe in this Chapter were performed by my two coworkers Dr. Himadri Gupta and Dr. Yi Zhang.

5.1 Introduction

In the design of advanced functional composites, a key characteristic is the assembly (either via self-organization or guided deposition) of sub-micron elements such as nanowires or nanofibres into a hierarchical and ordered system at multiple length scales between the molecular and microscopic levels. These include mineralised collagen fibrils in bone (Zimmermann, Gludovatz et al. 2013) ordered calcite nanocrystals in hierarchical clay nanocomposites (Bafna, Beaucage et al. 2003, Chu, Chen et al. 2014) ordered 2D materials inside 3D bio-mineralised materials (Giosia, Polishchuk et al. 2016) mechanically high performance polymer/nanoclay composites (Galgali, Agarwal et al. 2004) oriented TiO_2 nanocrystals assemblies for photo-catalysis (Chen, Cao et al. 2015) and semiconductor nanocrystals in superlattices (Boneschanscher, Evers et al. 2014). The precise orientation, strain and structure of the nanoscale inclusions in such systems is a crucial determining factor in enabling function and influencing a diverse range of designed material properties, including mechanics (Yang, Chen et al. 2013, Naleway, Porter et al. 2015, Giosia, Polishchuk et al. 2016) catalytic performance or semiconductor performance (Boneschanscher, Evers et al. 2014). In this regard, advances in

X-ray techniques including scanning nano-diffraction, ptychography and coherent X-ray diffraction have been applied to determine the strain, shape and texture of individual nanoparticles or composite aggregates (Keckes, Bartosik et al. 2012, Yang, Huang et al. 2013, Chamard, Allain et al. 2015).

However, an implicit assumption of much current X-ray scanning microprobe and *in situ* methods is a neglect of the depth dimension in the analysis of 2D diffraction maps. The 2D X-ray diffraction pattern obtained is a slice through the 3D reciprocal space intensity distribution (Warren 1990). This limits the application of most such methods to simple in-plane geometries or sections or special materials such as collagen fibrils with an ordered periodic structure at the nanoscale, while in most real-life systems, the 3D morphology may have no particular symmetry or alignment to sample shape. While recent innovative methods like 3D small-angle X-ray scattering (SAXS) tomography and white-beam X-ray diffraction (Grünewald, Rennhofer et al. 2016), which reconstruct 3D reciprocal space intensity in a model-free manner, circumvent this 2D limitation, these methods have limitations for *in situ* studies. SAXS tomography can take several hours of synchrotron time per reconstruction (Liebi, Georgiadis et al. 2015), and the white beam analysis requires several minutes with a specialised energy-dispersive detector (Grünewald, Rennhofer et al. 2016) or scanning the photon energy. 3D X-ray structural microscopy uses polychromatic radiation to measure grain orientation and strain in functionally graded materials and composites, but requires sample rotation (Poulsen 2004). Indeed, the *in situ* dynamics of the nanoscale inclusions can follow a complex and non-predetermined path of coupled rotation, stretching and phase transformation in 3D, and requires time-resolutions of the order of seconds or below, and do not

readily allow steps such as sample-rotation or energy scanning at each step of the process (Larson, Yang et al. 2002, Liebi, Georgiadis et al. 2015). Further, methods such as ptychography are suited for scanning with high (a few tens of nanometres) resolution to obtain structure information, but are also comparatively time consuming due to overlapping scans and are therefore not suited for *in situ* studies of samples in the millimetre size range (Chamard, Allain et al. 2015). There is therefore a significant need for multiscale 3D reconstruction methods for *in situ* nanoscale mechanics. This need is especially relevant for biological and bio-mimetic composites, where the hierarchical architecture leads to complex, multi-dimensional motifs (Naleway, Porter et al. 2015).

A prototypical example of such a multiscale bio-composite (**Appendix B**, **Figure A.1**) is the crustacean cuticle (Vincent and Wegst 2004, Nikolov, Petrov et al. 2010). At the nanoscale, the cuticle may be considered a three-phase composite of ~3 nm diameter chitin fibrils, crosslinked amorphous proteins and biogenic mineral (calcium carbonate), along with water. The mineralised fibrils aggregate into fibres at the scale of ~100 nm, which in turn form a characteristic continuous rotated layered plywood structure at the scale of ~10 μm, known as the Bouligand motif (**Figure 2.4 and Figure 2.15**) (Bouligand 1972). A network of pore canal fibres run perpendicular to these Bouligand layers, forming an interpenetrating network of nanofibers which has been likened to a honeycomb structure (Nikolov, Petrov et al. 2010). This structural motif has evolved into a range of functional specializations, from impact resistant exoskeletons like the dactyl and telson in the mantis shrimp, to hyper-extensible appendages for laying eggs (Havemann, Müller et al. 2008) to specialised sensory organs in

spiders (Erko, Younes-Metzler et al. 2015). In particular, the exoskeleton of the mantis shrimp has attracted considerable recent attention, due to its ability to resist high rate, repetitive loading with no structural damage serving as a template for bio-inspired composites (Patek and Caldwell 2005, Taylor and Patek 2010, Weaver, Milliron et al. 2012, Amini, Masic et al. 2014, Grunenfelder, Suksangpanya et al. 2014). While multiscale modelling studies of the (lobster) cuticle exist, suggesting that much of the variation of mechanical properties arises due to structure at the microscale and above (Nikolov, Fabritius et al. 2011), there is little direct experimental *in situ* evidence of the nanoscale and microscale mechanisms in crustacean cuticle.

In this chapter, my coworkers and I developed and apply an *in situ* multiscale X-ray diffraction/modelling scheme to determine the nanoscale and microscale deformation mechanisms in crustacean cuticle. By modelling the crustacean cuticle extracellular matrix as two interpenetrating fibre-lamellate structures at the sub-micron scale, the 3D X-ray diffraction intensity distributions from these fibres using an asymptotic integral approach was predicted(Bender and Orszag 1999). Under mechanical load, these distributions will alter in a manner dictated by the coupled effects of strain at the nanoscale along with 3D deformation and reorientation at larger scales. This work shows how, by modelling the fibre-level stress and strain fields by matching lamination theory to the experimental X-ray peak shifts (Hull and Clyne 1996) and subsequently accounting for larger mesoscale (> 10 μm) deformations at the scale of lamellae and interpenetrating fibre distributions, the *in situ* nano- and microscale mechanics of crustacean cuticle can be determined with high precision. This approach – solely relying on the existence of fibre symmetry at the molecular level – is designed to apply to

in situ studies of the structural dynamics of nanoscale inclusions in advanced multiscale functional materials, provides both mechanical strain as well as structural reorientation, and can be carried out using standard 2D X-ray detectors or lab-setups.

5.2 Ultrastructural Model and Experimental Results

To enhance the predictive power of mechanical models of bio-materials, not only do the models have to be improved, but also new experimental data needs to be matched to model predictions at multiple hierarchical levels. Experimental techniques, such as in situ tensile testing during synchrotron X-ray diffraction experiments can be used to characterize crustacean cuticle at multiple hierarchical levels from the nano- to the mesoscale (tissue level). A methodology to incorporate systematically the data acquired with this technique into a multiscale model of cuticle mechanics needs to be developed. Here, I propose such a model (including nano- micro-and meso-scale) based on the laminate theory to compute the mechanical properties and strain distributions in the plywood structure of the cuticle under tensile loading. In addition, a new approach is proposed to calculate fibre reorientation based on the shear strain that each sub-lamella bears under a unidirectional external tensile load.

5.2.1 Lamination theory

The mechanical response of the mantis shrimp's cuticle was investigated by using a combination of rules of mixtures (Voigt and Reuss models) and the expressions of the lamination theory (Berthelot 2012). Firstly, the Voigt rule of mixture was used to estimate the material properties of fibril and matrix within

the cuticle (**Equations 7-12**). In **Table 5.1** the symbols used for the following equations are explained.

$$E_f = E_{ch}\varphi_{ch} + E_{prf}\varphi_{prf} \tag{7}$$

$$\nu_f = \nu_{ch}\varphi_{ch} + \nu_{prf}\varphi_{prf} \tag{8}$$

$$E_m = E_{acc}\varphi_{acc} + E_{prm}\varphi_{prm} \tag{9}$$

$$\nu_m = \nu_{acc}\varphi_{acc} + \nu_{prm}\varphi_{prm} \tag{10}$$

$$G_f = \frac{E_f}{2(1+\nu_f)} \tag{11}$$

$$G_m = \frac{E_m}{2(1+\nu_m)} \tag{12}$$

Symbols	Meaning
E	Young's modulus
G	Shear modulus
φ	Volume fraction
ν	Poisson's ratio
f	fibril
ch	chitin
prf	protein content in fibril
m	matrix
acc	acc (amorphous calcium carbonate) spherules
prm	protein content in matrix

Table 5.1 - Nomenclature for the listed equations.

Secondly, a combination of Voigt and Reuss models was used to calculate the mechanical properties of the single lamina (Berthelot 2012) (**Equations 13-17**). Directions 1 and 2 are respectively parallel and perpendicular to the longitudinal axis of fibres and indicate the lamina reference frame.

$$E_1 = E_f \varphi_f + E_m \varphi_m \tag{13}$$

$$E_2 = \frac{1}{\left(\varphi_f / E_f\right) + \left(\varphi_m / E_m\right)} \tag{14}$$

$$G_{12} = \frac{1}{\left(\varphi_f / G_f\right) + \left(\varphi_m / G_m\right)} \tag{15}$$

$$v_{12} = v_f \varphi_f + v_m \varphi_m \tag{16}$$

$$v_{21} = \frac{v_{12} E_2}{E_1} \tag{17}$$

For a generic orthotropic lamina the stiffness matrix Q in the reference frame '1-2' is expressed by **Equations 18-22**.

$$Q = \begin{bmatrix} Q_{11} & Q_{12} & 0 \\ Q_{21} & Q_{22} & 0 \\ 0 & 0 & Q_{66} \end{bmatrix} \tag{18}$$

Where:

$$Q_{11} = \frac{E_1}{1 - v_{12}^2 \dfrac{E_2}{E_1}} \tag{19}$$

$$Q_{12} = \frac{v_{12} E_2}{\left(1 - v_{12} v_{21}\right)} = Q_{21} \tag{20}$$

$$Q_{22} = \frac{E_2}{1 - v_{12}^2 \dfrac{E_2}{E_1}} \tag{21}$$

$$Q_{66} = G_{12} \tag{22}$$

Equation 23 represents the transformation matrix which allows passing from a fixed frame x-y to the rotated one 1-2 (of a generic angle θ) (Berthelot 2012).

$$T = \begin{bmatrix} \cos^2\theta & \sin^2\theta & 2\cos\theta\sin\theta \\ \sin^2\theta & \cos^2\theta & -2\cos\theta\sin\theta \\ -\cos\theta\sin\theta & \cos\theta\sin\theta & \cos^2\theta - \sin^2\theta \end{bmatrix} \tag{23}$$

For engineering application the Reuter matrix is introduced to pass from the tensorial definition of strain to the engineering definition (**Equation 24**).

$$R = \begin{bmatrix} 1 & 0 & 0 \\ 0 & 1 & 0 \\ 0 & 0 & 2 \end{bmatrix} \tag{24}$$

All the steps to calculate the laminate stiffness matrix in the x-y reference frame are listed below (**Equations 25-45**).

$$\begin{bmatrix} \varepsilon_1 \\ \varepsilon_2 \\ \gamma_{12} \end{bmatrix}_{eng} = R \begin{bmatrix} \varepsilon_1 \\ \varepsilon_2 \\ \gamma_{12} \end{bmatrix}_{tens} = RT \begin{bmatrix} \varepsilon_x \\ \varepsilon_y \\ \gamma_{xy} \end{bmatrix}_{tens} = RTR^{-1} \begin{bmatrix} \varepsilon_x \\ \varepsilon_y \\ \gamma_{xy} \end{bmatrix}_{eng} \tag{25}$$

It is possible to demonstrate that:

$$RTR^{-1} = \left(T^{-1}\right)^T \tag{26}$$

The stiffness matrix for the lamina in the x-y frame can be calculated as follows:

$$\begin{bmatrix} \sigma_x \\ \sigma_y \\ \tau_{xy} \end{bmatrix}_{eng} = T^{-1} \begin{bmatrix} \sigma_1 \\ \sigma_2 \\ \tau_{12} \end{bmatrix}_{eng} = T^{-1}Q_{12} \begin{bmatrix} \varepsilon_1 \\ \varepsilon_2 \\ \gamma_{12} \end{bmatrix}_{eng} = T^{-1}Q_{12}RTR^{-1} \begin{bmatrix} \varepsilon_x \\ \varepsilon_y \\ \gamma_{xy} \end{bmatrix}_{eng} \tag{27}$$

Whence:

$$\begin{bmatrix} \sigma_x \\ \sigma_y \\ \tau_{xy} \end{bmatrix}_{eng} = T^{-1} Q_{12} \left(T^{-1} \right)^T \begin{bmatrix} \varepsilon_x \\ \varepsilon_y \\ \gamma_{xy} \end{bmatrix}_{eng} \tag{28}$$

Where:

$$T^{-1} = \begin{bmatrix} \cos^2 \theta & \sin^2 \theta & -2\cos\theta\sin\theta \\ \sin^2 \theta & \cos^2 \theta & 2\cos\theta\sin\theta \\ \cos\theta\sin\theta & -\cos\theta\sin\theta & \cos^2\theta - \sin^2\theta \end{bmatrix} \tag{29}$$

And:

$$\left(T^{-1} \right)^T = \begin{bmatrix} \cos^2 \theta & \sin^2 \theta & \cos\theta\sin\theta \\ \sin^2 \theta & \cos^2 \theta & -\cos\theta\sin\theta \\ -2\cos\theta\sin\theta & 2\cos\theta\sin\theta & \cos^2\theta - \sin^2\theta \end{bmatrix} \tag{30}$$

I can finally write:

$$Q_{xy} = T^{-1} Q_{12} \left(T^{-1} \right)^T \tag{31}$$

And also:

$$\begin{bmatrix} \sigma_x \\ \sigma_y \\ \tau_{xy} \end{bmatrix}_{eng} = Q_{xy} \begin{bmatrix} \varepsilon_x \\ \varepsilon_y \\ \gamma_{xy} \end{bmatrix}_{eng} \tag{32}$$

The inverse relation is:

$$\begin{bmatrix} \varepsilon_x \\ \varepsilon_y \\ \gamma_{xy} \end{bmatrix}_{eng} = S_{xy} \begin{bmatrix} \sigma_x \\ \sigma_y \\ \tau_{xy} \end{bmatrix}_{eng} \tag{33}$$

Each element of the matrix Q_{xy} is:

$$Q_{xx} = \cos^4\theta Q_{11} + \sin^4\theta Q_{22} + 2\cos^2\theta\sin^2\theta Q_{12} + 4\cos^2\theta\sin^2\theta Q_{66} \tag{34}$$

$$Q_{yy} = \sin^4\theta Q_{11} + \cos^4\theta Q_{22} + 2\cos^2\theta\sin^2\theta Q_{12} + 4\cos^2\theta\sin^2\theta Q_{66} \tag{35}$$

$$Q_{xy} = \cos^2\theta\sin^2\theta Q_{11} + \cos^2\theta\sin^2\theta Q_{22} + \left(\cos^4 + \sin^4 \right) Q_{12} - 4\cos^2\theta\sin^2\theta Q_{66} \tag{36}$$

$$Q_{xs} = \cos^3 \theta \sin \theta Q_{11} + \sin^3 \theta \cos \theta Q_{22} + \left(\cos^3 \theta \sin \theta - \sin^3 \theta \cos \theta\right)Q_{12} + 2\left(\cos^3 \theta \sin \theta - \sin^3 \theta \cos \theta\right)Q_{66}$$

(37)

$$Q_{ys} = \sin^3 \theta \cos \theta Q_{11} - \cos^3 \theta \sin \theta Q_{22} + \left(\cos^3 \theta \sin \theta - \sin^3 \theta \cos \theta\right)Q_{12} + 2\left(\cos^3 \theta \sin \theta - \sin^3 \theta \cos \theta\right)Q_{66}$$

(38)

$$Q_{ss} = \cos^2 \theta \sin^2 \theta Q_{11} + \cos^2 \theta \sin^2 \theta Q_{22} - 2\cos^2 \theta \sin^2 \theta Q_{12} + \left(\cos^2 - \sin^2\right)^2 Q_{66}$$ (39)

And each element of the matrix $\boldsymbol{S_{xy}}$ is:

$$S_{xx} = \cos^4 \theta S_{11} + \sin^4 \theta S_{22} + 2\cos^2 \sin^2 \theta S_{12} + \cos^2 \theta \sin^2 \theta S_{66}$$ (40)

$$S_{yy} = \sin^4 \theta S_{11} + \cos^4 \theta S_{22} + 2\cos^2 \theta \sin^2 \theta S_{12} + \cos^2 \theta \sin^2 \theta S_{66}$$ (41)

$$S_{xy} = \cos^2 \theta \sin^2 \theta S_{11} + \cos^2 \theta \sin^2 \theta S_{22} + \left(\cos^4 + \sin^4\right)S_{12} - \cos^2 \theta \sin^2 S_{66}$$ (42)

$$S_{xs} = 2\cos^3 \theta \sin \theta S_{11} + 2\sin^3 \theta \cos \theta S_{22} + 2\left(\cos^3 \theta \sin \theta - \sin^3 \theta \cos \theta\right)S_{12} + \left(\cos^3 \theta \sin \theta - \sin^3 \theta \cos \theta\right)S_{66}$$

(43)

$$S_{ys} = 2\sin^3 \theta \cos \theta S_{11} - 2\cos^3 \theta \sin \theta S_{22} + 2\left(\cos^3 \theta \sin \theta - \sin^3 \theta \cos \theta\right)S_{12} + \left(\cos^3 \theta \sin \theta - \sin^3 \theta \cos \theta\right)Q_{66}$$

(44)

$$S_{ss} = 4\cos^2 \theta \sin^2 \theta S_{11} + 4\cos^2 \theta \sin^2 \theta S_{22} - 8\cos^2 \theta \sin^2 \theta S_{12} + \left(\cos^2 - \sin^2\right)^2 S_{66}$$ (45)

A list of basic assumptions used for this approach is listed below (Reddy 2004):

- Each layer of the laminate is orthotropic.

- The layers are perfectly bonded together.

- The laminate is thin compared to the lateral dimensions.

- State of stress is plane stress ($\sigma_{zz} = \tau_{xz} = \tau_{yz}$ 0).

- All displacements are small compared to the laminate thickness.

- Straight lines normal to the middle surface remain straight and normal to that surface after deformation.

- The transverse shear strains are negligible ($\gamma_{xz} = \gamma_{yz} = 0$).

- Transverse normal strain ε_{zz} is negligible compared to the in plane strains ε_{xx} and ε_{yy}.

- Strain-displacement and stress-strain relations are linear.

The procedure to calculate the laminate stiffness matrix under the hypotheses of the Kirchoff's theory is shown below (**Equations 46-61**).

The in-plane displacements are (see also **Figure 5.1**):

$$u = u_0 - z\frac{\partial w}{\partial x} \tag{46}$$

$$v = v_0 - z\frac{\partial w}{\partial y} \tag{47}$$

$$w = w_0 \tag{48}$$
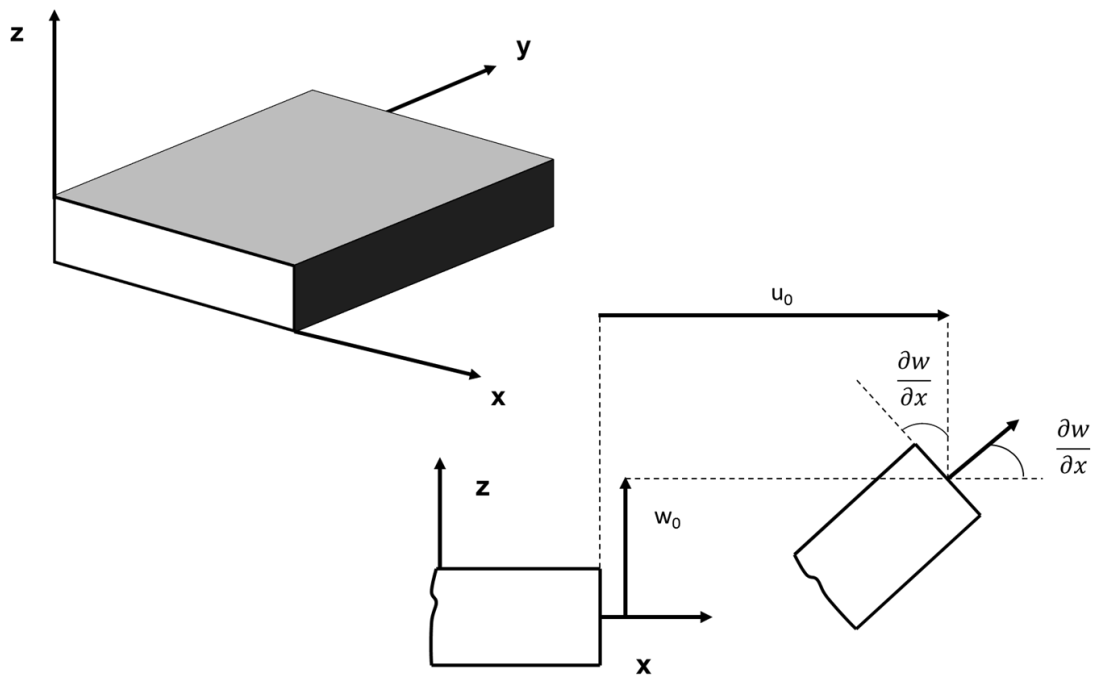
Figure 5.1 - Undeformed and deformed geometries of a single lamina under Kirchhoff's hypotheses.

The strain-displacement relations are:

$$\varepsilon_x = \frac{\partial u}{\partial x} = \frac{\partial u_0}{\partial x} - z\frac{\partial^2 w}{\partial x^2} \tag{49}$$

$$\varepsilon_y = \frac{\partial v}{\partial y} = \frac{\partial v_0}{\partial y} - z\frac{\partial^2 w}{\partial y^2} \tag{50}$$

$$\gamma_s = \frac{\partial u}{\partial y} + \frac{\partial v}{\partial x} = \frac{\partial u_0}{\partial y} + \frac{\partial v_0}{\partial x} - 2z\frac{\partial^2 w}{\partial x \partial y} \tag{51}$$

$$\varepsilon_z = \gamma_{xz} = \gamma_{yz} = 0 \tag{52}$$

Whence:

$$\begin{bmatrix} \varepsilon_x \\ \varepsilon_y \\ \gamma_s \end{bmatrix} = \begin{bmatrix} \varepsilon_x \\ \varepsilon_y \\ \gamma_s \end{bmatrix}_0 + z\begin{bmatrix} k_x \\ k_y \\ k_s \end{bmatrix} \tag{53}$$

Each lamina through the thickness may have a different stiffness due to its fibres orientation. The strain variation through the thickness (along z axis) is linear (as shown by **Equation 53**) while the stress variation is therefore discontinuous (**Figure 5.2**).
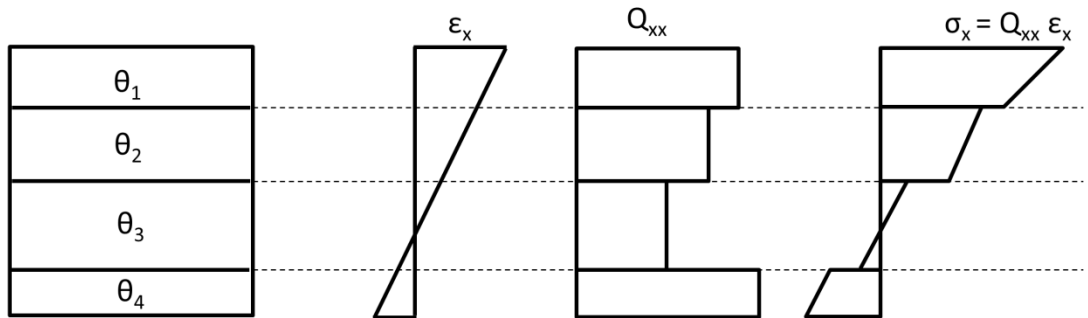
Figure 5.2 - Stress and strain variation through the laminate thickness.

The stress-strain relation for a generic lamina in the laminate's frame is:

$$\begin{bmatrix} \sigma_x \\ \sigma_y \\ \tau_s \end{bmatrix} = \begin{bmatrix} Q_{xx} & Q_{xy} & Q_{xs} \\ Q_{yx} & Q_{yy} & Q_{ys} \\ Q_{sx} & Q_{sy} & Q_{ss} \end{bmatrix} \begin{bmatrix} \varepsilon_x \\ \varepsilon_y \\ \gamma_s \end{bmatrix}_0 + z\begin{bmatrix} Q_{xx} & Q_{xy} & Q_{xs} \\ Q_{yx} & Q_{yy} & Q_{ys} \\ Q_{sx} & Q_{sy} & Q_{ss} \end{bmatrix} \begin{bmatrix} k_x \\ k_y \\ k_s \end{bmatrix} \tag{54}$$

Force and moments for the laminate (k indicates the generic lamina):

$$\begin{bmatrix} N_x \\ N_y \\ N_s \end{bmatrix} = \sum_{k=1}^{n} \left\{ \begin{bmatrix} Q_{xx} & Q_{xy} & Q_{xs} \\ Q_{yx} & Q_{yy} & Q_{ys} \\ Q_{sx} & Q_{sy} & Q_{ss} \end{bmatrix} \begin{bmatrix} \varepsilon_x \\ \varepsilon_y \\ \gamma_s \end{bmatrix}_0 \int\limits_{h_{k-1}}^{h_k} dz + \begin{bmatrix} Q_{xx} & Q_{xy} & Q_{xs} \\ Q_{yx} & Q_{yy} & Q_{ys} \\ Q_{sx} & Q_{sy} & Q_{ss} \end{bmatrix} \begin{bmatrix} k_x \\ k_y \\ k_s \end{bmatrix} \int\limits_{h_{k-1}}^{h_k} z\,dz \right\}$$

(55)

$$\begin{bmatrix} M_x \\ M_y \\ M_{xy} \end{bmatrix} = \sum_{k=1}^{n} \left\{ \begin{bmatrix} Q_{xx} & Q_{xy} & Q_{xs} \\ Q_{yx} & Q_{yy} & Q_{ys} \\ Q_{sx} & Q_{sy} & Q_{ss} \end{bmatrix} \begin{bmatrix} \varepsilon_x \\ \varepsilon_y \\ \gamma_s \end{bmatrix}_0 \int\limits_{h_{k-1}}^{h_k} z\,dz + \begin{bmatrix} Q_{xx} & Q_{xy} & Q_{xs} \\ Q_{yx} & Q_{yy} & Q_{ys} \\ Q_{sx} & Q_{sy} & Q_{ss} \end{bmatrix} \begin{bmatrix} k_x \\ k_y \\ k_s \end{bmatrix} \int\limits_{h_{k-1}}^{h_k} z^2 dz \right\}$$

(56)

The load-strain relations are:

$$\begin{bmatrix} N_x \\ N_y \\ N_s \\ M_x \\ M_y \\ M_s \end{bmatrix} = \begin{bmatrix} A_{xx} & A_{xy} & A_{xs} & B_{xx} & B_{xy} & B_{xs} \\ A_{yx} & A_{yy} & A_{ys} & B_{yx} & B_{yy} & B_{ys} \\ A_{sx} & A_{sy} & A_{ss} & B_{sx} & B_{sy} & B_{ss} \\ B_{xx} & B_{xy} & B_{xs} & D_{xx} & D_{xy} & D_{xs} \\ B_{yx} & B_{yy} & B_{ys} & D_{yx} & D_{yy} & D_{ys} \\ B_{sx} & B_{sy} & B_{ss} & D_{sx} & D_{sy} & D_{ss} \end{bmatrix} \begin{bmatrix} \varepsilon_{x0} \\ \varepsilon_{y0} \\ \gamma_{s0} \\ k_x \\ k_y \\ k_s \end{bmatrix}$$

(57)

Or in a more compact formulation:

$$\begin{bmatrix} N \\ M \end{bmatrix} = \begin{bmatrix} A & B \\ B & D \end{bmatrix} \begin{bmatrix} \varepsilon \\ k \end{bmatrix}$$

(58)

Where:

$$A_{i,j} = \sum_{k=1}^{n} Q_{i,j}^{k} \left(h_k - h_{k-1} \right)$$

(59)

$$B_{i,j} = \frac{1}{2} \sum_{k=1}^{n} Q_{i,j}^{k} \left(h_k^2 - h_{k-1}^2 \right)$$

(60)

$$D_{i,j} = \frac{1}{3} \sum_{k=1}^{n} Q_{i,j}^{k} \left(h_k^3 - h_{k-1}^3 \right)$$

(61)

Where the elements included in $Q_{i,j}^{k}$ are function of the material properties and of θ. In this case I only consider the matrix **A** because the laminate is symmetric (it implies that **B** = 0) and balanced (it implies that $A_{i,s} = 0$, where i =

157

x,y). Specifically, a laminate is symmetric when the plies above the mid-plane are a mirror image of those below the mid-plane. Instead, a laminate is balanced when it has equal numbers of – and + angled plies (Berthelot 2012). Hence, it is necessary to invert the matrix **A** to calculate the laminate strains (**Equation 62** and **63**).

$$a = A^{-1} \tag{62}$$

$$\varepsilon_{laminate} = aN \tag{63}$$

The mechanical properties of the laminate can be calculated as shown below (**Equations 64-68**), where h is the thickness of the laminate.

$$E_x = \frac{1}{ha_{xx}} \tag{64}$$

$$E_y = \frac{1}{ha_{yy}} \tag{65}$$

$$G_{xy} = \frac{1}{ha_{ss}} \tag{66}$$

$$v_{x,y} = -\frac{a_{yx}}{a_{xx}} \tag{67}$$

$$v_{y,x} = -\frac{a_{xy}}{a_{yy}} \tag{68}$$

The calculation of the stress and strain vectors for each lamina can be performed by using **Equations 69-70**.

$$\begin{bmatrix} \sigma_1 \\ \sigma_2 \\ \tau_{12} \end{bmatrix}_{eng} = T \begin{bmatrix} \sigma_x \\ \sigma_y \\ \tau_{xy} \end{bmatrix}_{eng} \tag{69}$$

$$\begin{bmatrix} \varepsilon_1 \\ \varepsilon_2 \\ \gamma_{12} \end{bmatrix}_{eng} = T_\varepsilon \begin{bmatrix} \varepsilon_x \\ \varepsilon_y \\ \gamma_{xy} \end{bmatrix}_{eng} \tag{70}$$

The matrix $[T]_\varepsilon$ is displayed in the **Equation 71**.

$$T_\varepsilon = RTR^{-1} = \begin{bmatrix} \cos^2\theta & \sin^2\theta & \cos\theta\sin\theta \\ \sin^2\theta & \cos^2\theta & -\cos\theta\sin\theta \\ -2\cos\theta\sin\theta & 2\cos\theta\sin\theta & \cos^2\theta - \sin^2\theta \end{bmatrix} \tag{71}$$

5.2.2 Analytical approach for coupled laminate deformation and reorientation of Bouligand layers

Classical lamination theory (Berthelot 1999) was used to analyze the fibre deformation and the fibre reorientation of the stomatopod cuticle. Indeed, the plywood structure of the Bouligand layer was studied as a laminate, i.e. a stack of different orientated composite plies. The reinforcement (fibre) was considered to be the mineralised chitin fibre, and the continuous phase (matrix) was taken to be the mineral-protein composite. Both materials were assumed to behave in a linear elastic manner, i.e. the analytical formulation would be expected to be valid to the cuticle elastic limit of about ~0.6-0.8% tissue strain. Each plywood lamina was assumed to be orthotropic and to exist in a state of plane stress.

The material properties of the components were taken from the literature (Nikolov, Fabritius et al. 2015). The chitin nanofibres were composed of a crystalline region of chitin (E_{ch} = 60 GPa, v_{ch} = 0.25, φ_{ch} = 0.31) and proteins (E_{pf} = 56 MPa, v_{prf} = 0.28, φ_{prf} = 0.69), whilst the mineral matrix is composed of amorphous calcium carbonate spherules (E_{ACC}= 37 GPa, v_{ACC} = 0.35, φ_{ACC} = 0.9) and different proteins (E_{prm} = 570 MPa, v_{prf} = 0.28, φ_{prf} = 0.1). Here, $E_{subscript}$ indicates the Young's modulus for the *subscript* phase, $v_{subscript}$ indicates the

Poisson's modulus and $\varphi_{subscript}$ the volume fraction of the component. Chitin modulus was taken from (Ogawa, Hori et al. 2011).

The homogenised material properties of a single lamina were found by applying a rule of mixture (combination of Voigt and Reuss models) model twice – first at the fibrillar and the next time at the fibre level (Berthelot 1999). At the fibrillar level, the Voigt model (Hull and Clyne 1996) was used to calculate the Young's moduli and Poisson coefficients of the chitin protein nanofibrils and of the mineral-protein matrix, using the volume fraction φ_{ch} listed above. Secondly, the mechanical properties of the orthotropic lamina (**Figure 5.3**) were found as standard for a composite material (Berthelot 1999), by (a) using the Voigt model to obtain the Young's modulus E_1 along the fibre direction (direction 1 in **Figure 5.3** parallel to fibre direction) and the Poisson's constant ν_{12}, and (b) obtaining the Young's modulus E_2 and the shear modulus G_{12} perpendicular to the fibre direction (direction 2 in **Figure 5.3**), with the Reuss model. The shear modulus of the fibre, which is a part of the expressions above, was calculated by knowing the volume fraction of the nanofibrils ($\varphi_{fibril} = 0.22$). The shear moduli of the fibre and of the matrix (G_{fibre} and G_{matrix}) were calculated by using the expression valid for isotropic linear elastic material (**Equation 72**).

$$G = \frac{E}{2(1+\nu)} \tag{72}$$
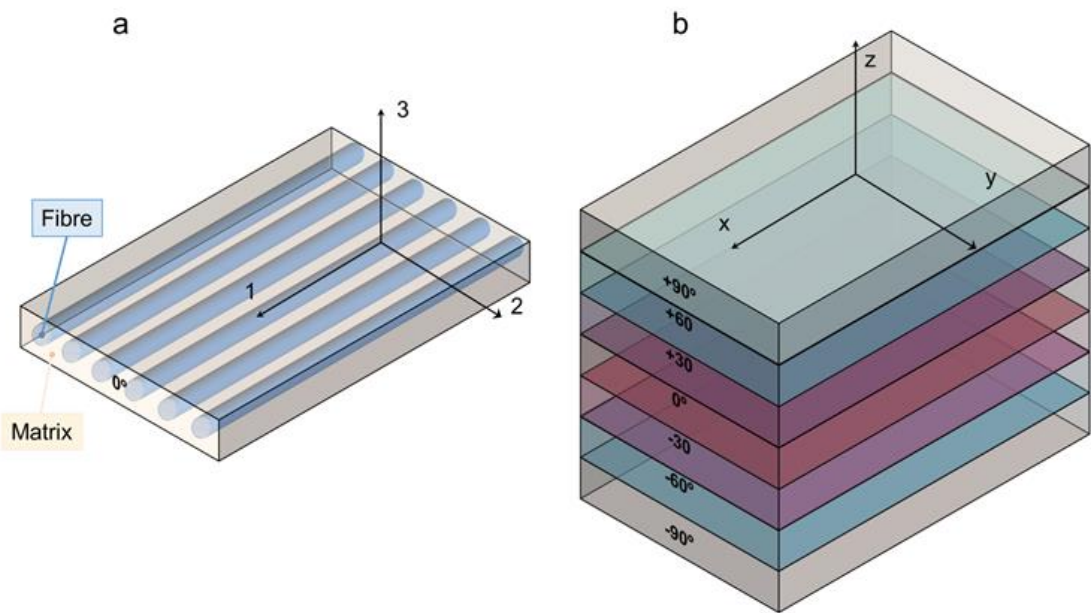
Figure 5.3 - Laminate composite model. (a) Schematic figure showing a single lamina made of fibres aligned along the direction 1 and embedded in a matrix. The thickness of each lamina is 0.1 μm. (b) Schematic figure of a plywood laminate. A quasi-continuously orientated structure made of 100 laminae (only 7 laminae were shown for convenience) is used for the analyses. The rotational angle between consecutive laminae considered for the analysis is 1.8 degrees.

After calculating the homogenised material properties for the lamina, the experimental Bouligand structure was approximated by applying the lamination theory to a 10 μm thick laminate (Raabe, Sachs et al. 2005), containing 100 laminae with an angular quasi-continuous distribution of plies (1.8 degrees between two consecutive laminae, from -90° to 90°). The main formula which links the loading to the deformation state of the laminate is the **Equation 58**, where N represents the 2 uniaxial forces (N_x and N_y) and the shear N_{xy} acting in the plane of the laminate (directions x-y), M_x and M_y the 2 static moments acting along directions x-y, and the torque M_{xy}. [A], [B] and [D] are the stiffness matrices of the laminate, while [ε] represents the strains and [κ] the curvatures of the laminate. Under the assumptions of lamination theory (Berthelot 1999)

161

the curvatures are neglected, and with **N** = [N_x, 0, 0] as the experimental load for uniaxially applied tension, the laminate strains can be calculated from **Equation 73**.

$$\boldsymbol{\varepsilon} = \boldsymbol{A}^{-1}\boldsymbol{N} \tag{73}$$

A can be calculated with the **Equation 74.**

$$A_{ij} = \sum_{k=1}^{n} [Q]_{ij}^{k} (h_k - h_{k-1}) \tag{74}$$

Where the matrix $[Q]_{ij}$ is the assembled matrix of the laminate and h_k represents the distance of the kth lamina from the mid-plane of the laminate. Once the laminate strains are obtained, the strain vectors in each lamina frame is calculated by multiplying $[\varepsilon]$ with the transformation matrix $\mathbf{T_\epsilon}$ previously shown (**Equation 71**).

The reorientation was calculated as laminar shear strain divided by 2, as per the **Figure 5.4**. Analytically, this results in the expression for angular reorientation $\Delta\gamma(\sigma_{xx})$ (**Equation 75**):

$$\Delta\gamma(\sigma_{xx}) = \frac{\varepsilon_{12}}{2} \tag{75}$$
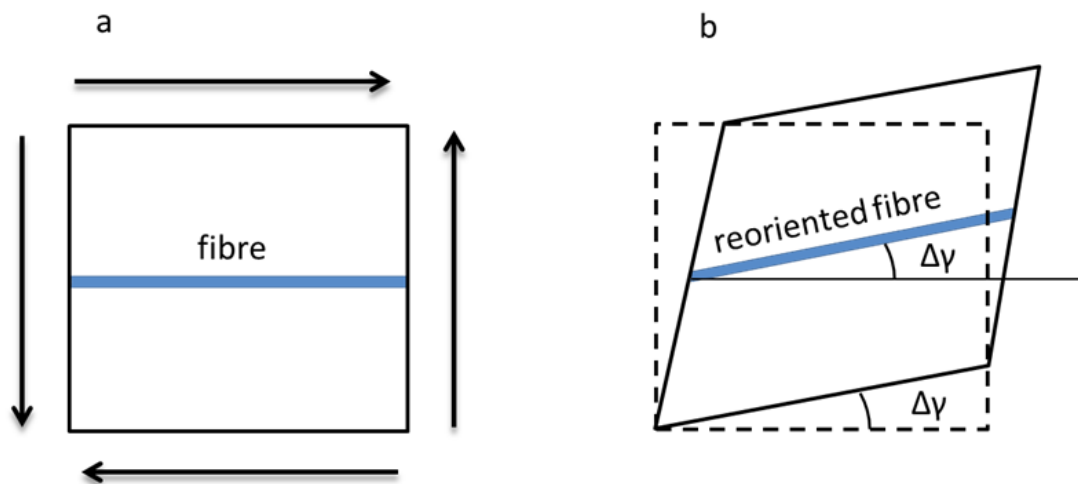
Figure 5.4 - In –plane angular reorientation of lamina under shear strain. a)
Undeformed configuration. b) Deformed configuration. Dashed line is used for
undeformed configuration. The fibre reorientation $\Delta\gamma$ was calculated as $\varepsilon_{12}/2$,
where ε_{12} is the engineering shear strain in the hypotheses of small
displacements. All the strain components are rotated in the reference frame of
each lamina. Hence, the strain components along and perpendicular to the
fibres direction do not contribute to reorientation.

5.2.3 Analytic 3D X-ray diffraction intensity distributions for interpenetrating nanofibre networks

Figure 5.5 shows the experimental protocol for *in situ* tensile testing during

synchrotron XRD experiment, and the relation of X-ray diffraction geometry to

the underlying nanofibre organization. Tergite specimens from the stomatopod

(**Figure 5.5a**) cuticle embedded in two orthogonal orientations (**Figure 5.5b**) are

deformed during synchrotron XRD (**Figure 5.5c**), leading to the acquisition of a

series of XRD patterns. The microstructure of cuticle consists of in-plane fibres

in a twisted plywood arrangement known as Bouligand layers (green fibres,

Figure 5.5d), interpenetrated with perpendicularly oriented pore-canal fibres

(blue fibres, **Figure 5.5d**). The basic microstructural unit in each scattering

volume element is therefore a combination of in-plane fibres (IP) (forming Bouligand plywood layers) and bundles of out-of-plane (OP) fibres (from the pore-canals) (**Figure 5.3d**) (Raabe, Al-Sawalmih et al. 2007). Here, both micro units as variations of an underlying planar fibre distribution $w(\gamma)$ (**Figure 5.5e** and **Appendix C**, **Table A.1-II**), with the Bouligand (IP-) phase corresponding to fibres equally oriented in all directions in the lamellar plane, and the pore-canal (OP) fibres oriented principally in one direction (along the pore) were considered. As the plane of the fibres in the sample may be oriented at nonzero angles to the principal coordinate axes of the lab-frame, I denote α and β (with respect to q_z^L and q_y^L axis respectively) as the Euler tilt angles of the plane with respect to the lab coordinate system (**Figure A.3**).

These micro-units are themselves comprised – at the nanoscale - of chitin fibres (Nikolov, Fabritius et al. 2011), made of α-chitin molecules arranged in a fibre-symmetric manner around the fibre axis **(Figure A.1)**. As a consequence, the diffraction intensity of the (*hk0*) reflections (such as the equatorial (110) peak) can be represented in reciprocal space as rings (Zhang, Paris et al. 2016) and the (*00l*) reflections (such as the (002) peak) as paired spots. To show the intensity distribution on the reciprocal space as a function of 3D orientation, a polar-sphere-like representation is used. The X-ray diffraction (XRD) intensity pattern corresponding to the model will be the 2D Ewald surface intersection with 3D volume of reciprocal space scattering intensity **(Figure A.2)**. Different spheres correspond to different reflections, and the spherical intensity variation correlates to the 3D orientation distributions of IP and OP fibres. As the full 3D intensity variation on the different reciprocal spheres cannot be fully captured

using a 2D detector at a single orientation, here my coworkers used two orthogonal tensile test geometries together with modelling to fully capture the deformation and reorientation information for both IP and OP fibres (**Figure 5.5b** and **5.5d**). Both the (002) and (110) reflections can be used to calculate the axial and radial fibrillar deformation respectively as well as orientation for the chitin fibres, but in this initial workonly results on the (002) reflection are presented.
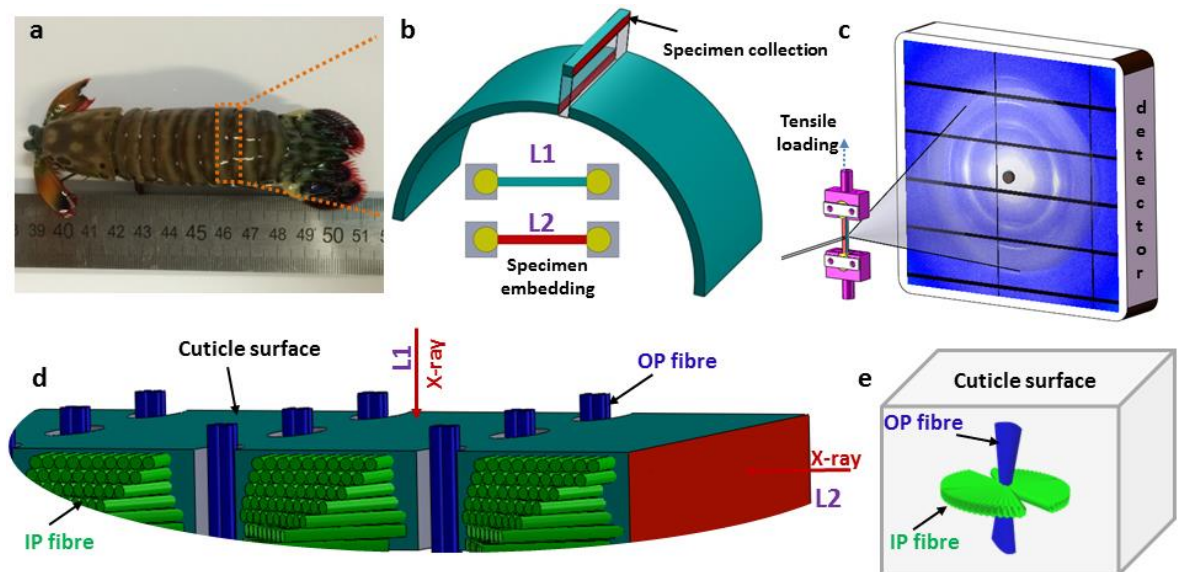
Figure 5.5 - Stomatopod tergite cuticle and experimental in situ XRD protocol. *(a) Image of a stomatopod. (b) Schematic of a single abdominal segment, which is sectioned into tensile test sections along the long axis of the animal. Lower schematics show the tensile test sample embedded in dental cement, with the direction of X-ray beam into the page. The two colour codes (blue and dark red; colour online) indicate different faces of the cuticle. Blue is normal to the cuticle surface, and red is the plane parallel to the cuticle surface. The rectangular-shaped sections are oriented in two directions when embedded in the dental cement holders (L1: X-ray normal to cuticle surface and L2: X-ray parallel to cuticle surface). (c) Schematic of in situ tensile testing of cuticle specimens during synchrotron XRD, with example 2D XRD pattern on detector. The specimen was hydrated in artificial sea water during the in situ testing. (d) Higher magnifications schematic of the cuticle section, showing the relation of the X-ray beam to the fibrous microstructure in the L1- and L2-configurations. Green fibre layers (colour online) represent the twisted plywood Bouligand lamellae (in-plane or IP-fibres), and blue cylinders the chitin fibres in the pore-canals running perpendicular to the cuticle surface (out-plane or OP-fibres). (e) The foregoing schematic is simplified to show the two groups of fibre distributions inside a scattering volume, and their orientation with regards to the cuticle surface.*

Figure 5.6a show the geometry of IP and OP fibres in the L1 configuration.

Figure 5.6b shows how, for the (110) reflection, constructive interference of the

(*hk*0) rings from the IP fibres leads to peaks only at the poles perpendicular to

the intersection plane between QS(110) sphere representing the reciprocal

space and Ewald sphere (a detailed explanation of these concepts is provided

166

in **Appendix B**) (Al-Sawalmih, Li et al. 2008, Zhang, Paris et al. 2016). Therefore, the intensity variation of (110) reflection from the major fibre component (IP) is not captured by the detector (Zhang, Paris et al. 2016). Concurrently, for the (002) reflection, the paired diffraction spots from individual fibres lead to rings parallel to the q_y-q_z plane due to the Bouligand distribution of the IP fibres (**Figure 5.6c**). In this study, the (002) reflection will be used to calculate the deformation and reorientation of IP fibres in the L1 configuration.
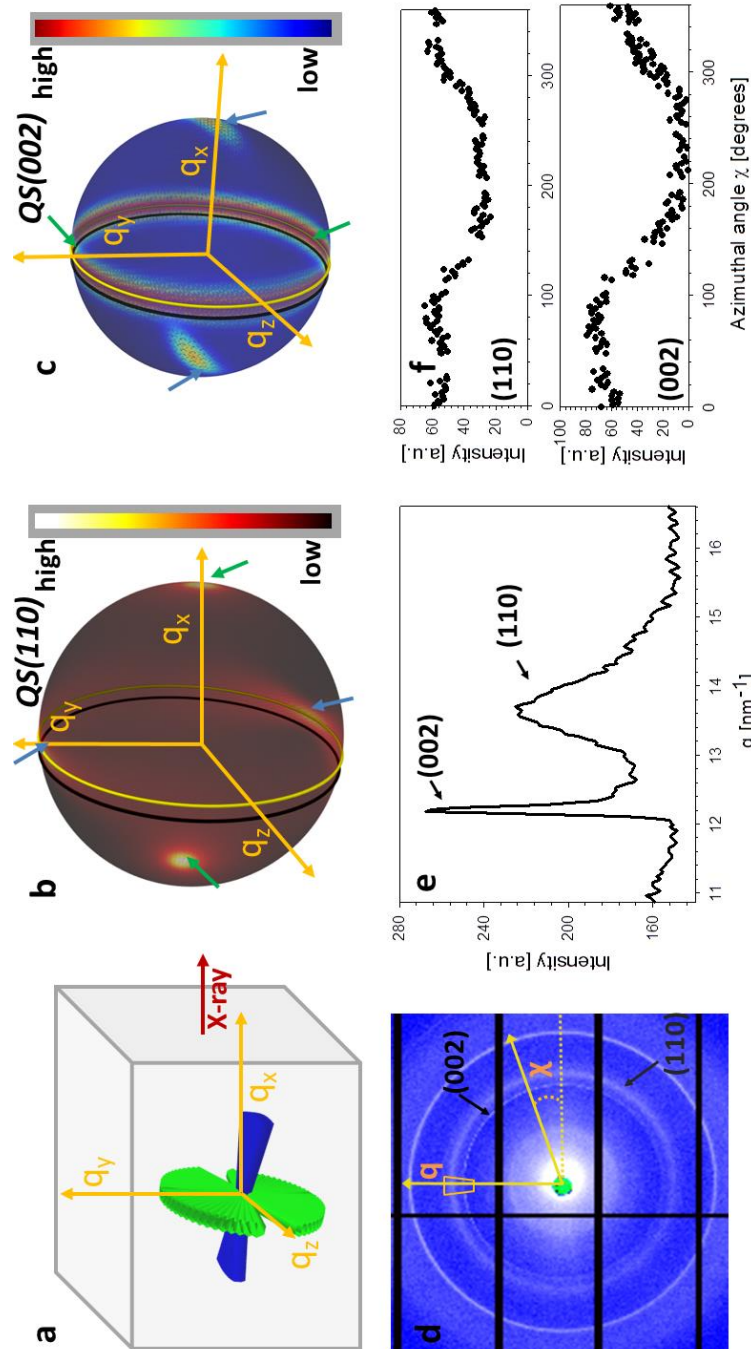
Figure 5.6 - Diffraction data analysis. *(a) Schematic showing the in-plane and out-of-plane chitin fibre distributions inside cuticle for L1 configuration (rotated by 90° with respect to figure 5.1e). (b) From the combined fibre distributions, the predicted intensity distributions of the (110) reciprocal lattice vector on a 3D sphere, based on the model described in Section 2. (c) Likewise, the model-based intensity distributions of the (002) reciprocal lattice vector on a 3D sphere. (d) A representative experimental 2D diffraction pattern from tergite cuticle (L1 configuration). Both (110) and (002) reflections from alpha chitin are indicated. (e) Azimuthally averaged intensity profiles showing the sharp (002) and broad (110) peaks. (f) Radially averaged azimuthal profiles for (002) and (110) reflections, showing non-uniform angular texture.*

168

These complex distributions in reciprocal space can be represented analytically. Consider the Bouligand lamella to be oriented in the $q_y^L - q_z^L$ plane (indicated with green fibres in **Figure 5.6a**). For a single fibre, the intensity distribution in reciprocal space can be written as in **Equation 76.**

$$I_{(002)}\left(q_x, q_y, q_z\right) = \frac{I_0}{\Delta q_{(002)}\sqrt{2\pi}}\exp\left(-\frac{q_x^2}{2\Delta q_{(002)}^2}\right)\delta\left(q_z\right) \tag{76}$$

The scattering vector q is given by $q = \sqrt{q_x^2 + q_y^2 + q_z^2} = \frac{4\pi}{\lambda}\sin\frac{2\Theta}{2}$, Θ the Bragg diffraction angle for the Miller index of (002) and $\Delta q_{(002)}$ the width of the (002) ring in reciprocal space (an analogous expressions for the (110) reflection is given in *SI*). The full XRD intensity is obtained by a weighted integration of the intensity in **Equation 76** over all possible fibre angles in the lamella, and these 3D spherical intensity distributions are plotted in **Figure 5.6b-c**. To obtain the intensity profile on the detector, the 3D reciprocal space distribution is transformed to 2D detector coordinates (q, χ) (transformation equations in ***Appendix C, Table A.1 V***). For a uniform fibre distribution $w(\gamma) = w_0$ in the lamellar plane (which represents Bouligand lamellae with fibres in the sub-lamellae at all possible angles), by taking the asymptotic limit of small $\Delta q_{(002)}$, it is possible to obtain a closed form of the azimuthal intensity profile (**Equation 77**).

$$I_{(002)}\left(\chi, 2\Theta, \kappa, \alpha, \beta\right) = \frac{w_0 I_0}{\Delta q_{(002)}\sqrt{2\pi}}\frac{\exp\left(-\frac{1}{2\kappa^2}\left(\sin\frac{2\Theta}{2}\cos\alpha + \cos\frac{2\Theta}{2}\sin\left(\chi - \beta\right)\sin\alpha\right)^2\right)}{\sqrt{1 - (\sin\frac{2\Theta}{2}\cos\alpha + \cos\frac{2\Theta}{2}\sin\left(\chi - \beta\right)\sin\alpha)^2}} \tag{77}$$

where $\kappa = \Delta q_{(002)} / q_{(002)}$ is a parameter denoting the relative width of the (002) ring ($q_{(002)}$ is the reciprocal lattice vector corresponding to the (002) peak) and χ

is the azimuthal angle with respect to q_z^L axis inside the intersection plane between the Ewald sphere with the QS(002) sphere. The width of the ring is a measure of the degree of misorientation of fibrils within a fibre at the nanoscale; fully parallel fibrils will lead to κ=0. Details of the integration, transformation equations and asymptotic limit are in **Appendix C: Tables A.1 I-III** and accompanying text. In the aligned state (where $\alpha = \beta = 0°$) and the Bouligand plane is parallel to the lab-frame, it is clear that the intensity of the (002) ring will be constant as a function of azimuthal angle χ, with a value shown in **Equation 78.**

$$I_{(002)}\left(\chi, 2\Theta, \kappa, 0, 0\right) = \frac{w_0 I_0}{\Delta q_{(002)}\sqrt{2\pi}} \frac{\exp\left(-\frac{1}{2\kappa^2}\sin^2\frac{2\Theta}{2}\right)}{\cos\frac{2\Theta}{2}} \tag{78}$$

In **Figure 5.6d** an example 2D XRD pattern is shown in the L1-orientation, with the (002) and (110) reflections indicated, whose peaks are shown on a radial profile in **Figure 5.6e**. Azimuthally resolved intensity plots are shown for these reflections in **Figure 5.6f**. A clear angular variation of intensity is observed in both subplots, which, when taken together with **Figures 5.6b-c**, implies slight nonzero value of the tilt angles α and β, and these tilts will be quantitatively determined in the following subsections. Shifts in the (002) peak positions (**Figure 5.6e**) will (in an angularly resolved sense to be described in the next section) be linked to the strain along the fibre axis (ε_f) induced by the tensile loading.

When the cuticle is deformed, *a priori* expectations are that the fibre distributions (both IP and OP) will undergo both (i) nanoscale axial deformation along the fibres and reorientation of the fibres in the Bouligand plane (changing

170

the planar fibre distribution $w(\gamma)$), as well as (ii) an overall angular movement of the Bouligand layer itself (change in α and β) at the mesoscale. While the analytic relations given previously are applicable in the general case, for the specific case considered here, where the fibre plane is nearly aligned with the lab-principal axes, it is possible to proceed via a simpler two-step approximation. First, given that the Euler tilt angles α and β are small to start with, the deformation of the fibres in the Bouligand plane can be obtained from the 2D XRD pattern in the same manner as would be for an un-tilted configuration. This step will provide the nanoscale strain and reorientation, and enable us to track the change in the fibre orientation distribution during the loading process, and is described in the next subsection.

5.2.4 Fibre mechanics in the Bouligand lamellae match laminate theory predictions at nanoscale

An averaged tensile stress-strain curves for the tergite cuticle is shown in **Figure 5.7a**, showing a linear increase of tissue stress with strain with a slight downward curvature evident at strains >0.6-0.8%. Concurrently, the radial peak profiles for the (002) reflection show shifts; for the direction parallel to the loading direction, to smaller wavevector (**Figure 5.7b**) implying a tensile deformation of the chitin fibres. **Figure 5.7c** shows the schematic of the plywood lamellae. The strain in the different sublayers of the Bouligand lamellae was calculated from shifts in the angularly resolved profiles of the (002) peak, and plotted in **Figure 5.7d**. The result shows that chitin fibres which orientated close to the tensile direction ($\psi = 0° - 40°$) exhibit a positive strain as the stress

increases, while fibres orientated further away (60° - 90°) from the tensile direction showed a negative strain (**Figure 5.7d**). In the transition region (40° - 60°) the chitin fibres showed no significant strain increments compared to the other regions. The experimental data appear to lie in three groups: 0-40°: tension, 50-60°: no change; 70-90°: compression.

The in-plane deformation and reorientation then were calculated using classical lamination theory (details of the lamination theory are provided in **Section 5.2.1**) to compare with the experimental results obtained from WAXD patterns. The plywood structured tergite sample was treated as a laminate comprising 100 Bouligand sublayers (laminae). The reinforcement (fibre) was considered to be the mineralised chitin fibre, and the continuous phase (matrix) was taken to be the mineral-protein composite. The fibre orientation in different laminae rotates around the normal axis of the whole laminate to match the plywood structure of the cuticle. Using initial estimates of the chitin, mineral and protein material properties and relative volume fractions from previous work (Nikolov, Petrov et al. 2010, Ogawa, Hori et al. 2011) the deformation (**Figure 5.7e**) of each lamina inside the whole laminate (Bouligand 1972, Grunenfelder, Suksangpanya et al. 2014) was calculated from an analytical formulation. Even without any parameter fitting of the literature values to the data, good qualitative agreement is observed between **Figures 5.7d-e**, although the deformation of the on-axis fibres is somewhat less in the experimental case than in the model. Fitting the model to the data as a function of the volume fraction, fibre moduli and other parameters is in principle possible in future work.
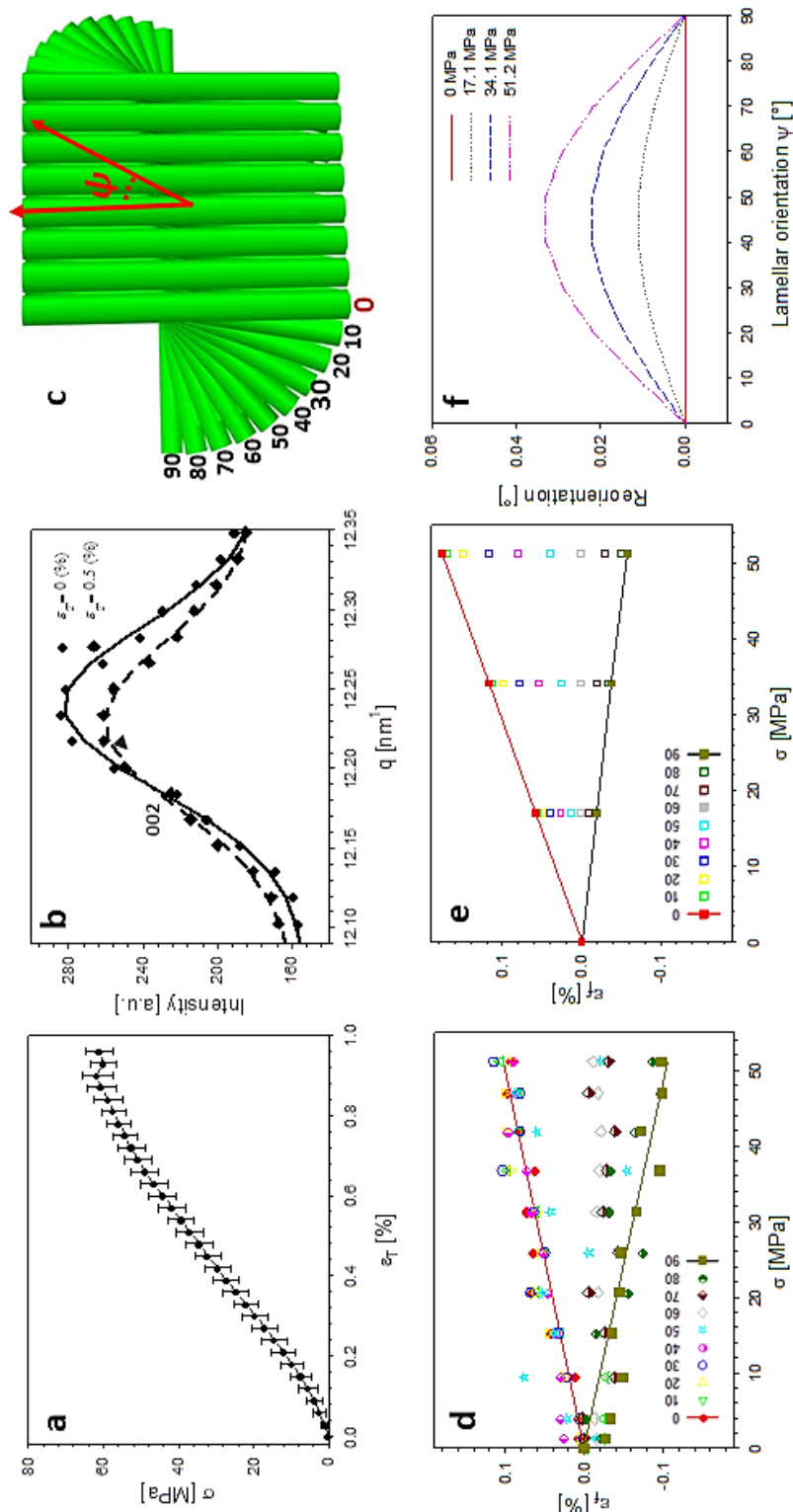
Figure 5.7 - In-plane deformation and reorientation of chitin nanofibres under L1 tensile configuration. *(a) An average stress and strain curve obtained from tensile tests. The results were averaged from five specimens. (b) Shifts in position of the (002) peak to smaller wavevector during tensile testing, showing elongation under tensile load. (c) Schematic representing the different sublamellae, parameterised by the angle* $\psi = 90° - \chi$ *. (d) The anisotropic*

173

experimental fibre strain (εf) from sublamellae oriented at differentψ, ranging from 0° to 90°, as a function of the increasing applied tissue stress (σT). Tensile deformation of fibres along the loading direction (ψ ~ 0°) and compression of fibres perpendicular to the loading direction (ψ near 90°) were observed. (e) Angularly resolved fibre strains predicted from a laminate model of the Bouligand layer, showing a similar trend as the experimental data. (f) Lamina reorientation calculated from the model, showing maximum fibre reorientation at $\psi = 45°$. Extent of fibre reorientation is very small (< 0.1° at maximum).

Generally, the fibre orientation distribution changes can be determined by tracking the angle-resolved I(χ) changes for the (002) reflection during tensile loading. The experimental results show that the normalised diffraction intensity is increasing in the angular region close to the tensile direction and decreasing in the angular region away to the tensile direction. However, the angle-resolved I(χ) changes can result both from in-plane fibre reorientation (from lamination theory) and the overall 3D tilting of the Bouligand lamellae. Therefore, the lamination model was used to factor out the in-plane reorientation effect.

From the modelled deformation of each lamina, it is possible to obtain the in-plane fibre reorientation (**Equation 75**). Under load, the angular intensity distribution is expected to narrow in width, as the fibres reorient towards the tensile axis. To describe this analytically, on application of a perturbing stressσ, a fibre originally at γ reorients to γ_σ according to the relation shown in **Equation 79** (more details are in **Appendix D**).

$$\gamma_\sigma = \gamma - \tilde{\sigma} f(\gamma) \tag{79}$$

where $\tilde{\sigma} = \sigma / \sigma_0$ is a dimensionless perturbation parameter (σ_0 = 100 MPa; as the experimentally observed ranges of stress are σ_T < 100 MPa, and $f(\gamma)$ << 1,

$\widetilde{\sigma f}(\gamma)$ is a small parameter). The new angular distribution (under stress) is denoted $w_\sigma(\gamma)$. Using first order perturbation, conservation of fibre number, and an initially uniform fibre distribution in the cuticle lamella $w_0 = 1/\pi$, it is possible to show that the changed distribution function is given by **Equation 80.**

$$w^\sigma(\gamma) \approx w_0\left(1 - 2\widetilde{\sigma}B\left(E_c, E_p, \phi_c, \phi_p\right)\cos 2\gamma\right) \tag{80}$$

Where *B* is a dimensionless function (obtainable from composite laminate analysis) of the cuticle material parameters. The angular change is, similarly, $\gamma_\sigma - \gamma = -\widetilde{\sigma}B\sin(2\gamma)$ which implies zero angular shift for fibres oriented parallel ($\gamma = \pi/2$) and perpendicular ($\gamma = 0$) to the loading direction. Using the same model parameters as used to predict the deformation of each layer, *B* can be calculated and the angular reorientation plotted (**Figure 5.7f**). It turns out that in this particular material (cuticle) the in-plane reorientation and change in orientation function is very small (angular changes of the order of 0.01°).

In this way, by using the parameters from fitting the fibre deformation in **Figure 5.7c** (with model results in **Figure 5.7d**), the changed fibre orientation distribution function at a given stress was obtained – as long as the stress remains below the elastic limit point of validity for laminate theory. While in the particular case of cuticle considered here the change of orientation function was negligible, in other layered composites like armored fish scales much larger reorientations have been observed via small-angle X-ray scattering (Zimmermann, Gludovatz et al. 2013). In general, the change in reorientation function will not necessarily be negligible in large-deformation scenarios, or in

deformation of very soft materials, where the ratio between stiffness of the reinforcing fibres and the surrounding matrix is very large (Barbieri and Pugno 2015).

5.2.5 Parametric analysis

A parametric analysis was performed to verify the effect of change of single parameters on the fibrillar strain distribution in each layer of the plywood structure (**Figure 5.8**).

Figure 5.8A shows that as the fibril volume fraction increases the strain carried in the laminae laying between 0° and 50° also increases. The laminae at 60° and 70°, instead, seem to be neutral to this change while the laminae at 80° and 90° feature a slight increment of compressive strain. Overall, the model is less sensitive to the change of fibril volume fraction. Indeed, following my assumption of biphasic model made of fibrils and matrix, even at low values of fibrils volume fraction, the contribution of the matrix (made of highly stiff mineral spherules with a Young's modulus of 37 GPa) to the mechanical properties of the entire system, are predominant..

In contrast, the effect of variation of the Young's modulus of mineral particles (E_{acc}) on the strain distribution in the plywood model (**Figure 5.8B**) is very significant. For lamellae angularly arranged between 0° and 50° the gradient of curves is negative and higher for lower values of E_{acc}. Again, the lamina at 60° has a near zero gradient versus E_{acc} while the laminae between 70° and 90° are characterized by a positive gradient although they remain under compression.

For instance, the lamina at 0° passes from a strain of 2% for E_{acc} = 1 GPa to a strain of 0.5% for E_{acc} = 10 GPa. Overall, the model is more sensitive to variations when Eacc is low. At E_{acc} = 20 GPa the curves start following an horizontal asymptote.

A similar description is valid for the set of curves parametrised with respect to the Young's modulus of chitin (E_{ch}) (**Figure 5.8C**). However, in this case, curves show lower gradients. Indeed, the 0° lamina deforms under tension of 0.5% for E_{ch} = 1GPa and of almost 0.3% for E_{ch} = 10 GPa. Also these curves follow a horizontal asymptote starting roughly from E_{ch} = 20 GPa. The lower sensitivity of the model to the changes of E_{ch} rather than of E_{acc} was expected. Indeed, in the rule of mixture that I applied, the matrix has been set with a volume fraction of 0.78 while the fibrils of 0.22. Since chitin is the main component of the fibrils and the mineral spherules are the main component of the matrix, it is clear that the mineral spherules will have a higher influence on the mechanics of the system which is, therefore, extremely sensitive to the change of their Young's modulus.
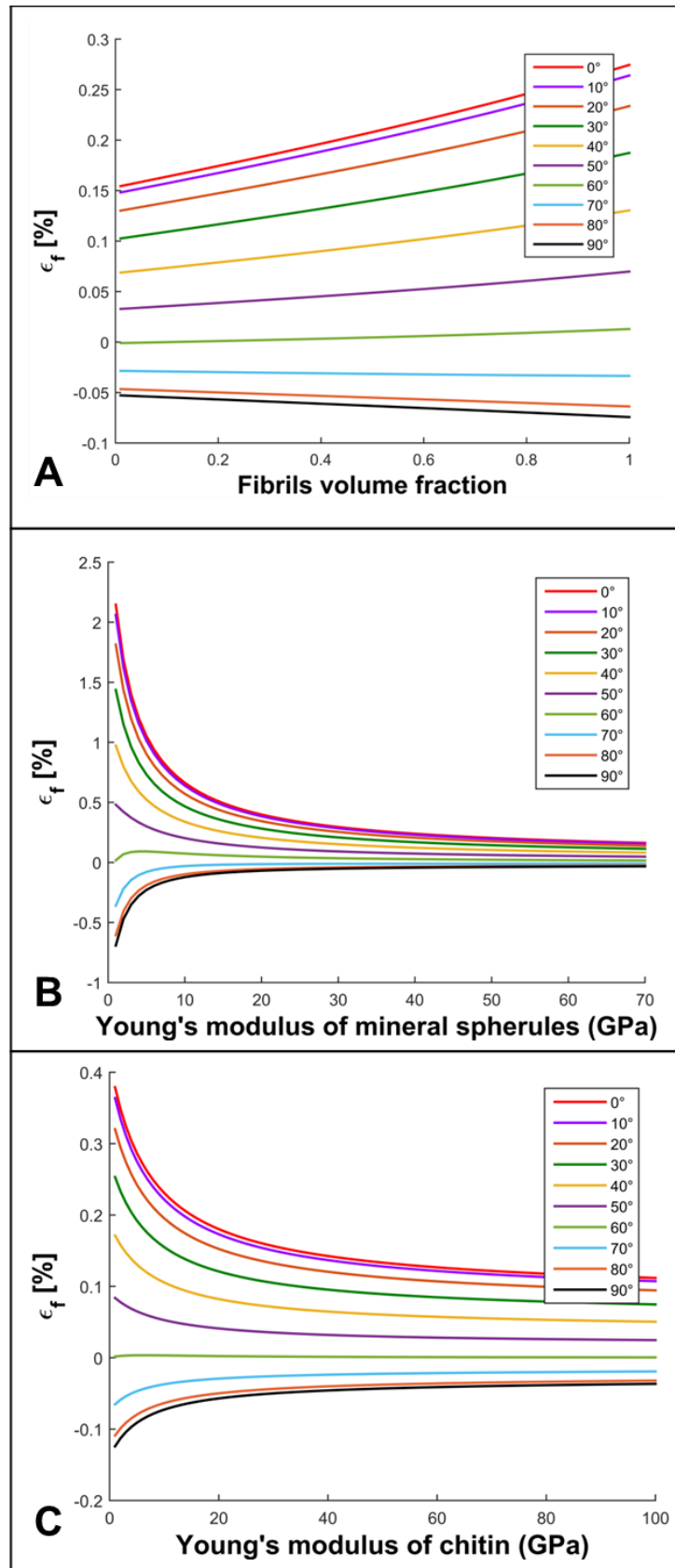
Figure 5.8 - Parametric study showing the strain distribution in the plywood simulated structure for an external applied stress of 51.2 MPa. *The parametrised variables are A) the fibril volume fraction, B) the Young's modulus of mineral spherules and C) the Young's modulus of chitin.*

5.2.6 Mesoscale reorientation shows layer alignment to tensile direction

The stress-altered fibre reorientation function $w_\sigma(\gamma)$ can now be inserted into **Equation 77** to factor out the in-plane nanoscale reorientation, enabling the mesoscale Euler tilt angles α and β to be fitted as functions of applied stress and strain (as stated in the previous section, for cuticle the change in $w(\gamma)$ is negligible). Specifically, four experimentally levels of tissue stress (0, 17.1, 34.1 and 51.2 MPa) were selected from the stress/strain curve of a cuticle sample. By applying these stress-levels to the laminate, the fibre-deformation and reorientation can be calculated using the laminate model equations (**Section 5.2.1**). Subsequently, the modified orientation function $w_\sigma(\gamma)$ (**Equation 80**) was obtained, and used in **Equation 77**, allowing a fit of the 3D orientation parameters (tilt angles α and β). To show the predicted diffraction model sensitivity to the tilt angles, **Figure 5.9a** and **d** show the deviation of the 2D and 1D intensity profiles (1D for (002) only) from a straight line due to nonzero but very small $\alpha = 2°$ (with no change in β or in the Bouligand layer fibre orientation function). **Figures 5.9b** and **e** show the diffraction intensity changes with a small β tilt while $\alpha = 0°$. **Figures 5.9c** and **f** show that a combination of α and β tilt can split the information acquired on the diffraction ring. It is clearly observed that major deviations from isotropy are observed for quite small α and β angles.

Figure 5.9 - 3D tilting of in-plane fibres under tensile loading. *(a)-(c) The rings represent sections of the 3D spherical intensity distributions shown in figure 5.2, for both (002) (inner ring) and (110) (outer ring). Rings are colour coded for intensity levels. The different images in (a) – (c) represent different orientations (via the tilt angles α, β), shown via the schematic of the Bouligand layer (green fibres; colour online) inside the ring. Yellow axes and fibre distribution represent the untilted ($\alpha = \beta = 0°$) reference state. (d)-(f) Corresponding azimuthal intensity plots I(χ) for the 2D intensity sections, with the horizontal reference line in each plot denoting the untilted configuration. (g) Stress-strain curve for a representative cuticle sample, with symbols I-III denoting from where the three azimuthal intensity curves in the following section (h) are taken. (h) Azimuthal intensity plots from points I-III in (g), vertically translated for representational clarity only. Solid lines denote fits to the analytical model (**Equation 77**). (i) Tilt angles α (left abscissa) and β (right abscissa) as a function of tissue strain, for the sample shown in (g), obtained by fits to the analytical model. A decrease of the off-axis tilt angleα, indicating load-induced alignment of the Bouligand layer toward the tensile axis, is observed.*

180

The qualitative reasoning for this sensitivity arises because there are two competing small parameters: the term $\left(\dfrac{4\pi}{\lambda}\right)\sin^2\dfrac{2\Theta}{2}=\dfrac{\lambda q^2}{4\pi}$ in **Equation 77** and width $\Delta q_{(002)}$ of the (002) ring in the q_x direction. Small movements of the cuticle layer will rapidly bring the intensity of the (002) ring into and out of the Ewald intersection (**Figure 5.6c**), resulting in a high sensitivity to angular changes. This feature, though fortuitous (it would cease to hold for large reciprocal lattice vectors q or wavelength λ), is useful in practice, as the changes in the angles themselves are expected to be quite small in linear elasticity, so having large changes in the intensity distribution for small angular changes improves fit sensitivity. **Figure 5.9h** shows the experimental I(χ) plots, and fitted curves, for three points I-III on a typical stress-strain curve of cuticle (**Figure 5.9g**). By fitting α and β over the whole strain range (**Figure 5.9i**), it is observed that α (denoting the deviation from the stress axis) reduces from ~2° to > 1° on application of load, with a similar change in β of about ~1°. Such a change in α is as expected, as under tensile load the Bouligand plane would align toward the loading direction.

5.2.7 Pore canal fibres compress whilst Bouligand fibres extend under loading

So far, the approach presented by my coworkers and I has considered only the deformation and reorientation of the IP fibre which is the majority phase of the interpenetrating nanofiber network. The OP fibres (**Appendix B, Figure A.1f** and **Figure 5.5d** and **e**) interpenetrating the Bouligand layer via the transversely

running pore canals will also contribute intensity on the QS(110) and QS(002) spheres. In the case of L2 geometry, the regions of (110) and (002) intensity arising from IP and OP fibre contributions are all captured in the detector (**Figure 5.10a-b**). It is seen that the intensity peaks of (002) reflection for each phase are nearly orthogonal to each other (IP- and OP-arrows in **Figure 5.10c**), permitting determination of peak changes in each phase individually. The 3D tilting of the lamellae plane in the L2 geometry can be directly determined using the (110) reflection and the associated model diffraction functions (**Appendix C**, **Table A.1V**).
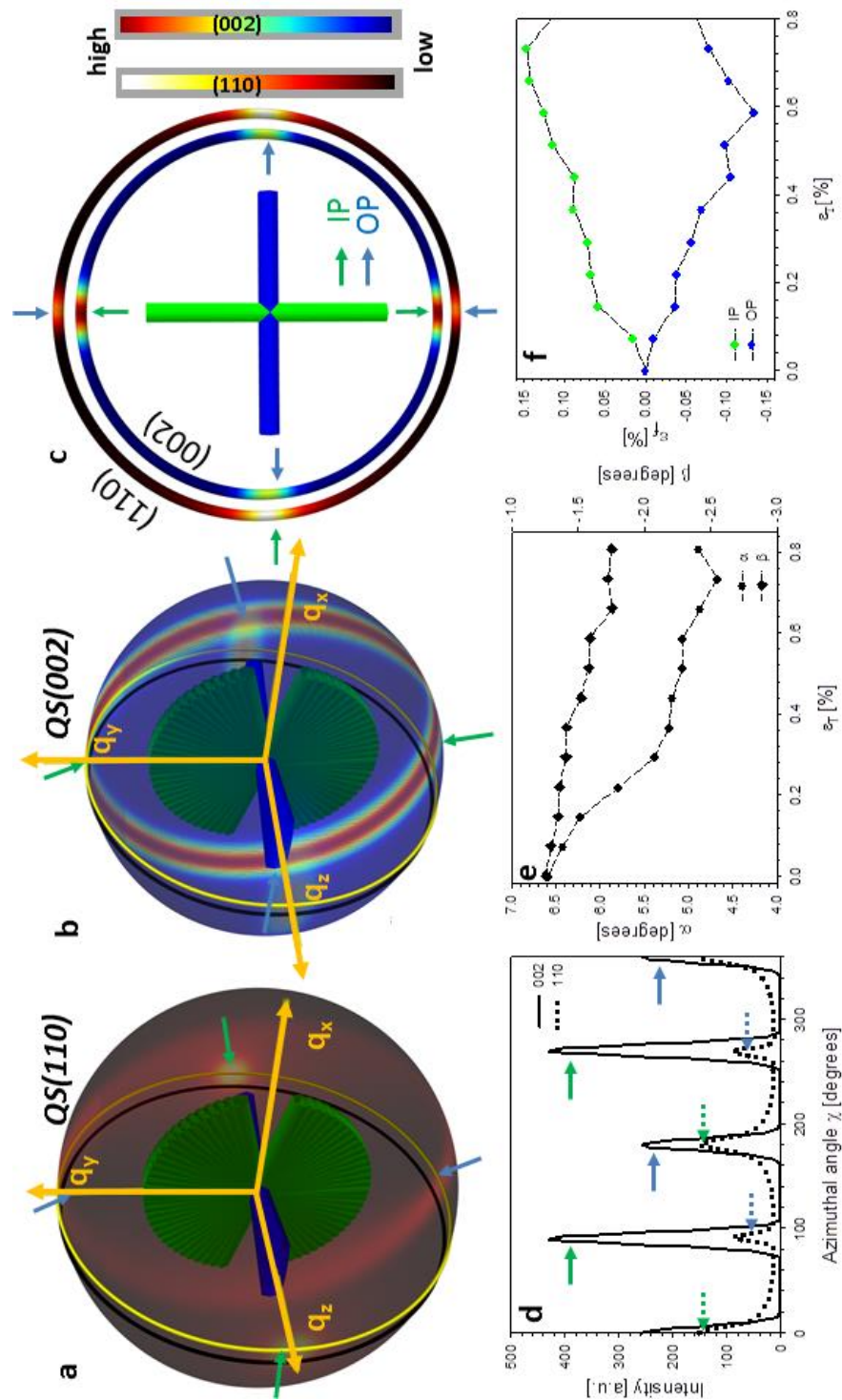
Figure 5.10 - The mechanical response of out-plane fibre from L2 configuration. *(a) The intensity distributions on QS(110) sphere corresponding to in-plane and out-of-plane fibres. (b) The intensity distributions on QS(002) sphere corresponding to in-plane and out-of-plane fibres. (c) The intensity distributions of (110) and (002) reflections on the intersection plane of the Ewald sphere and QS(110) and QS(002) spheres. (d)The azimuthal intensity profile I(χ) for (110) and (002) reflections. (e)The deformation for both in-plane fibre and out-of-plane fibres as a function of tissue strain (εT) during the L2 tensile test.*

183

The trace intersection of the Ewald sphere with the reciprocal lattice spheres is shown for (002) and (110) in **Figure 5.10c**. **Figure 5.10d** indicates the allocation of peaks for IP and OP fibres in the I(χ) curves. In **Figure 5.10f**, the strain increments for both pore-canal fibre and the IP fibre within the Bouligand lamellae are plotted against tissue strain. The result show that the OP fibre also exhibits a linear compressive response up to ~ -0.15 % (~0.6% tissue strain), shortly before the level at which macroscopic yielding and failure is observed (0.8%). It is clear that this phase of the nanofibre network (the pore-canal fibres) bears load and is expected to contribute to the overall mechanical properties. The corresponding reorientation dynamics of α and β deduced from the azimuthal angle changes of (110) reflection is shown in **Figure 5.10e**, and again, reorientation of the tilt angle α to smaller values (~6.5° to 4.5°) is observed, upon application of load.

5.3 Discussion and Conclusion

In summary, I determined, together with my coworkers, the 3D deformation and reorientation of two interpenetrating nanofiber networks in crustacean (stomatopod) cuticle, by developing a mathematical model to predict the 3D reciprocal diffraction intensity changes of (110) and (002) reflections of α-chitin fibres for two orthogonal diffraction geometries, in a combined *in situ* synchrotron mechanical test with X-ray diffraction. Taking advantage of the fibre symmetry, the deformation and reorientation at different hierarchical levels of the crustacean cuticle including the whole Bouligand fibre lamellae and pore-canal fibre bundles (mesoscale), each sub-lamellae (microscale) can be

quantitatively determined by simple experimental design with the assist of analytical formulae. As seen in **Figures 5.7** and **5.9**, my coworkers find that the method is highly sensitive to both strain and angular changes as induced by stress, as the X-ray azimuthal pattern changes significantly for shifts of less than one degree, and strains are typically less than 1%.

This method clearly overcomes the limitation of 2D XRD patterns in capturing 3D diffraction intensity changes in reciprocal space through a modelling approach, whilst other structural characterization methods (reviewed in the introduction) require time-consuming sample rotations and raises concern of radiation damage to the samples. Therefore it is very suitable for *in situ* or *in operando* study in materials science, when the deformation and orientation dynamics of crystalline phase is strongly correlated to the material function. In addition, I also employed the lamination theory simulation to decouple the intensity changes due to the in-plane anisotropic strain-induced reorientation effect from changes resulting from the 3D tilt of the whole Bouligand lamellae during the tensile test (**Figure 5.7**).
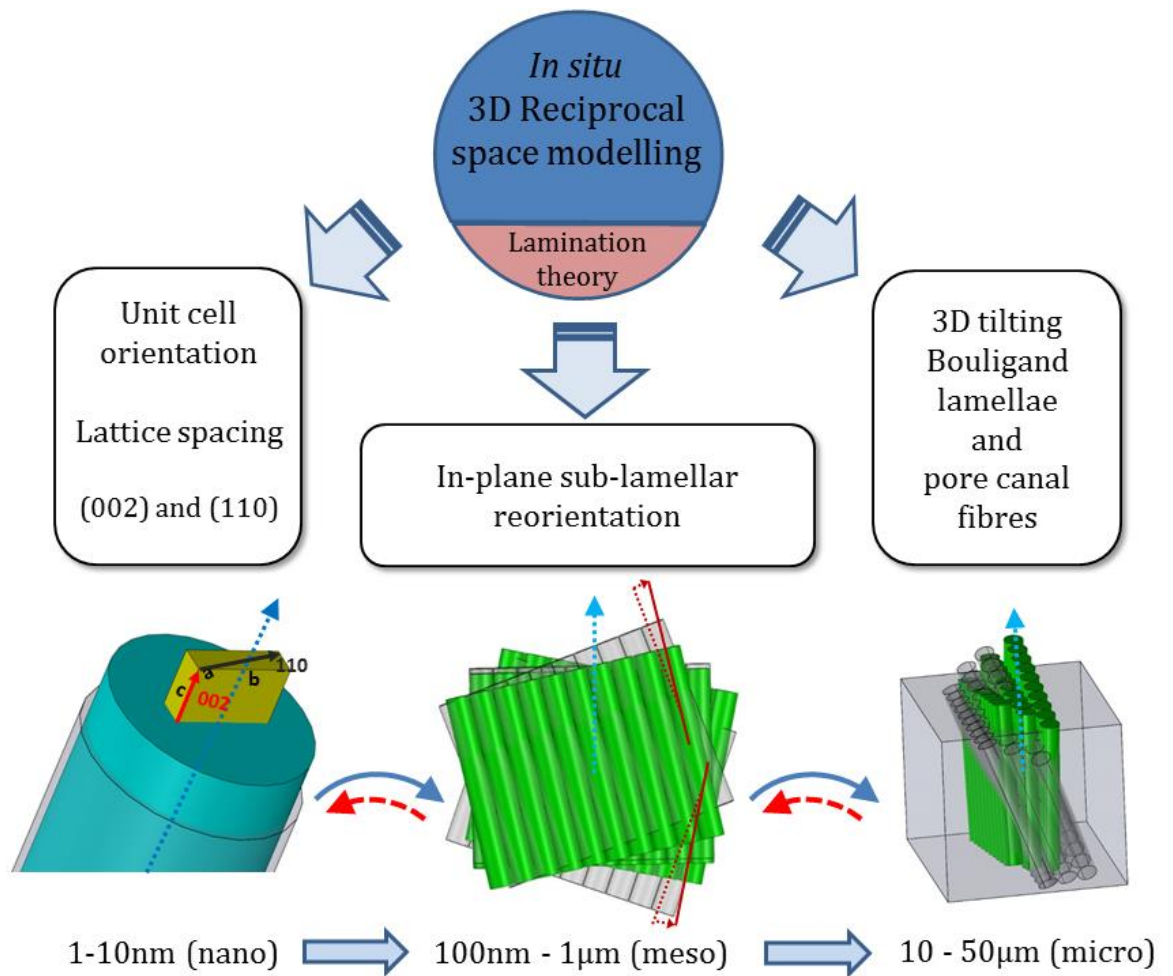
Figure 5.11 - Schematic of in situ determination of 3D strain and reorientation in nanofibre networks of cuticle. *Left: Molecular/nanoscale-level strain and orientation from unit-cell lattice spacing changes and c-axis direction in the chitin fibril. Middle: Correlated reorientation and strain of nanofibre layers at the mesoscale. Right: Compression of orthogonal nanofibre network in pore canals, and 3D reorientation of Bouligand lamellae. Solid arrows indicate sequence of steps in the current work; dashed arrows show the reverse procedure, which is in principle possible.*

One other interesting aspect of this method is that the decoupling of strain and reorientation between 2D and 3D is potentially reversible. By this I mean that by obtaining the 3D reorientation information in one specific diffraction geometry (e.g. L2), the (α,β) parameters could be determined first, and accounted for in the model for I(χ) (**Equation 77**), which would enable the purely in-plane

deformation and reorientation to be determined. Consequently, in an inverse problem approach (analytical or numerical), the results can thereby be inserted back into (for example) lamination theory simulations to deduce the material properties of different nanoscale components (**Figure 5.11**). This will be very helpful in identifying the material properties of components in nanostructured bio-composites like amorphous minerals or proteins which are difficult to characterise individually.

A characteristic of this approach is that it is applicable to any fibre network with molecular level fibre symmetry and (partial) crystalline order, and does not require the existence of special additional symmetries of periodicities at higher length scales (between 10-100 nm) such as in collagen (Gupta, Seto et al. 2006). As such this approach is especially suitable for fibre-based biological composites. Indeed, where a clear hierarchy of structural levels do not exist (in contrast to biological materials), and *in situ* mechanics are not needed, methods like 3D X-ray structural microscopy (Larson, Yang et al. 2002), which use sample rotation and aperture scanning, may be more appropriate. Strain evolution in nanocrystals can also be determined from coherent diffraction imaging (Yang, Huang et al. 2013), but such methods are usually focused on single particles rather than assemblies of them. Further, the approach presented here, to determine both real-time orientation and strain changes in 3D, can be applied to more complex systems even when the deformation and reorientation is small.

The angle–dependent deformation of fibres, shown to be consistent with lamination theory assuming a continuous distribution of fibre orientations, sheds

light on the underlying mechanisms enabling elasticity and toughness. The tensile elongation of fibres along the loading direction, transitioning to a compression perpendicular to the load, implies a strong interconnection between sublayers in the Bouligand lamellae. These interconnections are most likely the transversely–running pore-canal fibres (Nikolov, Petrov et al. 2010) which "stitch" the Bouligand fibre layers together. The smooth angular transition between rotating sublayers of the Bouligand structure (or sub-lamellae in the term used in bone) most likely accentuates the strong interconnection and increased toughness (Weaver, Milliron et al. 2012, Grunenfelder, Suksangpanya et al. 2014). The obtained results further highlights the mechanical importance of the pore-canal network, as a compressive strain in the pore-canal fibres, nearly equal in magnitude to the tensile strain in the Bouligand layer, is developed (**Figure 5.10f**, reaching a maximum magnitude of ~0.15 %). These results demonstrate that the pore-canal fibres also bear load, and support the concept of an interpenetrating, mechanically interlocked double network of fibres.

The importance of the interfibrillar matrix (mineralised protein) in enabling shear transfer between fibres is shown by the differences between the tissue and the fibre strain (a ratio of $\varepsilon_F/\varepsilon_T \sim 0.4$). Analogous interfibrillar shearing has been observed for the mineralised collagen fibres in bone with similar ratios from 0.4-0.6 (Gupta, Seto et al. 2006, Zimmermann, Schaible et al. 2011) which suggests this is a generic feature of mineralised fibrillar bio-composites. Prior work has implicated mechanisms such as sliding and rotation of fluoroapatite nanorods in the cuticle of the dactyl for its high fracture resistance (Amini, Masic et al. 2014). In contrast, the results I achieved together with my coworkers on

the chitin deformation provide information on the mechanisms of the organic fibres rather than the mineral, both of which are expected to play coupled and essential roles in determining material properties.

In relation to prior multiscale modelling work on cuticle (Nikolov, Petrov et al. 2010, Nikolov, Fabritius et al. 2011), such methods provide effective elastic properties at multiple length scales, from the molecular to the microscopic. Because the experimental probe conducted by my coworkers reports deformation and reorientation rather than effective moduli, a one-to-one comparison with multiscale models is not straightforward. A combination of such multiscale modelling and the current experimental method (especially at the microscale and above, where the honeycomb motif is integrated into the Bouligand structure) will be needed for a comprehensive structural understanding.

A weakness of the current experimental approach is that the XRD signal is an average of the patterns in both exo- and endocuticle in the L1 geometry, whose Bouligand layers have different stiffness, densities and ordering (Neville 1993). However, this is a limitation of the current sample-preparation protocol rather than the diffraction reconstruction method itself, and in future, sample preparation methods like focused ion beam milling or laser microdissection could enable isolation of distinct tissue regions. Also, as my coworkers focus on the crystalline diffraction signal from the chitin fibres, they do not separately account for the mineral phase deformation. The deformation of the fibres must therefore be interpreted as that of a mineralised chitin fibre. In L2 geometry, mineral reflections (corresponding to calcite) were observed only in the outer

parts of the tergite exocuticle, consistent with prior work on lobster cuticle showing calcite to be present only in the outer 50 μm (Al-Sawalmih, Li et al. 2009). The importance of different mineral chemical structures for impact resistance (e.g. fluoroapatite versus hydroxyapatite) has been shown before, and in the future (Amini, Masic et al. 2014) analysis of peak shifts of mineral, possibly in combination with spectroscopy (for the noncrystalline region) could shed light on the mineral phase mechanics.

In summary, using the in situ experimental results obtained by my coworkers, I explored the multiscale mechanisms of deformation in the chitinous cuticle of crustaceans. The cuticle has attracted considerable interest as an advanced bio-material, being the basic building block underlying several biological adaptations to sensation (Erko, Younes-Metzler et al. 2015) vision and impact resistance (Weaver, Milliron et al. 2012, Amini, Masic et al. 2014) inspiring development of bio-inspired composites. By showing explicitly the linkage between the diffraction intensity and the 3D multiscale deformation, both in the experimental results and the analytical formulae derived, this approach provides a template to apply this nanomechanical method to understand structure-function relations in these functionally diverse specializations. Furthermore, the presented method can be applied to study the correlation between structure and functional performance for biological and synthetic materials compromising crystalline and textured nanorod, nanofibres and nanoplatelets during in-situ or operando tests. Revealing the mechanisms of how the 3D structural changes of the crystalline components induce material functionality transformation hence will shed light on the designing of functional composites in different industries.

6 Multi-hit damage and perforation of metallic plates inspired by the attacks of the mantis shrimp

6.1 Introduction

Numerous studies reported the mechanisms of the impacts in biological structures. For instance, Butler and Kirbynson (Butler and Kirbyson 1979) described the hammering strategy that the *Haematopus bachmani* (black oystercatcher) adopts to separate the two valves of the oyster. They found that the bird uses its bill firstly to perforate the shell of the oyster and finally to sever the adductor muscles of the mollusc to prevent it from providing resistance. Other studies (Carlin and Gladstein 1989, Gronenberg 1995, Patek, Baio et al. 2006) focused on the smasher function of ant mandibles to catch preys and to defend against other ants. Ants use the mechanical energy stored in the mandible closer muscles to capture preys but also as propulsion to jump over competitor and escape. Deer fighting represents another example of biological impact (Currey, Landete-Castillejos et al. 2009) and high fracture toughness (Gupta, Krauss et al. 2013, Hang, Gupta et al. 2014). These animals, in fact, use their antler in the battles to gain access to female and defend (Clutton-Brock 1988). Although most of impact energy is absorbed by the neck muscles, antler contributes to locally dissipate energy and is designed to resist high impact loading without fracture. Similarly, antelopes, gazelles and goats (Kitchener 1987) use their horns as impact-resistant weapons for defence and offence.

The *Odontodactylus scyllarus* (subphylum: Crustacea, order: Stomatopoda, family: Gonodactylidae) (**Figure 6.1**) is one of the around 500 species of mantis shrimp that have been discovered. This crustacean possesses a very effective visual system (Cronin and Marshall 1989, Cronin, Caldwell et al. 2001, Thoen, How et al. 2014) and uses its hammer-like appendages to hunt and defend its burrows. The mantis shrimp's fast and powerful strikes can smash and perforate the shells of prey, like crabs, and snails which kill these animals instantaneously (Dingle and Caldwell 1969, Caldwell and Dingle 1975, Caldwell and Dingle 1976).
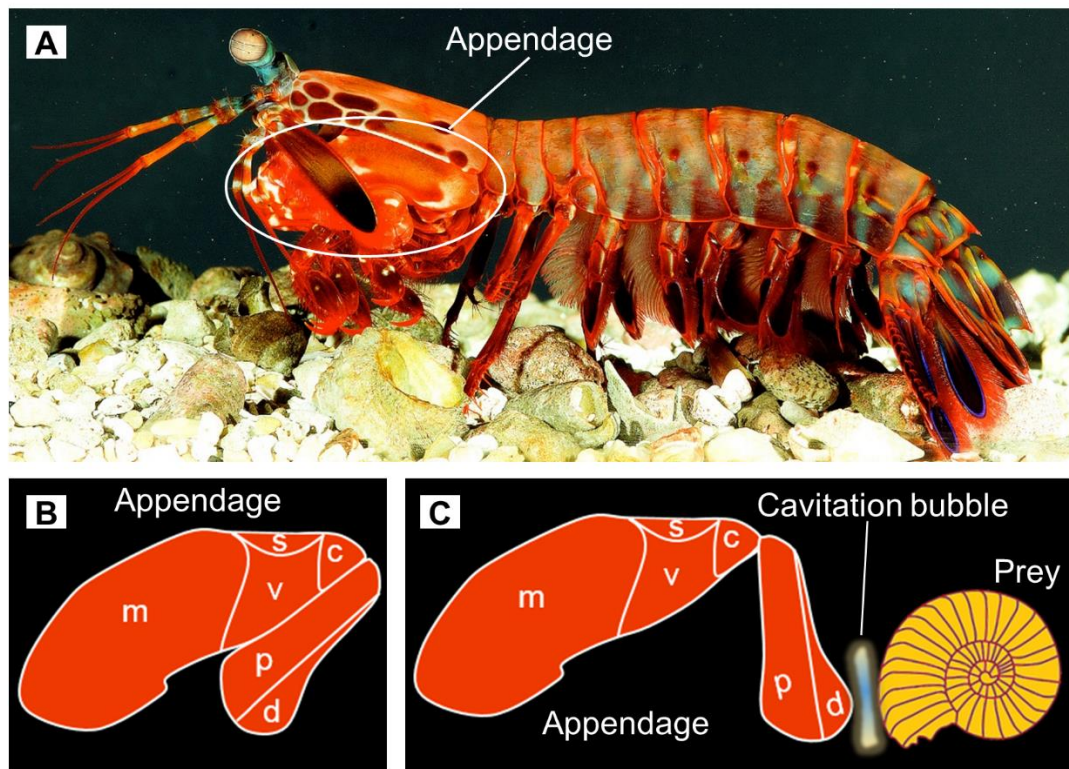
Figure 6.1 - The attack of the Odontodactylus scyllarus, commonly known as mantis shrimp. *A) A resting Odontodactylus scyllarus. The white circle highlights the appendage that the animal uses for hunting. B) Lateral view of the raptorial appendage in a resting position showing the morphology and nomenclature of the elements: d, dactyl; p, propodus; m, merus; s, saddle; c, carpus; v, meral-V. C) Lateral view of the appendage impacting the prey. As a result of the attack a cavitation bubble arises between the dactyl (marked as d in figure 1b) and the surface of prey.*

The high speed of strikes (23 m/s) is possible thanks to a rapid release of elastic stored energy in a click-joint power amplification mechanism (Patek, Nowroozi et al. 2007, Zack, Claverie et al. 2009, Claverie, Chan et al. 2011) made of flexor and extensor muscles which store a minimal amount of energy (Burrows 1969, Burrows and Hoyle 1972, McNeill, Burrows et al. 1972), a specialised saddle-shaped spring which is able to store 10% of the total elastic energy and a set of mineralised sclerites which are the structures where most of energy is stored (Patek, Korff et al. 2004, Patek, Rosario et al. 2012, Tadayon, Amini et al. 2015). Due to the extreme speed of these strikes, combined with their location underwater, cavitation occurs between the appendages and hard-shelled prey (Burrows and Hoyle 1972). First, the mantis shrimp impacts the target with its appendage determining a zone of low pressure (cavitation) in the fluid between the club of the appendage and the surface prey. Cavitation consists in the formation of bubbles as consequence of force acting upon a liquid, and their collapse generates large-amplitude shock waves, associated with the release of energy in the form of heat, noise and luminescence (Brennen 2013). Specifically, cavitation occurs at the interface between a solid structure and flow when nuclei containing small amount of gas become unstable and grow due to reduction of ambient pressure. This condition is verified during the mantis shrimp's attack due to the separated flow generated by the fast rebound of the dactyl after hitting the prey. The collapse of the cavitation bubble provokes a second impact, twice weaker than the first impact (Patek and Caldwell 2005). A previous research (Patek and Caldwell 2005) reported the intensity of the strike forces (approximately 480 and 240 N) and their time separation ($\approx$ 0.5 ms).

Explaining how these biological structures can absorb or dissipate impact energy without significantly damaging themselves (only the dactyl club which is the impacting region of the appendage suffers damage but its tissues are replaced during moulting) is a challenge for scientists. It is well known that the hierarchical organisation is the key success for the high toughness of bio-composites (Aizenberg, Weaver et al. 2005, Meyers, Lin et al. 2006, Wang and Gupta 2011). In these structures every level, from the nano- to the macro-scale length, contributes to the improvement of the mechanical properties of the total design through a set of mechanisms of deformation and energy dissipation. In fact, the basic constituents at the nanoscale are brittle minerals (with strength of 30 MPa and toughness $<<$ 1 MPa/m^2) and ductile proteins (with strength of 20 MPa) while the strength and fracture toughness measured at the macro-scale are up to 10 times higher than those of the initial constituents (Ji and Gao 2004). Two different approaches can be used to explore the fracture toughness mechanisms of the mantis shrimp's cuticle. The first one is based on understanding the contribution of material properties to structural toughness, while the second one focuses on comprehending the kinetics and dynamics of energy transfer. The first approach has been significantly followed. A study (Weaver, Milliron et al. 2012) gave a understanding of the high damage tolerance of the dactyl clubs. The results suggested that the helicoidal architecture and the material properties are keys to the success of this biological hammer. Other researchers (Amini, Tadayon et al. 2015) presented a study on the impact surface regions of the dactyl club of the crustacean. Their results indicated that both the outer and the inner parts of the club include mechanisms to prevent the macroscopic failure of the club and to absorb impact energy, such as interfacial sliding and rotation of fluorapatite nanorods.

194

Grunenfelder et al. (Grunenfelder, Suksangpanya et al. 2014) tested a set of carbon fiber-epoxy composite panels inspired by the helicoidal structure of the crustacean's dactyl club. Their experimental and numerical tests demonstrated that the helicoidal design is fundamental to enhance the residual strength and the capability of composites to absorb damage energy, and prevents crack propagation through the thickness of samples.

Although there is considerable work on the reasons for the high fracture toughness of the cuticle of the mantis shrimp (Weaver, Milliron et al. 2012, Amini, Masic et al. 2014, Amini, Tadayon et al. 2015) as well as on other species of cuticle (Raabe, Sachs et al. 2005, Raabe, Romano et al. 2006), there are fewer studies that analyse the kinetics and energy transfer of the impacts (Patek, Korff et al. 2004, Patek and Caldwell 2005, Claverie, Chan et al. 2011). To my knowledge, there have been no studies focused on whether the mantis shrimp uses an effective strategy to maximise the damage on the prey. Inspired by the double impact phenomenon observed during mantis shrimp predation, this study presents finite element simulations of single and multiple (double and triple) impacts to discover the best strategies to damage the target.

Damage is a physical process of deterioration when materials are subjected to loading. It consists, at the microscale level, in the accumulation of microstresses nearby defects or interfaces and breaking of bonds, in the growth and coalescence of microcracks into one crack (mesoscale level), and in the growth of the crack (macroscale level) (Lemaitre 2012). Although with different physical structures, all materials (such as metals, alloys, polymers, composites, ceramics, rocks, concrete and wood) show the same qualitative mechanical

behaviour on the meso and macro-scales. The first stage includes an elastic response, then yielding with an accumulation of plastic strain, anisotropy induced by strain, cyclic hysteresis, damage by monotonic loading or by fatigue, and crack growth under static or dynamic loads (Lemaitre and Desmorat 2005). Metallic targets feature damage mechanisms such as plastic deformation, plugging, spalling, scabbing, petalling, fragmentation, ductile hole enlargement and cavitation (Goldsmith 1999). In particular, during multiple impacts, initially, plastic deformation may take place once the von Mises stress exceeds the yield strength on the impact surface. Strain hardening then occurs, the yield strength possibly equals the fracture strength and no further plastic deformation will occur. At this point, the material becomes brittle, and the successive impacts[39] can remove part of the impacted surface. Understanding the mechanism of damage accumulation and material removal, even in the simplest scenario of spherical particles impacting a flat surface at normal incidence, is a difficult task (Woytowitz and Richman 1999).

The energy dissipated during the process of damage can be quantified by performing finite element impact simulations. Commercial finite element software, such as Abaqus (Hibbett, Karlsson et al. 1998) , allows to compute the damage energy dissipated during collisions of objects. The computation is based on the 'erosion method' which requires a set of input parameters to define when the damage starts occurring and how the damage curve evolves (a finite element is removed from the system when its stiffness reduces to the point that its load-carrying capability becomes null). It is clear that a complete characterization of the stress-strain curve of the material is necessary to implement this method. So far, such detailed and sufficient level of information

for the dactyl of the mantis shrimp is not available. Accordingly, impact simulations were performed, modelling a spherical bullet hitting a flat target, both made of aluminium, a generic but well established material suitable for the implementation of the erosion method through finite elements simulations.

A significant amount of numerical studies on impacts between metallic projectile and metallic targets analysing different geometrical configurations and materials is available in literature (Gupta, Ansari et al. 2001, Khan, Ansari et al. 2003, Gupta, Iqbal et al. 2007) but very few studies focused also on the effects of multiple bullet-impacts on metallic plates. An interesting study (Hong, Ooi et al. 2008) analysed the effect of multiple shots on metallic targets (with a thickness there time higher than the diameter of the spherical bullet) parametrizing the separation distance between impacting points, velocities of successive hits and separation time between two consecutive impacts. As a result, the authors found that these parameters affect the residual stress distribution of the target and specifically that the depth of the region where residual stresses develop increases as the number of hits and their velocity increases. No difference between the residual stress distributions caused by two sets of distinct double shots occurring at a separation distance equal to the diameter of the spherical bullet was found. However, as soon as this distance reduces, a larger magnitude of the maximum residual stress was found. Furthermore, the effect of different time delays between two impacts was studied (specifically, 2, 5, 10 and 20 μs). As a result, no particular difference between the residual stress profiles was found for these tests at different time delays.

Similarly, the shot-peening process was simulated through 3D finite element simulations of impacts between rigid spherical bullets and metallic plates (Meguid, Shagal et al. 1999). The effect of shot velocity, bullet shape and separation distance between two simultaneous hits. The authors found that the decrease in the aspect ratio of the ellipsoidal bullet provokes an increase of depth of the target where residual stresses arise. Furthermore, it was shown that the dynamic of simultaneous indentations at different locations of the target are similar to those obtained from single shots. The shot peening process (Frija, Hassine et al. 2006) involving simultaneous and numerous impacts was also numerically (FE simulations) analysed by measuring the superficial damage on the metallic target. The study shows that the damage of the target increases as the friction coefficient (Coulomb friction model) that models the interaction between spherical bullets and flat targets increases.

The aim of my study is to quantify the damage energy dissipated by the target and to reveal which are the most damaging sequences of consecutive impacts and their optimal time delay. Due to high complexity of the cavitation phenomenon I neglected it and I assumed all the strikes to be mechanical (caused by the physical interaction of the solid impactor and target). In other words, I supposed that the effect of a cavitation implosion can be represented by a second mechanical impact between two solid objects. The obtained knowledge can be valuable, for example, in designing safer protective armours.

6.2 Numerical modelling

6.2.1 Geometrical and elasto-plastic properties

The geometrical model includes a rigid spherical projectile and a flat target, made of an elastoplastic material. The Johnson-Cook model (Johnson and Cook 1983) was used to characterise the hardening and the damage process of the material here assumed to be aluminium alloy A2024-T351 (in the **Appendix E** there are the details of the model and in **Table A.2** the parameters). The target is clamped on its lateral sides while different values of velocities are conferred upon the sphere (**Figure 6.2**). Moreover, no fluid-structure interaction is considered and impacts occur in vacuum.
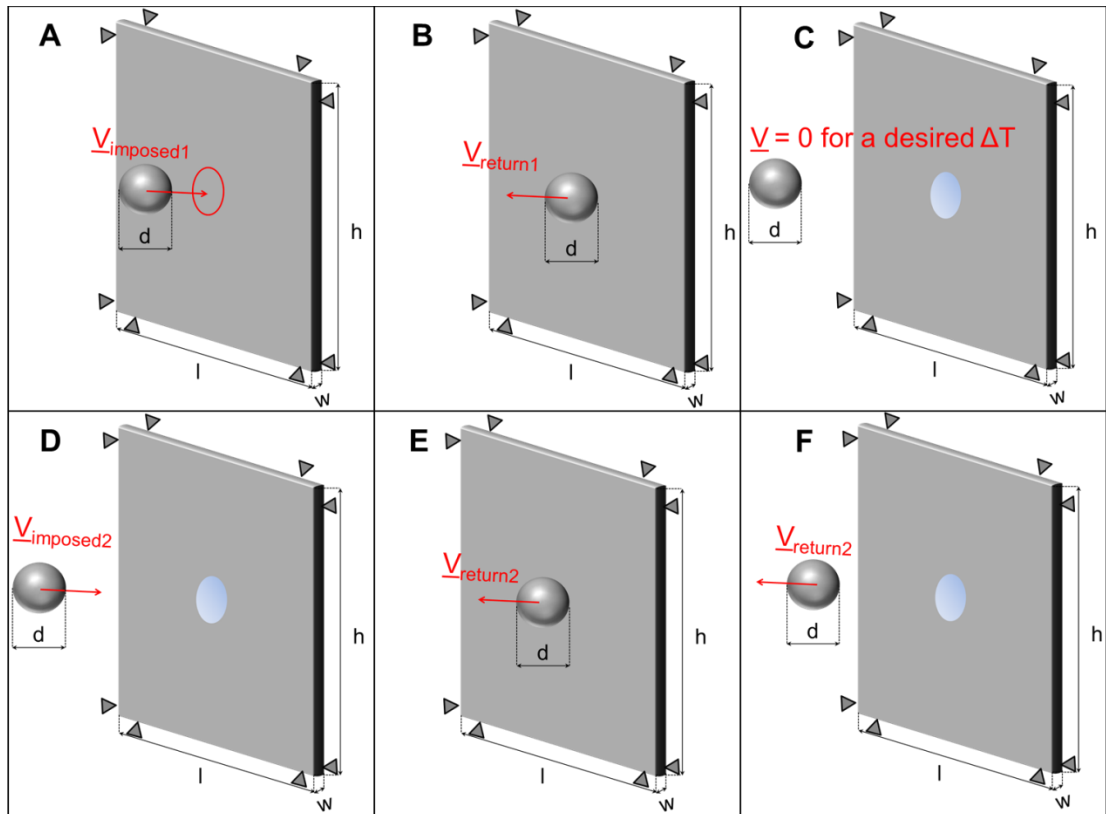
Figure 6.2 – Model for multiple impacts analysis made of a spherical bullet and a flat target. *The figure is representative of two impact analyses where: A) the bullet travels with the imposed velocity $V_{imposed1}$, reaches the target and B) bounces back with a non-controlled velocity $V_{return1}$. C) The bullet is then stopped for a desired interval of time and D) travels back toward the target with an imposed $V_{imposed2}$. Once the bullet hits the target for the second time, E) it bounces back with a velocity $V_{return2}$. F) The simulation is finally stopped.*

Three different diameter values for the projectile (4, 5 and 6 mm), approximating the size of the dactyl that an adult of mantis shrimp employs for its attack (which is ~ 4 mm (Amini, Tadayon et al. 2015), and a square target ($l = h = 24.12$ mm, $w = 0.5$ mm) were used. The target reproduces the size of the flat sensor used for experiments (Patek and Caldwell 2005). The impact, in the model, is caused by a projectile that moves at an initial constant velocity $V_{imposed1}$, hits the target for the first time, bounces back with a velocity $V_{return1}$ and immediately is halted (in the simulation, zero velocity) for a desired time (the time delay ΔT between consecutive impacts). Once the bullet has stopped for the necessary time, the

simulation can either terminate (single impact) or continue (multiple impacts), by assigning the bullet with the second impact (projectile velocity = $V_{imposed2}$) and eventually with the third impact repeating the steps described before (**Table 6.2**). In detail, the ΔT is the difference in time between two consecutive bullet/target surface contacts. The density of the material is 2700 Kg/m^3 (Mabrouki, Girardin et al. 2008). The mass is constant for a specific bullet size, and hence the kinetic energy related to the impacts depends only on the velocity, which can be used as a proxy for the energy.

6.2.2 Material and failure model

The Johnson-Cook model was also used to define the damage properties of the material of the target (in the **Appendix E** there are the details of the model and in **Table A.3** the parameters). Johnson-Cook is an empirical model which considers the effect of high strain rates, large strain, high temperature and pressure on materials under dynamic loading conditions. **Figure 6.3** shows a stress-strain curve in the presence of damage.
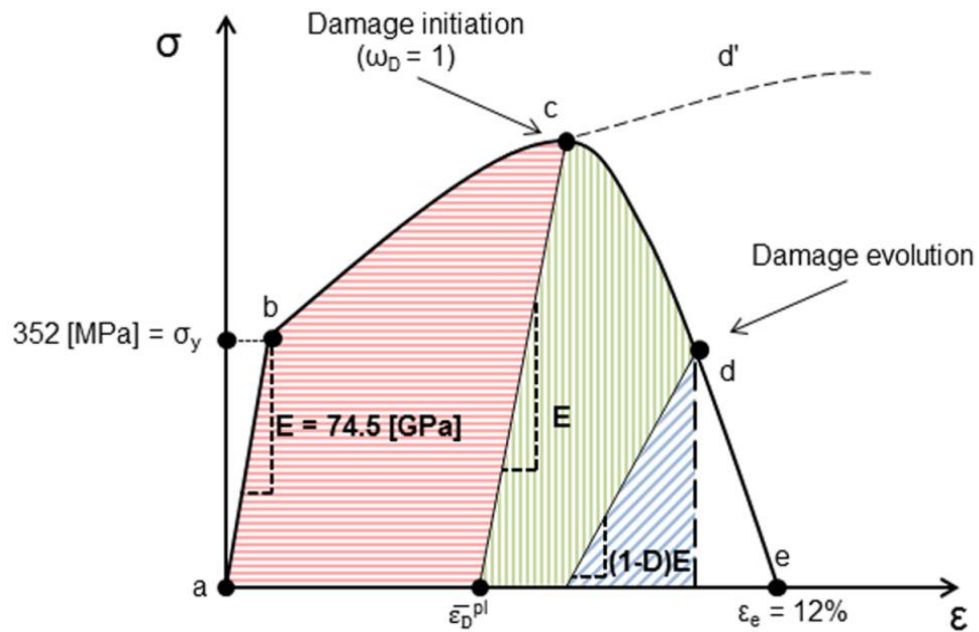
Figure 6.3 - Example of stress-strain response in the presence of damage.

A first linear pattern (curve a-b) is followed by yielding (point b) and by the strain hardening curve (b-c). When damage initiates (point c), the stress-strain curve starts showing strain softening. During damage evolution, loading/unloading curves follow the slope (1-D)E, where D is the variable indicating the level of damage and E Young's modulus. The material completely fails at point e. For a generic finite element at the evolution point d, the area highlighted by red and horizontal lines represents the inelastic strain energy per unit of volume; the area highlighted by green and vertical lines is the damage dissipated energy per unit of volume while the area highlighted by blue and oblique lines is the elastic strain energy per unit of volume.

The path a-b (**Figure 6.3**), representing the initial elastic response of the material, terminates at the plastic yielding point and is followed by the strain hardening curve (b-c). The damage initiation ($\omega_D = 1$), occurring at the point c, marks the beginning of a state of stiffness degradation, which ends when the

material is fully damaged (point e). The damage phenomenon, in fact, is characterised by a reduction of the material stiffness to the value of *(1-D)E,* where *D* ranges from 0 to 1 and is the dimensionless damage variable which decreases the material load-carrying capacity. In my simulations the evolution trend of the curve from the onset of the damage (point c) to the rupture (point e) was considered to be linear (linear softening) and the failure was defined by displacement. This value is 0.045 mm and was calculated by multiplying the value of the percent elongation at failure (12%) for the A2024-T351 aluminium alloy by the characteristic dimension of the single finite element (diagonal). At any given time during the analysis, the stress condition in the material is described by a scalar **Equation 81**, where $\bar{\sigma}$ is the effective or undamaged stress tensor or, in other words, the stress that would exist in absence of damage and that would follow the undamaged curve d' (**Figure 6.3**).

$$\sigma = (1-D)\bar{\sigma} \qquad (81)$$

When D = 1 a finite element loses all its load-carrying capacity. It is then removed from the model, and its contribution to the mass of the structure is eliminated.

6.2.3 Analysed configurations

The short time-duration force pulse caused by cavitation (in the biological system) is considered, in this work, as simply a second mechanical impact. The reason for this simplification is because simulating the damage that cavitation bubbles can cause upon collapsing is a very challenging modelling problem due to the unsteadiness of the phenomenon and of the interaction between fluid and

material (Brennen 2013) and it is beyond the scope of my simulations. Furthermore, it is important to note that although the damage is related to the energetic absorptive properties of the material, cavitation is independent of solid material behaviour.

The analysed configurations and the symbols to indicate the sequence of hits are listed in **Table 6.1**.

Number of impacts	Symbols	Configuration
Single	-	1 single
Double	==	2 equal
	↑↓	1st strong 2nd weak
	↓↑	1st weak 2nd strong
Triple	===	3 equal
	↓↑↑	1st weak 2nd strong 3rd strong
	↑↓↓	1st strong 2nd weak 3rd weak
	↑↓↑	1st strong 2nd weak 3rd strong
	↓↑↓	1st weak 2nd strong 3rd weak
	↑↑↓	1st strong 2nd strong 3rd weak
	↓↓↑	1st weak 2nd weak 3rd strong

Table 6.1 - Analysed configurations and list of symbols associated with them.

We analysed different dynamics characterised by various impact velocities. All the settings with the related velocities, are shown in **Table 6.2**.

1 IMPACT					
Bullet size [mm]	3		4		6
Velocity [m/s] (E = Kinetic energy) = 2.27 J	345		225		122
2 IMPACTS					
Bullet size [mm]	3		4		6
== [m/s] (0.5 E)	244	244	159	159	86	86
1st ↑ (0.67 E) 2nd ↓ (0.33 E) [m/s]	282	200	184	130	100	70
1st ↓ (0.33 E) 2nd ↑ (0.67 E) [m/s]	200	282	130	184	70	100
3 IMPACTS					
Bullet size [mm]	3		4		6

Bullet size [mm]	3			4			6		
=== [m/s] (0.33 E) (0.33 E) (0.33 E)	199	199	199	130	130	130	70	70	70
1st ↓ (0.2 E) 2nd ↑ (0.4 E) 3rd ↑ (0.4 E)[m/s]	154	218	218	101	142	142	55	77	77
1st ↑ (0.5E) 2nd ↓ (0.25E) 3rd ↓ (0.25 E) [m/s]	244	172	172	159	113	113	86	61	61
1st ↑ (0.4 E) 2nd ↓ (0.2 E) 3rd ↑ (0.4 E) [m/s]	218	154	218	142	101	142	77	55	77

1st ↓ (0.25 E) 2nd ↑ (0.5 E) 3rd ↓ (0.25 E) [m/s]	172	244	172	113	159	113	61	86	61
1st ↑ (0.4 E) 2nd ↑ (0.4 E) 3rd ↓ (0.2 E) [m/s]	218	218	154	142	142	101	77	77	55
1st ↓ (0.25 E) 2nd ↓ (0.25 E) 3rd ↑ (0.5 E) [m/s]	172	172	244	113	113	159	61	61	86

Table 6.2 - Simulated configurations for single and multiple impacts with a fixed total kinetic energy E = 2.27 J.

The minimum damage energy value, in the case of one impact and 4 mm spherical projectile (corresponding to a sphere velocity of 225 m/s) for which I observed a condition of partial damage, was 2.27 J. In this configuration the bullet provokes an hole and bounces back (a situation of partial damage is, for example, shown in **Figure 6.5b**). I considered this as a 'limit condition' between visible damage (high damage with complete perforation of the target, **Figure 6.5a**) and not visible damage (minimum damage with no perforation, **Figure 6.5c**) and I used it as basis of comparison with other simulations. Thus, the value 2.27 J was used to define, for all the configurations, the total kinetic energy of the projectile. In fact, watching the footages elaborated by the finite elements software was the first, fast and intuitive way to estimate the different dynamics and damage mechanisms qualitatively. The velocity values for the strong and weak impacts were calculated specifying that the sphere kinetic energy for the strong impact was twice as the one of the weak impact (**Equation 82**). Furthermore, I assumed that the sum of the kinetic energies related to the impacts is conserved and equal to the reference value $E_k{}^* = 2.27$ J, as shown in **Equation 83**.

$$\frac{1}{2}m_s V_{strong}^2 = 2\frac{1}{2}m_s V_{weak}^2 \qquad (82)$$

$$\frac{1}{2}m_s\sum_i^{2,3}V_i^2 = E_k^*$$

(83)

Variable time delays between consecutive impacts of 0.0 (the value tends to 0.0), 0.2, 0.4, 0.5, 0.6 and 0.8 ms were explored. The aim was to reproduce not only the mantis shrimp attack timing (0.5 ms) as found from experiments(Patek and Caldwell 2005), but also to explore different time delays within the same order of magnitude as the experimental value. The software used for simulation was *Abaqus 6.13 - 3*. The finite elements mesh was made of 43200 C3D8R (8-node linear bricks, reduced integration, hourglass control) elements for the target and 2200 C3D8R elements for the projectile. These values were achieved after mesh convergence tests. **Figure 6.4** shows the results from the mesh convergence test used to define the sufficient number of finite elements in the central region of the target which is the region mainly affected by the damage process.
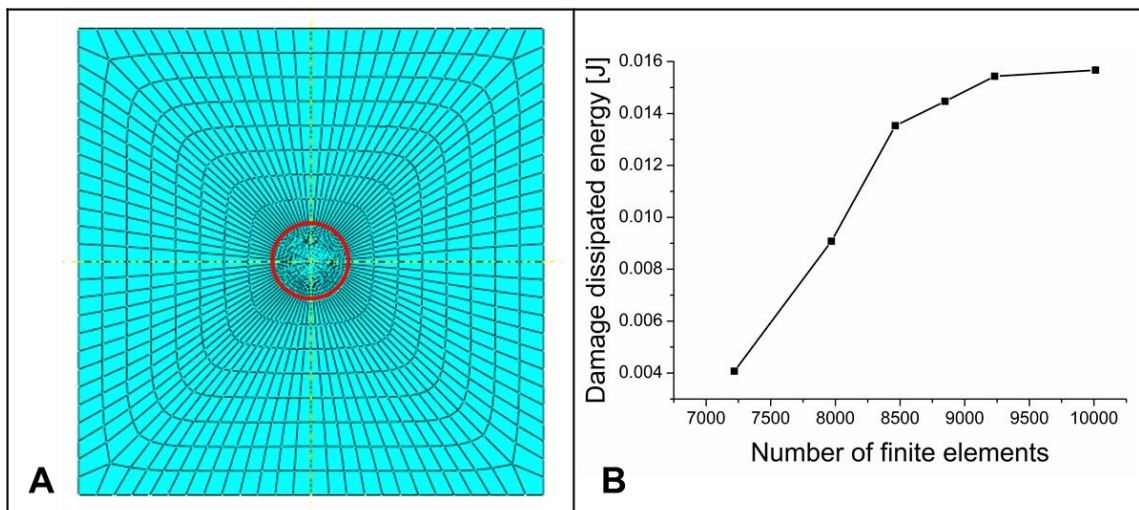
*Figure 6.4 - Mesh convergence test for the central region of the target. A) The mesh was obtained after partitioning the geometry into many sub-regions. B) Mesh convergence analysis was performed for the case 'single impact' of a 4 mm bullet. The test was achieved to define the sufficient number of finite elements in the central circular region (highlighted in red in **Figure 6.4A**) with a diameter equivalent to the diameter of the bullet.*

The size of elements of the target radially increases (smaller at the centre of the target) in order to have a higher computational precision on the region where impacts occur. Specifically, I used an 'approximate global size' of 0.6 mm for both smaller edges at the centre of target and bigger edges at its extremities. For the sphere an 'approximate global size' of 0.28 mm was used. Furthermore, no friction coefficient was imposed to characterise the impacts but only normal behaviour ('hard' contact).

6.2.4 Hertzian model for dynamic impacts

A Hertzian model was implemented to explain how the penetration power of projectiles depends on their size. In fact, it is possible to treat the dynamics of impacts as distributed applied static load by using the Hertz's theory for elastic collisions (Davies 1949). Davies (Davies 1949) analysed the case of a sphere of radius R impacting a flat target of the same material. At the impact, in particular at maximum compression, a circular surface contact arises between the two bodies. I report the main equations to calculate the radius of this circle of contact at maximum compression a_m (**Equation 84**), the maximum value of the total force P_m (**Equation 85**), the mean normal pressure $\bar{p}_m$ at maximum compression (**Equation 86**) and the pressure p'_m at the centre of the circle of contact at maximum compression (**Equation 87**).

$$a_m = \left[2.5\pi\rho \left(\frac{1-v^2}{E} \right) \right]^{\frac{1}{5}} R V^{\frac{2}{5}}$$ (84)

$$P_m = \frac{2}{3}\left(2.5\pi\rho\right)^{\frac{3}{5}} \left(\frac{E}{1-v^2} \right)^{\frac{2}{5}} R^2 V^{\frac{3}{2}}$$ (85)

$$\bar{p}_m = \frac{P_m}{\pi a_m^{\ 2}} = \frac{2}{3\pi}\left(2.5\pi\rho\right)^{\frac{1}{5}} \left(\frac{E}{1-v^2} \right)^{\frac{4}{5}} V^{\frac{2}{5}}$$ (86)

$$p_m^{'} = 1.5\bar{p}_m = \frac{(2.5\pi\rho)^{\frac{1}{5}}}{\pi}\left(\frac{E}{1-v^2}\right)^{\frac{4}{5}}V^{\frac{2}{5}} \tag{87}$$

ρ and E are the density and the Young's modulus of the material, v is the Poisson's constant, R is the radius of the contact circle and V is the velocity of the bullet. Furthermore, the normal pressure distribution, p, can be computed as function of size, material and velocity of the bullet, distance from the center of the contact surface r and radius of circle of contact (**Equation 88**).

$$p = p_m^{'} \frac{\sqrt{(a_m^2 - r^2)}}{a_m} \tag{88}$$

6.3 Results

6.3.1 Maximization of damage under particular impact combinations

The structural changes in the target can be divided into three classes corresponding to the size of the impactor bullet: high damage for the 3 mm diameter, partial damage with the formation of a central hole but without penetration in the case of 4 mm, and minimum damage for the 6 mm bullet (**Figure 6.5**).
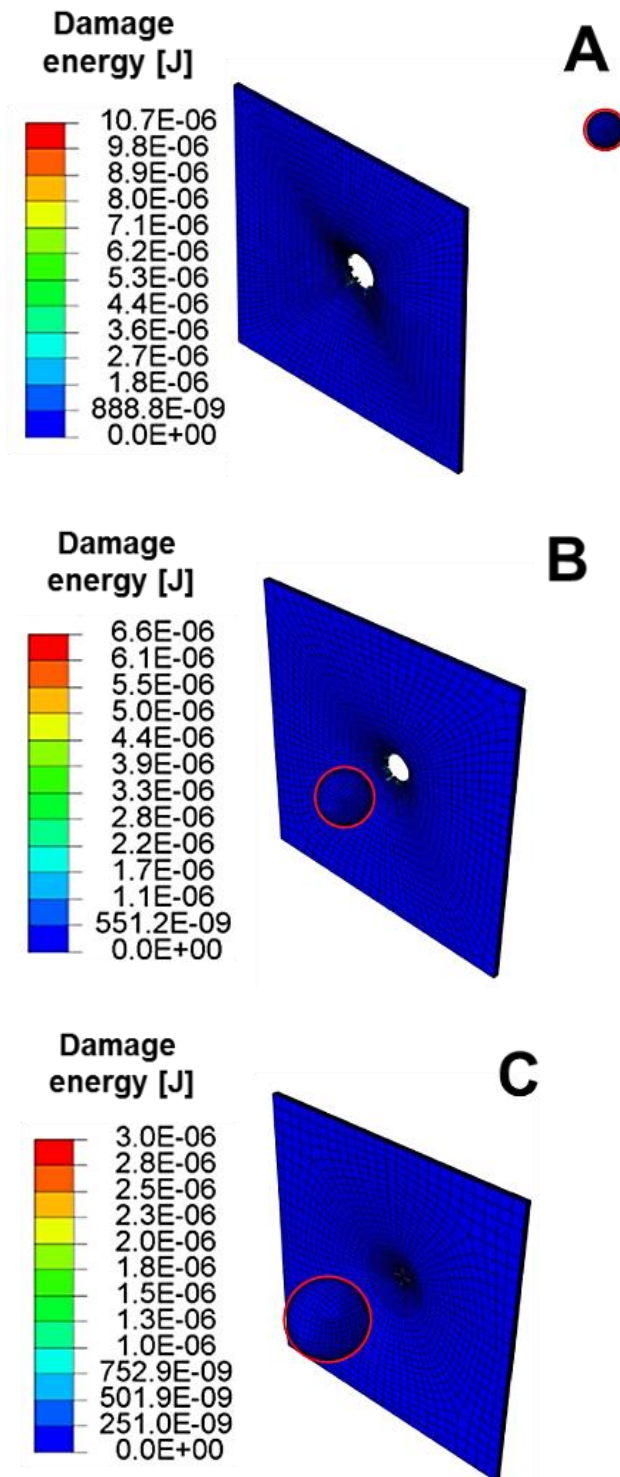
Figure 6.5 - Three different types of damage for the three sizes of the projectile. *a) High damage: complete perforation with a 3 mm diameter bullet. b) Partial damage: the 4 mm diameter bullet bounces back after provoking a hole on the target. c) Minimum damage: non-penetrating damage with a 6 mm diameter bullet. Images are taken for generic double impact configurations and are relative to the last instant of the simulations.*

In these results, the parametric dependency of damage on the interval between impacts as well as the impact protocol will be analysed. The choice of these parameters significantly affects the level of damage on the target. To show this more clearly, **Figure 6.6** presents the damage induced for the 'one/ two impacts' simulations in a two-dimensional grid with the impactor size as the second independent variable, while **Figure 6.7** summarises, analogously, the damage for the 'three impacts' configurations.
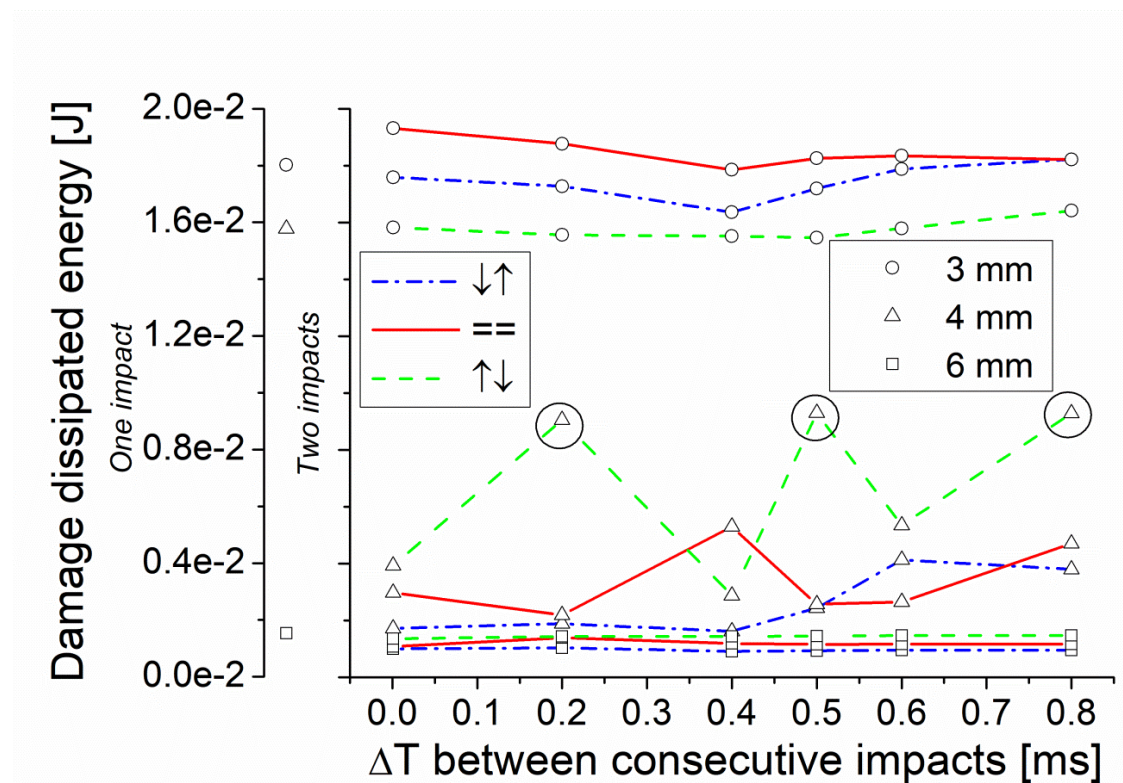
Figure 6.6 - One/two impact configurations (kinetic energy 2.27 J). *It is observed that for the intermediate impactor size, there are maxima for damage at two separate values of ΔT = 0.2, 0.5 and 0.8 ms (black circles), while a similar behaviour is not observed for the other two impactor sizes.*
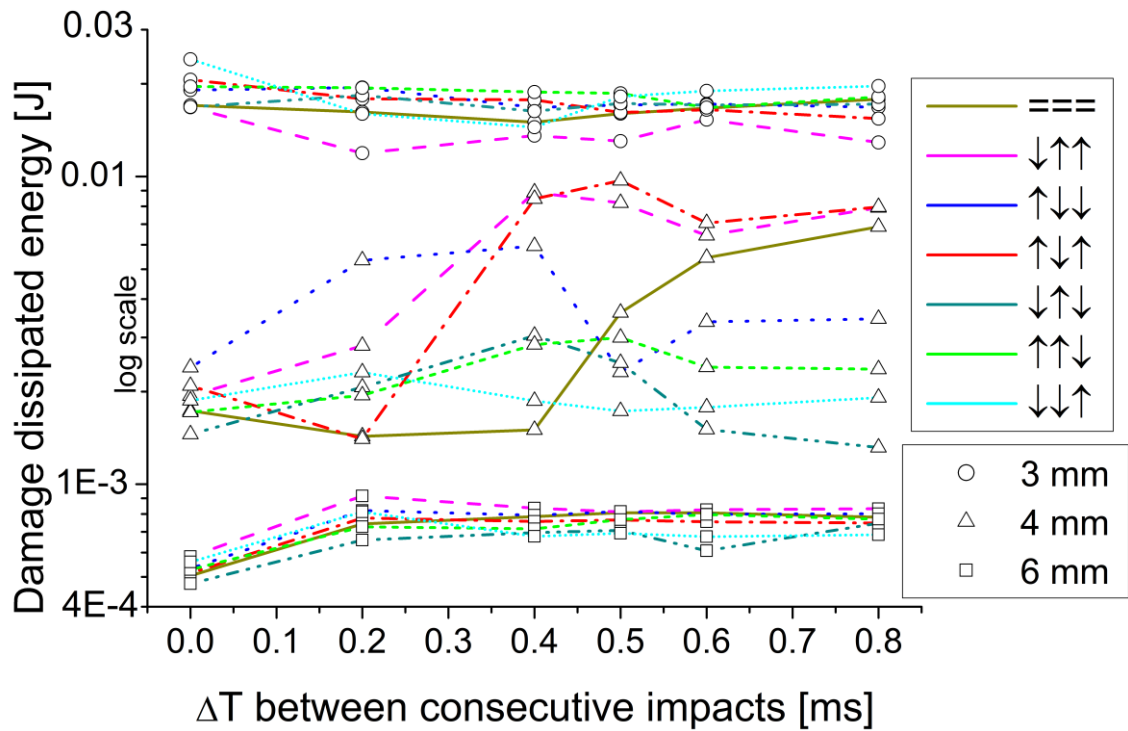
Figure 6.7 - Three impacts configuration (kinetic energy = 2.27 J) in a log scale graph.

On average, the highest values of damage dissipated energy were observed for a projectile diameter of 3 mm, displaying the highest penetration power of the smallest sphere, as expected (see **Section 6.3.3.2**), and the lowest penetration power of the biggest (**Figure 6.7**). In addition, as the highest standard deviation was found for the 4 mm bullet, it is possible to state that, for this impactor size, the results are very sensitive and strongly dependent on the different configurations (**Figure 6.8**).
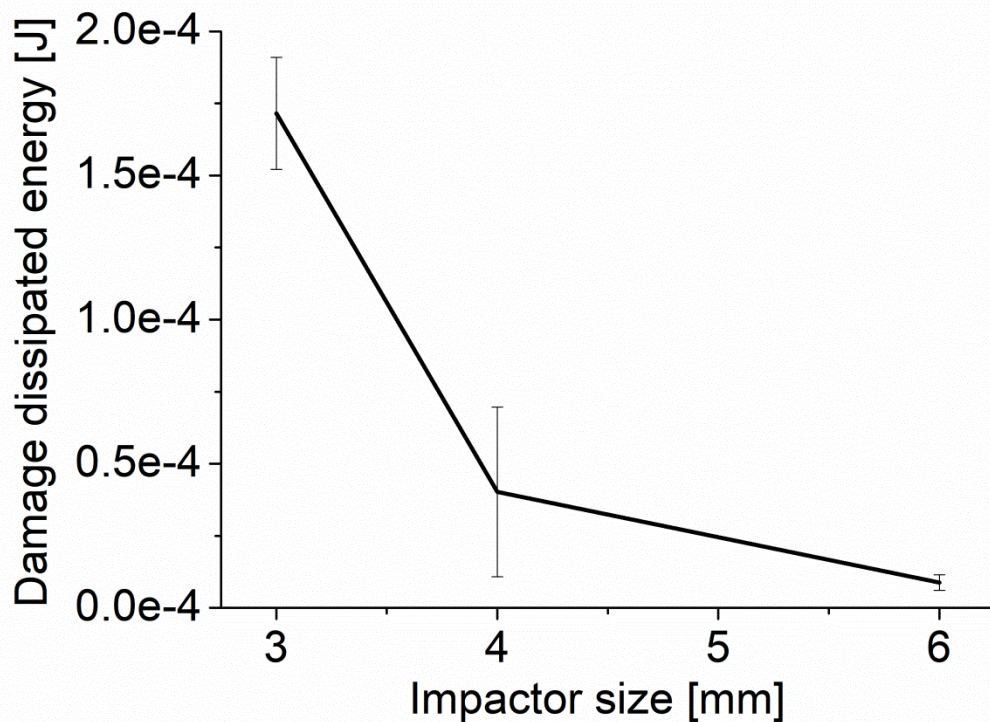
Figure 6.8 - 'Sensitivity analysis' for the three sizes of the bullet. *The values are obtained by averaging the damage energies from all the 11 configurations for single and multiple impacts. The vertical lines represent the standard deviation of the values. The highest standard deviation is observed for the 4 mm bullet, showing the high scattering of results.*

6.3.2 Parametric damage dependency as function of bullet size

For the 6 mm bullet (minimum damage) the values of damage dissipated energy are lower than the ones recorded for the 3 and 4 mm bullets. Furthermore, **Figure 6.6** and **Figure 6.7** do not show any peak or particular trend and all the values of damage dissipated energy (E_d) for single and multiple hits are included in the range 0.48 - 1.53 mJ, where the highest value corresponds to the one impact configuration (**Figure 6.6**).

For the 4 mm diameter (partial damage) results indicate that the one impact configuration (E_d = 15.78 mJ) is the most damaging. Among the 'two impacts

simulations' the highest value of damage was found in correspondence of the dynamics that the mantis shrimp usually adopts to kill its preys: first impact strong followed by a second twice weaker strike, with a time delay of ≈ 0.5 ms. I notice, in this particular impactor size, an oscillatory pattern with multiple maxima in the damage for several different impact combinations. Specifically, the curve ↑↓ features an oscillatory pattern with three peaks in correspondence of ΔT = 0.3, 0.5 and 0.8 ms. **Figure 6.9** shows different levels of plastic deformation and damage that occur with a 4 mm bullet, for three combinations of double impacts: a) ↑↓, b) ↓↑, c) ==. Among the three impact configurations, the highest damage value was found for ↑↓↑ (9.7 mJ) with a ΔT = 0.5 ms.

For 3 mm projectile (high damage) it is more effective to split the kinetic energy into three impacts rather than concentrate it in one or two. In fact, the highest peak (E_d = 24.04 mJ) was recorded for the configuration ↓↓↑ with a ΔT of 0.0 ms. In the case of single impact the damage dissipated energy was 18.2 mJ. For triple impacts the lowest peak (E_d = 11.91 mJ) was recorded for the case ↓↑↑ with a ΔT of 0.2 ms.
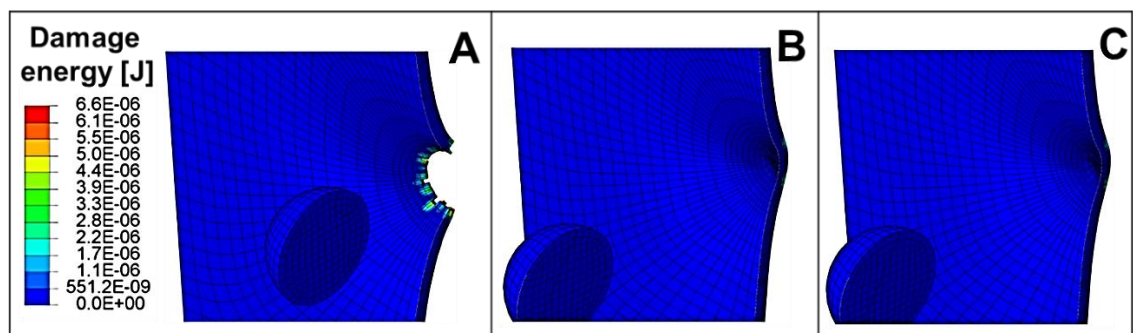
Figure 6.9 - Double impact for 4 mm bullet, with a ΔT of 0.5 ms. *Figures show the final instant (once simulations stopped) after the second impact. A) ↑↓. B) ↓↑. C) ==. Only for the configuration A) part of the target is detached from the structure once the bullet hits it for the second time.*

6.3.3 Possible models to explain maximization of damage

6.3.3.1 Modal analysis

Modal analysis was performed to verify the existence and influence of resonance phenomena, which are able to amplify the response of the target and then the damage on it in case of double impacts. This standard analysis solves the eigenvalue problem, shown by **Equation 89** (where ω^2 are the eigenvalues, **M** is mass, **K** is stiffness and **φ** are the eigenvectors of the target; in bold as they are vectors)**,** and allows to find the natural mode frequencies and the corresponding mode shapes of a structure (Ewins 1984).

$$\left(-\omega^2\,\mathbf{M}+\mathbf{K}\right)\boldsymbol{\varphi}=0 \qquad\qquad (89)$$

Table 6.3 shows a comparison of the force frequency values and target natural mode frequency. The force frequency was computed as number of impacts (two for this specific analysis) over the ΔT between the two collisions. As none of the force frequency values is equal or similar to the natural mode of the structure I am able to exclude that resonance phenomena occur on the target.

Force frequency [Hz]	Target natural mode frequency [Hz]
10000 (for ΔT = 0.2)	28149
5000 (for ΔT = 0.4)	23709
4000 (for ΔT = 0.5)	15953
3333 (for ΔT = 0.6)	15912
2500 (for ΔT = 0.8)	7730

Table 6.3 - Comparison between the force frequency values and the natural mode frequency values of the target. None of the values in the first column matches the ones in the second column (they are not even similar).

6.3.3.2 Pressure distribution from Hertzian model

Equation 88 was used to plot the values of normal pressure p versus the distance from the center of impact r for the three examined diameters by using the velocity values relative to the single-impact configurations (345 m/s for the 3 mm, 225 m/s for the 4 mm and 122 m/s for the 6mm bullet) (**Figure 6.10**). The Hertzian model is linear elastic and does not include plasticity deformation and damage mechanisms. Therefore, the graphs do not represent the real level of pressure occurring on the contact surface but are a useful tool to prove the higher penetration power of smaller projectiles. It is seen that (as expected) the smaller the projectile size the higher are the peaks in the pressure. Furthermore, the distribution of stress trends to concentrate toward the centre of the contact surface as the bullet becomes smaller, which is essentially as the area over which the bullet imparts contact stresses becomes smaller.
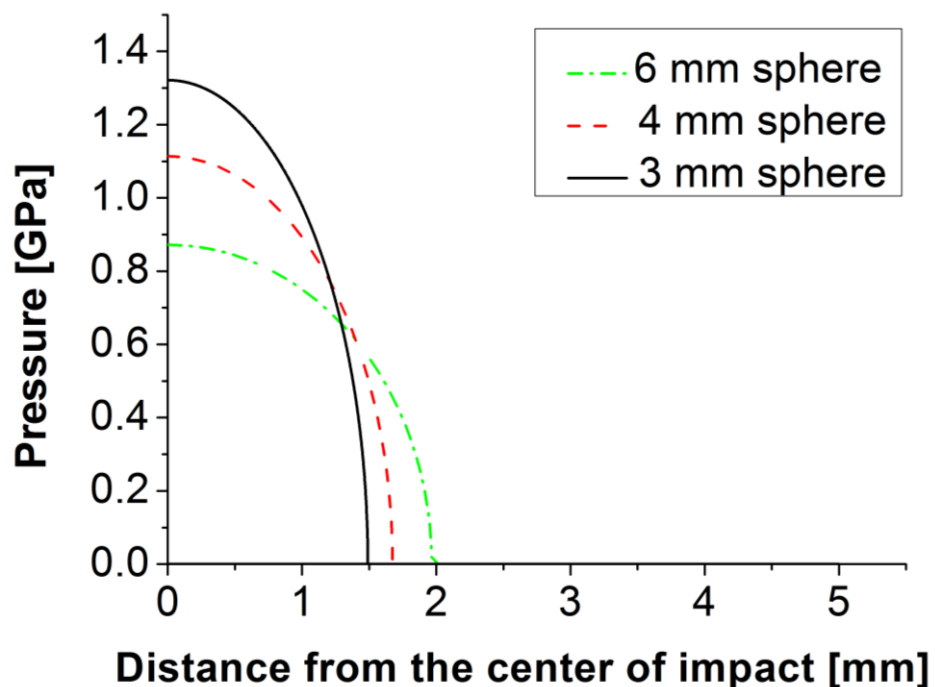
Figure 6.10 - Pressure distribution for 3 sizes of the examined bullets. *A smaller projectile size results in a higher pressure at the centre of the contact surface For smaller projectiles the zone affected by the impact reduces. The kinetic energy of impacts is constant and equal to 2.27 [J].*

6.3.3.3 Further simulations

Having identified the ↑↓ configuration as the impact scenario causing most damage among the double impacts for the 4mm bullet, I performed further simulations involving solely this configuration. This analysis was aimed at providing a further support to investigate the reasons of the peaks and oscillations observed particularly for the configuration ↑↓ and to check the influence of the geometry, stiffness and inertia of the target. **Figure 6.11** shows the results for different scenarios representing:

1) *Different material properties*: the original geometry with the only exception of the plate yield stress which was increased from 352 MPa to 752 MPa.

2) *Smaller target*: the original material properties for a modified plate: from (24.1 x 24.1 x 0.5) mm^3, which are the original dimensions, to (12.05 x 12.05 x 0.5) mm^3.

3) *Larger target*: the original material properties for a modified plate (from (24.1 x 24.1 x 0.5) mm^3 to (30 x 30 x 0.5) mm^3).
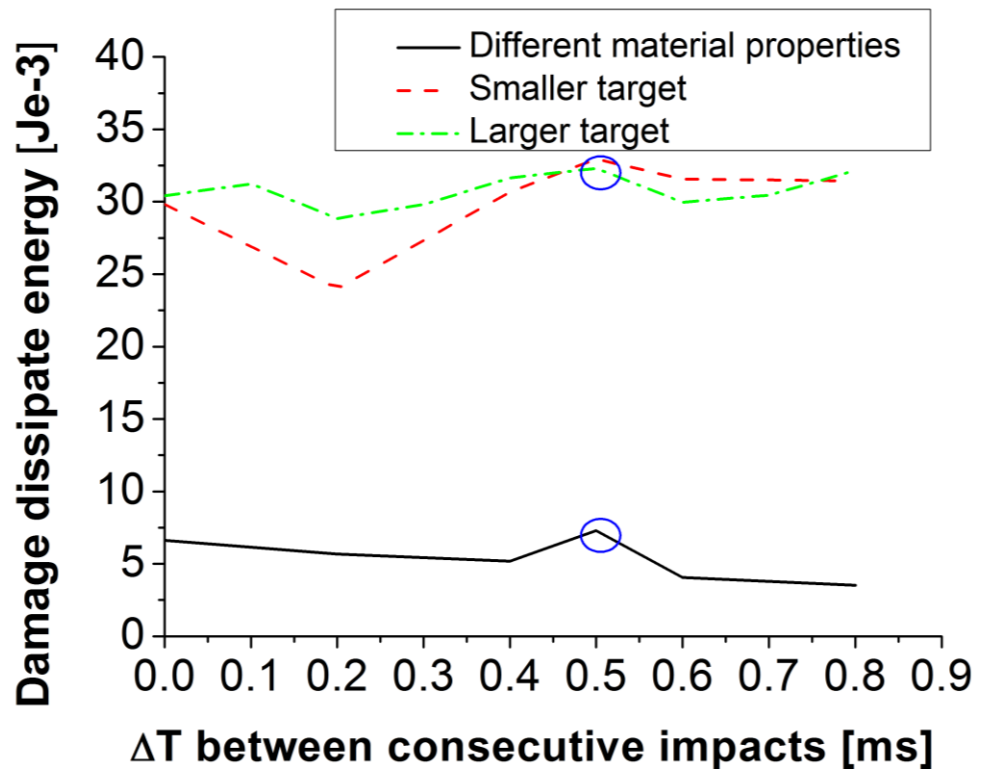
Figure 6.11 - Results for different material properties and sizes of the target. *The examined configuration is ↑↓. Each curve shows the peaks-values in correspondence to ΔT = 0.5 ms (blue circles), as already verified for the previous set of simulations (Section 6.3.1).*

I find that the time-interval between impacts (ΔT = 0.5 ms) – identified previously as leading to the maximum damage (**Section 6.3.1**) – remains the interval leading to the maximum damage over all three parametric variations 1) - 3) listed above. I believe that this provides a convincing clue that this time-interval is optimal for a damaging strategy for the ↑↓ (strong-weak) configuration.

6.4 Discussion

This chapter presented a set of parametric finite element analyses aimed at computing the damage provoked by multiple impacts. The source of inspiration for these simulations was an adult *Odontodactylus scyllarus*, a predatory crustacean which possesses raptorial appendages capable of strong and quick strikes. In the case of the crustacean, because of the presence of a second cavitation induced collapse, the prey/target actually encounters two impacts (of the ↑↓ variety (Patek and Caldwell 2005)) even though the impact of the dactyl club just occurs once. To mimic the damage that this type of impact would provide, I explored a purely impact-based scenario where the conditions for impact were varied around (in various parameters) the parameters found in the mantis shrimp strike. The aim was to capture the relevant mechanics rather than reproducing a "predator-prey" scenario. I tested three bullet diameters (3, 4 and 6 mm) and six different time delays between consecutive impacts (0.0, 0.2, 0.4, 0.5, 0.6, 0.8 ms) which approximate the sizes of the crustacean's appendage and the timings of its assaults (Patek and Caldwell 2005, Amini, Tadayon et al. 2015). The kinetic energy of the bullet was kept constant at the value of 2.27 J and the energy was distributed among single or multiple impacts by changing the velocity of the bullet.

Overall, three qualitatively different dynamics, associated with the three bullet sizes, were found (**Figure 6.5**):

a) For the 3 mm diameter, the bullet hit and perforated the target.

b) For the one of 4 mm, the bullet hit the target, led to a notable structural damage, typically a hole, and bounced back ('partial damage').

c) For the 6 mm diameter, the dynamics was characterised by minimal damage (the bullet bounced back without damaging the target by any great extent).

In the case a), although the most damaging case was ↓↓↑ with a ΔT of 0.0 ms, on average, the split of energy did not have any effect on the qualitative outcome. In fact, the measured damage values were similar for single, double and triple impacts. In detail, the most damaging configuration was obtained with one impact (18.02 mJ), while, on average, the damage energy reduced by 4% for double and by 5% for triple impacts. For the configuration b), it was more effective to concentrate all the kinetic energy in one impact. In this case the amount damage energy dissipated by the plate was 15.78 mJ. Splitting the energy in two impacts the damage on the target reduced, on average, by more than ~70%, whereas it reduced by ~80% in case of three impacts. For the dynamics c), the damage energy for a single impact was 1.53 mJ, while a reduction of ~20% in case of two impacts and of ~60% in case of three impacts was measured.

Furthermore, by splitting the fixed kinetic energy of the 4 mm projectile in two amounts, results showed that the damage on the target was visible only for the configuration which reproduces the time-interval characteristic of mantis shrimps (↑↓, with a time delay of ≈ 0.5 ms), whereas in the case of ↓↑ impacts and ==, the sphere bounced back without visibly damaging the target. Modal analysis, moreover, allowed me to exclude the influence of resonance phenomena on the damage mechanisms of the target in case of double impacts.

I hypothesise that the dynamics of oscillations, which the target exhibits after the first hit, has an important influence over the measured deformation and damage. During multiple collisions, the stiffness, the boundary conditions and the dimensions of the target are critical in determining for its unloading process once the bullet bounces back. In fact, considering the collision to be perfectly inelastic, the dissipated energy (assuming no variation of potential energy) is shown by **Equation 90**. K_i and K_f are the initial and final kinetic energy of the whole system, m are the masses, v are the vectorial velocities before colliding, V is the velocity of both bodies after collision; the subscript p indicates the projectile and t the target.

$$E_d = \Delta K = K_i - K_f = \frac{1}{2}m_p v_p^2 + \frac{1}{2}m_t v_t^2 - \frac{1}{2}\left(m_p + m_t\right)V^2 = \frac{1}{2}\frac{m_p m_t}{\left(m_p + m_t\right)}\left(v_p^2 + v_t^2 - 2v_p v_t\right)$$

(90)

I notice that the dissipated energy increases as the relative velocity between target and projectile increases. Therefore, the local velocity of the plate at the onset of the second or third collision affects significantly the amount of energy dissipated. In this sense, I hypothesise that the oscillatory motion of the plate is responsible for the different results obtained as ΔT varies. As demonstration of my previous statement, **Figure 6.12** displays the velocity patterns of a node in the central part of the target for ΔT = 0.4 mm (no peak) and ΔT = 0.5 mm corresponding to a peak, in the ↑↓ configuration.
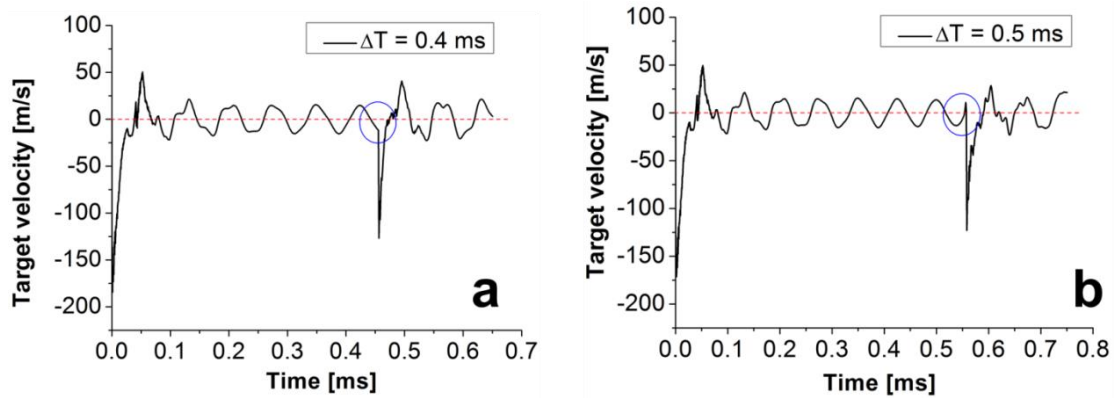
Figure 6.12 - Velocity curves of a single node on the central part of the target, for ↑↓ configuration. a) ΔT = 0.4 ms. b) ΔT = 0.5 ms.

The velocity of the projectile in the current convention was negative when it moves towards the target. I found that positive velocity of the target (opposite to the bullet) corresponds to a peak on the damage graph and vice versa. In other words, when the bullet and the local oscillating portion of target impact with opposite velocities, it is possible to observe the peaks of damage dissipated energy values. These oscillations are induced by the imposed boundary conditions (the four sides of the target are clamped) and by the material and geometrical properties of the target. In the real scenario, one expects the shell of the preys (snails, crustaceans and fishes) to be less flexible and the oscillations to be less evident, but it is still possible to hypothesise that such oscillating non-stationary phenomena occur and may have a central role in the energy dissipation mechanism.

6.5 Conclusions

This set of parametric finite element simulations demonstrated the existence of optimal damaging dynamics in multiple sequential hits for an aluminium alloy target and, in particular, showed that a double-impact strategy, as used by the

mantis shrimp, is the most damaging among the double impacts. However, I would like to remark that the experimental measurements of ΔT (Patek and Caldwell 2005), investigating the behaviour of the mantis shrimp attack are affected by standard deviation that was not considered in this study. In addition, in a real scenario multiple bubbles may form and collapse at different times after the first impact. Therefore the dynamics of the animal attack was only the source of inspiration for this work. My aim was not to reproduce the real scenario but to verify the existence of best damaging strategies for a fixed amount of kinetic energy of the impactor. However, the arbitrariness of the assumption behind the model, coupled with my results, lead me to hypothesise that the shrimp may use an 'optimal' damaging strategy that may be quite general for materials. Specifically, only the heel of the appendage resembles a sphere (as modelled in my simulations) while the preys' outer shells, usually snails, have complicated spiral geometries. In addition, the mineralised chitin composite constituting the shrimp's dactyl as well as the highly mineralised nacre shells have different mechanical properties from aluminium (Meyers, Lin et al. 2008). Therefore, the fact that a different material pair leads to maximum damage at the similar time interval suggests that the kinetic mechanism for damage may even be partly material-independent. Further studies are necessary to confirm my hypothesis. For instance, it would be useful to experimentally measure the forces and the timing of the crustacean attacks for target of different materials, to discover if and how the animal adapts its strategy to the surface it faces. Simultaneously, it would be opportune to reproduce these experimental scenarios and quantify the damage by fluid-structure interaction simulations, to understand if the animal's strategies are the most damaging. In fact, the use of optimization concepts are not foreign to biological

investigations, as for example applications of optimization theory and game theory to the evolutionary adaption in biology (Werner and Hall 1974, Stephens and Krebs 1986, Mangel and Clark 1988).

7   Conclusions and future developments

This aim of this thesis was to investigate and analyse new mechanisms of deformation and energy dissipation at different length scale in hierarchical bio-composites such as bone and arthropod cuticle (**Chapter 1**). These mechanisms combined with the intrinsic hierarchical design that these materials exhibit (**Chapter 2**) lead to improved mechanical properties (Ji and Gao 2004, Ritchie, Buehler et al. 2009, Launey, Buehler et al. 2010) and for this reason attracted the interest of scientists working in the experimental and modelling fields (**Chapter 3**).

In **Chapter 4** I presented a finite element model to examine the inelastic response of mineralised collagen fibrils in antler under cyclic loading. Results demonstrated that the hysteresis fibrillar behaviour is caused by the interfibrillar staggered configuration leading to localised plasticity while the heterogeneous stress patterns are due to the damageable cohesive interface between fibrils. The combination of these simulations and experimental data (Gupta, Krauss et al. 2013) provides the necessary information to explain two mechanisms of deformation and energy dissipation at the fibrillar level in bone. The new insights may be of inspiration for the creation of new impact resistant materials with modern manufacturing processes.

Recently, the fast growth of additive manufacturing allowed material scientists to create and analyse new complex materials. Previously, one of the main limits for the application of the bio-inspired principles to new materials was the need

of new manufacturing techniques. In fact, the traditional manufacturing techniques for composite materials were not sufficiently flexible and precise to incorporate the level of complexity that bio-inspired materials require. For this reason, only recently new studies are available in the field of 3D printed bio-materials (Dimas, Bratzel et al. 2013, Libonati, Gu et al. 2016, Parwani, Curto et al. 2016). Previous studies already investigated the effect of staggering on the mechanical performances of 3D printed material. Dimas et al. (Dimas, Bratzel et al. 2013) provided a first attempt at utilizing additive manufacturing to create tough bio-inspired composites. Their interest focused on the fracture mechanics of staggered prototype showing that crack deflection is one of the main toughening mechanisms in such systems. Zhang et al. (Zhang, Heyne et al. 2015) instead proved that the staggered configuration enhances the energy dissipated by 3D viscoelastic materials. Although this configuration attracts increasing interest, there is no evidence in literature of previous studies on the fatigue response of staggered materials. In fact, I believe that this design could be implemented to study the mechanics of 3D printed bone-like materials under cyclic loadings.

In **Chapter 5** I provided an analytical approach based on the lamination theory (described in details in the **Appendix C**) to compute fibre deformation and reorientation in arthropod cuticle. I believe that a similar method could be applied to other Bouligand structured materials such as bone, tendons and insects cuticle. Overall, the analytical formulation and experiments show that all the lamellae tend to rotate towards the tensile axis. On the contrary, recent studies (Zimmermann, Gludovatz et al. 2013) evidence that in another Bouligand structured material, such as the fish scale, under tensile loading

some groups of fibrils rotate towards the tensile axis while other sets rotate towards the opposite direction. These differences between similar Bouligand materials may be due to different material properties (for example higher stiffness of chitin compared to collagen fibres) but also to different interactions and deformation mechanisms between fibres and matrix. Investigating these mechanisms of deformation and reorientation, coupling different material models for fibres and matrix, may help to elucidate these differences. In addition, it would be of interest to create a modified version of the lamination theory which is able to analyse also the plastic behaviour of materials. This approach would allow me to compute the amount of energy dissipated by deformation and reorientation in these plywood materials providing an energetic quantitative analysis of these mechanisms.

In **Chapter 6,** inspired by the mantis shrimp's strategy, a set of parametric finite element simulations analysed the dynamics of a spherical bullet hitting a flat aluminium target exploring the effects of splitting a certain fixed amount of kinetic energy over multiple impacts. Results showed that the damage dissipated energy on the target is influenced by its oscillatory response. I believe that simulating these dynamic scenarios, reproducing the real structure and material properties of the mantis shrimp's dactyl and of the preys' shell, could unveil the existence of specific time delays between consecutive impacts that minimise the damage on the mantis shrimp's club and maximise the damage on the target. These studies could be useful to determine optimum damaging strategies with multiple hits.

I also suppose that the shape of the target covers an important role in its dynamics response. The stomatopod uses its wavy tail (telson) (**Figure 2.3**) to defend against the violent attack of other shrimps. Firstly, it would be of interest to experimentally explore the structural and material behaviour of the telson to verify if differences with the tergite (abdominal section of cuticle) at the micro and nano-scale exist. Secondly, it may be opportune to investigate the role of the shape at the mesoscale (the highest hierarchical level). I suppose that in this case the undulated shape leads to different stress distribution and energy absorption if compared to the curved tergite. In this perspective, the paper of Patek and co-workers (Taylor and Patek 2010) could already give some suggestions. In fact, they performed impact tests on both the tergite and telson of the animal measuring the coefficient of restitution. They found that the telson operates mostly as a 'punching bag' rather than a 'trampoline' (that, instead, characterises the response of tergite) and it is able to dissipate 69% of the impact energy while the abdomen dissipates only the 55% (Taylor and Patek 2010). In other words, the telson is able to plastically dissipate energy while the tergite behaves elastically returning most of the impact energy. This ability to dissipate energy may be due to the combination of material properties (for instance, the level of mineralization), geometry properties and mechanisms of energy dissipation occurring at multiple hierarchical levels. Unveiling these differences could be a fundamental key to discover new features potentially useful for the design of armours or protective human applications.

The different shapes that telson and tergite feature may be of inspiration also to understand how, starting from the same basic constituents, different parts of cuticle evolved. For instance, one may hypothesises that initially the cuticle was

228

uniform and that reached the actual configuration through a process of evolution. It could be of interest to discover if natures adopts 'buckling-technique' to obtain wavy geometries and to differentiate the shape in different zones of the same structural material. To prove this, buckling and post-buckling simulations of the complex structure of the tergite could be performed with the final aim of showing whether a telson-like structure can be obtained by buckling a tergite-like one.

I also believe that the application of optimization and topological techniques, normally used for structural engineering application, could be a useful tool to comprehend in details whether Nature optimised the hierarchical structure in bio-composites and which are the criteria that are used. Specifically, whether the wavy shape of the telson is optimised for impact resistance and energy dissipation could be possibly determined. For instance, it could be opportune to discover what is the optimum 'telson-like' shape (for example, given by a particular sinusoidal function) for these aims. Yaraghi and co-workers (Yaraghi, Guarín-Zapata et al. 2016) observed a fibrous herringbone (sinusoidal) pattern within the impact region of the dactyl club of the mantis shrimp with a wavelength of 45 µm and an amplitude that grades from 100 µm at the impact surface region (outer layer) to 50 µm at the inner layers of the impact region. They also performed finite element simulations combined with mechanical compressive tests on 3D printed prototypes to compare the 'classical' helicoidal with the herringbone structure. Results demonstrated that the herringbone-like structure is able to absorb up to 3.43 times more compressive energy than the helicoidal structure (Yaraghi, Guarín-Zapata et al. 2016). These results confirm

that the structural shape covers an important role in stress distribution and consequently in energy absorption/dissipation.

Inspired by the attack of the mantis shrimp, I believe that new insights could also arise from the investigation of the predatory behaviour of the animal. I think it may be fascinating to understand if the animal is able to sense the materials and structures is facing and adjust the speed of impacts to maximise the damage through cavitation effect. Mantis shrimp possesses an exceptional sensory system that plays a central role in its processes of learning and adapting (Cronin, Caldwell et al. 2006). In fact, like other crustaceans, it senses the external environment by flicking the antennules that extend quite far from its anterior region and also by using its large eyes that are located on mobile stalks driven by a system of muscles (Cronin, Caldwell et al. 2006). The antennules serve as chemoreceptors for feeding, sensing the presence of other animals and communicating (Mead, Wiley et al. 2003), while the eyes pre-process the information flows which are then transferred to central nervous system providing details about objects location, distance, motion and colours (Cronin and Marshall 2004). Whether this sensory system is optimised for the efficiency of the predatory sessions is still unknown but recent studies demonstrate the ability of the Stomatopod to learn and adjust the predatory strategy when facing different sizes of snails. In fact, Caldwell and Childress (Caldwell and Childress 1990) found that the animal, placed in an aquarium with thick-walled snails, learnt how to smash their shells with progressively fewer strikes proving its tendency to learn and adapt the strategy of attacks to the size of target. These findings could support my hypothesis and encourage further studies in this direction.

Overall, the findings of my thesis could support the development of new concepts and new design for ballistic resistant body armours. The main function of body armours is to impede projectile penetration into human body or, more generally, to diffuse the impact energy. Therefore, body armours are created to be damage-resistant, lightweight and energy dissipating (David, Gao et al. 2009). A key role for the achievement of these features is played by the material properties of their components and by the mechanisms of deformation and energy dissipation occurring at different length scales in their structure.

The materials used for the creation of ballistic armours are mainly fabric, ceramics and laminated composites. Ballistic fabrics are usually made of interlaced natural or synthetic fibres. These systems dissipate the impact energy through fibre deformations and inter-fibre friction when sliding against each other. Typically, these armours are made of many layers to ensure that all the impact energy is dissipated and a projectile is stopped. The presence of many layers rather than a unique one introduces two additional effects leading to energy dissipation. The first one is the relative frictional sliding between the different layers, while the second one is the represented by the increased region where stress waves can travel, specifically, not only within a single plane but also through the thickness of the multilayer armour (Barauskas 2005). Bi-layer ceramic armours, instead, are designed to take advantage of the mechanical impedance mismatch between a ceramic tile, which is the first layer exposed to the impact, and a backing plate, which is the underlying layer adjacent to the tile. For this type of armour, an impacting projectile provokes compressive stress waves that travel across the thickness of the ceramic tile

and that are reflected at the interface with the second layer due to the higher stiffness and mechanical impedance of the backing plate. The reflected waves are of tensile mode and act as a dumping mechanism for the other compressive waves. Therefore, the damage process and crack propagation mechanisms are controlled by the magnitude of the tensile stress waves in the ceramic layer and by the magnitude of the compression stress waves in the backing plate (Chen, Rajendran et al. 2007). Another important requirement is the mobility of the wearer which requires the armour to be lightweight. Laminated composites have been developed to satisfy this criterion. They are usually made of a ceramic hard layer connected either to a fibre reinforced or to an aluminium backing plate by an intermediate layer. The frontal ceramic layer fulfils the function of blunting and breaking the incoming projectile while the backing plate dissipates the kinetic energy of the projectile (David, Gao et al. 2009). The breakage of the bullet provoked by the first layer causes an increase of the contact area with the supporting plate and, therefore, a reduction of the local pressure (Übeyli, Yıldırım et al. 2007). An important function is covered by the intermediate layer. Interesting studies have shown that an intermediate layer made of metallic foam increases the capability of absorbing the stress waves resulting from the impacts through a mechanism of foam densification (Gama, Bogetti et al. 2001) (Schaeffler, Rajner et al. 2005).

Energy dissipation of armours can be improved also through specific internal micro-design. An interesting design was introduced by (Wynne 1998) who patented a multilayer armour made of many fabric layers and two flexible metallic plates with a pyramid-shaped surface designed to deviate and deform the projectiles. This design allows to increase the path of the projectile through

the thickness of the armour determining also an increment of the energy dissipated by the armour. In addition, the projectile is forced by the specific shape of pyramids to have a lateral sliding with the armour (**Figure 7.1**). This enhances the area of impact and reduces the local pressure.
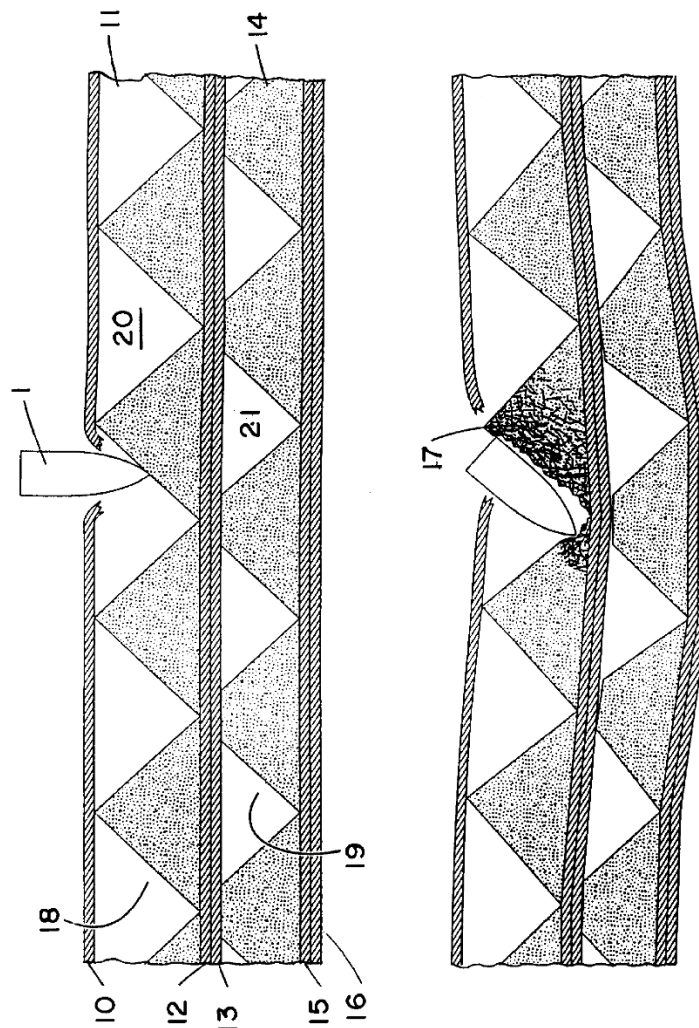
Figure 7.1 - Mechanism of deviation of a bullet in the pyramid-shaped armour designed by Wynne (Wynne 1998).

As shown, the choice of materials and design at different length scale determines the effectiveness and the behaviour of armours. In this context, I think that the mechanisms of deformation and energy dissipation that I studied in my thesis could contribute to the development of new bio-inspired armours.

233

For instance, it would be interesting to understand whether the mechanism of fibre reorientation, such as the one studied in **Chapter 5**, increases the ballistic limit and the energy dissipated during impacts in multi-layer composite armours. Indeed, fibre reorientation not only involves the deformation of fibres (and therefore potential plastic deformation) but also relative sliding between matrix and fibre and, therefore, frictional dissipation of energy. In **Chapter 4** I have shown that staggered arrangements of fibrils deforming plastically feature hysteretic energy mechanism of energy dissipation under tensile cyclic loading. The staggered design could be implemented to enhance the energy dissipating capability of composite bilayer armours where the external plate fails under tension, as explained above (Chen, Rajendran et al. 2007). Finally, the study presented in **Chapter 6** has shown that an important role in dissipating the energy deriving from multiple impacts is played by the specific dynamics of impacts. This concept could be applied to find optimized damaging dynamics with multiple bullets. However, the final goal should be to stimulate the research of new solutions and design for safer armours.

Appendix

A. Matlab scripts used to implement the laminate theory

Some examples of the *Matlab* scripts developed and used for implementing the

laminate theory (**Chapter 5**) are reported below.

```
clc; clear all
format short;
%Lamina material data

tply = 1e-7;                                  %ply thickness [m]
s1=(-90:1.8:88.2);   %lamination sequence

E_ch=60e9;  %cristallyne region of chitin inside the chitin protein nanofibrils
fi_ch=0.31;
ni_ch=0.25;
E_prf=56e6;  %protein region inside the chitin protein nanofibrils
fi_prf=0.69;
ni_prf=0.28;
E_acc=37e9;  %ACC spherules inside the mineral-protein matrix
fi_acc=0.9;
ni_acc=0.35;
E_prm=570e6;  %Proteins inside the mineral-protein matrix
fi_prm=0.1;
ni_prm=0.28;
```

```
fi_fibril=0.22;
fi_matrix=0.78;
```

```
%1st rule of mixture
E_fibril=(fi_ch*E_ch)+(fi_prf*E_prf);
ni_fibril=(fi_ch*ni_ch)+(fi_prf*ni_prf);
E_matrix=(fi_acc*E_acc)+(fi_prm*E_prm);
ni_matrix=(fi_acc*ni_acc)+(fi_prm*ni_prm);
G_fibril=E_fibril/(2*(1+ni_fibril));
G_matrix=E_matrix/(2*(1+ni_matrix));

%2nd rule of mixture
E1=(fi_fibril*E_fibril)+(fi_matrix*E_matrix);
E2=1/((fi_fibril/E_fibril)+(fi_matrix/E_matrix));
G12=1/((fi_fibril/G_fibril)+(fi_matrix/G_matrix));
ni12=(fi_fibril*ni_fibril)+(fi_matrix*ni_matrix);
ni21=ni12*E2/E1 ;          %Poisson's modulus


%--------------------------------%
nply=length(s1) ;
t=nply*tply

%Lamina stiffness matrix
Q12(1,1)=E1/(1-ni12*ni21);
Q12(2,2)=E2/(1-ni12*ni21);
Q12(1,2)=ni12*E2/(1-ni12*ni21);
```

```
Q12(2,1)=Q12(1,2);
Q12(3,3)=G12;

T=cell(1,100);
Ts=cell(1,100);
Qxy=cell(1,100);

for i=1:nply
teta=s1(i);
m=cosd(teta);
n=sind(teta);

T{i}=[ m^2  n^2   2*m*n
       n^2  m^2  -2*m*n
      -m*n m*n   m^2-n^2];
Ts{i}=inv(T{i});
Qxy{i}=Ts{i}*Q12*Ts{i}';

end

if   rem(nply,2)==0  %n is even
     h=(-nply/2:nply/2)*tply;
 else
     error('the number of plies is odd')
end

     A=zeros(3);
     B=zeros(3);
     D=zeros(3);

     for i=1:3
     for j=1:3
     A(i,j)=(Qxy{1}(i,j)*(h(2)-h(1)));
      B(i,j)=(Qxy{1}(i,j)*1/2*(h(2)^2-h(1)^2));
      D(i,j)=(Qxy{1}(i,j)*1/3*(h(2)^3-h(1)^3));

for   k=2:nply;
     A(i,j)=A(i,j)+(Qxy{k}(i,j)*(h(k+1)-h(k)));
     B(i,j)=B(i,j)+(Qxy{k}(i,j)*1/2*(h(k+1)^2-h(k)^2));
     D(i,j)=D(i,j)+(Qxy{k}(i,j)*1/3*(h(k+1)^3-h(k)^3));
end
     end
     end

% if max(max(abs(B)))<1e-6
     a=inv(A);
      d=inv(D) ;
% else
%    error('the laminate is not symmetric')
%end

%%Laminate mechanical properties
Ex=1/(a(1,1)*t)
Ey=1/(a(2,2)*t)
Gxy=1/(a(3,3)*t)
nixy=-a(1,2)/a(1,1)
niyx=nixy*Ey/Ex
```

```
%-------------------------------%

st_tissue=[0,0.00345, 0.00599, 0.008848];        %from experimental data
N2=[170.50;0;0];
N3=[341.00;0;0];
N4=[511.50;0;0];
N1=[0;0;0];

whole=[N1,N2,N3,N4];

st=A\whole;

format long;
st_1=st(:,1);      %laminate strain
st_2=st(:,2);
st_3=st(:,3);
st_4=st(:,4);


teta = 0:10:90;
st_lam=cell(10,1);
for i=1:numel(teta)
  th = teta(i);

   %lamina strain
m=cosd(th);
n=sind(th);


R=[ m^2   n^2    m*n
    n^2   m^2  -m*n
   -2*m*n 2*m*n  m^2-n^2];

st_lam{i,1} = R*st;

end
```

```
figure
for i=1:numel(teta)

    hold on
    E = {'k','b','r','g','y','m','c',[0.7 0.2 0.8],[0.1 0.4 0.5],[0.5 1 0.2]};
    title('epsilon laminate vs epsilon fiber')
    xlabel('Epsilon laminate %','FontSize',11,'FontWeight','bold','Color','r')
    ylabel('Epsilon fiber %','FontSize',11,'FontWeight','bold','Color','r')
    plot(st(1,:)*100, st_lam{i,1}(1,:)*100,'-','color',E{i},'LineWidth',2.0)

legend('0°','10°','20°','30°','40°','50°','60°','70°','80°','90°','Location','northwest'
)
    %axis([0,0.15,-0.15,0.15])
     set(legend,'FontSize',7)
     %set(gca,'xTick', 0:0.03:0.15)
    %set(gca,'YTick', -0.15:0.03:0.15)
```

```
        hold off
        disp('_____')
    for j=1:numel(whole(1,:))
        disp('-------------------------------')

        for k=1:3
            disp(['Angle = ',num2str(teta(i)),'°  Load = ',num2str(whole(1,j)),' N  Strain
component # ',num2str(k),'   ',num2str(st_lam{i}(k,j))]);
        end
    end
 end
```

```
figure
hold on
for i=1:numel(teta)
  plot(st_tissue*100, st_lam{i,1}(1,:)*100,'color',E{i},'LineWidth',2.0)
    title('epsilon tissue vs epsilon fiber')
    xlabel('Epsilon tissue %','FontSize',11,'FontWeight','bold','Color','r')
    ylabel('Epsilon fiber %','FontSize',11,'FontWeight','bold','Color','r')

legend('0°','10°','20°','30°','40°','50°','60°','70°','80°','90°','Location','northwest'
)
    %axis([0,1,-0.15,0.15])
     set(legend,'FontSize',7)
     %set(gca,'xTick', 0:0.1:1.0)
    %set(gca,'YTick', -0.15:0.03:0.15)
end
hold off
```

```
gamma=zeros(10,4);
 figure
 hold on
 for i=1:numel(teta)
     F={'.','.','.','.','.','*','p','>','<','o'};
     H={20,20,20,20,20,0.1,0.1,0.1,0.1,0.1};
     for j=1:numel(whole(1,:))
         gamma(i,j)=(st_lam{i}(3,j)/2)*57.3;
     end
     title('epsilon laminate vs reorientation [deg]')
     xlabel('Epsilon laminate %','FontSize',11,'FontWeight','bold','Color','r')
     ylabel('Reorietation [deg]','FontSize',11,'FontWeight','bold','Color','r')
      %set(gca,'xTick', 0:0.02:0.16)
     %set(gca,'YTick', 0:0.005:0.06)
     plot(st(1,:)*100, -gamma(i,:),'-
',','linewidth',2.0,'color',E{i},'marker',F{i},'MarkerSize',H{i})

legend('0°','10°','20°','30°','40°','50°','60°','70°','80°','90°','Location','northwest'
)
    %axis([0,0.16,0.0,0.06])
     set(legend,'FontSize',7)
 end
```

```
 figure
 hold on
 for i=1:numel(teta)
     F={'.','.','.','.','.','*','p','>','<','o'};
     H={20,20,20,20,20,0.1,0.1,0.1,0.1,0.1};
     for j=1:numel(whole(1,:))
         gamma(i,j)=(st_lam{i}(3,j)/2)*57.3;
```

```
        end
        title('epsilon tissue vs reorientation [deg]')
  xlabel('Epsilon tissue %','FontSize',11,'FontWeight','bold','Color','r')
  ylabel('Reorietation [deg]','FontSize',11,'FontWeight','bold','Color','r')
        %set(gca,'xTick', 0:0.1:1.0)
       %set(gca,'YTick', 0:0.005:0.06)
       plot(st_tissue*100, -gamma(i,:),'-
 ','linewidth',2.0,'color',E{i},'marker',F{i},'MarkerSize',H{i})


 legend('0°','10°','20°','30°','40°','50°','60°','70°','80°','90°','Location','northwest'
 )
     %axis([0,1.0,0.0,0.06])
        set(legend,'FontSize',7)
   end
```

```
 slope=zeros(1,10);

  for i=1:numel(teta)
  slope(i)=(gamma(i,3)-gamma(i,2))/(st(1,3)-st(1,2));%sign minus for our agreement
  end
```

B. Experimental approach for reorientation and deformation calculations in cuticle

This Appendix provides further information on the experimental work described in **Chapter 5** and performed by Dr. Himadri Gupta and Dr. Yi Zhang.

The experimental approach used to calculate deformation and reorientation in cuticle is described below **(Figure A.1-A.3).**
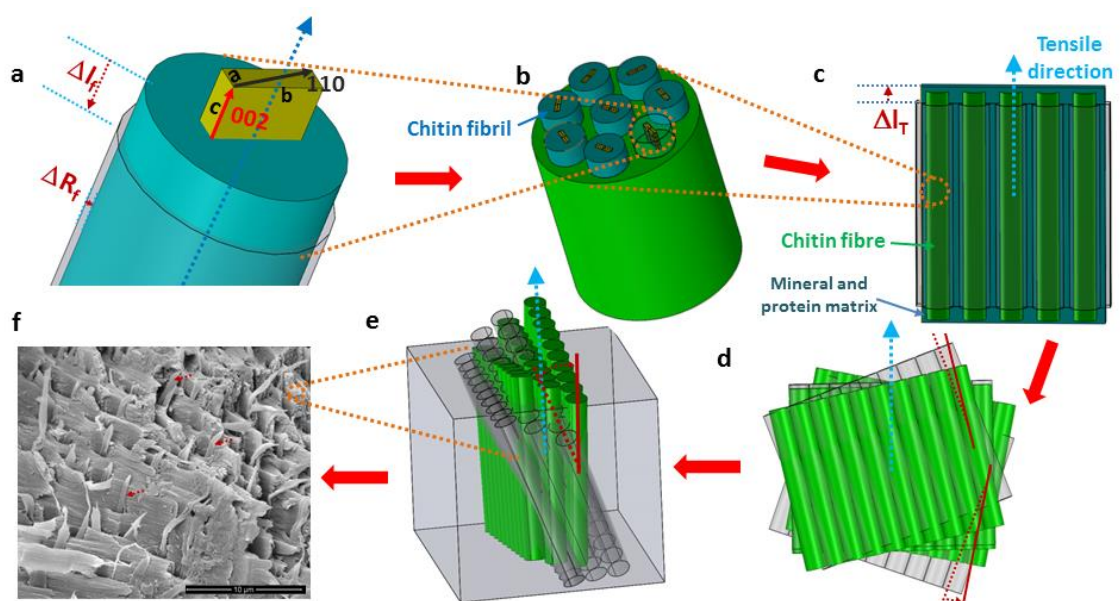
Figure A.1 - Hierarchical structure of stomatopod cuticle and corresponding mechanical parameters. (a) Schematic of a chitin fibre which is formed by N-acetyl-glucosamine molecules arranged in an orthorhombic crystal structure and proteins. (b) A mineralised chitin fibre which contains multiple fibres arranged in random orientations. The c axis of the chitin unit cell is coincided with both of the fibril and fibre axis which can be used as a proxy of the axial deformation of the chitin nanofibres. (c) The deformation of the fibre plane composed of parallely arranged chitin fibres surrounded by protein and mineral matrix. (d) Schematic shows the in-plane rotation of mineralised chitin fibres due to external tensile load. (e) Schematic showing 3D fibre plane tilting due to external tensile load. (f) Scanning electron micrograph showing the plywood structure of In-plane chitin fibres is interrupted by the out-of-plane fibres running through the pore-canal system in the cuticle.
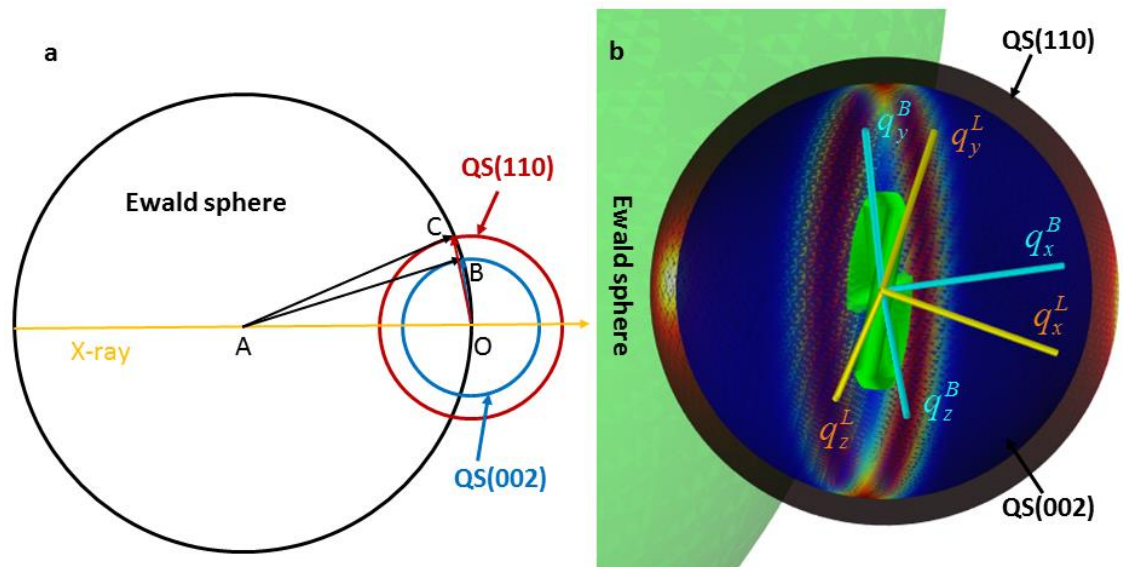
Figure A.2 - Ewald construction for (110) and (002) reflections in 2D and 3D. *(a) Two-dimensional drawing of Ewald sphere construction with the reciprocal space intensity spheres for (110) and (002), denoted QS(110) and QS(002) respectively. The length of AC=AO is 2π/λ. Point C and B are located on the intersection ring between Ewald sphere and QS(110), QS(002) respectively. OC indicates the scattering vector q for (110) reflection, and OB the scattering vector for (002) reflection. (b) Three-dimensional rendering of the geometry in (a), showing the Ewald sphere intersection with QS(110) and QS(002) in 3D. The uniform initial fibre distribution in the Bouligand layer leads to a uniform band of (002) diffraction intensity in the vertical plane (red-orange in the figure).*
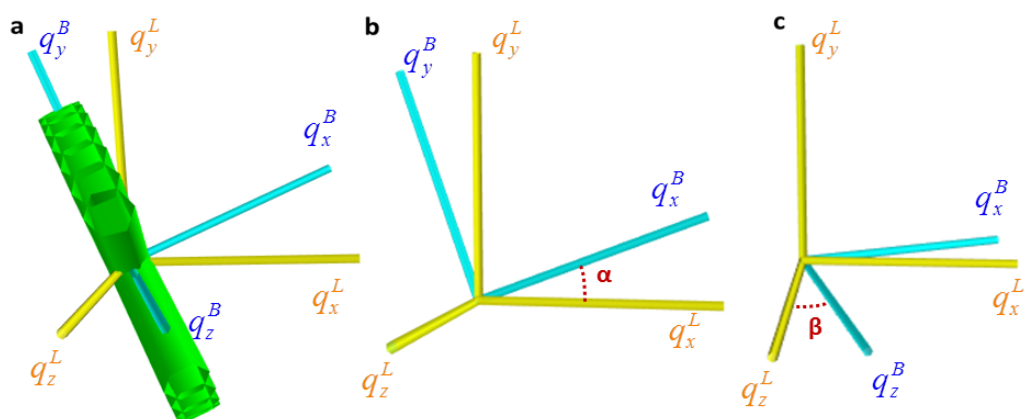
Figure A.3 - Linear transformation matrix between body-fixed frame and Lab-fixed frame. *(a) Schematic plot showing a fibre plane is tilted in 3D in the Lab-fixed frame (yellow) while the plane is fixed in its body-fixed coordinate system (blue). (b-c) Schematic plot showing α (b) tilt and β (c) tilt of the body-fixed coordinate system from the body-fixed coordinate system.*

241

The linear transformation matrix which translates coordinates (q_x^B, q_y^B, q_z^B

q_x^L, q_y^L, q_z^L) from body-fixed frame into laboratory-fixed coordinates (q_x^L, q_y^L, q_z^L

q_x^L, q_y^L, q_z^L) can be expressed by the **Equation 91.**

$$\begin{bmatrix} q_x^L \\ q_y^L \\ q_z^L \end{bmatrix} = \begin{bmatrix} \cos(\alpha)\cos(\beta) & -\sin(\alpha)\cos(\beta) & \sin(\beta) \\ \sin(\alpha) & \cos(\alpha) & 0 \\ -\cos(\alpha)\sin(\beta) & \sin(\alpha)\sin(\beta) & \cos(\beta) \end{bmatrix} \begin{bmatrix} q_x^B \\ q_y^B \\ q_z^B \end{bmatrix} \tag{91}$$

C. X-ray diffraction model functions

This Appendix provides further information on the experimental work described

in **Chapter 5** and performed by Dr. Himadri Gupta and Dr. Yi Zhang.

The following **Equations 92-109** describe the functions and equations used for

the X-ray diffraction method (**Table A.1**).

I: Delta functions (without 3D tilt):

In the formulae following, the diffraction intensity of rings or spots on the reciprocal

spheres was modelled using peaked Gaussians which approach Dirac δ-functions as

$\Delta q_{x(002)} \to 0$ (Bender and Orszag 1999). In the following, the angle γ refers to the

angle of the fibre in the q_y-q_z plane of **Figure 5.4** (main text). The Bouligand lamellar

unit lies in that plane, so a fibre at angle γ refers to the fibres in the sublamella

(lamina) inclined at an angle γ in the Bouligand unit. In the L2 geometry, γ is replaced

by α (**Equation 97**). In evaluating the asymptotic limit to the integral, the relation

$\delta(f(x)) = \delta(x)/|f'(x_0)|$ with x_0 a root of the function f(x) is also used, which accounts for

the denominator in some of the terms.

Configuration	Reflection	Function
L1	110	$$\delta_{(110)}^{L1} = \frac{1}{\sqrt{2\pi}\Delta q_{(110)}} \exp\left(-\frac{1}{2}\left(\frac{q_y \cos\gamma + q_z \sin\gamma}{\Delta q_{(110)}} \right)^2 \right) \quad (92)$$
L1	002	$$\delta_{(002)}^{L1} = \frac{\frac{1}{\sqrt{2\pi}\Delta q_{(002)}} \exp\left(-\frac{1}{2}\left(\frac{q_x}{\Delta q_{(002)}} \right)^2 \right)}{\sqrt{\left(q_{(002)}\right)^2 - (q_x)^2}} \quad (93)$$
L2	110	$$\delta_{(110)}^{L2} = \frac{1}{\sqrt{2\pi}\Delta q_{(110)}} \exp\left(-\frac{1}{2}\left(\frac{q_y \cos\alpha + q_x \sin\alpha}{\Delta q_{(110)}} \right)^2 \right) \quad (94)$$
L2	002	$$\delta_{(002)}^{L2} = \frac{\frac{1}{\sqrt{2\pi}\Delta q_{(002)}} \exp\left(-\frac{1}{2}\left(\frac{q_z}{\Delta q_{(002)}} \right)^2 \right)}{\sqrt{\left(q_{(002)}\right)^2 - (q_z)^2}} \quad (95)$$

II: Weight functions for the fibre distribution before mechanical loading:.

The weight functions will change on mechanical loading. The changes of weight functions and I(χ) with the tissue strain (ε_T) for (002) reflection under L1 configuration are described later in **Appendix E**).

Configuration	Fibre group	Function
L1	IP	$w_0 = 1/\pi$ $\qquad\qquad$ (96)
L1	OP	$$w(\gamma;\gamma_0,\Delta\gamma_0) = \frac{1}{\sqrt{2\pi}\Delta\gamma_0} \exp\left(-\frac{1}{2}\left(\frac{\gamma - \gamma_0}{\Delta\gamma_0} \right)^2 \right) \quad (97)$$
L2	IP	$$w(\alpha;\alpha_{IP},\Delta\alpha_{IP}) = \frac{1}{\sqrt{2\pi}\Delta\alpha_{IP}} \exp\left(-\frac{1}{2}\left(\frac{\alpha - \alpha_{IP}}{\Delta\alpha_{IP}} \right)^2 \right) \quad (98)$$

L2	OP	$w\left(\alpha;\alpha_{OP},\Delta\alpha_{OP}\right)=\dfrac{1}{\sqrt{2\pi}\Delta\alpha_{OP}}\exp\left(-\dfrac{1}{2}\left(\dfrac{\alpha-\alpha_{OP}}{\Delta\alpha_{OP}}\right)^{2}\right)$ (99)

III: Coordinates on the intersection ring

Reflection	Function
110	$q_{x}^{110}=-\dfrac{q_{(110)}^{2}}{2q_{(ES)}}$ $q_{y}^{110}=\dfrac{q_{(110)}}{2q_{(ES)}}\sqrt{\left(2q_{(ES)}+q_{(110)}\right)\left(2q_{(ES)}-q_{(110)}\right)}\sin\chi$ (100) $q_{z}^{110}=\dfrac{q_{(110)}}{2q_{(ES)}}\sqrt{\left(2q_{(ES)}+q_{(110)}\right)\left(2q_{(ES)}-q_{(110)}\right)}\cos\chi$
002	$q_{x}^{002}=-\dfrac{q_{(002)}^{2}}{2q_{(ES)}}$ $q_{y}^{002}=\dfrac{q_{(002)}}{2q_{(ES)}}\sqrt{\left(2q_{(ES)}+q_{(002)}\right)\left(2q_{(ES)}-q_{(002)}\right)}\sin\chi$ (101) $q_{z}^{002}=\dfrac{q_{(002)}}{2q_{(ES)}}\sqrt{\left(2q_{(ES)}+q_{(002)}\right)\left(2q_{(ES)}-q_{(002)}\right)}\cos\chi$

IV: Delta functions with 3D tilt

$$\delta_{(110)}^{L1}\left(q_{x},q_{y},q_{z};\gamma,\Delta q_{(110)},\alpha,\beta\right)=$$

$$\frac{1}{\sqrt{2\pi}\Delta q_{(110)}}\exp\left(-\frac{1}{2}\left(\frac{\left(q_{x}\sin\alpha+q_{y}\cos\alpha\right)\cos\gamma+\left(-q_{x}\cos\alpha\sin\beta+q_{y}\sin\alpha\sin\beta+q_{z}\cos\beta\right)\sin\gamma}{\Delta q_{(110)}}\right)^{2}\right)$$

(102)

$$\delta_{(002)}^{L1}\left(q_{x},q_{y},q_{z};\gamma,\Delta q_{(002)},\alpha,\beta\right)=$$

$$\frac{\dfrac{1}{\sqrt{2\pi}\Delta q_{(002)}}\exp\left(-\left(\dfrac{q_{x}\cos\alpha\cos\beta-q_{y}\sin\alpha\cos\beta+q_{z}\sin\beta}{\Delta q_{(002)}}\right)^{2}\right)}{\sqrt{\left(q_{(002)}\right)^{2}-\left(q_{x}\cos\alpha\cos\beta-q_{y}\sin\alpha\cos\beta+q_{z}\sin\beta\right)^{2}}}$$

   (103)

$$\delta_{(110)}^{L2}\left(q_x, q_y, q_z; \gamma, \Delta q_{(110)}, \alpha, \beta\right) =$$

$$\frac{1}{\sqrt{2\pi}\Delta q_{(110)}} \exp\left(-\frac{1}{2}\left(\frac{\left(q_y\cos\gamma - q_z\sin\gamma\right)\cos\alpha + \left(-q_x\cos\beta + q_y\sin\gamma\sin\beta + q_z\cos\gamma\sin\beta\right)\sin\alpha}{\Delta q_{(110)}}\right)^2\right)$$

(104)

$$\delta_{(002)}^{L2}\left(q_x, q_y, q_z; \gamma, \Delta q_{(002)}, \alpha, \beta\right) =$$

$$\frac{\dfrac{1}{\sqrt{2\pi}\Delta q_{(002)}} \exp\left(-\left(\dfrac{q_x\sin\beta + q_y\sin\alpha\cos\beta + q_z\cos\alpha\cos\beta}{\Delta q_{(002)}}\right)^2\right)}{\sqrt{\left(q_{(002)}\right)^2 - (q_x\sin\beta + q_y\sin\alpha\cos\beta + q_z\cos\alpha\cos\beta)^2}}$$

(105)

V: Intensity distribution on the intersection ring ($I(\chi)$):

The measured intensity is the integral of the diffraction intensities of each fibre weighted by the fibre orientation distribution.

Configuration	Reflection	Function
L1	110	$I_{110(\chi)}^{L1} = \lambda_{IP}\int_{-\frac{\pi}{2}}^{\frac{\pi}{2}} w_0 \times \delta_{(110)}^{L1}(q_x^{110}, q_y^{110}, q_z^{110}; \gamma, \Delta q_{(110)}, \alpha_{IP}, \beta_{IP})d\gamma +$ $\lambda_{OP}\int_{-\frac{\pi}{2}}^{\frac{\pi}{2}} w(\gamma; \gamma_0, \Delta\gamma) \times \delta_{(110)}^{L1}(q_x^{110}, q_y^{110}, q_z^{110}; \gamma, \Delta q_{(110)}, \alpha_{OP}, \beta_{OP})d\gamma$ (106)
L1	002	$I_{002(\chi)}^{L1} = \lambda_{IP}\int_{-\frac{\pi}{2}}^{\frac{\pi}{2}} w_0 \times \delta_{(002)}^{L1}(q_x^{002}, q_y^{002}, q_z^{002}; \gamma, \Delta q_{(002)}, \alpha_{IP}, \beta_{IP})d\gamma +$ $\lambda_{OP}\int_{-\frac{\pi}{2}}^{\frac{\pi}{2}} w(\gamma; \gamma_0, \Delta\gamma) \times \delta_{(002)}^{L1}(q_x^{002}, q_y^{002}, q_z^{002}; \gamma, \Delta q_{(002)}, \alpha_{OP}, \beta_{OP})d\gamma$ (107)

L2	110	$$I^{L2}_{110(\chi)} = \lambda_{IP}\int_{-\frac{\pi}{2}}^{\frac{\pi}{2}} w\left(\alpha;\alpha_{IP},\Delta\alpha_{IP}\right)\times\delta^{L2}_{(110)}(q_x^{110},q_y^{110},q_z^{110};\gamma,\Delta q_{(110)},\alpha_{IP},\beta_{IP})d\alpha$$ $$+\lambda_{OP}\int_{-\frac{\pi}{2}}^{\frac{\pi}{2}} w\left(\alpha;\alpha_{OP},\Delta\alpha_{OP}\right)\times\delta^{L2}_{(110)}(q_x^{110},q_y^{110},q_z^{110};\gamma,\Delta q_{(110)},\alpha_{OP},\beta_{OP})d\alpha$$ (108)
L2	002	$$I^{L2}_{002(\chi)} = \lambda_{IP}\int_{-\frac{\pi}{2}}^{\frac{\pi}{2}} w\left(\alpha;\alpha_{IP},\Delta\alpha_{IP}\right)\times\delta^{L2}_{(002)}(q_x^{002},q_y^{002},q_z^{002};\gamma,\Delta q_{(002)},\alpha_{IP},\beta_{IP})d\alpha$$ $$+\lambda_{OP}\int_{-\frac{\pi}{2}}^{\frac{\pi}{2}} w\left(\alpha;\alpha_{OP},\Delta\alpha_{OP}\right)\times\delta^{L2}_{(002)}(q_x^{002},q_y^{002},q_z^{002};\gamma,\Delta q_{(002)},\alpha_{OP},\beta_{OP})d\alpha$$ (109)

VI: Symbol definitions:

γ: The fibre orientation respect to the q_z^L axis in the lab coordinate system;

λ_{IP}: scaling factor proportional to amount of in-plane (IP) fibres in the scattering volume;

λ_{OP}: scaling factor proportional to amount of out-of-plane (OP) fibres in the scattering volume;

$q_{(ES)}$: The radius of Ewald sphere $2\pi/\lambda$ (AC in **Figure A.2a**);

$q_{(002)}$: The radius of *QS(002)* sphere (OB in **Figure A.2a**);

$q_{(110)}$: The radius of *QS(110)* sphere (OC in **Figure A.2a**)

Table A.1 - Mathematical functions for intensity distributions on the QS(110) and QS(002) spheres and the corresponding intersection rings.

D. Calculation of changed orientation function (in-plane) upon fibre reorientation

Consider a small angular sector of fibres (e.g. within one lamina). The number of fibres is w(γ)$\Delta\gamma$ (up to normalization constants). Under deformation, this sector moves to a new angular position γ_σ and also changes in width $\Delta\gamma_\sigma$ (e.g.

under tensile load, γ will move closer to loading direction and the width will reduce). Most importantly, the fibre distribution will also change from w(γ) to $w_\sigma(\gamma_\sigma)$. Therefore, as no fibres are created or destroyed, **Equation 110** is obtained**.**

$$w(\gamma)\Delta\gamma = w_\sigma(\gamma_\sigma)\Delta\gamma_\sigma \tag{110}$$

As the change in angle is expected to be proportional (to first order) to the perturbing parameter (stress), **Equation 111** can be written**.**

$$\gamma_\sigma = \gamma - \tilde{\sigma}f(\gamma) \tag{111}$$

f(γ) is an a priori unknown function and the stress variable was scaled by a large parameter (100 MPa that is a value close to the maximum applied stress) to obtain a dimensionless stress parameter $\tilde{\sigma} = (\dfrac{\sigma}{\sigma_0})$.

Then I can substitute in **Equation 110** to get, using first order perturbation expansions (Bender and Orszag 1999) (**Equation 112**).

$$w_\sigma(\gamma) \approx w(\gamma) + \tilde{\sigma}\left(f(\gamma)\frac{dw}{d\gamma} + w(\gamma)\frac{df}{d\gamma}\right) = w(\gamma) + \tilde{\sigma}\frac{d(f(\gamma)w(\gamma))}{d\gamma} \tag{112}$$

In cuticle, I start with a uniform fibril distribution $w(\gamma)=w_0=1/\pi$ to get **Equation 113.**

$$w_\sigma(\gamma) \approx w_0\left(1 + \tilde{\sigma}\frac{df}{d\gamma}\right) \tag{113}$$

From the lamination theory **Equation 114** can be found**.**

$$f(\gamma) = \frac{(-2\cos\theta\sin\theta\varepsilon_x + 2\cos\theta\sin\theta\varepsilon_y + \gamma_{xy}\cos^2\theta - \gamma_{xy}\sin^2\theta)}{2} \tag{114}$$

Simplifying the **Equation 114** I obtain **Equation 115.**

$$f(\gamma) \approx A\cos 2\gamma + B\sin 2\gamma \tag{115}$$

where $A = \frac{\gamma_{xy}}{2}$ and $B = \frac{(\varepsilon_y - \varepsilon_x)}{2}$ are constants depending on the material parameters of the chitin, mineral and protein components of the cuticle. Using this form, the final result is obtained (**Equation 116**).

$$w_\sigma(\gamma) \approx w_0 \left(1 + 2\tilde{\sigma}\left(-A\sin 2\gamma + B\cos 2\gamma\right)\right) \tag{116}$$

It is possible to show from **Equation 115** that the element in the matrix **A**$^{-1}$ which couples the laminate shear strain γ_{xy} and the applied uniaxial load N_x is null. Hence, $A = 0$ while $B = -2.28 \times 10^{-3} \times \tilde{\sigma}$ [no units]. **Figure A.4** shows a comparison between experimental and analytical calculations of $\Delta w = w_\sigma - w_0$.
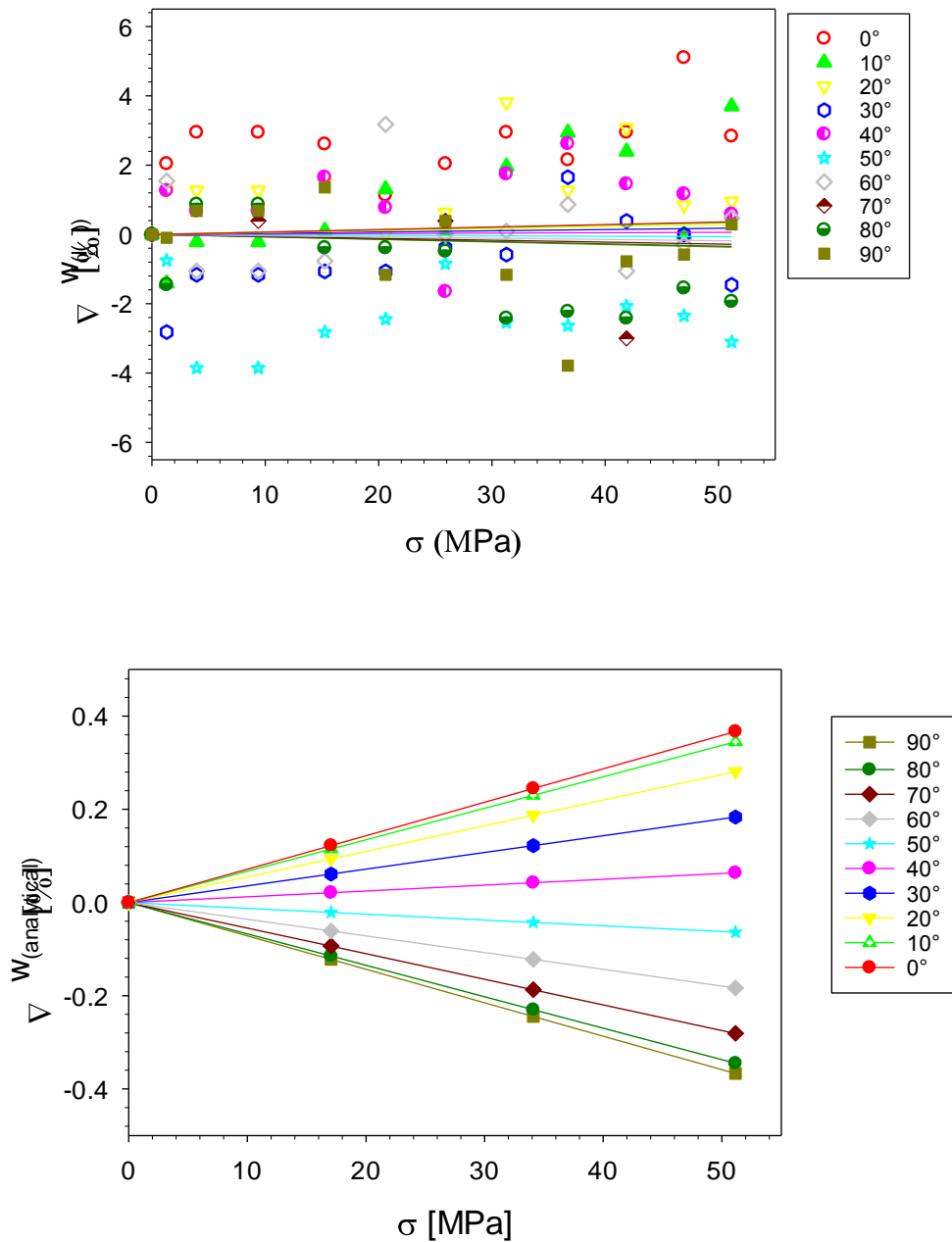
Figure A. 4 - Angular-resolved experimental and analytically calculated I(ψ) changes with respect to tensile stress. *a) The normalised diffraction intensity w(I(ψ)) changes with respect to the tensile stress. The use of w(I(ψ)) instead of I(ψ) is to factor out the overall diffraction intensity changes due to the radiation damage during the tensile test. Note the angular-resolved I(ψ) values are obtained from radial integration in each azimuthal sectors (angular width 10°, center at χ=90°-ψ) of the (002) reflection ring. b) The simulated normalised diffraction intensity w(I(ψ)) changes merely due to in-plane reorientation with respect to the tensile stress (zoom from figure a).*

E. Johnson-Cook material and failure model

The Johnson-Cook is a particular model of isotropic hardening that assumes the plastic flow stress to be in the form reported in **Equation 117**, where $\bar{\sigma}$ is the Von Mises stress, *A, B, n, m* and *C* are material parameters that need to be calibrated from experiment, $\bar{\varepsilon}_{pl}$ is the equivalent plastic strain, $\dot{\bar{\varepsilon}}$ is the equivalent plastic strain rate and $\dot{\varepsilon}_0$ is the reference strain rate assumed to be 1 (Johnson and Cook 1983).

$$\bar{\sigma} = \left(A + B\bar{\varepsilon}_{pl}{}^{n} \right) \left[1 + C\ln\frac{\dot{\bar{\varepsilon}}_{pl}}{\dot{\varepsilon}_0} \right] \left[1 - \hat{\theta}^{m} \right] \qquad (117)$$

$\hat{\theta}$ is the non-dimensional temperature defined as in **Equations 118**, where θ is the current temperature, θ_{melt} is the melting temperature and θ_{trans} is the transition temperature, defined as the one at or below which the flow stress stops depending on the temperature.

$$\hat{\theta} = \begin{cases} 0 & for\,\theta < \theta_{trans} \\ \left(\dfrac{\theta - \theta_{trans}}{\theta_{melt} - \theta_{trans}} \right) & for\,\theta_{trans} \leq \theta \leq \theta_{melt} \\ 1 & for\,\theta > \theta_{melt} \end{cases} \qquad (118)$$

All the Johnson-Cook parameters and material properties are listed in **Table A.2**, as reported in a previous paper (Mabrouki, Girardin et al. 2008).

A [GPa]	B [GPa]	n	m	C	Density [Kg/m^3]	Elastic Modulus [GPa]	Poisson's ratio	θ melt [°C]	θ trans [°C]
0.352	0.440	0.42	1	0.0083	2700	74.5	0.33	520	25

Table A. 2 - Johnson-Cook parameters and material properties used to simulate the behaviour of A2024-T351.

To simulate the damage phenomenon, it was necessary to introduce the Johnson-Cook damage model. In detail it was defined the equivalent plastic strain at the onset of the damage $\overline{\varepsilon_D}^{pl}$ (**Equation 119**).

$$\overline{\varepsilon}_D^{pl} = \left[d_1 + d_2 e^{(-d_3\eta)} \right] \left[1 + d_4 ln\left(\frac{\dot{\overline{\varepsilon}}^{pl}}{\dot{\varepsilon}_0} \right) \right] \left[1 + d_5\theta \right] \qquad (119)$$

The failure parameters d_1, d_2, d_3, d_4, d_5, listed in **Table A.3,** are material-dependent and are extrapolated from a previous paper (Mabrouki, Girardin et al. 2008). $\eta = -p/q$ is the stress triaxiality, where p is the pressure stress and q is the Von Mises equivalent stress.

d_1	d_2	d_3	d_4	d_5
0.13	0.13	1.5	0.011	0

Table A. 3 - Damage parameters describing the onset of the damage for the aluminium A2024-T351.

By imposing a null value for d_5, the physics of the problem was simplified and no temperature effects on the onset of damage were assumed. **Equation 119** differs from the original formula (Johnson and Cook 1985) in the sign of the parameter d_3 for the fact that most of materials experience a decrease in ε_D^{pl} with increasing stress triaxiality (Hibbett, Karlsson et al. 1998): ductility at

failure and triaxiality are nonlinearly inversely proportional (Hancock and Mackenzie 1976, Bonora 1997).

The damage process initiates when the following criterion is satisfied (**Equation 120**), where ω_D is the state variable that increases monotonically with plastic deformation.

$$\omega_D = \int \frac{d\bar{\varepsilon}^{pl}}{\bar{\varepsilon}_D^{pl}} = 1 \qquad (120)$$

References

Abdel-Wahab, A. A., A. R. Maligno and V. V. Silberschmidt (2012). "Micro-scale modelling of bovine cortical bone fracture: Analysis of crack propagation and microstructure using X-FEM." Computational Materials Science **52**(1): 128-135.

Aizenberg, J., J. C. Weaver, M. S. Thanawala, V. C. Sundar, D. E. Morse and P. Fratzl (2005). "Skeleton of Euplectella sp.: structural hierarchy from the nanoscale to the macroscale." Science **309**(5732): 275-278.

Al-Sawalmih, A., C. H. Li, S. Siegel, H. Fabritius, S. B. Yi, D. Raabe, P. Fratzl and O. Paris (2008). "Microtexture and Chitin/Calcite Orientation Relationship in the Mineralized Exoskeleton of the American Lobster." Advanced Functional Materials **18**(20): 3307-3314.

Al-Sawalmih, A., C. H. Li, S. Siegel, P. Fratzl and O. Paris (2009). "On the Stability of Amorphous Minerals in Lobster Cuticle." Advanced Materials **21**(40): 4011-+.

Al-Sawalmih, A., C. Li, S. Siegel, H. Fabritius, S. Yi, D. Raabe, P. Fratzl and O. Paris (2008). "Microtexture and chitin/calcite orientation relationship in the mineralized exoskeleton of the American lobster." Advanced Functional Materials **18**(20): 3307-3314.

Alexander, B., T. L. Daulton, G. M. Genin, J. Lipner, J. D. Pasteris, B. Wopenka and S. Thomopoulos (2012). "The nanometre-scale physiology of bone: steric modelling and scanning transmission electron microscopy of collagen–mineral structure." Journal of the Royal Society Interface **9**(73): 1774-1786.

Amini, S., A. Masic, L. Bertinetti, J. S. Teguh, J. S. Herrin, X. Zhu, H. Su and A. Miserez (2014). "Textured fluorapatite bonded to calcium sulphate strengthen stomatopod raptorial appendages." Nature communications **5**.

Amini, S., A. Masic, L. Bertinetti, J. S. Teguh, J. S. Herrin, X. Zhu, H. Su and A. Miserez (2014). "Textured fluorapatite bonded to calcium sulphate strengthen stomatopod raptorial appendages." Nature Communications **5**: 3187.

Amini, S., M. Tadayon, S. Idapalapati and A. Miserez (2015). "The role of quasi-plasticity in the extreme contact damage tolerance of the stomatopod dactyl club." Nature materials **14**(9): 943-950.

Ascenzi, A., P. Baschieri and A. Benvenuti (1990). "The bending properties of single osteons." Journal of biomechanics **23**(8): 763-771.

Ascenzi, A., P. Baschieri and A. Benvenuti (1994). "The torsional properties of single selected osteons." Journal of biomechanics **27**(7): 875879-877884.

Ascenzi, A., A. Benvenuti, F. Mango and R. Simili (1985). "Mechanical hysteresis loops from single osteons: technical devices and preliminary results." Journal of biomechanics **18**(5): 391-398.

Ascenzi, A. and E. Bonucci (1967). "The tensile properties of single osteons." The Anatomical Record **158**(4): 375-386.

Ascenzi, A. and E. Bonucci (1968). "The compressive properties of single osteons." The Anatomical Record **161**(3): 377-391.

Ascenzi, A., E. Bonucci, A. Ripamonti and N. Roveri (1978). "X-ray diffraction and electron microscope study of osteons during calcification." Calcified Tissue International **25**(1): 133-143.

Bafna, A., G. Beaucage, F. Mirabella and S. Mehta (2003). "3D Hierarchical orientation in polymer–clay nanocomposite films." Polymer **44**(4): 1103-1115.

Bar-On, B. and H. D. Wagner (2011). "Mechanical model for staggered bio-structure." Journal of the Mechanics and Physics of Solids **59**(9): 1685-1701.

Bar-On, B. and H. D. Wagner (2012). "Effective moduli of multi-scale composites." Composites Science and Technology **72**(5): 566-573.

Bar-On, B. and H. D. Wagner (2013). "Structural motifs and elastic properties of hierarchical biological tissues–A review." Journal of structural biology **183**(2): 149-164.

Barauskas, R. (2005). Combining mezzo-and macro-mechanical approaches in a computational model of a ballistic impact upon textile targets. Proceedings of the Fifth WSEAS International Conference on Simulation, Modeling and Optimization.

Barbieri, E. and N. M. Pugno (2015). "A computational model for large deformations of composites with a 2D soft matrix and 1D anticracks." International Journal of Solids and Structures **77**: 1-14.

Barthelat, F. (2007). "Biomimetics for next generation materials." Philosophical Transactions of the Royal Society of London A: Mathematical, Physical and Engineering Sciences **365**(1861): 2907-2919.

Barthelat, F. and R. Rabiei (2011). "Toughness amplification in natural composites." Journal of the Mechanics and Physics of Solids **59**(4): 829-840.

Bender, C. M. and S. A. Orszag (1999). Advanced mathematical methods for scientists and engineers. New York, Springer.

Berthelot, J.-M. (1999). Classical Laminate Theory. Composite Materials: Mechanical Behavior and Structural Analysis. J.-M. Berthelot. New York, NY, Springer New York**:** 287-311.

Berthelot, J.-M. (2012). Composite materials: mechanical behavior and structural analysis, Springer Science & Business Media.

Bonderer, L. J., A. R. Studart and L. J. Gauckler (2008). "Bioinspired design and assembly of platelet reinforced polymer films." Science **319**(5866): 1069-1073.

Boneschanscher, M. P., W. H. Evers, J. J. Geuchies, T. Altantzis, B. Goris, F. T. Rabouw, S. A. van Rossum, H. S. van der Zant, L. D. Siebbeles, G. Van Tendeloo, I. Swart, J. Hilhorst, A. V. Petukhov, S. Bals and D. Vanmaekelbergh (2014). "Long-range orientation and atomic attachment of nanocrystals in 2D honeycomb superlattices." Science **344**(6190): 1377-1380.

Bonfield, W. and E. Clark (1973). "Elastic deformation of compact bone." Journal of Materials Science **8**(11): 1590-1594.

Bonora, N. (1997). "On the effect of triaxial state of stress on ductility using nonlinear CDM model." International Journal of Fracture **88**(4): 359-371.

Bosia, F., T. Abdalrahman and N. M. Pugno (2012). "Investigating the role of hierarchy on the strength of composite materials: evidence of a crucial synergy between hierarchy and material mixing." Nanoscale **4**(4): 1200-1207.

Bosia, F., T. Abdalrahman and N. M. Pugno (2014). "Self-healing of hierarchical materials." Langmuir **30**(4): 1123-1133.

Bosia, F., M. J. Buehler and N. M. Pugno (2010). "Hierarchical simulations for the design of supertough nanofibers inspired by spider silk." Physical Review E **82**(5): 056103.

Boßelmann, F., P. Romano, H. Fabritius, D. Raabe and M. Epple (2007). "The composition of the exoskeleton of two crustacea: The American lobster Homarus americanus and the edible crab Cancer pagurus." Thermochimica Acta **463**(1): 65-68.

Bouligand, Y. (1972). "TWISTED FIBROUS ARRANGEMENTS IN BIOLOGICAL-MATERIALS AND CHOLESTERIC MESOPHASES." Tissue & Cell **4**(2): 189-+.

Bouligand, Y. (1972). "Twisted fibrous arrangements in biological materials and cholesteric mesophases." Tissue and Cell **4**(2): 189192-190217.

Brennen, C. E. (2013). Cavitation and bubble dynamics, Cambridge University Press.

Bruet, B., H. Qi, M. Boyce, R. Panas, K. Tai, L. Frick and C. Ortiz (2005). "Nanoscale morphology and indentation of individual nacre tablets from the gastropod mollusc Trochus niloticus." Journal of Materials Research **20**(09): 2400-2419.

Bruet, B. J., J. Song, M. C. Boyce and C. Ortiz (2008). "Materials design principles of ancient fish armour." Nature materials **7**(9): 748-756.

Buehler, M. J. (2007). "Molecular nanomechanics of nascent bone: fibrillar toughening by mineralization." Nanotechnology **18**(29): 295102.

Buehler, M. J. (2007). "Nano-and micromechanical properties of hierarchical biological materials and tissues." Journal of Materials Science **42**(21): 8765-8770.

Buehler, M. J. (2008). "Nanomechanics of collagen fibrils under varying cross-link densities: atomistic and continuum studies." Journal of the mechanical behavior of biomedical materials **1**(1): 59-67.

Buehler, M. J., S. Keten and T. Ackbarow (2008). "Theoretical and computational hierarchical nanomechanics of protein materials: Deformation and fracture." Progress in Materials Science **53**(8): 1101-1241.

Buehler, M. J. and Y. C. Yung (2009). "Deformation and failure of protein materials in physiologically extreme conditions and disease." Nature materials **8**(3): 175-188.

Burrows, M. (1969). "The mechanics and neural control of the prey capture strike in the mantid shrimps Squilla and Hemisquilla." Zeitschrift für vergleichende Physiologie **62**(4): 361-381.

Burrows, M. and G. Hoyle (1972). "Neuromuscular physiology of the strike mechanism of the mantis shrimp, Hemisquilla." Journal of Experimental Zoology **179**(3): 379-393.

Butler, R. W. and J. W. Kirbyson (1979). "Oyster predation by the black oystercatcher in British Columbia." The Condor **81**(4): 433-435.

Caldwell, R. L. and M. J. Childress (1990). Prey selection and processing in a stomatopod crustacean. Behavioural mechanisms of food selection, Springer**: 143-164.

Caldwell, R. L. and H. Dingle (1975). "Ecology and evolution of agonistic behavior in stomatopods." Naturwissenschaften **62**(5): 214-222.

Caldwell, R. L. and H. Dingle (1976). "Stomatopods." Scientific American.

Carlin, N. F. and D. S. Gladstein (1989). "The "bouncer" defense of Odontomachus ruginodis and other odontomachine ants (Hymenoptera: Formicidae)." Psyche **96**(1-2): 1-20.

Chaichian, M., I. Merches and A. Tureanu (2012). Mechanics: an intensive course, Springer Science & Business Media.

Chamard, V., M. Allain, P. Godard, A. Talneau, G. Patriarche and M. Burghammer (2015). "Strain in a silicon-on-insulator nanostructure revealed by 3D x-ray Bragg ptychography." Scientific Reports **5**: 9827.

Chen, F., F. Cao, H. Li and Z. Bian (2015). "Exploring the Important Role of Nanocrystals Orientation in TiO_2 Superstructure on Photocatalytic Performances." Langmuir **31**(11): 3494-3499.

Chen, P.-Y., A. Stokes and J. McKittrick (2009). "Comparison of the structure and mechanical properties of bovine femur bone and antler of the North American elk (Cervus elaphus canadensis)." Acta Biomaterialia **5**(2): 693-706.

Chen, W. W., A. Rajendran, B. Song and X. Nie (2007). "Dynamic fracture of ceramics in armor applications." Journal of the American Ceramic Society **90**(4): 1005-1018.

Choi, K., J. L. Kuhn, M. J. Ciarelli and S. A. Goldstein (1990). "The elastic moduli of human subchondral, trabecular, and cortical bone tissue and the size-dependency of cortical bone modulus." Journal of biomechanics **23**(11): 1103-1113.

Chu, C.-Y., M.-H. Chen, M.-L. Wu, H.-L. Chen, Y.-T. Chiu, S.-M. Chen and C.-H. Huang (2014). "Hierarchical Structure and Crystal Orientation in Poly(ethylene oxide)/Clay Nanocomposite Films." Langmuir **30**(10): 2886-2895.

Claverie, T., E. Chan and S. N. Patek (2011). "Modularity and scaling in fast movements: power amplification in mantis shrimp." Evolution **65**(2): 443-461.

Clutton-Brock, T. (1988). Reproductive success: studies of individual variation in contrasting breeding systems, University of Chicago Press.

Clutton-Brock, T. H., S. Albon, R. Gibson and F. E. Guinness (1979). "The logical stag: adaptive aspects of fighting in red deer (Cervus elaphus L.)." Animal Behaviour **27**: 211-225.

Compton, B. G. and J. A. Lewis (2014). "3D-printing of lightweight cellular composites." Advanced Materials **26**(34): 5930-5935.

Cox, H. (1952). "The elasticity and strength of paper and other fibrous materials." British journal of applied physics **3**(3): 72.

Cronin, T. W., R. L. Caldwell and J. Marshall (2001). "Sensory adaptation: tunable colour vision in a mantis shrimp." Nature **411**(6837): 547-548.

Cronin, T. W., R. L. Caldwell and J. Marshall (2006). "Learning in stomatopod crustaceans." International Journal of Comparative Psychology **19**(3).

Cronin, T. W. and J. Marshall (2004). "The unique visual world of mantis shrimps." Complex worlds from simpler nervous systems. MIT Press, Cambridge, MA: 239-268.

Cronin, T. W. and N. J. Marshall (1989). "A retina with at least ten spectral types of photoreceptors in a mantis shrimp." Nature **339**(6220): 137-140.

Currey, J. D. (1979). "Mechanical properties of bone tissues with greatly differing functions." Journal of biomechanics **12**(4): 313-319.

Currey, J. D. (1999). "The design of mineralised hard tissues for their mechanical functions." Journal of Experimental Biology **202**(23): 3285-3294.

Currey, J. D. (2002). Bones: structure and mechanics, Princeton university press.

Currey, J. D., K. Brear and P. Zioupos (1996). "The effects of ageing and changes in mineral content in degrading the toughness of human femora." Journal of biomechanics **29**(2): 257-260.

Currey, J. D., T. Landete-Castillejos, J. Estevez, F. Ceacero, A. Olguin, A. Garcia and L. Gallego (2009). "The mechanical properties of red deer antler bone when used in fighting." Journal of Experimental Biology **212**(24): 3985-3993.

Cutler, B. (1980). "Arthropod cuticle features and arthropod monophyly." Experientia **36**(8): 953.

Danielsen, C., L. Mosekilde, J. Bollerslev and L. Mosekilde (1994). "Thermal stability of cortical bone collagen in relation to age in normal individuals and in individuals with osteopetrosis." Bone **15**(1): 91-96.

David, N., X.-L. Gao and J. Zheng (2009). "Ballistic resistant body armor: contemporary and prospective materials and related protection mechanisms." Applied Mechanics Reviews **62**(5): 050802.

Davies, R. (1949). The determination of static and dynamic yield stresses using a steel ball. Proceedings of the Royal Society of London A: Mathematical, Physical and Engineering Sciences, The Royal Society.

Díaz-Rojas, E. I., W. M. Argüelles-Monal, I. Higuera-Ciapara, J. Hernández, J. Lizardi-Mendoza and F. M. Goycoolea (2006). "Determination of chitin and protein contents during the isolation of chitin from shrimp waste." Macromolecular bioscience **6**(5): 340-347.

Dimas, L. S., G. H. Bratzel, I. Eylon and M. J. Buehler (2013). "Tough composites inspired by mineralized natural materials: computation, 3D printing, and testing." Advanced Functional Materials **23**(36): 4629-4638.

Dingle, H. and R. L. Caldwell (1969). "The aggressive and territorial behaviour of the mantis shrimp Gonodactylus bredini Manning (Crustacea: Stomatopoda)." Behaviour **33**(1): 115-136.

Doghri, I. (2013). Mechanics of deformable solids: linear, nonlinear, analytical and computational aspects, Springer Science & Business Media.

Dunlop, J. W. and P. Fratzl (2010). "Biological composites." Annual Review of Materials Research **40**: 1-24.

Dutta, P. K. (2015). Chitin and chitosan for regenerative medicine, Springer.

Erko, M., O. Younes-Metzler, A. Rack, P. Zaslansky, S. L. Young, G. Milliron, M. Chyasnavichyus, F. G. Barth, P. Fratzl, V. Tsukruk, I. Zlotnikov and Y. Politi (2015). "Micro- and nano-structural details of a spider's filter for substrate vibrations: relevance for low-frequency signal transmission." Journal of the Royal Society Interface **12**(104).

Ewins, D. J. (1984). Modal testing: theory and practice, Research studies press Letchworth.

Fabritius, H. O., C. Sachs, P. R. Triguero and D. Raabe (2009). "Influence of Structural Principles on the Mechanics of a Biological Fiber-Based Composite Material with Hierarchical Organization: The Exoskeleton of the Lobster Homarus americanus." Advanced materials **21**(4): 391-400.

Fantner, G. E., T. Hassenkam, J. H. Kindt, J. C. Weaver, H. Birkedal, L. Pechenik, J. A. Cutroni, G. A. Cidade, G. D. Stucky and D. E. Morse (2005). "Sacrificial bonds and hidden length dissipate energy as mineralized fibrils separate during bone fracture." Nature materials **4**(8): 612-616.

Fernandez, J. G. and D. E. Ingber (2014). "Manufacturing of Large-Scale Functional Objects Using Biodegradable Chitosan Bioplastic." Macromolecular Materials and Engineering **299**(8): 932-938.

Fleck, C. and D. Eifler (2003). "Deformation behaviour and damage accumulation of cortical bone specimens from the equine tibia under cyclic loading." Journal of biomechanics **36**(2): 179-189.

Focher, B., A. Naggi, G. Torri, A. Cosani and M. Terbojevich (1992). "Structural differences between chitin polymorphs and their precipitates from solutions— evidence from CP-MAS 13C-NMR, FT-IR and FT-Raman spectroscopy." Carbohydrate Polymers **17**(2): 97-102.

Fratzl, P., H. S. Gupta, F. D. Fischer and O. Kolednik (2007). "Hindered crack propagation in materials with periodically varying Young's modulus—lessons from biological materials." Advanced Materials **19**(18): 2657-2661.

Fratzl, P. and R. Weinkamer (2007). "Nature's hierarchical materials." Progress in Materials Science **52**(8): 1263-1334.

Frija, M., T. Hassine, R. Fathallah, C. Bouraoui, A. Dogui and L. de Génie Mécanique (2006). "Finite element modelling of shot peening process: Prediction of the compressive residual stresses, the plastic deformations and the surface integrity." Materials Science and Engineering: A **426**(1): 173-180.

Galgali, G., S. Agarwal and A. Lele (2004). "Effect of clay orientation on the tensile modulus of polypropylene–nanoclay composites." Polymer **45**(17): 6059-6069.

Gama, B. A., T. A. Bogetti, B. K. Fink, C.-J. Yu, T. D. Claar, H. H. Eifert and J. W. Gillespie Jr (2001). "Aluminum foam integral armor: a new dimension in armor design." Composite Structures **52**(3-4): 381-395.

Gao, H., B. Ji, I. L. Jäger, E. Arzt and P. Fratzl (2003). "Materials become insensitive to flaws at nanoscale: lessons from nature." Proceedings of the national Academy of Sciences **100**(10): 5597-5600.

García-Bellido, D. C. and D. H. Collins (2004). "Moulting arthropod caught in the act." Nature **429**(6987): 40-40.

Gautieri, A., M. J. Buehler and A. Redaelli (2009). "Deformation rate controls elasticity and unfolding pathway of single tropocollagen molecules." Journal of the Mechanical Behavior of Biomedical Materials **2**(2): 130-137.

Gautieri, A., S. Vesentini, A. Redaelli and M. J. Buehler (2011). "Hierarchical structure and nanomechanics of collagen microfibrils from the atomistic scale up." Nano letters **11**(2): 757-766.

Gere, J. M. and B. J. Goodno (2001). "Mechanics of Materials 5th." Brooks Cole.

Ghorashi, S. S., N. Valizadeh and S. Mohammadi (2012). "Extended isogeometric analysis for simulation of stationary and propagating cracks." International Journal for Numerical Methods in Engineering **89**(9): 1069-1101.

Giosia, M. D., I. Polishchuk, E. Weber, S. Fermani, L. Pasquini, N. M. Pugno, F. Zerbetto, M. Montalti, M. Calvaresi, G. Falini and B. Pokroy (2016). "Bioinspired

Nanocomposites: Ordered 2D Materials Within a 3D Lattice." Advanced Functional Materials **26**(30): 5569-5575.

Goldsmith, W. (1999). "Non-ideal projectile impact on targets." International Journal of Impact Engineering **22**(2): 95-395.

GREENAWAY, P. (1985). "Calcium balance and moulting in the Crustacea." Biological Reviews **60**(3): 425-454.

Gronenberg, W. (1995). "The fast mandible strike in the trap-jaw ant Odontomachus." Journal of Comparative Physiology A **176**(3): 399-408.

Grunenfelder, L., N. Suksangpanya, C. Salinas, G. Milliron, N. Yaraghi, S. Herrera, K. Evans-Lutterodt, S. Nutt, P. Zavattieri and D. Kisailus (2014). "Bio-inspired impact-resistant composites." Acta biomaterialia **10**(9): 3997-4008.

Grunenfelder, L. K., N. Suksangpanya, C. Salinas, G. Milliron, N. Yaraghi, S. Herrera, K. Evans-Lutterodt, S. R. Nutt, P. Zavattieri and D. Kisailus (2014). "Bio-inspired impact-resistant composites." Acta Biomaterialia **10**(9): 3997-4008.

Grünewald, T. A., H. Rennhofer, P. Tack, J. Garrevoet, D. Wermeille, P. Thompson, W. Bras, L. Vincze and H. C. Lichtenegger (2016). "Photon Energy Becomes the Third Dimension in Crystallographic Texture Analysis." Angewandte Chemie International Edition **55**(40): 12190-12194.

Gupta, H., S. Krauss, M. Kerschnitzki, A. Karunaratne, J. Dunlop, A. Barber, P. Boesecke, S. Funari and P. Fratzl (2013). "Intrafibrillar plasticity through mineral/collagen sliding is the dominant mechanism for the extreme toughness of antler bone." Journal of the mechanical behavior of biomedical materials **28**: 366-382.

Gupta, H., S. Schratter, W. Tesch, P. Roschger, A. Berzlanovich, T. Schoeberl, K. Klaushofer and P. Fratzl (2005). "Two different correlations between nanoindentation modulus and mineral content in the bone–cartilage interface." Journal of structural biology **149**(2): 138-148.

Gupta, H. S., P. Fratzl, M. Kerschnitzki, G. Benecke, W. Wagermaier and H. O. Kirchner (2007). "Evidence for an elementary process in bone plasticity with an activation enthalpy of 1 eV." Journal of the Royal Society Interface **4**(13): 277-282.

Gupta, H. S., J. Seto, W. Wagermaier, P. Zaslansky, P. Boesecke and P. Fratzl (2006). "Cooperative deformation of mineral and collagen in bone at the nanoscale." Proceedings of the National Academy of Sciences of the United States of America **103**(47): 17741-17746.

Gupta, H. S., J. Seto, W. Wagermaier, P. Zaslansky, P. Boesecke and P. Fratzl (2006). "Cooperative deformation of mineral and collagen in bone at the nanoscale." Proceedings of the National Academy of Sciences **103**(47): 17741-17746.

Gupta, H. S., W. Wagermaier, G. A. Zickler, D. Raz-Ben Aroush, S. S. Funari, P. Roschger, H. D. Wagner and P. Fratzl (2005). "Nanoscale deformation mechanisms in bone." Nano Letters **5**(10): 2108-2111.

Gupta, N., R. Ansari and S. Gupta (2001). "Normal impact of ogive nosed projectiles on thin plates." International Journal of Impact Engineering **25**(7): 641-660.

Gupta, N., M. Iqbal and G. Sekhon (2007). "Effect of projectile nose shape, impact velocity and target thickness on deformation behavior of aluminum plates." International Journal of Solids and Structures **44**(10): 3411-3439.

Hamed, E. and I. Jasiuk (2013). "Multiscale damage and strength of lamellar bone modeled by cohesive finite elements." journal of the mechanical behavior of biomedical materials **28**: 94-110.

Hamed, E., Y. Lee and I. Jasiuk (2010). "Multiscale modeling of elastic properties of cortical bone." Acta Mechanica **213**(1-2): 131-154.

Hamed, I., F. Özogul and J. M. Regenstein (2016). "Industrial applications of crustacean by-products (chitin, chitosan, and chitooligosaccharides): A review." Trends in Food Science & Technology **48**: 40-50.

Hancock, J. and A. Mackenzie (1976). "On the mechanisms of ductile failure in high-strength steels subjected to multi-axial stress-states." Journal of the Mechanics and Physics of Solids **24**(2-3): 147-160.

Hang, F. and A. H. Barber (2011). "Nano-mechanical properties of individual mineralized collagen fibrils from bone tissue." Journal of the Royal Society Interface **8**(57): 500-505.

Hang, F., H. S. Gupta and A. H. Barber (2014). "Nanointerfacial strength between non-collagenous protein and collagen fibrils in antler bone." Journal of The Royal Society Interface **11**(92): 20130993.

Hassenkam, T., G. E. Fantner, J. A. Cutroni, J. C. Weaver, D. E. Morse and P. K. Hansma (2004). "High-resolution AFM imaging of intact and fractured trabecular bone." Bone **35**(1): 4-10.

Havemann, J., U. Müller, J. Berger, H. Schwarz, M. Gerberding and B. Moussian (2008). "Cuticle differentiation in the embryo of the amphipod crustacean Parhyale hawaiensis." Cell and Tissue Research **332**(2): 359-370.

Hibbett, Karlsson and Sorensen (1998). ABAQUS/standard: User's Manual, Hibbitt, Karlsson & Sorensen.

Hight, T. K. and J. F. Brandeau (1983). "Mathematical modeling of the stress strain-strain rate behavior of bone using the Ramberg-Osgood equation." Journal of Biomechanics **16**(6): 445-450.

Hong, T., J. Ooi and B. Shaw (2008). "A numerical simulation to relate the shot peening parameters to the induced residual stresses." Engineering Failure Analysis **15**(8): 1097-1110.

Hull, D. and T. W. Clyne (1996). An introduction to composite materials. Cambridge, UK, Cambridge University Press.

Jäger, I. and P. Fratzl (2000). "Mineralized collagen fibrils: a mechanical model with a staggered arrangement of mineral particles." Biophysical journal **79**(4): 1737-1746.

Ji, B. and H. Gao (2004). "Mechanical properties of nanostructure of biological materials." Journal of the Mechanics and Physics of Solids **52**(9): 1963-1990.

Johnson, G. R. and W. H. Cook (1983). A constitutive model and data for metals subjected to large strains, high strain rates and high temperatures. Proceedings of the 7th International Symposium on Ballistics, The Hague, The Netherlands.

Johnson, G. R. and W. H. Cook (1985). "Fracture characteristics of three metals subjected to various strains, strain rates, temperatures and pressures." Engineering fracture mechanics **21**(1): 31-48.

Katz, E. P. and S.-T. Li (1973). "Structure and function of bone collagen fibrils." Journal of molecular biology **80**(1): 1-15.

Keckes, J., M. Bartosik, R. Daniel, C. Mitterer, G. Maier, W. Ecker, J. Vila-Comamala, C. David, S. Schoeder and M. Burghammer (2012). "X-ray nanodiffraction reveals strain and microstructure evolution in nanocrystalline thin films." Scripta Materialia **67**(9): 748-751.

Khan, W., R. Ansari and N. Gupta (2003). "Oblique impact of projectile on thin aluminium plates." Defence Science Journal **53**(2): 139.

Kisailus, D. and P. Zavattieri (2015). Uncovering and Validating Toughening Mechanisms in High Performance Composites, DTIC Document.

Kitchener, A. (1987). "Fracture toughness of horns and a reinterpretation of the horning behaviour of bovids." Journal of Zoology **213**(4): 621-639.

Koester, K. J., J. Ager and R. Ritchie (2008). "The true toughness of human cortical bone measured with realistically short cracks." Nature materials **7**(8): 672-677.

Krauss, S., P. Fratzl, J. Seto, J. D. Currey, J. A. Estevez, S. S. Funari and H. S. Gupta (2009). "Inhomogeneous fibril stretching in antler starts after macroscopic yielding: indication for a nanoscale toughening mechanism." Bone **44**(6): 1105-1110.

Kuballa, A. V., D. J. Merritt and A. Elizur (2007). "Gene expression profiling of cuticular proteins across the moult cycle of the crab Portunus pelagicus." BMC biology **5**(1): 45.

Kuhn-Spearing, L., C. Rey, H.-M. Kim and M. J. Glimcher (1996). "Carbonated apatite nanocrystals of bone." Synthesis and processing of nanocrystalline powder.

Kulin, R. M., F. Jiang and K. S. Vecchio (2011). "Effects of age and loading rate on equine cortical bone failure." Journal of the Mechanical Behavior of Biomedical Materials **4**(1): 57-75.

Lai, Z. B. and C. Yan (2017). "Mechanical behaviour of staggered array of mineralised collagen fibrils in protein matrix: Effects of fibril dimensions and failure energy in protein matrix." Journal of the Mechanical Behavior of Biomedical Materials **65**: 236-247.

Larson, B. C., W. Yang, G. E. Ice, J. D. Budai and J. Z. Tischler (2002). "Three-dimensional X-ray structural microscopy with submicrometre resolution." Nature **415**(6874): 887-890.

Launey, M. E., M. J. Buehler and R. O. Ritchie (2010). "On the mechanistic origins of toughness in bone." Annual review of materials research **40**: 25-53.

Lemaitre, J. (2012). A course on damage mechanics, Springer Science & Business Media.

Lemaitre, J. and R. Desmorat (2005). Engineering damage mechanics: ductile, creep, fatigue and brittle failures, Springer Science & Business Media.

Libonati, F., G. X. Gu, Z. Qin, L. Vergani and M. J. Buehler (2016). "Bone-Inspired Materials by Design: Toughness Amplification Observed Using 3D Printing and Testing." Advanced Engineering Materials.

Libonati, F., A. K. Nair, L. Vergani and M. J. Buehler (2013). "Fracture mechanics of hydroxyapatite single crystals under geometric confinement." Journal of the mechanical behavior of biomedical materials **20**: 184-191.

Liebi, M., M. Georgiadis, A. Menzel, P. Schneider, J. Kohlbrecher, O. Bunk and M. Guizar-Sicairos (2015). "Nanostructure surveys of macroscopic specimens by small-angle scattering tensor tomography." Nature **527**(7578): 349-352.

Lin, A. Y.-M., P.-Y. Chen and M. A. Meyers (2008). "The growth of nacre in the abalone shell." Acta Biomaterialia **4**(1): 131-138.

Lin, L., J. Samuel, X. Zeng and X. Wang (2017). "Contribution of extrafibrillar matrix to the mechanical behavior of bone using a novel cohesive finite element model." Journal of the Mechanical Behavior of Biomedical Materials **65**: 224-235.

Lubarda, V., E. Novitskaya, J. McKittrick, S. Bodde and P.-Y. Chen (2012). "Elastic properties of cancellous bone in terms of elastic properties of its mineral and protein phases with application to their osteoporotic degradation." Mechanics of materials **44**: 139-150.

Luo, Q., R. Nakade, X. Dong, Q. Rong and X. Wang (2011). "Effect of mineral–collagen interfacial behavior on the microdamage progression in bone using a probabilistic cohesive finite element model." Journal of the mechanical behavior of biomedical materials **4**(7): 943-952.

Luquet, G. (2012). "Biomineralizations: insights and prospects from crustaceans." Zookeys **176**: 103-121.

Mabrouki, T., F. Girardin, M. Asad and J.-F. Rigal (2008). "Numerical and experimental study of dry cutting for an aeronautic aluminium alloy (A2024-T351)." International Journal of Machine Tools and Manufacture **48**(11): 1187-1197.

Mangel, M. and C. W. Clark (1988). Dynamic modeling in behavioral ecology, Princeton University Press.

Manton, S. M. (1977). The Arthropoda: habits, functional morphology, and evolution, Clarendon Press Oxford.

Martin, R. B. and D. B. Burr (1989). Structure, function, and adaptation of compact bone, Raven Pr.

McKittrick, J., P.-Y. Chen, L. Tombolato, E. Novitskaya, M. Trim, G. Hirata, E. Olevsky, M. Horstemeyer and M. Meyers (2010). "Energy absorbent natural materials and bioinspired design strategies: a review." Materials Science and Engineering: C **30**(3): 331-342.

McNeill, P., M. Burrows and G. Hoyle (1972). "Fine structure of muscles controlling the strike of the mantis shrimp, Hemisquilla." Journal of Experimental Zoology **179**(3): 395-415.

Mead, K. S., M. B. Wiley, M. Koehl and J. R. Koseff (2003). "Fine-scale patterns of odor encounter by the antennules of mantis shrimp tracking turbulent plumes in wave-affected and unidirectional flow." Journal of Experimental Biology **206**(1): 181-193.

Meguid, S., G. Shagal, J. Stranart and J. Daly (1999). "Three-dimensional dynamic finite element analysis of shot-peening induced residual stresses." Finite elements in analysis and design **31**(3): 179-191.

Mercer, C., M. He, R. Wang and A. Evans (2006). "Mechanisms governing the inelastic deformation of cortical bone and application to trabecular bone." Acta Biomaterialia **2**(1): 59-68.

Meyers, M. A., P.-Y. Chen, A. Y.-M. Lin and Y. Seki (2008). "Biological materials: structure and mechanical properties." Progress in Materials Science **53**(1): 1-206.

Meyers, M. A., A. Y.-M. Lin, P.-Y. Chen and J. Muyco (2008). "Mechanical strength of abalone nacre: role of the soft organic layer." Journal of the Mechanical behavior of biomedical materials **1**(1): 76-85.

Meyers, M. A., A. Y. Lin, Y. Seki, P.-Y. Chen, B. K. Kad and S. Bodde (2006). "Structural biological composites: an overview." Jom **58**(7): 35-41.

Mischinski, S. and A. Ural (2011). "Finite element modeling of microcrack growth in cortical bone." Journal of Applied Mechanics **78**(4): 041016.

Mohsin, S., F. O'Brien and T. Lee (2006). "Microcracks in compact bone: a three-dimensional view." Journal of anatomy **209**(1): 119-124.

Murphy, E. and S. Patek (2012). "Strike mechanics of an ambush predator: the spearing mantis shrimp." Journal of Experimental Biology **215**(24): 4374-4384.

Nagasawa, H. (2012). "The crustacean cuticle: structure, composition and mineralization." Front Biosci **4**: 711-720.

Naleway, S. E., M. M. Porter, J. McKittrick and M. A. Meyers (2015). "Structural Design Elements in Biological Materials: Application to Bioinspiration." Advanced Materials **27**(37): 5455-5476.

Nalla, R. K., J. H. Kinney and R. O. Ritchie (2003). "Mechanistic fracture criteria for the failure of human cortical bone." Nature materials **2**(3): 164-168.

Neville, A. C. (1993). Biology of fibrous composites: Development beyond the cell membrane. New York, NY, Cambridge University Press.

Neville, A. C. (2012). Biology of the arthropod cuticle, Springer Science & Business Media.

Nikolov, S., H. Fabritius, M. Friak and D. Raabe (2015). "Integrated multiscale modeling approach for hierarchical biological nanocomposites applied to lobster cuticle." Bulgarian Chemical Communications **47**: 423-432.

Nikolov, S., H. Fabritius, M. Friák and D. Raabe (2015). "Integrated multiscale modeling approach for hierarchical biological nanocomposites applied to lobster cuticle." Bulg. Chem. Commun. **47**.

Nikolov, S., H. Fabritius, M. Petrov, M. Friak, L. Lymperakis, C. Sachs, D. Raabe and J. Neugebauer (2011). "Robustness and optimal use of design principles of arthropod exoskeletons studied by ab initio-based multiscale simulations." Journal of the Mechanical Behavior of Biomedical Materials **4**(2): 129-145.

Nikolov, S., H. Fabritius, M. Petrov, M. Friák, L. Lymperakis, C. Sachs, D. Raabe and J. Neugebauer (2011). "Robustness and optimal use of design principles of arthropod exoskeletons studied by ab initio-based multiscale simulations." Journal of the mechanical behavior of biomedical materials **4**(2): 129-145.

Nikolov, S., M. Petrov, L. Lymperakis, M. Friak, C. Sachs, H. O. Fabritius, D. Raabe and J. Neugebauer (2010). "Revealing the Design Principles of High-Performance Biological Composites Using Ab initio and Multiscale Simulations: The Example of Lobster Cuticle." Advanced Materials **22**(4): 519-+.

Nikolov, S., M. Petrov, L. Lymperakis, M. Friák, C. Sachs, H. O. Fabritius, D. Raabe and J. Neugebauer (2010). "Revealing the Design Principles of High-Performance Biological Composites Using Ab Initio and Multiscale Simulations: The Example of Lobster Cuticle." Advanced Materials **22**(4): 519-526.

Nikolov, S. and D. Raabe (2008). "Hierarchical modeling of the elastic properties of bone at submicron scales: the role of extrafibrillar mineralization." Biophysical journal **94**(11): 4220-4232.

Nishino, T., R. Matsui and K. Nakamae (1999). "Elastic modulus of the crystalline regions of chitin and chitosan." Journal of Polymer Science Part B: Polymer Physics **37**(11): 1191-1196.

Nissan, A. H. (1976). "H-bond dissociation in hydrogen bond dominated solids." Macromolecules **9**(5): 840-850.

Novitskaya, E., P.-Y. Chen, E. Hamed, L. Jun, V. A. Lubarda, I. Jasiuk and J. McKittrick (2011). "Recent advances on the measurement and calculation of the elastic moduli of cortical and trabecular bone: a review." Theoretical and Applied Mechanics **38**(3): 209-297.

Ogawa, Y., R. Hori, U.-J. Kim and M. Wada (2011). "Elastic modulus in the crystalline region and the thermal expansion coefficients of α-chitin determined using synchrotron radiated X-ray diffraction." Carbohydrate Polymers **83**(3): 1213-1217.

Ogawa, Y., S. Kimura, M. Wada and S. Kuga (2010). "Crystal analysis and high-resolution imaging of microfibrillar α-chitin from Phaeocystis." Journal of structural biology **171**(1): 111-116.

Oliver, W. C. and G. M. Pharr (2004). "Measurement of hardness and elastic modulus by instrumented indentation: Advances in understanding and refinements to methodology." Journal of materials research **19**(01): 3-20.

Parker, G. A. and J. M. Smith (1990). "Optimality theory in evolutionary biology." Nature **348**(6296): 27-33.

Parwani, R., M. Curto, A. P. Kao, P. J. Rowley, M. Pani, G. Tozzi and A. H. Barber (2016). "Morphological and mechanical biomimetic bone structures." ACS Biomaterials Science & Engineering.

Patek, S., J. Baio, B. Fisher and A. Suarez (2006). "Multifunctionality and mechanical origins: ballistic jaw propulsion in trap-jaw ants." Proceedings of the National Academy of Sciences **103**(34): 12787-12792.

Patek, S. and R. Caldwell (2005). "Extreme impact and cavitation forces of a biological hammer: strike forces of the peacock mantis shrimp Odontodactylus scyllarus." Journal of Experimental Biology **208**(19): 3655-3664.

Patek, S., W. Korff and R. Caldwell (2004). "Biomechanics: deadly strike mechanism of a mantis shrimp." Nature **428**(6985): 819-820.

Patek, S., B. Nowroozi, J. Baio, R. Caldwell and A. Summers (2007). "Linkage mechanics and power amplification of the mantis shrimp's strike." Journal of Experimental Biology **210**(20): 3677-3688.

Patek, S., M. Rosario and J. Taylor (2012). "Comparative spring mechanics in mantis shrimp." Journal of Experimental Biology: jeb. 078998.

Patek, S. N. and R. L. Caldwell (2005). "Extreme impact and cavitation forces of a biological hammer: strike forces of the peacock mantis shrimp Odontodactylus scyllarus." Journal of Experimental Biology **208**(19): 3655-3664.

Pidaparti, R., A. Chandran, Y. Takano and C. Turner (1996). "Bone mineral lies mainly outside collagen fibrils: predictions of a composite model for osternal bone." Journal of biomechanics **29**(7): 909-916.

Planchard, D. (2017). SOLIDWORKS 2017 Reference Guide, SDC Publications.

Poulsen, H. F. (2004). Three-dimensional X-ray diffraction microscopy: mapping polycrystals and their dynamics, Springer Science & Business Media.

Poundarik, A. A., T. Diab, G. E. Sroga, A. Ural, A. L. Boskey, C. M. Gundberg and D. Vashishth (2012). "Dilatational band formation in bone." Proceedings of the National Academy of Sciences **109**(47): 19178-19183.

Pugno, N. M. (2006). "Mimicking nacre with super-nanotubes for producing optimized super-composites." Nanotechnology **17**(21): 5480.

Raabe, D., A. Al-Sawalmih, S. Yi and H. Fabritius (2007). "Preferred crystallographic texture of α-chitin as a microscopic and macroscopic design principle of the exoskeleton of the lobster Homarus americanus." Acta Biomaterialia **3**(6): 882-895.

Raabe, D., A. Al-Sawalmih, S. B. Yi and H. Fabritius (2007). "Preferred crystallographic texture of α-chitin as a microscopic and macroscopic design principle of the exoskeleton of the lobster Homarus americanus." Acta Biomaterialia **3**(6): 882-895.

Raabe, D., P. Romano, C. Sachs, H. Fabritius, A. Al-Sawalmih, S.-B. Yi, G. Servos and H. Hartwig (2006). "Microstructure and crystallographic texture of the chitin–protein network in the biological composite material of the exoskeleton of the lobster Homarus americanus." Materials science and engineering: A **421**(1): 143-153.

Raabe, D., C. Sachs and P. Romano (2005). "The crustacean exoskeleton as an example of a structurally and mechanically graded biological nanocomposite material." Acta Materialia **53**(15): 4281-4292.

Rabiei, R., S. Bekah and F. Barthelat (2010). "Failure mode transition in nacre and bone-like materials." Acta biomaterialia **6**(10): 4081-4089.

Reddy, J. N. (2004). Mechanics of laminated composite plates and shells: theory and analysis, CRC press.

Reilly, D. T., A. H. Burstein and V. H. Frankel (1974). "The elastic modulus for bone." Journal of biomechanics **7**(3): 271IN9273-9272IN12275.

Rhee, Y. W., H. W. Kim, Y. Deng and B. R. Lawn (2001). "Brittle fracture versus quasi plasticity in ceramics: a simple predictive index." Journal of the American Ceramic Society **84**(3): 561-565.

Rho, J.-Y., L. Kuhn-Spearing and P. Zioupos (1998). "Mechanical properties and the hierarchical structure of bone." Medical engineering & physics **20**(2): 92-102.

Rho, J. Y., R. B. Ashman and C. H. Turner (1993). "Young's modulus of trabecular and cortical bone material: ultrasonic and microtensile measurements." Journal of biomechanics **26**(2): 111-119.

Ritchie, R. O., M. J. Buehler and P. Hansma (2009). "Plasticity and toughness in bone." Physics Today **62**(6): 41-47.

Roer, R. and R. Dillaman (1984). "The structure and calcification of the crustacean cuticle." American Zoologist **24**(4): 893-909.

Ruiz-Herrera, J. (1991). Fungal cell wall: structure, synthesis, and assembly, CRC press.

Runkle, J. and J. Pugh (1975). "The micro-mechanics of cancellous bone. II. Determination of the elastic modulus of individual trabeculae by a buckling analysis." Bulletin of the Hospital for Joint Diseases **36**(1): 2.

Sabet, F. A., A. R. Najafi, E. Hamed and I. Jasiuk (2016). "Modelling of bone fracture and strength at different length scales: a review." Interface focus **6**(1): 20150055.

Sachs, C., H. Fabritius and D. Raabe (2006). "Hardness and elastic properties of dehydrated cuticle from the lobster Homarus americanus obtained by nanoindentation." Journal of materials research **21**(08): 1987-1995.

Sasaki, N., A. Tagami, T. Goto, M. Taniguchi, M. Nakata and K. Hikichi (2002). "Atomic force microscopic studies on the structure of bovine femoral cortical bone at the collagen fibril-mineral level." Journal of Materials Science: Materials in Medicine **13**(3): 333-337.

Schaeffler, P., W. Rajner, D. Claar, T. Trendelenburg and H. Nishimura (2005). Production, Properties, and Applications of Alulight® Closed-Cell Aluminum Foams. Proceedings of the Fifth International Workshop on Advanced Manufacturing Technologies.

Schwiedrzik, J., R. Raghavan, A. Bürki, V. LeNader, U. Wolfram, J. Michler and P. Zysset (2014). "In situ micropillar compression reveals superior strength and ductility but an absence of damage in lamellar bone." Nature materials **13**(7): 740-747.

Shen, Z. L., M. R. Dodge, H. Kahn, R. Ballarini and S. J. Eppell (2008). "Stress-strain experiments on individual collagen fibrils." Biophysical Journal **95**(8): 3956-3963.

Siegmund, T., M. R. Allen and D. B. Burr (2008). "Failure of mineralized collagen fibrils: modeling the role of collagen cross-linking." Journal of biomechanics **41**(7): 1427-1435.

Siperko, L. and W. Landis (2001). "Aspects of mineral structure in normally calcifying avian tendon." Journal of structural biology **135**(3): 313-320.

Stephens, D. W. and J. R. Krebs (1986). Foraging theory, Princeton University Press.

Sun, J. and B. Bhushan (2012). "Hierarchical structure and mechanical properties of nacre: a review." Rsc Advances **2**(20): 7617-7632.

Tadayon, M., S. Amini, A. Masic and A. Miserez (2015). "The Mantis Shrimp Saddle: A Biological Spring Combining Stiffness and Flexibility." Advanced Functional Materials **25**(41): 6437-6447.

Tai, K., M. Dao, S. Suresh, A. Palazoglu and C. Ortiz (2007). "Nanoscale heterogeneity promotes energy dissipation in bone." Nature materials **6**(6): 454-462.

Tai, K., F.-J. Ulm and C. Ortiz (2006). "Nanogranular origins of the strength of bone." Nano letters **6**(11): 2520-2525.

Taylor, J. and S. Patek (2010). "Ritualized fighting and biological armor: the impact mechanics of the mantis shrimp's telson." Journal of Experimental Biology **213**(20): 3496-3504.

Taylor, J. R. A. and S. N. Patek (2010). "Ritualized fighting and biological armor: the impact mechanics of the mantis shrimp's telson." Journal of Experimental Biology **213**(20): 3496-3504.

Thoen, H. H., M. J. How, T.-H. Chiou and J. Marshall (2014). "A different form of color vision in mantis shrimp." Science **343**(6169): 411-413.

Thurner, P. J., C. G. Chen, S. Ionova-Martin, L. Sun, A. Harman, A. Porter, J. W. Ager, R. O. Ritchie and T. Alliston (2010). "Osteopontin deficiency increases bone fragility but preserves bone mass." Bone **46**(6): 1564-1573.

Townsend, P. R., R. M. Rose and E. L. Radin (1975). "Buckling studies of single human trabeculae." Journal of biomechanics **8**(3-4): 199IN5201-5200IN5206.

Übeyli, M., R. O. Yıldırım and B. Ögel (2007). "On the comparison of the ballistic performance of steel and laminated composite armors." Materials & design **28**(4): 1257-1262.

Ural, A. (2009). "Prediction of Colles' fracture load in human radius using cohesive finite element modeling." Journal of biomechanics **42**(1): 22-28.

Vagaggini, E., J. M. Domergue and A. G. Evans (1995). "Relationships between hysteresis measurements and the constituent properties of ceramic matrix composites: I, theory." Journal of the American Ceramic Society **78**(10): 2709-2720.

Van de Velde, K. and P. Kiekens (2004). "Structure analysis and degree of substitution of chitin, chitosan and dibutyrylchitin by FT-IR spectroscopy and solid state 13 C NMR." Carbohydrate polymers **58**(4): 409-416.

Vashishth, D., J. Behiri and W. Bonfield (1997). "Crack growth resistance in cortical bone: concept of microcrack toughening." Journal of biomechanics **30**(8): 763-769.

Vasiliev, V. and E. V. Morozov (2013). Advanced mechanics of composite materials and structural elements, Newnes.

Vincent, J. F. and U. G. Wegst (2004). "Design and mechanical properties of insect cuticle." Arthropod structure & development **33**(3): 187-199.

Vincent, J. F. V. and U. G. K. Wegst (2004). "Design and mechanical properties of insect cuticle." Arthropod Structure & Development **33**(3): 187-199.

Wagner, D. W., D. P. Lindsey and G. S. Beaupre (2011). "Deriving tissue density and elastic modulus from microCT bone scans." Bone **49**(5): 931-938.

Wang, R. and H. S. Gupta (2011). "Deformation and fracture mechanisms of bone and nacre." Annual Review of Materials Research **41**: 41-73.

Wang, Y., T. Azaïs, M. Robin, A. Vallée, C. Catania, P. Legriel, G. Pehau-Arnaudet, F. Babonneau, M.-M. Giraud-Guille and N. Nassif (2012). "The predominant role of collagen in the nucleation, growth, structure and orientation of bone apatite." Nature materials **11**(8): 724-733.

Warren, B. E. (1990). X-ray diffraction. New York, Dover Publications.

Weaver, J. C., G. W. Milliron, A. Miserez, K. Evans-Lutterodt, S. Herrera, I. Gallana, W. J. Mershon, B. Swanson, P. Zavattieri and E. DiMasi (2012). "The stomatopod dactyl club: a formidable damage-tolerant biological hammer." Science **336**(6086): 1275-1280.

Weaver, J. C., G. W. Milliron, A. Miserez, K. Evans-Lutterodt, S. Herrera, I. Gallana, W. J. Mershon, B. Swanson, P. Zavattieri, E. DiMasi and D. Kisailus (2012). "The Stomatopod Dactyl Club: A Formidable Damage-Tolerant Biological Hammer." Science **336**(6086): 1275-1280.

Weiner, S., W. Traub and H. D. Wagner (1999). "Lamellar bone: structure–function relations." Journal of structural biology **126**(3): 241-255.

Weiner, S. and H. D. Wagner (1998). "The material bone: structure-mechanical function relations." Annual Review of Materials Science **28**(1): 271-298.

Welinder, B. S. (1975). "The crustacean cuticle—II. Deposition of organic and inorganic material in the cuticle of Astacus fluviatilis in the period after moulting." Comparative Biochemistry and Physiology Part B: Comparative Biochemistry **51**(4): 409-416.

Werner, E. E. and D. J. Hall (1974). "Optimal foraging and the size selection of prey by the bluegill sunfish (Lepomis macrochirus)." Ecology **55**(5): 1042-1052.

Wess, T. and D. Cairns (2005). "Nanoarchitectures of the animal extracellular matrix: opportunities for synchrotron radiation studies on collagen and fibrillin." Journal of synchrotron radiation **12**(6): 751-757.

Woytowitz, P. and R. Richman (1999). "Modeling of damage from multiple impacts by spherical particles." Wear **233**: 120-133.

Wynne, R. C. (1998). Flexible, lightweight, compound body armor, Google Patents.

Xia, W., L. Ruiz, N. M. Pugno and S. Keten (2016). "Critical length scales and strain localization govern the mechanical performance of multi-layer graphene assemblies." Nanoscale **8**(12): 6456-6462.

Xu, X.-P. and A. Needleman (1994). "Numerical simulations of fast crack growth in brittle solids." Journal of the Mechanics and Physics of Solids **42**(9): 1397-1434.

Yamaguchi, I., S. Itoh, M. Suzuki, M. Sakane, A. Osaka and J. Tanaka (2003). "The chitosan prepared from crab tendon I: the characterization and the mechanical properties." Biomaterials **24**(12): 2031-2036.

Yang, W., I. H. Chen, B. Gludovatz, E. A. Zimmermann, R. O. Ritchie and M. A. Meyers (2013). "Natural flexible dermal armor." Adv Mater **25**(1): 31-48.

Yang, W., X. Huang, R. Harder, J. N. Clark, I. K. Robinson and H.-k. Mao (2013). "Coherent diffraction imaging of nanoscale strain evolution in a single crystal under high pressure." Nature Communications **4**: 1680.

Yang, W., V. R. Sherman, B. Gludovatz, M. Mackey, E. A. Zimmermann, E. H. Chang, E. Schaible, Z. Qin, M. J. Buehler and R. O. Ritchie (2014). "Protective role of Arapaima gigas fish scales: structure and mechanical behavior." Acta biomaterialia **10**(8): 3599-3614.

Yaraghi, N. A., N. Guarín-Zapata, L. K. Grunenfelder, E. Hintsala, S. Bhowmick, J. M. Hiller, M. Betts, E. L. Principe, J. Y. Jung and L. Sheppard (2016). "A Sinusoidally Architected Helicoidal Biocomposite." Advanced Materials **28**(32): 6835-6844.

Younes, I. and M. Rinaudo (2015). "Chitin and chitosan preparation from marine sources. Structure, properties and applications." Marine drugs **13**(3): 1133-1174.

Yukitaka, M. and E. Masahiro (1983). "Quantitative evaluation of fatigue strength of metals containing various small defects or cracks." Engineering Fracture Mechanics **17**(1): 1-15.

Zack, T., T. Claverie and S. Patek (2009). "Elastic energy storage in the mantis shrimp's fast predatory strike." Journal of Experimental Biology **212**(24): 4002-4009.

Zehnder, A. (2012). Fracture Mechanics: Lecture Notes in Applied and Computational Mechanics Vol. 62, Springer.

Zhang, P., M. A. Heyne and A. C. To (2015). "Biomimetic staggered composites with highly enhanced energy dissipation: Modeling, 3D printing, and testing." Journal of the Mechanics and Physics of Solids **83**: 285-300.

Zhang, Y. (2016). "Nanostructure and nanomechanics of stomatopod cuticle." Doctoral Thesis.

Zhang, Y., O. Paris, N. J. Terrill and H. S. Gupta (2016). "Uncovering three-dimensional gradients in fibrillar orientation in an impact-resistant biological armour." Sci Rep **6**: 26249.

Zienkiewicz, O. C., R. L. Taylor and R. L. Taylor (1977). The finite element method, McGraw-hill London.

Zimmermann, E. A., B. Gludovatz, E. Schaible, N. K. Dave, W. Yang, M. A. Meyers and R. O. Ritchie (2013). "Mechanical adaptability of the Bouligand-type structure in natural dermal armour." <u>Nature communications</u> **4**.

Zimmermann, E. A., B. Gludovatz, E. Schaible, N. K. N. Dave, W. Yang, M. A. Meyers and R. O. Ritchie (2013). "Mechanical adaptability of the Bouligand-type structure in natural dermal armour." <u>Nature Communications</u> **4**: 2634.

Zimmermann, E. A., E. Schaible, H. Bale, H. D. Barth, S. Y. Tang, P. Reichert, B. Busse, T. Alliston, J. W. Ager, 3rd and R. O. Ritchie (2011). "Age-related changes in the plasticity and toughness of human cortical bone at multiple length scales." <u>Proc Natl Acad Sci U S A</u> **108**(35): 14416-14421.

Zioupos, P. and J. Currey (1994). "The extent of microcracking and the morphology of microcracks in damaged bone." <u>Journal of Materials Science</u> **29**(4): 978-986.